UNIVERSITÉ DU LUXEMBOURG

PhD-FSTM-2022-073

The Faculty of Science, Technology and Medicine

DISSERTATION

Defence held on 27/06/2022 in Luxembourg

to obtain the degree of

DOCTEUR DE L'UNIVERSITÉ DU LUXEMBOURG

EN INFORMATIQUE

by

Ehsan RAEI

Born on 14 September 1983 in Tehran (Iran)

mmWave Cognitive Radar: Adaptive Waveform Design and Implementation

Dissertation defence committee

Dr Mohammad Alaee-Kerahroodi, dissertation supervisor
Research Scientist, Université du Luxembourg

Dr Antonio De Maio
Professor, Università degli studi di Napoli Federico II

Dr Maria Sabrina Greco
Professor, Università di Pisa

Dr Björn Ottersten, Chairman
Professor, Université du Luxembourg

Dr Bhavani Shankar, Vice Chairman
Assistant Professor, Université du Luxembourg

Dissertation Defence Committee:

Committee members:

Prof. Dr. Björn Ottersten, Chairman
Professor and Director of SnT, University of Luxembourg

Prof. Dr. Bhavani Shankar, Deputy Chairman
Assistant Professor , SnT, University of Luxembourg

Prof. Dr. Antonio DeMaio, Member
Professor, University of Naples, Italy

Prof. Dr. Maria Sabrina Greco, Member
Professor, University of Pisa, Italy

Supervisor:

Dr. Mohammad Alaee-Kerahroodi
Research Scientist, SnT, University of Luxembourg

Doctoral School membership

Affidavit

I hereby confirm that the PhD thesis entitled "mmWave Cognitive Radar: Adaptive Waveform Design and Implementation" has been written independently and without any other sources than cited.

Luxembourg, _____ _____

Ehsan Raei

Abstract

This research focuses on waveform design and implementation for mmWave *cognitive radar* systems. Cognitive radar refers to systems that can interact intelligently with their surroundings by adapting both the transmitter and the receiver. Indeed, the radio frequency spectrum will continue to become more crowded, and in this context, the new generation of radar systems will require to sense the environment and avoid making interference for other systems, like communications. To this end, cognitive radars require to have intelligent transmission strategies by utilizing *waveform diversity* and performing *resources management*. In general, the most essential resources available for radar systems are time (range), frequency, polarization, and spatial, and managing these results in waveform diversity for radar systems. Diverse waveforms and Multiple-Input Multiple-Output (MIMO) radars are concepts that are inextricably linked.

When compared to the traditional phased array systems, MIMO radar offers a variety of transmission strategies derived from different optimization objectives and constraints that improve angular estimation and detection performance. In colocated MIMO radars, waveform design can be divided into two categories; uncorrelated and correlated waveform sets. In the first group, waveform optimization is being performed in order to provide a set of nearly orthogonal sequences to exploit the advantages of the largest possible virtual aperture. In this case, the sequences in the waveform set needs to be orthogonal to one another in order to be separated on the received side. In addition, small auto-correlation sidelobes avoids masking of weak targets by the range sidelobes of strong targets and mitigates the deleterious effects of distributed clutter. In this context, we propose Weighted BSUM sEquence SeT (WeBEST) approach to minimize the ℓ_p-norm ($p \geq 2$ and $0 < p \leq 1$) of auto- and cross-correlation based on Block Successive Upper Bound Minimization (BSUM) method. This work offers a flexible framework to design waveform with different properties. For instance by choosing $p = 2$, $p \to \infty$ and $p \to 0$ a waveform with good Integrated Sidelobe Level (ISL), Peak Sidelobe Level (PSL) and sparse auto- and cross-correlation can be obtained, respectively. Through the numerical results we compare the performance of our method with the state of the art. We show that the proposed method is able to meet the ISL lower bound when $p = 2$ and decrease the PSL gap with the Welch lower bound when $p \to \infty$. Furthermore, by selecting the appropriate weights we can focus the sidelobe minimization in specific range. In the second category, a correlated set of waveforms is transmitted to form a directional probing beampattern on the transmit side. Because only the waveform correlation matrix needs to be optimized in this case, phase shifters can be removed in the both sides of transmit and receive arrays, lowering hardware costs, which is important in mass production. As a result, the probing signal can be used as a tool to improve radar performance by increasing the SINR. This,

however, necessitates knowledge from the environment, which can be obtained through a cognitive paradigm. In this context, we offer multiple beampattern shaping metrics for MIMO radar systems, including spatial-ISLR and beampattern matching. To tackle the resulting problems, we introduce several optimization strategies based on Coordinate Descent (CD), Semi-definite Relaxation (SDR), penalty approach, and BSUM. We exhibit the performance of the proposed methods and compare them to their state-of-the-art equivalents in the numerical results.

In the third investigation, we show that a good beampattern response results in a correlated waveform, whereas orthogonality necessitates as much uncorrelated waveforms as possible. As a result, beampattern shaping and orthogonality are mutually contradictory. In this regards, we propose UNImodular set of seQUEnce design (UNIQUE) method to make a trade-off between these two metrics, based on CD approach. In this method we consider the weighted sum of spatial-Integrated Sidelobe Level Ratio (ISLR) and range-ISLR as design metric. Adjusting the weight between these two ISLR, plays important role to make the trade-off. In the numerical results we show that, by choosing an appropriate weight, the waveform is able to discriminate the target and mitigate the interference simultaneously. However, this cannot be achieved when minimizing just the spatial- or range-ISLR individually.

We look at resource management for three different types of resources in the fourth study: time, frequency, and spatial domains. We propose Waveform design for beampattern shapIng and SpEctral masking (WISE) as a framework for tailoring the beampattern in MIMO radar systems while maintaining the proposed waveform's unimodularity, desirable spectral occupancy, and orthogonality. The problem formulation leads to a non-convex quadratic fractional programming. We propose an effective iterative to solve the problem, where each iteration is composed of a Semi-Definite Programming (SDP) followed by eigenvalue decomposition. Some numerical simulations are provided to illustrate the superior performance of our proposed over the state-of-the-art.

The next research study focuses on maximizing Signal to Interference and Noise Ratio (SINR) through joint waveform and filter design. Two algorithms based on CD and the Alternating Direction Method of Multipliers (ADMM) are proposed. The numerical results reveal the improvements made by the proposed algorithms over the state of the art.

The final study looks at the problem of joint spectral shaping and waveform orthogonality in MIMO radar systems. The Parseval theorem is used in the first part to combine the two objectives related to orthogonality and spectral behaviour of the waveforms into one objective. In the second part, we use CD framework to optimize a weighted sum of the two aforementioned objectives. The waveforms, along with the receive processing, are

designed to enhance the radar detection performance while avoiding certain frequency bands occupied by communications interference. For a representative scenario of cognitive radars, the designed system without loss of generality is then implemented using a custom built Software Defined Radio (SDR) based prototype developed on Universal Software Radio Peripheral (USRP) from national instruments. These USRPs are quite flexible in terms of transmitting waveforms, but operate at sub-6 GHz frequencies with a maximum instantaneous bandwidth of 160 MHz. However, the implemented framework and the design methodologies can be applied and utilized in mmWave frequencies.

This thesis concludes with summarizing the main research findings and some remarks on future directions and open problems.

Acknowledgements

This work was supported by FNR (Luxembourg) through the BRIDGES project "Adaptive mm-Wave Radar platform for Enhanced Situational Awareness: Design and Implementation (AWARDS)" under Grant CPPP17/IS/11827256/AWARDS.

First of all, I would like to express my gratitude to my supervisor, Dr. Mohammad Alaee-Kerahroodi, for his continuous support and encouragement throughout my PhD studies which was vital in making this thesis a reality. He is the true definition of a leader and the ultimate role model, whose guidance from the initial step in research enabled me to develop an understanding of the subject. I am thankful for the extraordinary experiences he arranged for me and for providing opportunities for me to grow professionally. I would also like to thank my co-supervisor, Prof. Dr. Bhavani Shankar. His daily supervision and his positive attitude played a crucial role in the accomplishment of this thesis. Throughout my PhD, I had numerous meeting with Prof. Dr. Shankar discussing various issues ranging from my research to daily issues. I am grateful for his friendly personality; he was not only my co-supervisor, but also, sometimes acted as a big brother or a friend under different circumstances.

Moreover, I would like to thank my PhD committee member, Prof. Dr. Antonio DeMaio. His extensive knowledge and experience helped me to be on the right track with my research. I grateful to Prof. Dr. Maria Sabrina Greco and Prof. Dr. Björn Ottersten for accepting to be in my defense committee.

I also wish to thank all my (current and past) colleagues of the SPARC/SIGCOM group of SnT for creating an enjoyable working environment. Specially, I would like to thank Saeid, Alireza, Arsham, Mahdi, Robin, Gabriel and Hossein.

Finally, my foremost gratitude and recognition goes to my family for their unwavering support. Let me start with my wife Monireh amd Mehrsana thanks a lot for showing me how to love and for always being there for me. My deepest appreciation goes to my parents Morteza and Josephine, and my siblings, Hossein and Farideh for their unconditional and insatiable dedication and love.

Ehsan Raei
Luxembourg, March 2022

Contents

List of Figures

List of Tables

Acronyms

ADAS	Advanced Driver Assistance Systems
ADC	Analog to Digital Converter
ADMM	Alternating Direction Method of Multipliers
BCD	Block Coordinate Descent
BIC	Beampattern Optimization With Spectral Interference Control
BiST	Binary Sequences seTs
BS	Base Station
BSUM	Block Successive Upper Bound Minimization
CA	Cyclic Algorithm
CAN	Cyclic Algorithm-New
CD	Coordinate Descent
CDMA	Code-Division Multiple Access
CFAR	Constant False Alarm Rate
CM	Constant Modulus
CNR	Clutter to Noise Ratio
CP	Continuous Phase
CPI	Coherent Pulse Interval
CW	Continuous Wave
DAC	Digital to Analog Converter
DDMA	Doppler-Division Multiple Access
DFT	Discrete Fourier Transform
DP	Discrete Phase
DSP	Digital Signal Processing
DUC	Digital Up Converter
ED	Eigenvalue Decomposition

FDMA Frequency-Division Multiple Access

FFT Fast Fourier Transform

FMCW Frequency Modulated Continuous Wave

FPGA Field Programmable Gate Array

GD Gradient Descent

GFP Generalized Fractional Programming

GUI Graphical User Interface

HW Hardware

IADPM Inexact Alternating Direction Penalty Method

IBS Iterative Beampattern with Spectral design

ICCL Integrated Cross Correlation Level

IF Intermediate Frequency

INR Interference to Noise Ratio

ISL Integrated Sidelobe Level

ISLR Integrated Sidelobe Level Ratio

LFM Linear Frequency Modulation

LNA Low Noise Amplifier

LRR Long-Range Radar

LTE Long Term Evolution

MBI Maximum Block Improvement

MCS Modulation and Coding Schemes

MIA Majorized Iterative Algorithm

MIMO Multiple-Input Multiple-Output

MM Majorization-Minimization

MPSK M-ary Phase Shift Keying

MRMC MIMO Radar and MIMO Communication

MRR Mid-Range Radar

MTI Moving Target Indicator

MVDR Minimum Variance Distortionless Response

NI National Instruments

NSGA Non-Dominated Sorting Genetic Algorithm

OTA Over-The-Air

PA Power Amplifier

PAC Perception/Action Cycle

PAR Peak-to-Average Ratio

PDCCH Physical Downlink Control Channel

PDSCH Physical Downlink Shared Channel

PDR Projection, Descent, and Retraction

PMCW Phase Modulated Continuous Wave

PMM Proximal Method of Multipliers

PRF Pulse Repetition Frequency

PRI Pulse Repetition Interval

PSL Peak Sidelobe Level

PSL Peak Sidelobe Level

QCQP Quadratic Constraint Quadratic Programming

QSDR Quantized Semi-definite Relaxation

RCS Radar Cross Section

RF Radio Frequency

ROC Receiver Operating Characteristic

SD Steepest Descent

SDP Semi-definite Programming

SDR Semi-definite Relaxation

SDR Software-Defined Radio

SILR Spectral Integrated Level Ratio

SINR Signal to Interference plus Noise Ratio

SIMO Single-Input Multiple-Output

SISO Single-Input Single-Output

SNR Signal to Noise Ratio

SQP Semidefinite Quadratic Programming

SRR Short-Range Radar

STAP Space Time Adaptive Processing

STTC Space-Time Transmitting Code

SVD Single Value Decomposition

TDMA Time-Division Multiple Access

ULA Uniform Linear Array

UNIQUE UNImodular set of seQUEnce design

VCO Voltage-Controlled Oscillator

USRP Universal Software Radio Peripheral

WeBEST Weighted BSUM sEquence SeT

WISE Waveform design for beampattern shapIng and SpEctral masking

"The moving finger writes; and, having writ, moves on: nor all thy piety nor wit shall lure it back to cancel half a line, nor all thy tears wash out a word of it."

Omar Khayyam

Chapter 1

Introduction

High-resolution Millimeter Wave (mmWave) radar sensors are becoming integral in applications ranging from automotive safety and autonomous driving to health monitoring of infants and the elderly. These sensors link the physical world with the virtual world of information processing are ideal in different applications such as autonomous vehicles, in-cabin monitoring, occupancy sensing, drones, multi-copters, gesture recognition, smart buildings, smart street lighting, factories, healthcare and robotics.

The rapid development of high-performance, low-cost integrated MIMO radar systems in the mmWave spectrum motivate this study. Millimeter waves are kind of radio frequency that their wavelength are in millimeter range, between 1 mm to 1 cm, which their frequency are between 30 GHz to 300 GHz equivalently. This kind of radio frequencies have several advantages including the following,

- **Small size:** In general, the electronics components such as capacitors, resistors and antennas, in short wavelength (high frequency) are smaller rather than lower frequencies. Therefore, the size of system components required to process mmWave signals are small [4].
- **Lower cost fabrication:** Smaller component size leads to lower power consumption and lower fabrication cost of the final product. This property is attractive for radar hardware designers to incorporate lots of components for building MIMO radar systems, such as transmitters, receivers, antennas, Analog to Digital Converter (ADC) and Digital Signal Processing (DSP) processors [5].
- **High range and angular resolution and high accuracy:** Range resolution is the ability of discriminating of two or more objects in range domain. The range resolution in radar systems is highly depended on the bandwidth of the signal.

Since mmWave radars are able to use larger bandwidth in compare with other radio frequencies, in general they are capable to obtain higher resolution [5, 6]. For example a mmWave Frequency Modulated Continuous Wave (FMCW) radar provides about 4 GHz bandwidth which is able to achieve 3.5cm resolution [4].

In addition, using MIMO technology and transmitting orthogonal waveform, the array in the receiver can be enlarged virtually and subsequently enhances the angular resolution [5].

Finally, mmWave radar systems operating at 76–81GHz or $58-62$ GHz (with a corresponding wavelength of about $4mm$), will have the ability to detect movements that are as small as a fraction of a millimeter [4]

Automotive: mmWave MIMO radars systems are being increasingly integrated into commercial vehicles to support the Advanced Driver Assistance Systems (ADAS) by enabling robust and high performance target detection, localization, as well as interference (clutter) mitigation. Automotive radar sensors should be able to detect every single elements of the environment, and one solution to this end is equipping the vehicle with three types of radar, namely, Long-Range Radar (LRR) (for adaptive cruise control), Mid-Range Radar (MRR) (for cross traffic alert and lane change assist) and Short-Range Radar (SRR) (for parking aid, obstacle/pedestrian detection).

Smart buildings: mmWave radar sensors, can be installed in public areas, like airports hospitals, universities, and smart public buildings to help in crowd control and provide precise information about the scene by joint processing while respecting privacy.

Healthcare: Monitoring bio-signals include respiratory and heartbeat signals, which not only reveal a patient's physical health status but also make it easier to run some public health systems daily. Currently, conventional contacted (ECG, optics, airflow sensing, chest wall mechanical displacement sensing, and blood pressure sensing) and radar-based non-contacted detection are used to detect breathing and heartbeat. Despite having good accuracy and consistency, contact vital sign detection is not perfect. For patients with burns, skin infections, etc., it is not helpful. In contrast, by sensing millimetre-scale displacement of the thoracic surface, the mmWave radar sensors are used to extract respiratory and heartbeat signals utilizing a variety of signal processing techniques. The mmWave radar detection system offers significant development potential [7].

Traffic control and monitoring: Intersection control, speed monitoring, vehicle counting, and collision avoidance are only a few of the complex issues that need to be addressed in traffic control and infrastructure monitoring. The installed sensors' information is used by the infrastructure systems for traffic management and monitoring in a variety of ways, including dynamic green-light control, statistics gathering, measurement of position and velocity, and identification of fast moving objects across large areas. mmWave radars as opposed to optical system sensors like cameras and LiDAR sensors, is unaffected by variations in the brightness of its surroundings. Additionally, mmWave radars can easily penetrate through mist, rain and fog. Consequently, neither the time of day nor the weather have a significant impact on their ability to identify objects. The use of mmWave radar as infrastructure sensors is being highlighted by these benefits. [8, 9].

Despite of the advantages of using mmWave, due rather large absorption in the atmosphere, these radio frequency are used mainly in short-range radar systems [10].

1.1 Cognitive Radar Waveform Design

Cognitive MIMO radar systems are smart sensors which interact with the environment to enhance their performance [11]. Time (range), spatial and spectrum are the most important resources, and resources management is one important aspects in cognitive MIMO radar systems (Figure 1.1).

This resources management necessitates an adaptive waveform design approach. Generally, *auto- and cross-correlation sidelobes minimization*, *beampattern shaping* and *spectral shaping* and are the approaches which can be considered for managing the time, spatial and spectrum, respectively. FMCW is the conventional solution for implementing a MIMO mmWave radar system which the block diagram is given in Figure 1.2 [12]. As can be seen in the transmitter part, the waveform generator determines a sequence of large bandwidth of Linear Frequency Modulation (LFM) (range of GHz) that are generated by the Voltage-Controlled Oscillator (VCO). Then, the signal is amplified by a Power Amplifier (PA) and transmitted. In the receiver part, the received signal is processed by a Low Noise Amplifier (LNA) and then down converted in frequency using the same VCO signal before being filtered. Thanks to the combination of VCO and mixer in the receiver, a part of signal processing (stretch processing) is done in analog domain. This approach significantly decreases the bandwidth of the receive signal, which leads to lower sampling rate for the ADC (range of 10 MHz). The main drawback of FMCW radar is that there aren't many options for modifying the transmit waveform's parameters.

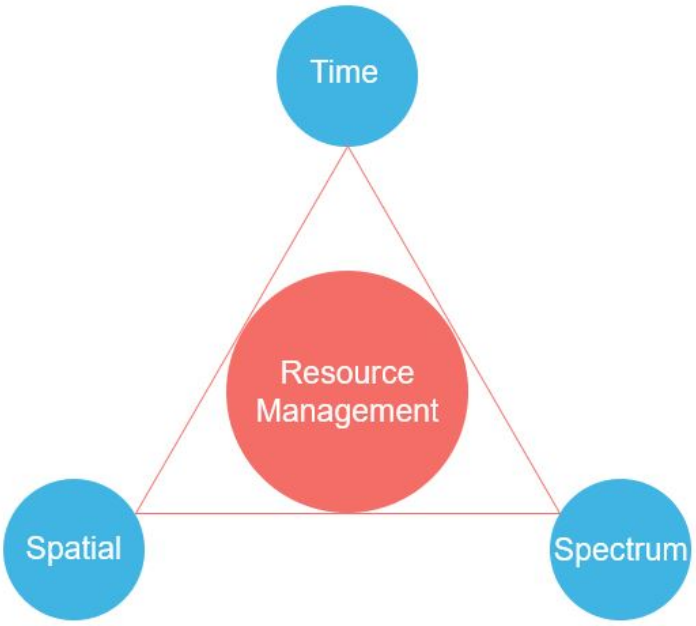

FIGURE 1.1: The three main resources in MIMO radar systems.

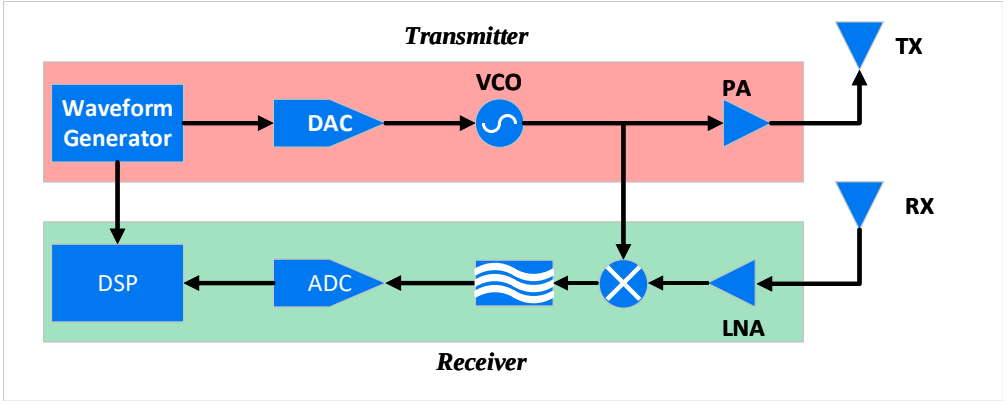

FIGURE 1.2: Block Diagram of an FMCW radar System [12].

On the other hand, Phase Modulated Continuous Wave (PMCW) radar system is an emerging technology for mmWave radar systems [13–15]. The block diagram of typical PMCW radar is given in Figure 1.3 [12]. The Digital to Analog Converter (DAC) output is modulated from an oscillator to generate a phase modulated continuous waveform signal. In this case, due to obtaining a large bandwidth baseband signal, high sampling rate (order of GHz) DAC and ADC are required which increase the power consumption but lead to higher capability of noise mitigation. Tho most advantages of PMCW radars arises from using arbitrary phase codded waveforms, which has several advantages:

- **Flexibility:** Using an arbitrary waveform gives the flexibility to radar engineers for designing waveform in three main domains, time (range), space and spectrum

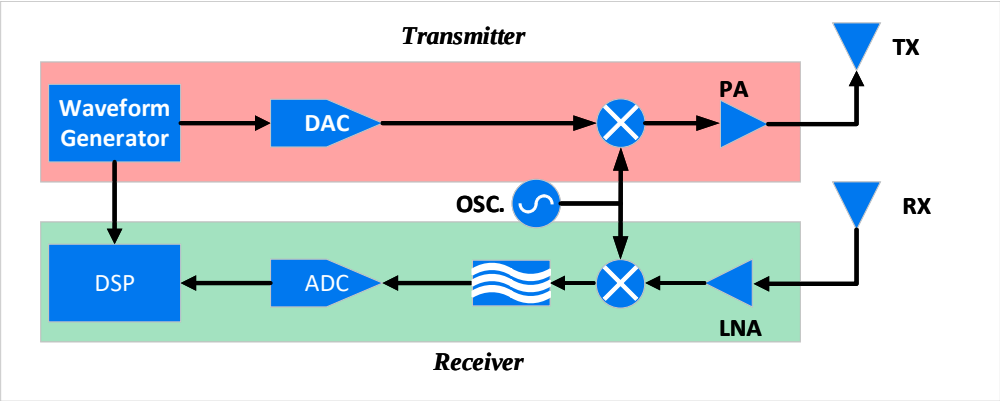

FIGURE 1.3: Block Diagram of an PMCW radar System [12].

[12].

- **Interference:** The interference in FMCW radar is highly dependent on the LFM. However, since PMCW is a kind of pseudo noise waveform they are more robust against the interference [12, 16].

Due to the advantages and flexibility of using phase codded waveforms, in this study we focus on designing of phase codded waveforms. This kind of waveforms are constant modulus which play important role in enhancing the performance of MIMO radar systems. Constant modulus waveforms are attractive for radar system designers due to efficient utilization of the limited transmitter power of PA and simplicity of hardware implementation.

In the following we enumerate the state of the arts in *auto- and cross-correlation sidelobes minimization*, *beampattern shaping* and *spectral shaping* via waveform design for MIMO radar systems.

1.1.1 Auto and Cross Correlation Minimization in MIMO Radars

Unlike the conventional phased array radars the MIMO radar systems are capable to transmit different waveforms through the all antennas. This waveform diversity enables the MIMO radar system to form the virtual array which enhances the performance of MIMO radar, in terms of spatial resolution, probability of detection, localization, identification, classification, etc [17]. Figure 1.4 shows the concept of the virtual array in MIMO radars. In this figure the number of transmitter and receiver are $M_T = 3$ and $M_R = 4$, respectively. Each transmitter transmits an arbitrary waveform, which is indicated by the colors green, red, and dark blue. Each receiver has three match filters that correspond to each transmitter in order to build the virtual array. In this case the virtual array can be formed by arranging the matched filter output as shown in

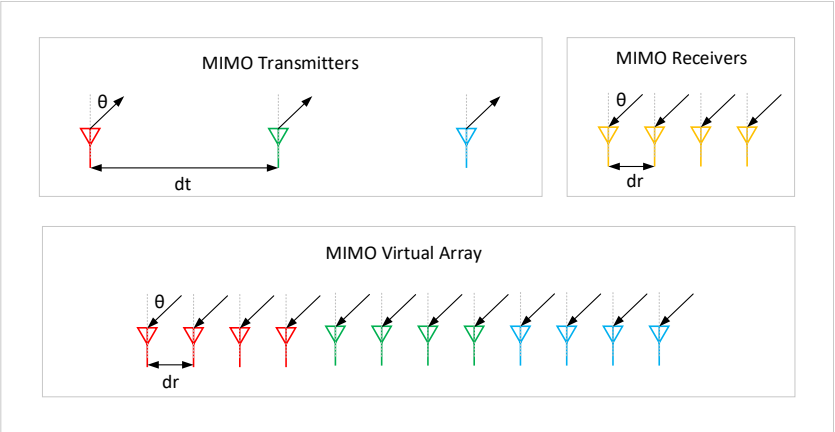

FIGURE 1.4: The virtual array concept in MIMO radars.

Figure 1.4. Please note that in this figure, $d_T = M_T d_R$, where d_T and d_R be the distance between the transmitter and receiver antennas respectively.

In order to form the virtual array and enhancing the angular resolution, the received signal in MIMO radar system should be separable (orthogonal) in receiver while a set of arbitrary waveforms are adopted in the transmit side. In general there are four main techniques to achieve orthogonality, namely Time-Division Multiple Access (TDMA), Frequency-Division Multiple Access (FDMA), Doppler-Division Multiple Access (DDMA) and Code-Division Multiple Access (CDMA) [18, 19]. Among them, TDMA, FDMA,and DDMA can provide almost perfect orthogonality. However,comparing with CDMA, they suffer from strong azimuth-Doppler coupling, lower amount of maximum Doppler frequency and shorter target detection range, respectively [18]. In this context, we investigate a CDMA-MIMO radar system with low cross-correlations, which has historically been utilized as a measure for designing a set of approximately orthogonal sequences and leveraging the virtual array. Low auto-correlation, on the other hand, is a necessity in every radar system to prevent masking weak targets by a strong target's range sidelobes and to limit the harmful effects of distributed clutter returns close to the target of interest [20]. Figure 1.5 shows the masking of a weak target with the sidelobes of strong target.

As a result, in MIMO radar systems, decreasing auto- and cross-correlation is a need. This necessity naturally led to the usage of ISLR/ PSLR minimization as the design metric, which is pursued via a variety of methods, including CAN, MM, ADMM and CD. The authors in [2, 21] proposed the CAN algorithm to optimize sequence with good ISL using the alternating minimization technique. However, instead of directly solving the ISL minimization, they solved its approximation. To solve the ISL minimization problem the authors in [3] proposed the MM-Corr algorithm and the authors in [22] proposed the ISL-NEW algorithm, both using the majorization-minimization technique. The authors

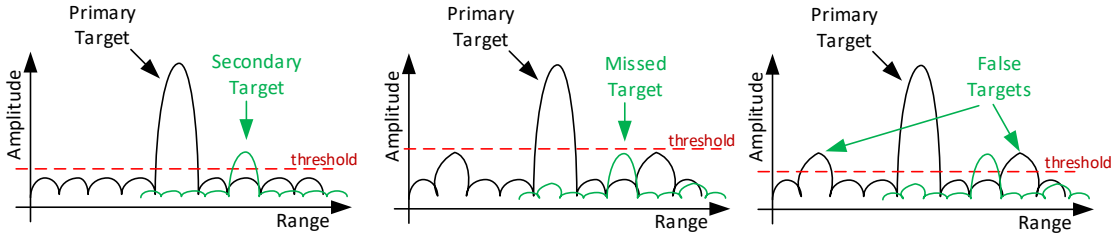

(A) Correct detection (B) Missed target (C) False targets

FIGURE 1.5: Sketch of matched filter output, displaying the effects of waveform optimization in detecting weak signals. In (a), two targets are correctly detected when a waveform with low PSL is adopted as the transmitting signal. In (b) the secondary target is missed, and in (c) false targets are detected due to the large sidelobes of the transmitted waveform.

in [23] used the ADMM technique to solve an approximation of the ISL minimization problem. The authors in [24] used the CD technique, to minimize a weighed sum of ISL and PSL under discrete phase constraint. They have reported superior performance comparing with the state-of-the art by using the CD approach.

1.1.2 Beampattern Shaping

Transmit beampattern shaping, which involves manipulating the spatial distribution of transmit power, can help improve radar performance by increasing power efficiency, boosting detection probability, enhancing target identification, and improving interference mitigation. The idea behind transmit beam shaping is to concentrate transmit power at desirable angles while reducing it at undesirable ones [25]. From a waveform design perspective, there are two methods for beampattern shaping, indirect and direct methods [26, 27]. In indirect (two-step) method, the waveform correlation matrix is firstly designed and the waveform matrix is subsequently obtained through one of the decomposition methods [28–36] while in direct method, the waveform is designed in one step [26, 27, 37–43]. On the other hand, there are several metrics (objective functions) to obtain the optimum beampattern such as, beampattern matching, spatial-ISLR/PSLR minimization, and SINR maximization.

Beampattern Matching The goal of beampattern matching is to reduce the gap between the desired and designed beampattern. For instance, the following papers have worked on designing the waveform covariance matrix employing beampattern matching. The authors in [28] devised a method to address the joint beampattern shaping and the cross-correlation minimization in spatial domain through Semidefinite Quadratic Programming (SQP) technique. In [29], Cyclic Algorithm (CA) is presented to shape the beampattern under low PAR constraint. In [34, 35], the authors propose a covariance matrix design

method based on Discrete Fourier Transform (DFT) coefficients and Toeplitz matrices. The DFT-based technique provides a well-match transmit beampattern at low complexity. However, the drawback of the DFT-based method is that, for small number of antennas, the performance of the DFT-based method is slightly poorer. On the other hand, several papers focus on designing directly the transmit waveforms for beampattern shaping. For example, in [26], two optimization algorithms based on ADMM are proposed under constant modulus constraint for the probing waveform. In [27], a method based in ADMM is proposed to design a beampattern in wide-band systems. In [41], a method for beampattern matching is addressed based on gradient decent which they term it Projection, Descent, and Retraction (PDR). In [42], the authors propose a method based on MM for beampattern matching under PAR constraint in two cases of wide- and narrow-band.

Spatial-ISLR and PSLR minimization In Spatial-ISLR and PSLR minimization approach, the aim is to minimize the ratio of *summation of beampattern response on undesired over desired angles*, and to minimize the ratio of *maximum beampattern response on undesired angles over minimum beampattern response on desired angles*, respectively. In [32], a method based on SDR under constant energy and 3 dB main beam-width constraint is proposed to minimize the spatial-ISLR. In [44], the robust designs of waveform covariance matrix through optimizing the worst case transmit beampattern are considered to minimize the spatial-ISLR and -PSLR of beampatterns, respectively. Unlike two aforementioned methods, [37, 40, 43] propose a direct waveform design solution. The authors in [37] propose the efficient UNIQUE algorithm based on CD method to minimize spatial- and range-ISLR under four different constraints, namely, limited energy, PAR, continuous and discrete phase constraints. The method proposed in [43] is similar to UNIQUE without considering range-ISLR metric and PAR and limited energy constraints. A method based on ADMM is proposed in [40] to minimize the spatial-PSLR under constant modulus constraint.

SINR maximization In SINR optimization approaches, the problem does not deal with the beampattern directly. However, the beampattern is implicitly shaped as a result of transmit waveform optimization. For example [30, 31] address the problem of waveform design in the presence of signal dependence clutter. In these works, an iterative approach is presented to jointly optimize the transmit waveform and receive filter to maximize the output SINR. The authors in [45] propose Majorized Iterative Algorithm (MIA) based on MM method for joint waveform and filter design under similarity, constant modulus (MIA-CMC) and PAR (MIA-PC) constraints. While STTC [46] is proposed based on CD to solve the problem under similarity, uncertain steering matrices, continuous or

discrete phase constraints. In [46], a Dinkelbach based method and exhaustive search is proposed for continuous and discrete phase constraints respectively.

1.1.3 Spectral Shaping

In cognitive MIMO radar systems, spectral shaping is a key part of resource management. The cognitive radar system can effectively use the available bandwidth with this method. Coexistence of communications and cognitive MIMO radar systems, in which the entire bandwidth is shared between these two systems based on priorities, is one appealing application of spectral shaping [47]. There are several methods for spectral shaping. For instance, in [1, 23, 48–51] spectral matching approach is proposed to shape the spectral of the transmit waveform. In [52, 53], the authors consider a waveform design approach to maximize SINR, while the spectral behaviour is considered as a constraint. In [54, 55], the ratio of the maximum stop-band level to the minimum pass-band level is considered as the objective function to shape the spectrum. SILR minimization approach is consider under continuous and discrete phase constraints in [47]. The design of constant modulus waveform for beampattern matching under spectral constraint are addressed in [50, 56]. To tackle the non-convex optimization problem the authors in [50] and [56] propose Iterative Beampattern with Spectral design (IBS) and Beampattern Optimization With Spectral Interference Control (BIC) methods respectively.

1.2 Thesis Outline

The focus of this thesis will be on agile waveform design for modern radar systems. Many waveform design techniques could not be successfully implemented for several decades in the mid-twentieth century due to the inherent complexity and hardware considerations. Although the implementation of such algorithms is rather versatile at this time, there are still numerous developments in the field that require a new look and novel techniques, as discussed below:

- Chapter 2 addresses a framework for generalized auto- and cross-correlation minimization. In this chapter we consider the ℓ_p-norm of weighted auto- and cross-correlation under discrete and continuous phase constraint as design metric. To obtain a local optimum solution we proposed WeBEST method based on Block Successive Upper Bound Minimization (BSUM) approach. Choosing an appropriate value for p gives the flexibility to design a waveform with different properties, such as good ISL, PSL and sparse auto- and cross-correlation, while the weighting can

focus the sidelobe reduction in a specific regions. Through the numerical results we show that the propose method meets the lower bound of ISL and decreases the PSL gap with the Welch lower bound, by choosing $p = 2$ and $p \to \infty$, respectively.

- Chapter 3 is devoted for beampattern shaping approaches in MIMO radar systems via waveform design. In this chapter we introduce different beampattern shaping approaches such as, beampattern matching and spatial-ISLR minimization. Subsequently, in order to obtain the sub optimum waveform, we propose different methods based on CD, SDR, BSUM and penalty method.

- Chapter 4 addresses the trade off between spatial and range-ISLR minimization under four practical constraints, namely, limited budget energy, PAR, continuous and discrete phase. We propose UNIQUE algorithm to solve the weighted sum of spatial- and range-ISLR as design metric. First, we show the contradictory between these two ISLRs (orthogonality and beampattern shaping) in MIMO radar systems. On the other words, the optimum beampattern response leads to correlated waveform which is equivalent to phase array radar whereas, the orthogonal waveform needs to be uncorrelated as much as possible. However, the numerical results indicates that, UNIQUE is able to make a good trade-off between having a good beam pattern response and having orthogonality by selecting appropriate values for the scalarization parameter in objective function.

- Chapter 5 considers the resource management in time (range), spatial and spectral domains. This chapter investigates the problem of beampattern shaping with 3 dB beam width, similarity (orthogonality), spectral masking and constant modulus constraints. In order to obtain a local optimum solution, we propose an effective iterative algorithm, where each iteration is composed of a Semi-Definite Programming (SDP) followed by eigenvalue decomposition. By adjusting the parameters such as, similarity and spectral masking level, this algorithm is able to make trade-off between spatial, spectral and time. through the numerical results we show the efficiency of WISE method.

- Chapter 6 presents the joint waveform and filter design for SINR maximization. In this chapter we consider the clutters as signal dependent interference. Based on this assumption we proposed two iterative joint waveform and filter design algorithms to enhance SINR in radar systems, based on CD and ADMM, respectively.

- Chapter 7 considers the joint spectral shaping and orthogonality problem. In this chapter we consider two approaches to consider these two metrics. In the first approach we integrate the range-ISL with spectral shaping in one objective using Parseval theorem, whereas in the second approach we consider the weighted sum

method of SILR and ICCL. For both problem, we consider using CD method to obtain a local optimum solution. In order to demonstrate the performance of the proposed method in real application, is then implemented using a custom built Software-Defined Radio (SDR) based prototype developed on Universal Software Radio Peripheral (USRP) from National Instruments (NI).

Appendices

- Appendices A, B, C, F, D and E include the detailed calculation of the coefficients, proofs of the Theorems and Lemmas given in Chapters 2, 3, 4, 5, 6 and 7 respectively.

1.3 Notations

Please note that, each chapter has its own notation and we define it at each chapter.

1.4 Publications

The work presented in this thesis has resulted in a number of peer-reviewed journal and conference papers, currently published or under revision. The publications included in this thesis are listed here below.

Journals

- J1: **E. Raei**, M. Alaee-Kerahroodi and M. R. B. Shankar, "Spatial- and Range-ISLR Trade-Off in MIMO Radar Via Waveform Correlation Optimization," in IEEE Transactions on Signal Processing, vol. 69, pp. 3283-3298, 2021, doi: 10.1109/TSP.2021.3082460 [37].

- J2: **E. Raei**, S. Sedighi, M. Alaee-Kerahroodi and M. R. B. Shankar, "MIMO Radar Transmit Beampattern Shaping for Spectrally Dense Environments," Submitted to *IEEE Transactions on Aerospace and Electronic Systems*, Accepted on the 22$^{\text{th}}$ July, 2022 [57].

- J3: **E. Raei**, M. Alaee-Kerahroodi, P. Babu and M. R. B. Shankar, "Generalized Waveform Design for Sidelobe Reduction in MIMO Radar Systems," Resubmitted to *IEEE Transactions on Signal Processing* on the 14$^{\text{th}}$ March, 2022 [58].

- J4: M. Alaee-Kerahroodi, **E. Raei**, S. Kumar and M. R. B. Shankar, "Cognitive Radar Waveform Design and Prototype for Coexistence with Communications,"

in *IEEE Sensors Journal*, vol. 22, no. 10, pp. 9787-9802, 15 May15, 2022, doi: 10.1109/JSEN.2022.3163548. [47].

Conferences

- C1: **E. Raei**, M. Alaee-Kerahroodi and B. M. R. Shankar, "Waveform Design for Beampattern Shaping in 4D-imaging MIMO Radar Systems," 2021 21st International Radar Symposium (IRS), 2021, pp. 1-10, doi: 10.23919/IRS51887.2021.9466196 [43].

- C2: **E. Raei**, M. Alaee-Kerahroodi and M. R. Bhavani Shankar, "ADMM Based Transmit Waveform and Receive Filter Design in Cognitive Radar Systems," 2020 IEEE Radar Conference (RadarConf20), 2020, pp. 1-6, doi: 10.1109/RadarConf2043947.2020.9266386 [59].

- C3: **E. Raei**, M. Alaee-Kerahroodi and B. S. M. R., "Beampattern Shaping for Coexistence of Cognitive MIMO Radar and MIMO Communications," 2020 IEEE 11th Sensor Array and Multichannel Signal Processing Workshop (SAM), 2020, pp. 1-5, doi: 10.1109/SAM48682.2020.9104272. pp. 880-883 [39].

- C4: **E. Raei**, M. Alaee-Kerahroodi, B. S. M. R. and B. Ottersten, "Transmit Beampattern Shaping via Waveform Design in Cognitive MIMO Radar," ICASSP 2020 - 2020 IEEE International Conference on Acoustics, Speech and Signal Processing (ICASSP), 2020, pp. 4582-4586, doi: 10.1109/ICASSP40776.2020.9054519 [38].

- C5: **E. Raei**, M. Alaee-Kerahroodi, B. Shankar M.R. and B. Ottersten, "Designing MPSK Sequences and Doppler Filter Bank in Cognitive Radar Systems," 2019 International Radar Conference (RADAR), 2019, pp. 1-6, doi: 10.1109/RADAR41533.2019.171291 [60].

- C6: **E. Raei**, M. Alaee-Kerahroodi and B. Shankar, "MIMO Radar Transmit Beampattern Matching Based on Block Successive Upper-bound Minimization," Accepted by 30$^{\text{th}}$ *European Signal Processing Conference, EUSIPCO 2022.*

- C7: **E. Raei**, M. Alaee-Kerahroodi and B. Shankar, "Waveform Design for Range-ISL Minimization with Spectral Compatibility in MIMO Radars," Accepted by 19$^{\text{th}}$ *European Radar Conference (EuRAD 2022).*

- C8: **E. Raei**, M. Alaee-Kerahroodi and B. Shankar, "ℓ_p-norm Minimization for Auto and Cross Correlation Sidelobe Reduction in MIMO Radar," Accepted by 22$^{\text{nd}}$ *International Radar Symposium, IRS 2022.*

- C9: **E. Raei**, M. Modarres-Hashemi and M. R. Bhavani Shankar, "Range Cell Migration Correction by Fractional Fourier Transform in Synthetic Aperture Radars," 2019 20th International Radar Symposium (IRS), 2019, pp. 1-10, doi: 10.23919/IRS.2019.8768127 [61].

  Note: This work is not included in this thesis to keep it consistent.

Book Chapters

- B1: A. Augusto, N. Mohammad, Mahdi, **R. Ehsan**, A.-K. Mohammad, and M. Bhavani, Shankar, Radar Waveform Design Based on Optimization Theory. IET, 2020, ch. Optimizing radar transceiver for Doppler processing via non-convex programming, pp. 63–92. [62]

Collaborating in:

- B2: Artech House Book - Mathematical Techniques for Signal Design in Modern Radar Systems. Chapter 6: Other Optimization Methods.
- B3: Artech House Book - Mathematical Techniques for Signal Design in Modern Radar Systems. Chapter 8: Waveform Design in 4D-Imaging MIMO Radars.

Chapter 2

Generalized Waveform Design for Sidelobe Reduction in MIMO Radar Systems

MIMO radars transmit a set of sequences that exhibit small cross-correlation sidelobes, to enhance sensing performance by separating the waveforms at the matched filter outputs. The waveforms also require small auto-correlation sidelobes to avoid masking of weak targets by the range sidelobes of strong targets and to mitigate deleterious effects of distributed clutter. In light of these requirements, in this chapter, we design a set of phase-only (constant modulus) sequences that exhibit near-optimal properties in terms of PSL and ISL. At the design stage, we adopt the weighted ℓ_p-norm of auto- and cross-correlation sidelobes as the objective function and minimize it for a general p value, using BSUM. Considering the power output limitation of radar amplifiers, we design unimodular sequences which make the design problem non-convex and NP-hard. To tackle the problem, in every iteration of the BSUM algorithm, we introduce different local approximation functions and optimize them concerning a block, containing a code entry or a code vector.

2.1 Introduction

A complex problem in radar pulse compression (intra-pulse modulation) is the design of waveforms exhibiting small PSL. PSL shows the maximum auto-correlation sidelobe of a transmit waveform in a typical Single-Input Single-Output (SISO)/Single-Input Multiple-Output (SIMO), or phased-array radar system. If this value is not small, then either a false detection or a miss detection may happen, based on the way the Constant

False Alarm Rate (CFAR) detector is tuned [63]. In MIMO radars, PSL minimization is more complex since the cross-correlation sidelobes of transmitting set of sequences need to be also considered. Small value in cross-correlation sidelobes helps the radar receiver to separate the transmitting waveforms and form a MIMO virtual array.

Similar properties hold for ISL of transmitting waveforms where, in case of SISO/SIMO or phased-array radars, the energy of auto-correlation sidelobes should be small to mitigate the deleterious effects of distributed clutter. In solid state-based weather radars, ISL needs to be small to enhance reflectively estimation and improve the performance of hydrometer classifier [64]. In MIMO radar systems, ISL shows the energy leakage of different waveforms in addition to the energy of non-zero auto-correlation sidelobes. Indeed, correlation sidelobes are a form of self-noise that reduce the effectiveness of transmitting waveforms in every radar system [65].

In a MIMO radar system, different multiplexing schemes can be used to eliminate/reduce the cross-correlations level of the transmitting waveforms. Frequency Division Multiplexing (FDM), Doppler Division Multiplexing (DDM), and Time Division Multiplexing (TDM) as some examples [18]. Currently, TDM-MIMO radars are commercialized in the automotive industry with a variety of functionalities from de-chirping and Doppler processing to angle estimation and tracking [66, 67]. However, Code Division Multiplexing (CDM)-MIMO is the next step of the industry, which it can use more efficiently the available resources (time and frequency) [68].

In this chapter, we devise a method called WeBEST to design transmitting waveforms for CDM-MIMO radars. To this end, we adopt the weighted ℓ_p-norm of auto- and cross-correlation sidelobes as the objective function and minimize it under Continuous Phase (CP) and Discrete Phase (DP) constraints. The weighting and p values in the provided formulation create a possibility for intelligent transmission considering the prevailing environmental conditions, where the appropriate p can be selected based on the presence of distributed clutter or strong targets [69–72]. For example, choosing $p \to 0$ and minimizing the ℓ_p-norm of auto- and cross-correlation sidelobes, a set of sequences with sparse sidelobes will be obtained. With $p = 2$, the resulting optimized set of sequences will have small ISL value which performs well in the presence of clutter. Further, by minimizing the ℓ_p-norm when $p \to +\infty$, the optimized set of sequence will have small PSL and are well suited for enhancing the detection of point targets.

2.1.1 Background and Related Works

Waveform design based on sidelobe reduction in SISO/SIMO or phased-array radar systems: Research into design of waveforms with small ISL and PSL values has significantly

increased over the past decade for single waveform transmitting radar systems [23, 65, 73–80]. In case of ISL minimization, several optimization frameworks are proposed, including power method-like iterations, MM, CD, GD, ADMM, Inexact Alternating Direction Penalty Method (IADPM), Proximal Method of Multipliers (PMM) and MM-MDR to name a few [23, 73–84]. In [65], an algorithm based on steepest descent is proposed for designing long binary sequences. Joint ISL and PSL minimization based on CD under DP and CP constraints is proposed in [78]. In the proposed method of this chapter, ℓ_p-norm of auto-correlation sidelobes when $p \to +\infty$ is considered for the initialization. Similarly, several papers have considered ℓ_p-norm minimization to design waveform with small PSL values. In [79], a GD based approach is proposed to design sequences with small sidelobes based on ℓ_p-norm criteria for SISO radar systems. The proposed algorithm is applicable when p is an even number, i.e., $p = 2n, n \in \mathbb{Z}^+$. In [76, 77], MM based approach are proposed for ℓ_p-norm minimization when $p \geq 2$. The results in [76–78] depict that by gradually increasing p during the minimization of the ℓ_p-norm of auto-correlation sidelobes, sequences with very small PSL values can be obtained. Motivated by this observation, this chapter investigates ℓ_p-norm minimization of auto- and cross-correlation functions to obtain set of sequences with very small PSL values for MIMO radar systems.

Waveform design based on sidelobe reduction in MIMO radar systems: In order to design set of sequences with small auto- and cross-correlation sidelobes, several approaches including Multi-CAN/Multi-PeCAN [2], Iterative Direct Search [85], ISLNew [22], MM-Corr [3] and CD [37, 86, 87], are proposed, all considering the ISL as the design metric. On the other hand, few papers have focused on PSL minimization for MIMO radars [24, 88]. In [24, 89] a CD based approach is proposed to minimize PSL. In [88, 90] a MM based approach is proposed to directly minimize the PSL and design set of sequences for MIMO radar systems. The authors in [91] solve the problem based on Chebyshev distance minimization. In the current study, we design set of sequences with very small PSL values by minimizing ℓ_p-norm of auto- and cross-correlation sidelobes for a set of sequences which was not addressed previously in the literature. In contrast to the previous studies, we solve the problem for a general p value ($p > 0$) under DP constraint, and solve it for $p \in (0, 1] \cup p \geq 2$ under CP constraint. Interestingly, the obtained PSL values are close to the Welch lower bound and fill the gap between that and the best of literature.

2.1.2 Contributions

The main contributions of the current chapter are summarized below.

- *Unified optimization framework:* We propose a unified framework based on the BSUM paradigm to solve a general ℓ_p-norm minimization problem under practical design constraints. The formulation makes the problem non-convex, non-smooth and NP-hard. The proposed problem formulation includes ℓ_1/ℓ_0-norm of the auto-correlation sidelobe which relatively have lower number of local minima comparing with ℓ_2-norm. Also, the local minima of those cost functions would correspond to sequences with good auto-correlation sidelobe levels. For instance, in the simulation analysis we show that any local minima of ℓ_0-norm of auto-correlation would have many zeros (sparse auto-correlation) which can enhance the detection performance in the presence of distributed clutter.

- *Entry- and vector-based solutions:* BSUM is an iterative method that, in each iteration, the variable is divided in several blocks, then the problem is optimized with respect to that block. The blocks can be a portion of the variable or in the smallest case it can be one entry. In this regards, in each iteration of BSUM, we propose two approaches, i.e, entry- and vector-based solutions. In the entry-based optimization, we formulate the problem with respect to a single variable; this enable us to find the critical points and obtain the global optimum solution in each step. For vector-based optimization we propose a solution based on GD. This approach is faster than the entry-based method. However, the entry-based method has a better performance in terms of minimizing the objective function due to obtaining the global optimum solution in each step.

- *Trade-off and flexibility:* By conducting thorough performance assessment, we propose a flexible tool to design set of sequences with different properties. We show that the ℓ_p-norm optimization framework provides the flexibly of controlling the optimization objective by choosing p, where $p \to \infty$ leads to design set of waveforms with good PSL property. Choosing $p \to 0$ leads to sparse auto- and cross-correlation and choosing $p = 2$ leads to design set of waveforms with good ISL property.

While BSUM offers a generic framework, the contribution of the chapter lies in devising different solutions based on simplifying the complexity and obtaining a good performance. We finally propose a direct solution for the discrete phase constraint using Fast Fourier Transform (FFT)-based technique.

2.1.3 Organization and Notations

The rest of this chapter is organized as follows. In Section 2.2, we formulate the ℓ_p-norm minimization for MIMO radar systems, then we introduce the BSUM method as the

Optimization framework and finally we define the local approximation functions suitable for ℓ_p-norm problem. We develop the BSUM framework to solve the problem in Section 2.3 and provide numerical experiments to verify the effectiveness of proposed algorithm in Section 2.4.

Notations This chapter uses lower-case and upper-case boldface for vectors ($\boldsymbol{a}$) and matrices ($\boldsymbol{A}$) respectively. The set of complex and positive integer numbers are denoted by $\mathbb{C}$ and $\mathbb{Z}^+$ respectively. The transpose, conjugate transpose and sequence reversal are denoted by the $(.)^T$, $(.)^H$ and $(.)^r$ symbols respectively. Besides the Frobenius norm, ℓ_p norm, absolute value and round operator are denoted by $\|.\|_F$, $\|.\|_p$, $|.|$ and $\lfloor . \rceil$, respectively. For any complex number a, $\Re(a)$ and $\Im(a)$ denotes the real and imaginary part respectively. The letter j represents the imaginary unit (i.e., $j = \sqrt{-1}$), while the letter (i) is used as step of a procedure. Finally $\odot$ and $\circledast$ denotes the Hadamard product and cross-correlation operator respectively.

2.2 Problem Formulation

We consider a narrow-band MIMO radar system with M transmitters and each transmitting a sequence of length N in the fast-time domain. Let the matrix $\boldsymbol{X} \in \mathbb{C}^{M\times N}$ denote the set of transmitted sequences in baseband, whose the m^{th} row indicates the N samples of m^{th} transmitter whereas the n^{th} column indicates the n^{th} time-sample across the M transmitters. Let $\mathbf{x}_m \triangleq [x_{m,1}, x_{m,2}, \ldots, x_{m,N}]^T \in \mathbb{C}^N$ be the transmitted signal from m^{th} transmitter. The aperiodic cross-correlation of $\mathbf{x}_m$ and $\mathbf{x}_l$ is defined as,

$$r_{m,l}(k) \triangleq (\mathbf{x}_m \circledast \mathbf{x}_l)_k = \sum_{n=1}^{N-k} x_{m,n} x_{l,n+k}^*, \tag{2.1}$$

where $m, l \in \{1, \ldots, M_t\}$ are the transmit antennas indices and $k \in \{-N+1, \ldots, N-1\}$ is the lag of cross-correlation. If $m = l$, (2.1) represents the aperiodic auto-correlation of signal $\mathbf{x}_m$. The zero lag of auto-correlation ($r_{m,m}(0)$) represent the peak of the m^{th} matched filter output. Also $|r_{m,m}(0)|$ contains the energy of sequence which for constant modulus sequences is equal to N. The other lags ($k \neq 0$) are referred to the sidelobes. The weighted ℓ_p-norm of auto- and cross correlation in MIMO radar can be written as,

$$\left(\sum_{m=1}^{M}\sum_{l=1}^{M}\sum_{k=-N+1}^{N-1} |w_k r_{m,l}(k)|^p - M(w_0 N)^p\right)^{\frac{1}{p}}, \tag{2.2}$$

where, $0 \leq w_k \leq 1$. The $M(w_0 N)^p$ term in (2.2) is the weighted ℓ_p-norm of the mainlobes, where $\sum_{m=1}^{M} |w_0 r_{m,m}(0)|^p = M(w_0 N)^p$. Since the term $M(w_0 N)^p$ in (2.2) is constant,

the weighted ℓ_p-norm minimization can be equivalently written as,

$$\begin{cases} \min\limits_{\mathbf{X}} \quad f(\mathbf{X}) \triangleq \sum\limits_{m=1}^{M}\sum\limits_{l=1}^{M}\sum\limits_{k=-N+1}^{N-1} |w_k r_{m,l}(k)|^p \\ s.t. \quad x_{m,n} \in \mathcal{X}_\infty \quad \text{or} \quad \mathcal{X}_L, \end{cases} \tag{2.3}$$

where, $\mathcal{X}_\infty$ and $\mathcal{X}_L$ indicating the unimodular and discrete phase with L alphabet size sequences. More precisely, we consider $\mathcal{X}_\infty = \{e^{j\phi} | \phi \in \Omega_\infty\}$ and $\mathcal{X}_L = \{e^{j\phi} | \phi \in \Omega_L\}$, where $\Omega_\infty \triangleq (-\pi, \pi]$ and $\Omega_L \triangleq \{0, \frac{2\pi}{L} \ldots, \frac{2\pi(L-1)}{L}\}$. The unimodular and discrete phase are equality constraints and they are not an affine set. Therefore the optimization problem is non-convex, multi-variable and NP-hard in general. Note that, due to the existence of the parameter p in $f(\mathbf{X})$, direct solution of (2.3) is complicated.

2.3 Proposed Method

In this chapter, we propose a method based on BSUM framework to tackle the non-convex problem (2.3). The BSUM framework provides a connection between Block Coordinate Descent (BCD) and MM, by successively optimizing a certain upper bound of the original objective in a coordinate wise manner[1]. In this context, BSUM requires to find an approximation function for the objective function in (2.3), and then the approximation function should be written in a simplified form with respect to one variable block while other blocks are held fixed. In this regard, the term $|w_k r_{m,l}(k)|^p$ in (2.3) can be majorized by the following local approximation functions (see Appendix A.1 for more details),

$$u(w_k r_{m,l}(k)) = \eta_{mlk} |w_k r_{m,l}(k)|^2 + \psi_{mlk} |w_k r_{m,l}(k)| + \nu_{mlk} \tag{2.4}$$

where[2],

$$\eta_{mlk} \triangleq \begin{cases} \dfrac{\tau^p + (p-1)|w_k r_{m,l}^{(i)}(k)|^p - p\tau |w_k r_{m,l}^{(i)}(k)|^{p-1}}{(\tau - |w_k r_{m,l}^{(i)}(k)|)^2} & p \geq 2 \\ \begin{cases} \dfrac{p\epsilon^{(p-2)}}{2} & |w_k r_{m,l}(k)| \leqslant \epsilon \\ \dfrac{p|w_k r_{m,l}(k)|^{(p-2)}}{2} & |w_k r_{m,l}(k)| > \epsilon \end{cases} & 0 < p \leq 1, \end{cases} \tag{2.5}$$

[1] Details of BSUM and different ways of choosing approximation functions of this chapter can be found in Appendix A.1.

[2] Since ν_{mlk} is a constant term and does not affect the optimization procedure we do not reported its value.

$$\tau \triangleq \left(\sum_{-N-1}^{N-1} |w_k r_{m,l}^{(i)}(k)|^p \right)^{\frac{1}{p}}. \tag{2.6}$$

and

$$\psi_{mlk} \triangleq \begin{cases} p|w_k r_{m,l}^{(i)}(k)|^{p-1} - 2\eta_{mlk}|w_k r_{m,l}^{(i)}(k)| & p \geq 2 \\ 0 & 0 < p \leq 1, \end{cases} \tag{2.7}$$

In (2.5), ϵ is a positive and small value ($\epsilon > 0$ and $\epsilon \to 0$) to incorporated in the objective function for avoiding the singularity problem for $0 < p \leq 1$.

Consequently, (2.3) can be equivalently replaced with,

$$\mathcal{P} \begin{cases} \min\limits_{\mathbf{X}} \quad u(\mathbf{X}) \triangleq \sum\limits_{m=1}^{M} \sum\limits_{l=1}^{M} \sum\limits_{k=-N+1}^{N-1} u(w_k r_{m,l}(k)) \\ s.t. \quad x_{m,n} \in \mathcal{X}_\infty \quad \text{or} \quad \mathcal{X}_L, \end{cases} \tag{2.8}$$

Let $\mathbf{x}_t$ ($t \in \{1, \ldots, M\}$) be the only variable block, while other blocks are held fixed and stored in the matrix $\mathbf{X}_{-t} \triangleq [\mathbf{x}_1^T; \ldots; \mathbf{x}_{t-1}^T; \mathbf{x}_{t+1}^T; \ldots; \mathbf{x}_M^T] \in \mathbb{C}^{(M-1)\times N}$. In this case, the approximation function $u(\mathbf{X})$ can be decomposed to a term independent of the optimization variable $\mathbf{x}_t$, and two other terms, one indicating the auto-correlation of $\mathbf{x}_t$, and the other is its cross-correlation with the other sequences of the set $\mathbf{X}_{-t}$. Precisely,

$$u(\mathbf{X}) = u_m(\mathbf{X}_{-t}) + u_{au}(\mathbf{x}_t) + u_{cr}(\mathbf{x}_t, \mathbf{X}_{-t}), \tag{2.9}$$

where

$$\begin{aligned} u_m(\mathbf{X}_{-t}) &= \sum_{\substack{m,l=1 \\ m,l\neq t}}^{M} \sum_{k=-N+1}^{N-1} u(w_k r_{m,l}(k)), \\ u_{au}(\mathbf{x}_t) &= \sum_{k=-N+1}^{N-1} u(w_k r_{t,t}(k)), \\ u_{cr}(\mathbf{x}_t, \mathbf{X}_{-t}) &= 2 \sum_{\substack{l=1 \\ l\neq t}}^{M} \sum_{k=-N+1}^{N-1} u(w_k r_{t,l}(k)). \end{aligned} \tag{2.10}$$

In the sequel, we provide different approaches for minimizing $u(\mathbf{X})$ under the aforementioned constraints.

2.3.1 Code entry optimization

To design the code vector $\mathbf{x}_t$, one possible solution is to optimize its code entry sequentially. Let $x_{t,d}$ ($t \in \{1,\dots,M\}$ and $d \in \{1,\dots,N\}$) be the only entry variable of vector $\mathbf{x}_t$ while other entries are held fixed and stored in vector $\mathbf{x}_{t,-d} \triangleq [x_{t,1},\dots,x_{t,d-1},0,x_{t,d+1},\dots,x_{t,N}]^T \in \mathbb{C}^N$. Further, to consider the unimodularity constraint, we can substitute $x_{t,d}$ with $e^{j\phi}$. In this case, it can be shown that (see Appendix A.2),

$$\begin{aligned} w_k r_{t,t}(k,\phi) &= c_{ttdk} + a_{ttdk}e^{j\phi} + b_{ttdk}e^{-j\phi}, \\ w_k r_{t,l}(k,\phi) &= c_{tldk} + a_{tldk}e^{j\phi}. \end{aligned} \tag{2.11}$$

Observe that the term $u_m(\mathbf{X}_{-t})$ in (2.9) is independent to the optimization variable $x_{t,d}$. Thus, the optimization problem (2.8) with respect to $x_{t,d}$ becomes,

$$\begin{cases} \min\limits_{\phi} & \sum\limits_{k=-N+1}^{N-1} u(w_k r_{t,t}(k,\phi)) + 2\sum\limits_{\substack{l=1 \\ l\neq t}}^{M}\sum\limits_{k=-N+1}^{N-1} u(w_k r_{t,l}(k,\phi)) \\ s.t. & \phi \in \Omega_\infty, \end{cases} \tag{2.12}$$

In this case, by some mathematics manipulation the objective function in (2.12) can be explicitly written based on ϕ as (see Appendix A.3),

$$\mathcal{P}_e \begin{cases} \min\limits_{\phi} & u(\phi) \triangleq \Re\left\{\sum\limits_{n=-2}^{2} v_n e^{jn\phi}\right\} \\ s.t. & \phi \in \Omega_\infty, \end{cases} \tag{2.13}$$

where the coefficients v_n are defined in Appendix A.3.

The solution to $\mathcal{P}_e$ can be calculated by finding the critical points of the problem and select the solution that minimizes the objective. In this regards we find the real roots of the first order derivative of the objective function. Then we evaluate the objective function in these points and the boundaries and select the solution that minimizes the objective. In this regards, the derivative of $u(\phi)$ can be obtained by,

$$u'(\phi) = \Re\left\{ j\sum_{n=-2}^{2} n v_n e^{jn\phi} \right\}, \tag{2.14}$$

Then, we perform the change of variable $z \triangleq \tan(\frac{\phi}{2})$ in (2.14), and use $\cos(\phi) = (1-\tan^2(\frac{\phi}{2}))/(1+\tan^2(\frac{\phi}{2}))$, $\sin(\phi) = 2\tan(\frac{\phi}{2})/(1+\tan^2(\frac{\phi}{2}))$ trigonometric equations. By doing so, it can be shown that finding the roots of $\frac{du(\phi)}{d\phi} = 0$ is equivalent to find the

roots of the following 4 degree real polynomials (see Appendix A.4 for details),

$$\sum_{k=0}^{4} s_k z^k = 0, \tag{2.15}$$

where the coefficients are given in Appendix A.4.

We only admit the real roots for (2.15). Let us assume that z_k $(k = \{1, \ldots, 4\})$ be the roots of $\sum_{k=0}^{4} s_k z^k = 0$. Hence, the critical points of $u(\phi)$ can be expressed as,

$$\Omega_u = \left\{ 2 \arctan\left(z_k\right) | \Im(z_k) = 0 \right\} \tag{2.16}$$

Therefore, the optimum solution would be,

$$\phi^\star = \arg\min_{\phi} \left\{ u(\phi) | \phi \in \Omega_u \right\}. \tag{2.17}$$

Subsequently the optimum solution for $x_{t,d}$ is, $x_{t,d}^{(i)} = e^{j\phi^\star}$.

Remark 2.1. Since, $u(\phi)$ is a function of $\cos\phi$ and $\sin\phi$, it is periodic, real and differentiable. Therefore, it has at least two extrema and hence its derivative has at least two real roots; thus Ω_u never becomes a null set. As a result in each iteration, the problem has a solution and never becomes infeasible.

Remark 2.2. To design sequences with discrete phase constraint, an elegant solution can be obtained for $0 < p < \infty$ by using the FFT as detailed below. In this case, the optimization problem with respect to the phase variable ϕ by removing the constant terms can be written as,

$$\mathcal{P}_d \begin{cases} \min\limits_{\phi} & 2 \sum\limits_{\substack{l=1 \\ l \neq t}}^{M} \sum\limits_{k=-N+1}^{N-1} |c_{tldk} + a_{tldk} e^{j\phi}|^p + \\ & \sum\limits_{k=-N+1}^{N-1} |c_{ttdk} + a_{ttdk} e^{j\phi} + b_{ttdk} e^{-j\phi}|^p \\ s.t. & \phi \in \Omega_L, \end{cases} \tag{2.18}$$

Note that in (2.18), all the discrete points lie on the boundary of the optimization problem; hence, all of them are critical points for the problem. Interestingly, the solution to (2.18) can be obtained efficiently using an FFT operation due to the fact that the objective function represents the modulus of the L-point DFT of a sequence associated with coefficients c_{ttdk}, a_{ttdk}, b_{ttdk}, c_{tldk}, and a_{tldk}. Precisely, we find the index $l'^\star$ by (see Appendix A.5),

Algorithm 1 :WeBEST-entry optimization framework

Input: Initial set of feasible sequences, $\mathbf{X}^{(0)}$.
Initialization: $i := 0$.
Optimization:

1. **while**, the stopping criteria is not met, **do**
2. **for** $t = 1, \ldots, M$ **do**
3. **for** $d = 1, \ldots, N$ **do**
4. Optimize $x_{t,d}^{(i)}$ and obtain $x_{t,d}^{\star}$;
5. Update $x_{t,d}^{(i+1)} = x_{t,d}^{\star}$;
6. $\mathbf{X}^{(i+1)} = \mathbf{X}_{-(t,d)}^{(i+1)}|_{x_{t,d}=x_{t,d}^{(i+1)}}$;
7. **end for**
8. **end for**
9. $i := i + 1$;
10. **end while**

Output: $\mathbf{X}^{\star} = \mathbf{X}^{(i+1)}$.

$$l'^{\star} = \arg \min_{l=1,\ldots,L} 2 \sum_{\substack{l=1 \\ l \neq t}}^{M} \sum_{k=-N+1}^{N-1} |\mathcal{F}_L\{a_{tldk}, c_{tldk}\}|^p + \sum_{k=-N+1}^{N-1} |\mathcal{F}_L\{a_{ttdk}, c_{ttdk}, b_{ttdk}\}|^p, \tag{2.19}$$

where, F_L is L-point DFT operator. Hence, $\phi^{\star} = \frac{2\pi(l'^{\star}-1)}{L}$ and the optimum entry is $x_{t,d}^{(i)} = e^{j\phi^{\star}}$.

The summary of the proposed method, called WeBEST-entry based design optimization framework is given by **Algorithm 1**, where, $x_{t,d}^{\star} = e^{j\phi^{\star}}$ is the optimized solution. To obtain this solution, WeBEST-e (entry optimization) considers a feasible set of sequences as the initial waveforms. Then, at each iteration, it selects $x_{t,d}^{(i)}$ as the variable and updates that with optimized $x_{t,d}^{\star}$, denoted by $x_{t,d}^{(i+1)}$. This procedure is repeated for other entries and is undertaken until all the entries are optimized at least once. After optimizing the MN^{th} entry, the algorithm examines the convergence metric for the objective function. If the stopping criteria is not met the algorithm repeats the aforementioned steps.

Algorithm 2 : Backtracking line search

Input: $\Delta\boldsymbol{\varphi}_t^{(i)}$, α $(0 < \alpha < 0.5)$ and β $(0 < \beta < 1)$.
Initialization: $\delta^{(i)} := 1$

1. **while** $f(\boldsymbol{\varphi}_t^{(i)} + \delta^{(i)}\Delta\boldsymbol{\varphi}_t^{(i)}) > f(\boldsymbol{\varphi}_t^{(i)}) + \alpha s \nabla f(\boldsymbol{\varphi}_t^{(i)})\Delta\boldsymbol{\varphi}_t^{(i)}$
2. $\quad \delta^{(i)} := \delta^{(i)}\beta$;
3. **end while**

2.3.2 Code vector optimization

One alternative approach to solve (2.8) and minimize $u(\mathbf{X})$ is to consider the entire code vector $\mathbf{x}_t$ as the optimization variable. Let $\boldsymbol{\Phi} \triangleq \angle\mathbf{X} \in \mathbb{R}^{M\times N}$, $\boldsymbol{\Phi}_{-t} \triangleq \angle\mathbf{X}_{-t} \in \mathbb{R}^{(M-1)\times N}$ and $\boldsymbol{\varphi}_t \triangleq \angle\mathbf{x}_t \in \mathbb{R}^N$ be the phases corresponding to the matrices $\mathbf{X}$, $\mathbf{X}_{-t}$ and the vector variable $\mathbf{x}_t$ respectively. Hence, with respect to $\boldsymbol{\varphi}_t$, the optimization problem is

$$\begin{cases} \min\limits_{\boldsymbol{\varphi}_t} & u_m(\boldsymbol{\Phi}_{-t}) + u_{au}(\boldsymbol{\varphi}_t) + u_{cr}(\boldsymbol{\varphi}_t, \boldsymbol{\Phi}_{-t}) \\ s.t. & \phi_{t,n} \in \Omega_\infty. \end{cases} \tag{2.20}$$

To solve (2.20), one possible solution is to use GD framework, which is a first-order iterative optimization algorithm for finding a local minimum of a differentiable function. In general, the GD procedure starts with an initial solution $(\boldsymbol{\Phi}^{(0)})$, then at i^{th} iteration, each block $(\boldsymbol{\varphi}_t)$ is updated by the following equation [92],

$$\boldsymbol{\varphi}_t^{(i+1)} = \boldsymbol{\varphi}_t^{(i)} + \delta^{(i)}\Delta\boldsymbol{\varphi}_t^{(i)} \tag{2.21}$$

where, $\delta^{(i)}$ and $\Delta\boldsymbol{\varphi}_t^{(i)}$ are the *step size* (*step length*) and the *search direction* at i^{th} iteration, respectively. After updating all of the blocks, the phase matrix is updated by $\boldsymbol{\Phi}^{(i+1)} \triangleq [\boldsymbol{\varphi}_1^{(i+1)}, \ldots, \boldsymbol{\varphi}_M^{(i+1)}]^T$. In gradient descent method, the search direction is equal to the opposite direction of the gradient i.e. $\Delta\boldsymbol{\varphi}_t^{(i)} = -\nabla u(\boldsymbol{\varphi}_t^{(i)})$. Note that, the convergence behavior of GD methods is highly depended on choosing the step size and the step direction. In order to achieve the monotonic descent behavior in each step $(u(\boldsymbol{\varphi}_t^{(i+1)}) \leq u(\boldsymbol{\varphi}_t^{(i)})$), *backtracking line search* can be used for choosing the step size, where it depends on two constants α and β with $0 < \alpha < 0.5$ and $0 < \beta < 1$, indicated in **Algorithm 2** [92].

Algorithm 3, called WeBEST-v shows the procedure of vector optimization of ℓ_p-norm minimization. In this algorithm, matrix $\nabla\boldsymbol{\Phi}^{(i)} \in \mathbb{R}^{M\times N}$ contains the gradient of objective function with respect to sequence phases at i^{th} iteration, i.e., $\nabla\boldsymbol{\Phi}^{(i)} \triangleq$

Algorithm 3 : WeBEST-vector optimization framework

Input: $\mathbf{X}^{(0)}$

Initialization: $i := 0$, $\mathbf{\Phi}^{(i)} = \angle \mathbf{X}^{(0)}$.

1. **while**, the stopping criteria is not met, **do**
2. **for** $t := 1 : M$
3. $\Delta\boldsymbol{\varphi}_t^{(i)} := -\nabla_{\boldsymbol{\varphi}_t} u(\boldsymbol{\varphi}_t^{(i)})$;
4. obtain $\delta^{(i)}$ using backtracking line search;
5. $\boldsymbol{\varphi}_t^{(i+1)} := \boldsymbol{\varphi}_t^{(i)} + \delta^{(i)}\Delta\boldsymbol{\varphi}_t^{(i)}$;
6. **end for**
7. $i := i + 1$;
8. **end while**

$[\nabla_{\boldsymbol{\varphi}_1} u(\boldsymbol{\varphi}_1^{(i)}), \ldots, \nabla_{\boldsymbol{\varphi}_M} u(\boldsymbol{\varphi}_M^{(i)})]^T$. This procedure will be continued until the algorithm meet the stopping criteria[3].

Algorithm 3 requires calculation of the gradients of $\nabla_{\boldsymbol{\varphi}_t} u(\boldsymbol{\varphi}_t^{(i)})$, which can be obtained used the following lemma.

Lemma 2.1. *The gradient of* $\nabla_{\boldsymbol{\varphi}_t} u(\boldsymbol{\varphi}_t^{(i)})$ *is equal to,*

$$\begin{aligned}\nabla_{\boldsymbol{\varphi}_t} u(\boldsymbol{\varphi}_t^{(i)}) = 4\Im\{\mathbf{x}_t^* \odot ((\boldsymbol{\vartheta}_{tt}^2 \odot (\mathbf{x}_t \circledast \mathbf{x}_t)) \circledast \mathbf{x}_t)_{k+N-1}\} \\ + 4\textstyle\sum_{\substack{l=1 \\ l\neq t}}^{M} \Im\{\mathbf{x}_t^* \odot ((\boldsymbol{\vartheta}_{tl}^2 \odot (\mathbf{x}_l \circledast \mathbf{x}_t)^r) \circledast \mathbf{x}_l^*)_{k+N-1}\},\end{aligned} \tag{2.22}$$

where, $\boldsymbol{\vartheta}_{tt} \triangleq [\vartheta_{tt}(-N+1), \ldots, \vartheta_{tt}(N-1)]^T | \vartheta_{tt}(k) \triangleq w_k\sqrt{\mu_{ttk}}$, $\mu_{ttk} \triangleq \frac{p}{2}|w_k r_{t,t}^{(i)}(k)|^{p-2}$ *and* $\boldsymbol{\vartheta}_{tl} \triangleq [\vartheta_{tl}(-N+1), \ldots, \vartheta_{tl}(N-1)]^T | \vartheta_{tl}(k) \triangleq w_k\sqrt{\mu_{tlk}}$, $\mu_{tlk} \triangleq \frac{p}{2}|w_k r_{t,l}^{(i)}(k)|^{p-2}$.

proof: Since the third term in (2.4) is a constant, it does not affect the gradient calculation and it can be removed. Beside, according to lemma A.2, the ℓ_1-norm in the second term ($|w_k r_{m,l}(k)|$) can be majorized by the following equation [93],

$$\frac{1}{2}|w_k r_{m,l}^{(i)}(k)|^{-1}|w_k r_{m,l}(k)|^2 - \frac{1}{2}|w_k r_{m,l}^{(i)}(k)|. \tag{2.23}$$

Substituting (2.23) with the $|w_k r_{m,l}(k)|$ term in (2.4), becomes,

$$\bar{u}(w_k r_{m,l}(k)) \triangleq \mu_{mlk}|w_k r_{m,l}(k)|^2 + \varsigma_{mlk}, \tag{2.24}$$

[3]Please note that the WeBEST-v is proposed for $2 \leq p < \infty$. For $0 < p \leq 1$, we can simply replace $f(\boldsymbol{\varphi}_M^{(i)})$ with $g_h^{\epsilon}(\boldsymbol{\varphi}_M^{(i)})$.

where,

$$\begin{aligned}\mu_{mlk} &\triangleq \frac{p}{2}|w_k r_{m,l}^{(i)}(k)|^{p-2} \\ \varsigma_{mlk} &\triangleq \eta_{mlk}|w_k r_{m,l}^{(i)}(k)|^2 - \frac{1}{2}\psi_{mlk}|w_k r_{m,l}^{(i)}(k)| \\ &\quad - (p-1)|w_k r_{m,l}^{(i)}(k)|^p,\end{aligned} \tag{2.25}$$

Now we define $\bar{u}(\boldsymbol{\Phi}) \triangleq u_m(\boldsymbol{\Phi}_{-t}) + \bar{u}_{au}(\boldsymbol{\varphi}_t) + \bar{u}_{cr}(\boldsymbol{\varphi}_t, \boldsymbol{\Phi}_{-t})$, where,

$$\begin{aligned}\bar{u}_{au}(\boldsymbol{\varphi}_t) &= \sum_{k=-N+1}^{N-1}\Big(\mu_{ttk}|w_k r_{t,t}(k)|^2 + \varsigma_{ttk}\Big) \\ &= \big\|\boldsymbol{\varrho}_{tt} \odot (\mathbf{x}_t \circledast \mathbf{x}_t)_k\big\|_2^2 + \sum_{k=-N+1}^{N-1}\varsigma_{ttk},\end{aligned} \tag{2.26}$$

and,

$$\begin{aligned}\bar{u}_{cr}(\boldsymbol{\varphi}_t, \boldsymbol{\Phi}_{t-1}) &= 2\sum_{\substack{l=1\\l\neq t}}^{M}\sum_{k=-N+1}^{N-1}\Big(\mu_{tlk}|w_k r_{t,l}(k)|^2 + \varsigma_{tlk}\Big) \\ &= 2\sum_{\substack{l=1\\l\neq t}}^{M}\big\|\boldsymbol{\varrho}_{tl} \odot (\mathbf{x}_l \circledast \mathbf{x}_t)_k\big\|_2^2 + 2\sum_{\substack{l=1\\l\neq t}}^{M}\sum_{k=-N+1}^{N-1}\varsigma_{tlk}.\end{aligned} \tag{2.27}$$

The second terms in (2.26) and (2.27) are constant and can be ignored. To this end it can be shown that [79],

$$\begin{aligned}&\nabla_{\boldsymbol{\varphi}_t}\big\|\boldsymbol{\varrho}_{tt} \odot (\mathbf{x}_t \circledast \mathbf{x}_t)_k\big\|_2^2 = \\ &\quad 4\Im\{\mathbf{x}_t^* \odot ((\boldsymbol{\varrho}_{tt}^2 \odot (\mathbf{x}_t \circledast \mathbf{x}_t)) \circledast \mathbf{x}_t)_{k+N-1}\}\end{aligned} \tag{2.28}$$

$$\begin{aligned}&\nabla_{\boldsymbol{\varphi}_t}\big\|\boldsymbol{\varrho}_{tl} \odot (\mathbf{x}_l \circledast \mathbf{x}_t)_k\big\|_2^2 = \\ &\quad 2\Im\{\mathbf{x}_t^* \odot ((\boldsymbol{\varrho}_{tl}^2 \odot (\mathbf{x}_l \circledast \mathbf{x}_t)^r) \circledast \mathbf{x}_l^*)_{k+N-1}\}\end{aligned} \tag{2.29}$$

Please note that, since $\bar{u}(\boldsymbol{\Phi})$ majorizes the $|w_k r_{m,l}(k)|$ term of $u(\boldsymbol{\Phi})$, therefore, according to the MM properties, the gradient of $\bar{u}(\boldsymbol{\Phi})$ is equal to $\bar{u}(\boldsymbol{\Phi})$ at $\boldsymbol{\varphi}_t$ i.e. $\nabla_{\boldsymbol{\varphi}_t}\bar{u}(\boldsymbol{\Phi}) = \nabla_{\boldsymbol{\varphi}_t}u(\boldsymbol{\Phi})$. Likewise, $\bar{u}(\boldsymbol{\Phi})$ is a majorizer function for $f(\boldsymbol{\Phi})$, thus, $\nabla_{\boldsymbol{\varphi}_t}\bar{u}(\boldsymbol{\Phi}) = \nabla_{\boldsymbol{\varphi}_t}u(\boldsymbol{\Phi}) = \nabla_{\boldsymbol{\varphi}_t}f(\boldsymbol{\Phi})$.

Therefore, considering the equations (2.28), (2.29), (2.26) and (2.27) readily the gradient in (2.22) can be obtained which completes the proof.

2.3.3 Convergence

The convergence of proposed method can be discussed in two aspects, the convergence of objective function and the convergence of the waveform set $\mathbf{X}$. With regard to objective function, as $u(\mathbf{X}) > 0$, this expression is also valid for the optimum solution of WeBEST-e and WeBEST-v ($u(\mathbf{X}^\star) > 0$).

On the other hand, both WeBEST-e and WeBEST-v minimize the objective function in each step leading to a monotonic decrease of the function value. Since the function value is lower bounded, it can be argued that the algorithm converges to a specific value. Particularly, if the algorithm starts with feasible $\mathbf{X}^{(0)}$ we have,

$$u(\mathbf{X}^{(0)}) \geqslant \cdots \geqslant u(\mathbf{X}^{(i)}) \geqslant \cdots \geqslant u(\mathbf{X}^\star) > 0.$$

The convergence of the argument requires additional conditions and its investigation is beyond the scope of this chapter. However, for the optimization problem considered in this chapter, we numerically observed that the argument converges as well as objective function.

2.3.4 Computational Complexity

In the following we evaluate the computational complexity of WeBEST-e and WeBEST-v.

Complexity of WeBEST-e: This algorithm needs to perform the following steps in each iteration:

- *Calculate the coefficient* v_n *in* (2.13): The maximum complexity of the coefficients are related to v_{-1}, v_0 and v_1 (see Appendix A.3 for details). Without loss of generality, we consider $\tilde{v}_{-1} \triangleq 2\sum_{\substack{l=1\\l\neq t}}^{M}\sum_{k=-N+1}^{N-1}\eta_{tlk}a^*_{tldk}c_{tldk}$ to obtain the computational complexity. As can be seen, $\tilde{v}_{-1}$ needs to calculate the terms η_{tlk}, a_{tldk} and c_{tldk}. Among these three terms, c_{tldk} is the most complex term (see (A.13) and (A.15) in Appendix A.2 for details), which substantially is the cross-correlation of t^{th} and l^{th} transmitters. Thus, calculating c_{tldk} requires $N\log_2(N)$ operations due to using fast convolution [94]. In addition, calculating $\tilde{v}_{-1}$ needs MN summation. Therefore $\tilde{v}_{-1}$ needs $MN^2\log_2(N)$ operations in overall. Using a recursive equation, the computational complexity can be reduced more.

- *Solving the optimization problem* (2.13): WeBEST-e needs finding the roots of 4 degree polynomials[4] in (2.15), which take 4^3 operations. In case of discrete phase constraint we obtain (2.19) using two L-points FFT which each has $L\log_2(L)$ operations.
- *Optimizing all the entries of matrix* $\mathbf{X}$: To this end we need to repeat the two aforementioned steps MN times.

Let us assume that $\mathcal{K}$ iterations are required for convergence of the algorithm. Therefore, the overall computational complexity of WeBEST-e is $\mathcal{O}(\mathcal{K}MN(4^3+MN^2\log_2(N)))$, for continuous phase constraint, while under discrete phase constraint is $\mathcal{O}(\mathcal{K}MN(L\log_2(L)+MN^2\log_2(N)))$.

Complexity of WeBEST-v: This algorithm needs to perform the following steps in each iteration:

- *Calculate the gradient of auto- and cross-correlation*: The gradient in (2.22) is expressed in terms of correlations; therefore the gradient needs $N\log_2(N)$ operations due to using fast convolution [79]. Since we need to calculate the gradient of auto-correlation for one time and cross-correlation for $M-1$ times, therefore the overall computational complexity would be $MN\log_2(N)$.
- *Obtain the step size*: This step comprises calculating the auto- and cross-correlation part of objective functions i.e. $f_{au}(\mathbf{X})$ and $f_{cr}(\mathbf{X})$, which needs $MN\log_2(N)$ operations. Lets assume that this step needs $\mathcal{S}$ iterations to find the step size, therefore the complexity of this step would be $\mathcal{S}MN\log_2(N)$.
- *Optimizing all the entries of matrix* $\mathbf{X}$: To this end we need to repeat the two aforementioned steps M times.

Let us assume that $\mathcal{K}$ iterations are required for convergence of the WeBEST-v. Therefore, the overall computational complexity of WeBEST-v is $\mathcal{O}(\mathcal{K}\mathcal{S}M^2N\log_2(N))$.

2.4 Numerical Results

In this section, we provide representative numerical examples to illustrate the effectiveness of the proposed framework. We consider $\Delta\mathbf{X}^{(i+1)} \triangleq \left\|\mathbf{X}^{(i+1)}-\mathbf{X}^{(i)}\right\|_F \leq \zeta$ as the stopping

[4]For finding the roots of polynomial we use "roots" function in MATLAB. This function is based on computing the eigenvalues of the companion matrix. Thus the computational complexity of this method is $\mathcal{O}(k^3)$, where k is the degree of the polynomial [95, 96]

criterion of WeBEST-e and WeBEST-v, where ζ is the stopping threshold ($\zeta > 0$). We set $\zeta = 10^{-9}$ for all the following numerical examples. We further stop the algorithm if the number of iterations exceed 10^5. Also, we consider $\epsilon = 0.05$ in (2.4). In this section, by $L \to \infty$ we denote the set of continuous phase sequences i.e. the set of sequences with infinity alphabet sizes. Besides, we use $10\log(.)$ to report the results on decibel scale.

2.4.1 Convergence

Figure 2.1 depicts the convergence time (behavior) of the proposed method. We consider a set of random MPSK sequences ($\mathbf{X}_0 \in \mathbb{C}^{M\times N}$) with number of transmitters $M = 4$, code-length $N = 64$, and alphabet size $L = 8$, as the initial waveform set. For the initialization sequences, every code entry is given by,

$$x_{m,n}^{(0)} = e^{j\frac{2\pi(l_{m,n}-1)}{L}}, \tag{2.30}$$

where $l_{m,n}$ is a random integer variable uniformly distributed in $[1, L]$. Figure 2.1a and 2.1b show the objective function for $p = 3$ ($f(\mathbf{X})$) and $p = 0.75$ ($u(\mathbf{X})$) respectively. Observe that, due to the convergence property of BSUM framework, in both cases the objective decreases monotonically. Since for $0 < p \leq 1$ we incorporate ϵ in the objective function, the algorithm is not dealing directly with ℓ_p-norm metric, and the convergence of $f(\mathbf{X})$ (ℓ_p-norm metric) is not monotonic. This fact is shown in Figure 2.1c. However, in case of $0 < p \leq 1$, $f(\mathbf{X})$ mimics the monotonous decreasing behavior of the smooth approximation function. This shows the accuracy of the smooth approximation function. Figure 2.1d shows the convergence of the argument when $p = 3$ and $p = 0.75$. In all the cases and considering the constant modulus constraint, the vector optimization offers less run-time than entry optimization.

2.4.2 ℓ_2-norm (ISL) minimization

In this part, we evaluate the performance of proposed method when $p = 2$. In this case, the proposed method minimizes the ISLR metric (ISLR $\triangleq \frac{\text{ISL}}{N^2}$) where the lower bound in this case can be calculated by $10\log(M(M-1))$ [dB] [3]. Table 2.1 compares the average ISLR values of the proposed method with Multi-CAN [2], MM-Corr [3], BiST [24] and the lower bound, when $N = 64$ for different number of transmit antennas. Similar to the other methods, the proposed method meets the lower bound under continuous phase constraint. Interestingly, using the proposed method even for alphabet size $L = 8$, the ISLR values of the optimized sequences are very close to the lower bound.

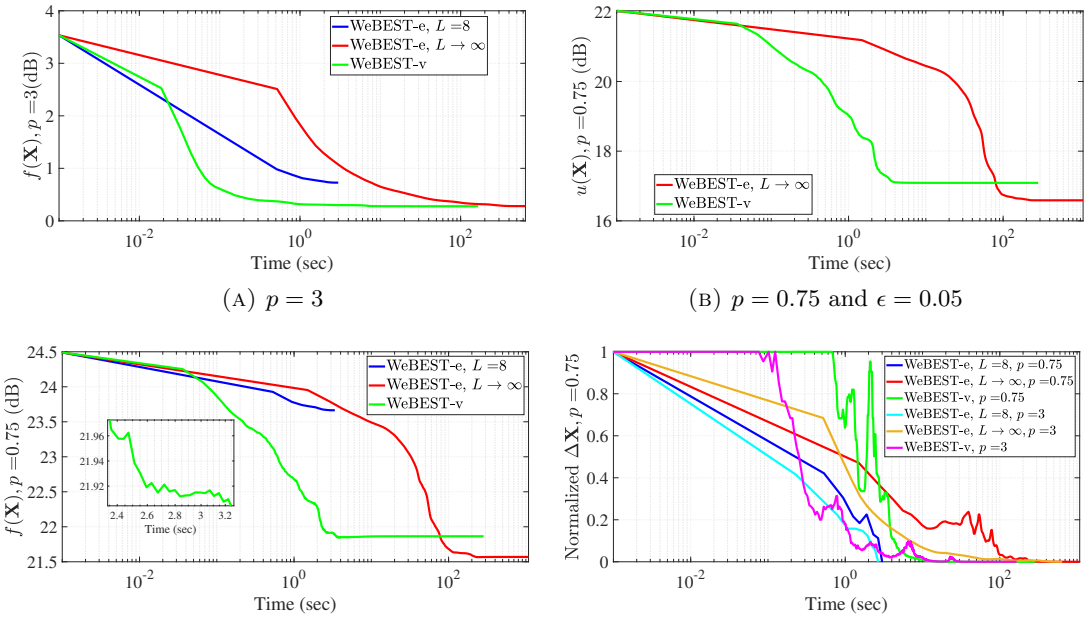

(A) $p = 3$ (B) $p = 0.75$ and $\epsilon = 0.05$

(C) ℓ_p-norm correspond to (b). (D) Argument

FIGURE 2.1: The convergence time of proposed method. (a) The ℓ_p-norm ($f(\mathbf{X})$) for $p = 3$, (b) the approximation function ($u(\mathbf{X})$) for $p = 0.75$, (c) the ℓ_p-norm correspond to fig (b), and (d) the argument ($\Delta\mathbf{X}^{(i)}$) ($M = 4$ and $N = 64$).

TABLE 2.1: Comparison between the ISLR (dB) of the proposed method with other methods ($p = 2$, $N = 64$).

M	2	4	6	8	9	10
Initial	5.92	11.91	15.55	18.05	19.20	19.97
Lower bound	3.01	10.79	14.77	17.48	18.57	19.54
WeBEST-e, $L \to \infty$	3.01	10.79	14.77	17.48	18.57	19.54
WeBEST-v	3.01	10.79	14.77	17.48	18.57	19.54
Multi-CAN	3.01	10.79	14.77	17.48	18.57	19.54
MM-Corr	3.01	10.79	14.77	17.48	18.57	19.54
WeBEST-e, $L = 8$	3.25	10.82	14.78	17.48	18.57	19.54
BiST ($\theta = 0$, $L = 8$)	3.26	10.82	14.79	17.48	18.57	19.54

TABLE 2.2: The ISLR obtained by the proposed method under discrete phase constraint with different length ($p = 2$, $M = 4$).

N	64	128	256	512	1024
$L = 8$	10.82	10.82	10.82	10.82	10.82

By keeping $M = 4$ and $L = 8$, Table 2.2 shows the optimized ISLR values under discrete phase constraint for different sequence lengths. Referring to the lower bound in the Table 2.1, we observe that the ISLR values of the optimized sequences are very close to the lower bound.

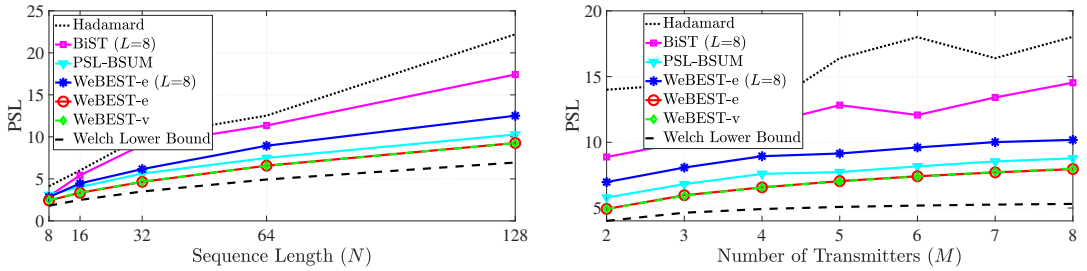

(A) PSL versus sequence length ($M = 4$). (B) PSL versus antenna number ($N = 64$).

FIGURE 2.2: Comparing the performance of the proposed method with Multi-CAN, BiST and Welch lower bound in terms of PSL.

2.4.3 ℓ_p-norm minimization for $p > 2$

To perform PSL minimization, we consider an increasing scheme for selection of p in several steps. Precisely, we select $p_1, p_2, \ldots, p_T$, such that $2 \leq p_1 < p_2 < \cdots < p_T < \infty$. We initialize the algorithm with a set of random sequences. Then we select the optimized solution of ℓ_{p_1}-norm as the initial waveform for ℓ_{p_2} minimization, and so on. Subsequently we repeat this procedure until we cover all of the p_i values ($i \in 1, \ldots, T$).

In Figure 2.2a, we fix the number of transmit antennas ($M = 4$) and report the PSL values of the optimized sequences at different sequence length. Vice versa in Figure 2.2b, we fix the sequence length $N = 64$ and report the PSL values of the optimized sequences for different number of transmitters. In both figures we compare the performance of proposed method with BiST [24] ($\theta = 1$), BSUM-PSL [90], and the available lower band for PSL, which is [97],

$$B_{PSL} = \sqrt{\frac{M-1}{2MN - M - 1}}. \tag{2.31}$$

In this figure, we consider *Hadamard Code* as initial waveform for all the algorithms. Further, for a fair comparison, we drop the spectral constraint in BSUM-PSL. It can be observed that, considering the discrete phase constraint, WeBEST-e outperforms the BiST method ($L = 8$). In case of continuous phase constraint, the performance of WeBEST-v and WeBEST-e ($L \to \infty$) are almost the same and they outperform the BSUM-PSL. Indeed, WeBEST-v and WeBEST-e ($L \to \infty$) fill the available gap between PSL values of the state-of-the-art and Welch lower bound.

2.4.4 ℓ_p-norm minimization for $0 < p \leq 1$

In this part, unlike to the PSL minimization we consider a decreasing scheme for the values of p, i. e., $1 \geq p_1 > p_2 > \cdots > p_T > 0$. To identify the sparsity, we consider a threshold for the lags of auto- and cross-correlation sidelobes. If the absolute value of

the lags is less than that the threshold, we assume that the lags is zero, and count it as a sparse lag. We choose 1 as the threshold, since $|r_{m,l}(N-1)| = |x_{m,N}x_{l,1}^*| = 1$ is the lowest possible PSL value for unimodular sequences [98]. Let N_s be the numbers of lags of auto- and cross-correlations which their absolute value is less than 1. We define the sparsity value as,

$$S_p = \frac{N_s}{M^2(2N-1)},$$

where $S_p \in [0,1]$, and the denominator $(M^2(2N-1))$ is the total number of lags of auto and cross-correlations. By this definition, if $S_p \to 1$ means that the auto- and cross-correlation of set of sequences is sparse, and vice versa if $S_p \to 0$ means that the auto- and cross-correlation of the set of sequences is not sparse.

Figure 2.3 shows the sparsity behavior of the optimized sequences at different p, N, and M. In this figure, we use *Hadamard Code as the initial set of sequence. Comparing with BiST ($\theta = 0$) [24] and Multi-CAN, Figure 2.3b and Figure 2.3c show a higher sparsity performance for the proposed methods of this chapter.*

2.4.5 The impact of weighting

In this part, we evaluate the impact of the weight parameter $(\mathbf{w})$ on the auto- and cross-correlation sidelobes of the optimized sequences. Let $\mathcal{V}$ and $\mathcal{U}$ be the desired and undesired correlation lags for a MIMO radar system, respectively. These two sets satisfy $\mathcal{V} \cup \mathcal{U} = \{-N+1, \ldots, N-1\}$ and $\mathcal{V} \cap \mathcal{U} = \emptyset$. We assume that,

$$\begin{cases} w_k = 1, & k \in \mathcal{V} \\ w_k = 0, & k \in \mathcal{U} \end{cases}$$

Figure 2.4 shows the impact of $\mathbf{w}$ for different values of p when $M = 2$, $N = 256$. In this figure, we consider different regions for the desired lags, precisely we set $\mathcal{V} = [-90, 90]$, $\mathcal{V} = [-64, 64]$ and $\mathcal{V} = [-38, 38]$. It can be observed from Figure 2.4 that nulls can be deeper if the interval of $\mathcal{V}$ is smaller.

In Figure 2.5, we compare the performance of the proposed method with MM-WeCorr [3] and Multi-WeCAN [2]. In this figure, we assume that $p = 2$, $M = 2$, $N = 512$, and we consider $\mathcal{V} = [-51, 51]$. As can be seen, the proposed method outperforms the Multi-WeCAN method. Note that, the vector optimization approach has similar performance comparing to MM-WeCorr. However, the entry optimization approach offers lower sidelobes in the lag region $\mathcal{V} = [-51, 51]$ when compared to MM-WeCorr.

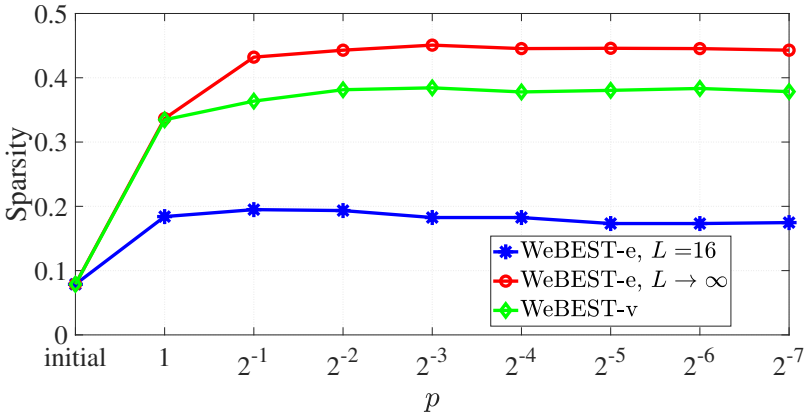

(A) Sparsity versus p ($M = 4$ and $N = 64$).

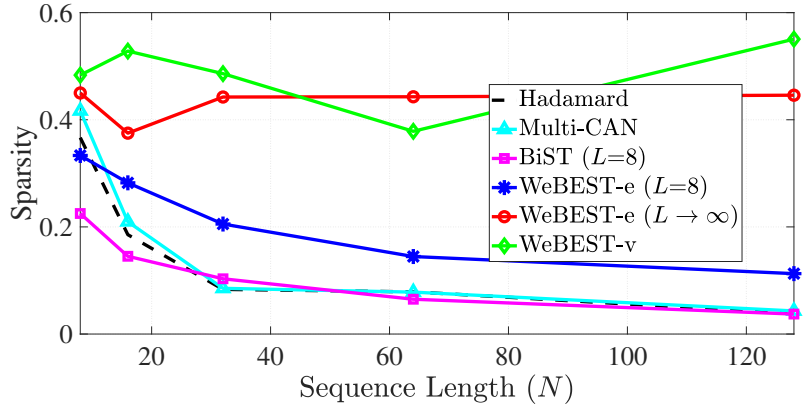

(B) Sparsity versus sequence length ($M = 4$).

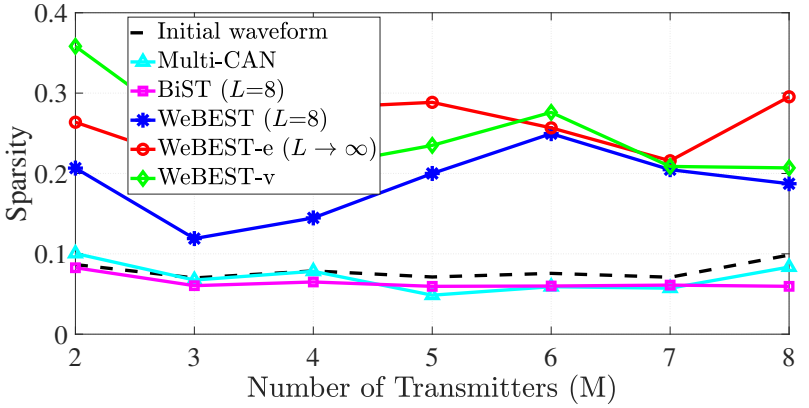

(C) Sparsity versus transmitter ($N = 64$).

FIGURE 2.3: The Sparsity behavior and comparing the performance of the proposed method with other methods.

2.4.6 Computational Time

In this subsection, we assess the run-time of WeBEST and compare it with Multi-WeCAN and MM-WeCorr. In this regard, we report the computational time using a desktop PC with Intel (R) Core (TM) i9-9900K CPU @ 3.60GHz with installed memory (RAM)

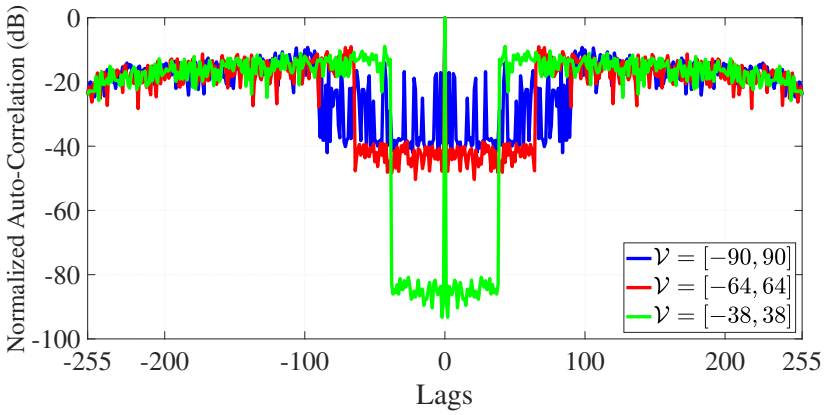

(A) $p \to 0$.

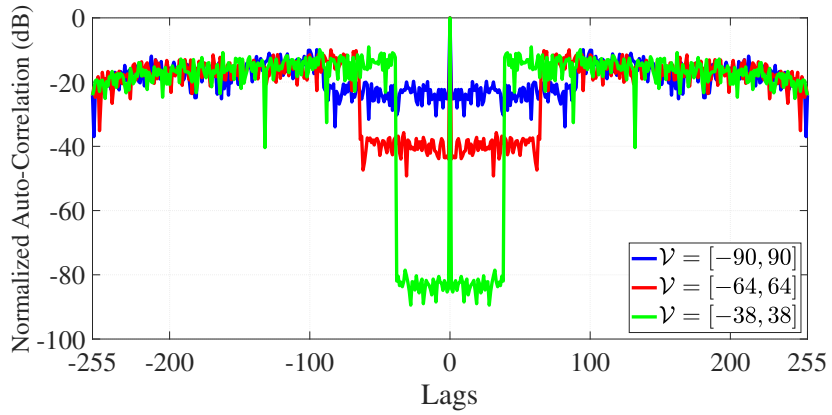

(B) $p = 2$.

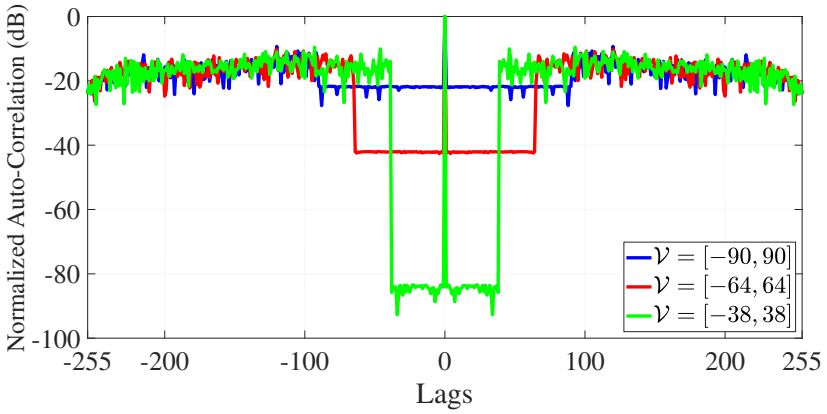

(C) $p \to \infty$.

FIGURE 2.4: The impact of weighting in WeBEST-e with different values of p ($L \to \infty$, $M = 2$ and $N = 256$).

64.00 GB. Figure 2.6 shows the computational time of WeBEST, Multi-WeCAN and MM-WeCorr with $p = 2$, $M = 2$, $l = 64$ at different sequence lengths. In this figure, we assume that the desired lags are located at $\mathcal{V} = [-\lfloor 0.1N \rceil, \lfloor 0.1N \rceil]$. For fair comparison, we assume $\Delta \mathbf{X} = 10^{-3}$ as stopping threshold for all methods.

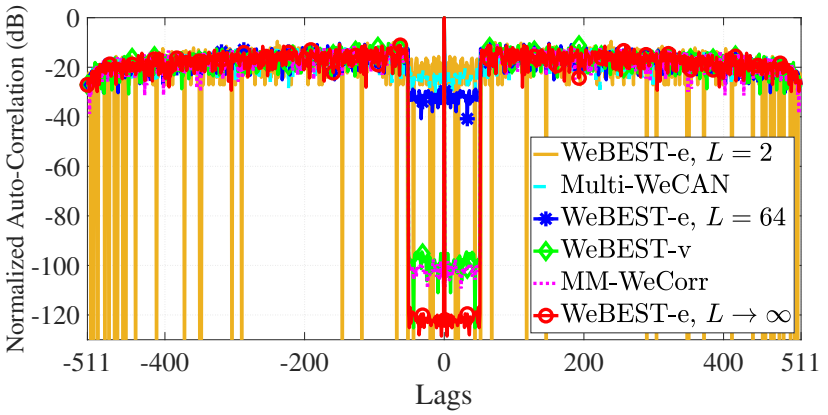

(A) The Auto-Correlation of the first waveform.

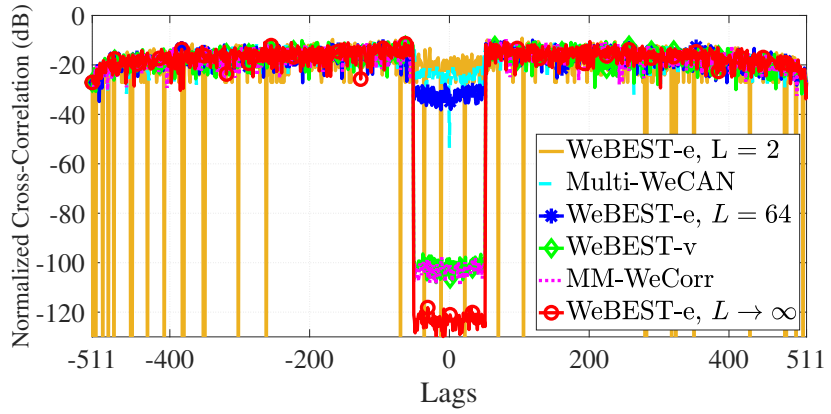

(B) The Cross-Correlation of the first and second waveforms.

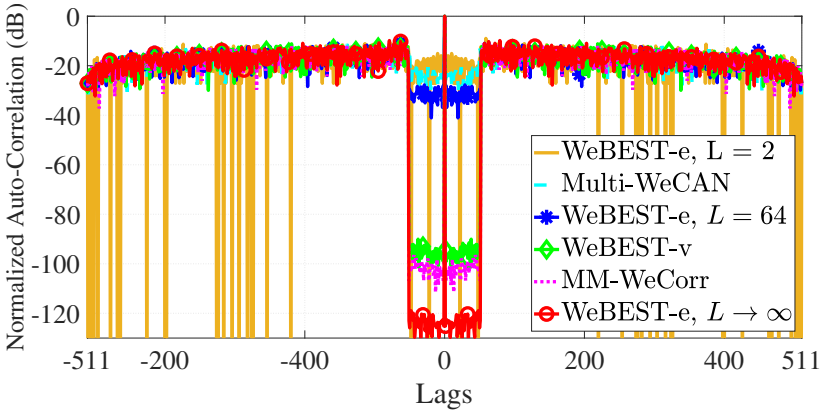

(C) The Auto-Correlation of the second waveform.

FIGURE 2.5: Comparison of the performance of the weighted ISL minimization of the proposed method with MM-WeCorr and Multi-WECAN unde discrete phase, entry and vector optimization ($p = 2$, $M = 2$ and $N = 512$).

2.5 Performance Comparison in SISO case

Figure 2.7 shows the performance of WeBEST-v and GD-based method [79] in terms of PSL, for different values of p and different initial waveforms, when $M = 1$. In this figure,

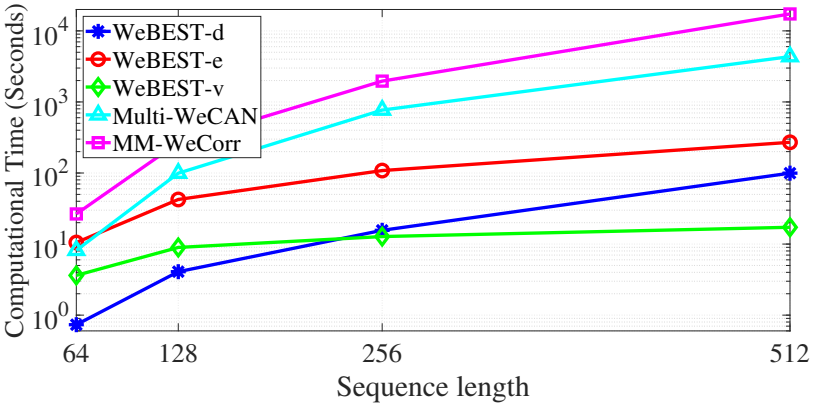

FIGURE 2.6: Comparison of the run-time of WeBEST with other methods. ($p = 2$, $M = 2$ and $L = 64$)

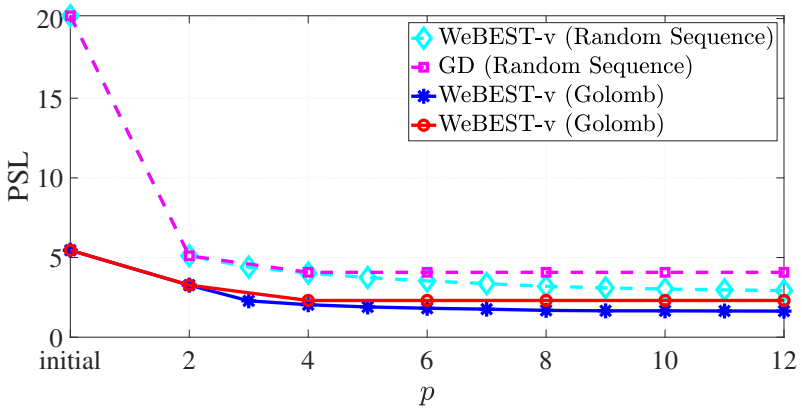

FIGURE 2.7: The comparison of the PSL value of WeBEST-v and GD-based method with different values of p ($M = 1$, $N = 128$, $p \in \{2, 4, 6, 8, 10, 12\}$ for GD-based method [79] and $p \in \{2, 3, 4, 5, 6, 7, 8, 9, 10, 11, 12\}$ for WeBEST-v method).

we consider Golomb and random phase sequences of length $N = 128$ as initial waveforms. Besides, since the GD-based method [79] just admit the even values of p, we consider an increasing scheme of p in the set $p = \{2, 4, 6, 8, 10, 12\}$ (from the lowest to the largest value of p), while for WeBEST-v, we consider the set $p = \{1, 2, 3, 4, 5, 6, 7, 8, 9, 10, 11, 12\}$. The termination threshold is $\zeta = 10^{-9}$ for both the methods. It can be observed from the figure that regardless of the initial waveform, WeBEST-v offers better PSL in compare to GD-based method. Observe that, the GD-based method, does not solve the problem for odd values of p, while WeBEST-v solves the ℓ_p-norm problem in these points. Probably, solving the ℓ_p-norm at odd points caused to obtain a better performance in compare with GD-based method.

Table 2.3 compares the convergence time of WeBEST-v and GD-based method. In this table the simulation setup is similar to Figure 2.8. It can be observed from the table that the proposed method offers lower convergence time in comparison with GD-based method.

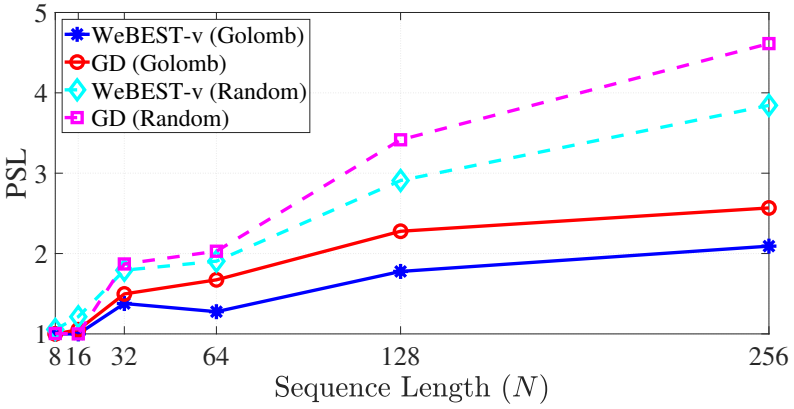

FIGURE 2.8: The comparison of the PSL of WeBEST-v and GD-based method with different sequence length ($M = 1$).

TABLE 2.3: Convergence time (sec) of WeBEST-v and GD-based method ($M = 1$).

N	8	16	32	64	128	256
WeBEST-v (Golomb)	0.7	1.4	4.3	7.2	25	78
GD (Golomb)	212	300	204	400	559	379
WeBEST-v (Random)	1.2	1.5	3.2	7.8	62	50
GD (Random)	141	39	207	415	1020	970

2.6 Sparse auto- and cross-correlation

In this part, we show how we can design waveform with sparse auto- and cross-correlation sidelobes using the $\ell_{p\to 0}$ metric. To this end, Figure 2.9 shows range-Doppler profile for the cases when $\ell_{p\to 0}$ and ℓ_{32} was considered as the objective function for the waveform design problem under discrete phase constraint. In this figure, we assume $N = 1024$, $M = 3$, and alphabet size $L = 32$. First, we consider three targets located at $[40, 50, 60]^T$ meters distance to the radar, at the same velocity $30km/h$, angle 30^o and similar Radar Cross Section (RCS) $30m^2$. In this case, the both waveforms have almost equivalent performance in terms of possibility of detecting targets. Then, we consider distributed targets are located from 50 to 55 meter distance to the radar. In this case, waveforms which are optimized using ℓ_0-norm can identify more targets. This is due to the fact that, because of the sparsity in the auto- and cross-correlation functions of the waveforms optimized by ℓ_0-norm, a smaller number of targets are masked in this case in comparison to ℓ_{32}-norm.

2.7 Conclusion

In this chapter, we considered the ℓ_p-norm of auto- and cross-correlation functions of a set of sequences as the objective function and optimized the sequences under unimodular

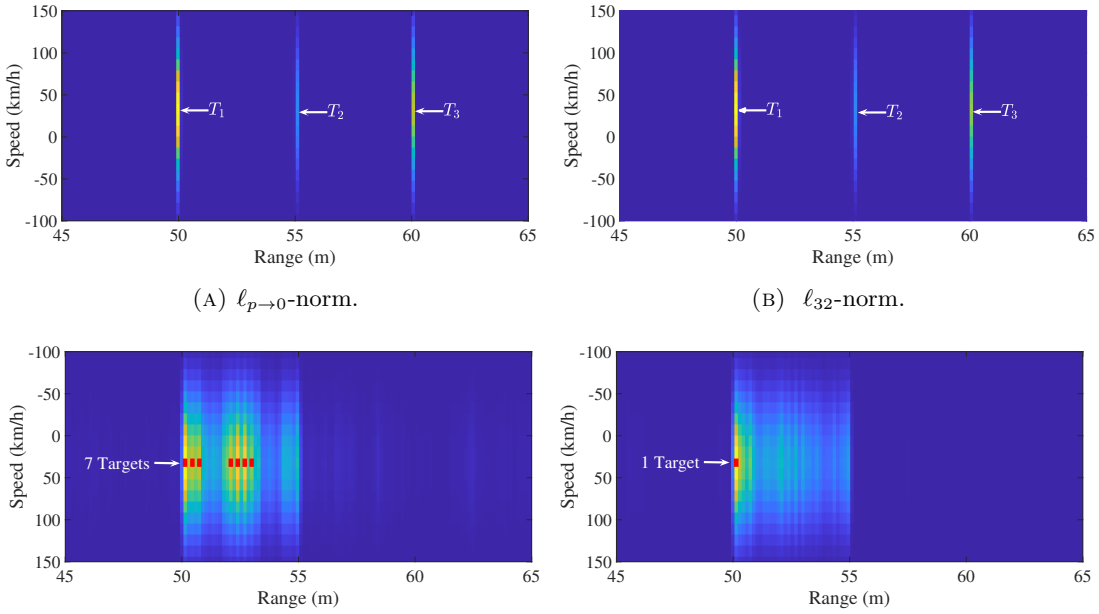

(A) $\ell_{p\to 0}$-norm. (B) ℓ_{32}-norm.

(C) $\ell_{p\to 0}$-norm. (D) ℓ_{32}-norm.

FIGURE 2.9: Range-Doppler profile of $\ell_{p\to 0}$ and ℓ_{32}-norm with point and continuous targets ($M = 3$, $N = 1024$ and $L = 32$).

constraint using BSUM framework. This problem formulation, provided further the flexibility for selecting p and adapting waveforms based on the environmental conditions, a key requirement for the emerging cognitive radar systems. To tackle the problem, in every iteration of BSUM algorithm, we utilized a local approximation function to minimize the objective function. Specifically we introduced entry- and vector-based solutions where in the former we obtain critical points and in the latter we obtain the gradient to find the optimized solution. We further used an FFT-based method for designing discrete phase sequences. Simulation results have shown the monotonicity of the proposed framework in minimizing the objective function. Besides, the proposed framework meets the lower bound in case of ISL minimization, and outperform the counterparts in terms of PSL, ℓ_0-norm and computational time values.

Chapter 3

Beampattern Shaping in MIMO radar systems

Transmit beampattern shaping plays important role to improve the performance of MIMO radars in different aspects. Such as, enhancing the SINR, probability of detection, coexistence with other Radio Frequency (RF) transmitter, etc. This chapter aims to address different waveform design approaches for transmit beampattern shaping in MIMO radar systems, under practical constraints, such as, continuous and discrete phase. In general, these approaches leads to multi-variable, non-convex and NP-hard optimization problem. To tackle the problems, we propose several algorithm based on CD, SDR, BSUM and penalty method. In the numerical results, we show the performance of the proposed method and compare it with the state-of-the art.

3.1 Waveform Design for Beampattern Shaping in 4D-imaging MIMO Radar Systems

In this section we design transmit beampattern for 4D-imaging automotive radar systems. To this end, we consider spatial-Integrated Sidelobe Level (ISLR) as the design metric and optimize it under continuous and discrete phase constraints. The problem formulation leads to a quadratic fractional programming, where we propose an effective Coordinate Descent (CD) -based method to solve the problem, which minimizes the objective function monotonically. In every iterations of the proposed method, we find global optimum solution for a single variable problem under continuous phase constraint. Under discrete phase constraint, we use Fast Fourier Transform (FFT) to solve problem which is efficient in terms of implementation. Through numerical simulations, we illustrate the performance of our proposed method and compare it with state-of-the art.

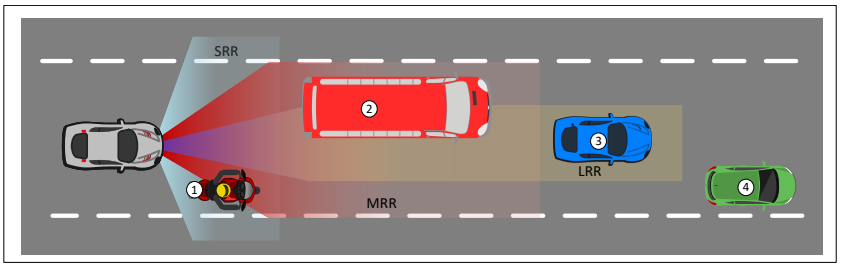

(A) Current automotive MIMO radar systems.

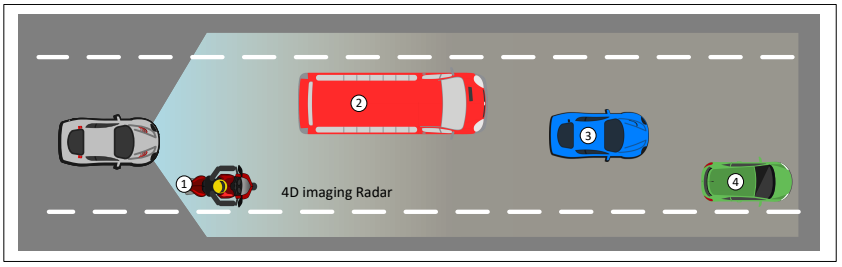

(B) 4D imaging automotive MIMO radar systems.

FIGURE 3.1: A comparison between the conventional and 4D imaging MIMO radar system.

MIMO radars systems are being increasingly integrated into commercial vehicles to support the ADAS by enabling robust and high performance target detection, localization, as well as interference (clutter) mitigation. Automotive radar sensors should be able to detect every single elements of the environment, and one solution to this end is equipping the vehicle with three types of radar, namely, LRR (for adaptive cruise control), MRR (for cross traffic alert and lane change assist) and SRR (for parking aid, obstacle/pedestrian detection). 4D-imaging is an alternative solution that provides the possibility of merging SRR, MRR, and LRR applications with one antenna configuration, which also provides high angular resolution in the entire radar operation range. To achieve this goal, a requirement is to design radar transmit beampattern by controlling the spatial distribution of the transmit power via adaptive waveform design approach, as it is depicted in Figure 3.1.

Beampattern shaping in MIMO radar: Transmit beampattern shaping by controlling the spatial distribution of the transmit power can play an important role to improve the radar performance through enhanced power efficiency, better detection probability, target identification, improved interference mitigation etc. The goal is to focus the transmit power on desired angles while minimizing for undesired angles [26]. Recently, the beampattern shaping via waveform design has been widely studied. On the point of view of the designed waveform, there are two methods for beampattern shaping, two-step and direct methods [26, 27]. In two-step method, the waveform correlation matrix is designed and then the original waveform matrix is obtained through one of

the decomposition methods [28, 30–36] and in direct method the waveform is designed directly [27, 41, 42].

On the other hand, regarding the objective function, in general there are two approaches, namely, beampattern matching [26–29, 34, 35, 41, 42] and spatial-ISLR minimization [40, 44]. In beampattern matching, the aim is minimizing the difference between the desired and designed beampattern. However in spatial-ISLR minimization approach, the aim is maximizing and minimizing the beampattern response on desired and undesired angles respectively. In this regards, several papers have been devoted to minimize the spatial-ISLR as design metric. For instance MIA [45] and STTC [46] is proposed to enhance the the SINR by spatial-ISLR minimization. The MIA approach is proposed based on MM for joint waveform and filter design under similarity, constant modulus and PAR constraints. In STTC a CD based method is proposed to design space-time codes under similarity, uncertain steering matrices, continuous or discrete phase constraints. The authors propose a Dinkelbach based method and exhaustive search for continuous and discrete phase constraints, respectively.

In this section, we consider beampattern shaping through the minimization of the spatial-ISLR by directly designing the waveform. Further, due to the need for higher power efficiency in automotive radars applications and ease of hardware implementation, the continuous and discrete phase (MPSK) waveform are preferred [99]. Our approach is to optimize the waveform iteratively using CD method which offers an efficient and low complexity methodology. Particularly, we propose derivative based method and Fast Fourier Transform (FFT) under continuous and discrete phase constraints. To this end, the section is organized as follow. Subsection 3.1.1 introduces the system model and describes the problem formulation. Subsection 3.1.2 presents the proposed framework whose performance is numerically assessed in subsection 3.1.3 .

Notations: We adopt the notation of using lower case boldface for vectors ($\mathbf{a}$) and capital boldface for matrix ($\boldsymbol{A}$). The transpose, conjugate transpose, conjugate and absolute value are denoted by the $(.)^T$, $(.)^\dagger$, $(.)^*$ and $|.|$ respectively. The letter j represents the imaginary unit ($j = \sqrt{-1}$), while the letter (i) is use as step of a procedure.

3.1.1 System Model and Problem Formulation

We consider a colocated narrow-band MIMO radar system, with M transmitters, each transmitting N pulses in the fast-time domain. Let the matrix $\boldsymbol{X} \in \mathbb{C}^{M\times N}$ denotes the

transmitted waveform in the base-band,

$$\boldsymbol{S} \triangleq \begin{bmatrix} s_{1,1} & s_{1,2} & \dots & s_{1,N} \\ s_{2,1} & s_{2,2} & \dots & s_{2,N} \\ \vdots & \vdots & \vdots & \vdots \\ s_{M,1} & s_{M,2} & \dots & s_{M,N} \end{bmatrix} \in \mathbb{C}^{M\times N}$$

whose m^{th} row indicates the pulses of m^{th} transmitter while the n^{th} column indicates the n^{th} pulse of all the transmitters. At time sample n, the waveform transmitted through the M antennas is denoted by $\mathbf{x}_n$, where,

$$\mathbf{x}_n = [x_{1,n}, x_{2,n}, \dots, x_{M,n}]^T \in \mathbb{C}^M. \tag{3.1}$$

In (3.1), $x_{m,n}$ is the n^{th} pulse of m^{th} transmitter. Let the arbitrary position vector of the m^{th} antenna be $\mathbf{p}_m \triangleq [p_{x_m}, p_{y_m}, p_{z_m}]^T$ and $\mathbf{r} \triangleq [\sin(\theta)\cos(\phi), \sin(\theta)\sin(\phi), \cos(\theta)]^T$. Thus, the steering vector can be written as [100],

$$\mathbf{a}(\theta,\phi) \triangleq [a_1(\theta,\phi), \dots, a_M(\theta,\phi)]^T \in \mathbb{C}^M. \tag{3.2}$$

where, $a_m(\theta,\phi) \triangleq e^{-j\frac{2\pi}{\lambda}\mathbf{p}_m^T\mathbf{r}(\theta,\phi)}$. In this case, the antenna beampattern is given by [28, 44, 101],

$$g(\boldsymbol{X},\theta,\phi) = \sum_{n=1}^{N} \left|\mathbf{a}^\dagger(\theta,\phi)\mathbf{x}_n\right|^2 = \sum_{n=1}^{N} \mathbf{x}_n^\dagger \boldsymbol{A}(\theta,\phi)\mathbf{x}_n \tag{3.3}$$

where, $\boldsymbol{A}(\theta,\phi) \triangleq \mathbf{a}(\theta,\phi)\mathbf{a}^\dagger(\theta,\phi)$. Let us denote $\boldsymbol{\Psi}_D = \{(\theta_k,\phi_k), k = \{1,\dots,K\}\}$ and $\boldsymbol{\Psi}_U = \{(\theta'_u,\phi'_u), u = \{1,\dots,U\}\}$ respectively, be the sets of desired and undesired angles in spatial domain and are obtained by cognitive paradigm. We are interested in minimizing the spatial-ISLR under continuous and discrete phase as follows,

$$\mathcal{P}\begin{cases} \min\limits_{\boldsymbol{X}} & f(\boldsymbol{X}) \triangleq \dfrac{\sum_{u=1}^{U} g(\boldsymbol{X},\theta'_u,\phi'_u)}{\sum_{k=1}^{K} g(\boldsymbol{X},\theta_k,\phi_k)} = \dfrac{\sum_{n=1}^{N}\mathbf{x}_n^\dagger \boldsymbol{A}_U \mathbf{x}_n}{\sum_{n=1}^{N}\mathbf{x}_n^\dagger \boldsymbol{A}_D \mathbf{x}_n} \\ s.t & \boldsymbol{X} \in C_1 \text{ or } C_2, \end{cases} \tag{3.4}$$

where, $\boldsymbol{A}_U \triangleq \sum_{u=1}^{U}\boldsymbol{A}(\theta'_u,\phi'_u)$, $\boldsymbol{A}_D \triangleq \sum_{k=1}^{K}\boldsymbol{A}(\theta_k,\phi_k)$, $C_1 \triangleq \{\boldsymbol{X} \mid x_{m,n} = e^{j\nu_{m,n}}, \nu_{m,n} \in \Omega_\infty\}, \Omega_\infty = [0, 2\pi)$ is constant modulus constraint and $C_2 \triangleq \{\boldsymbol{X} \mid x_{m,n} = e^{j\nu_{m,n}}, \nu_{m,n} \in \Omega_L\}, \Omega_L = \left\{0, \frac{2\pi}{L}, \dots, \frac{2\pi(L-1)}{L}\right\}$ is discrete phase constraint. In fact, Ω_L indicates the MPSK with alphabet size L. Since $f(\boldsymbol{X})$ is a fractional quadratic function, the objective function is non-convex. The C_1 and C_2 constraints are not affine sets. Besides the C_2 constraint is non-continuous and non-differentiate set. Therefore, the optimization problem $\mathcal{P}$ is non-convex, multi-variable and NP-hard problem. A promising approach

that directly finds the solution is CD method [92, 102]. The CD based methods are intuitively appealing and very simple to implement, yet they exhibit powerful performance in emerging radar waveform design applications in several aspects, such as beampattern shaping [38, 39, 100, 101], sidelobe reduction [24, 58, 78, 101] and spectral shaping [47, 53].

3.1.2 Proposed Method

In particular, we consider one entry of $\boldsymbol{X}$ as being the only variable while keeping the others fixed; for this identified variable, we optimize the objective function. The methodology is efficient when the objective function can be written in a simplified form for that identified variable. In this regard, let us assume that $x_{t,d}$ is the only variable at $(i)^{th}$ iteration of the optimization procedure. The resulting single-variable objective function at $(i)^{th}$ iteration can be written as (see Appendix B.1),

$$f(x_{t,d}, \boldsymbol{X}^{(i)}_{-(t,d)}) = \frac{a_0 x_{t,d} + a_1 + a_2 x^*_{t,d}}{b_0 x_{t,d} + b_1 + b_2 x^*_{t,d}}.$$

Here, $\boldsymbol{X}^{(i)}_{-(t,d)} = \boldsymbol{X}^{(i)}|_{s_{t,d}=0}$ refers to the fixed entries. By substituting $x_{t,d} = e^{j\nu}$ the problem $\mathcal{P}$ depends only on parameter ν [1] and $\mathcal{P}$ can be recast as follows,

$$\mathcal{P}^{(i)} \begin{cases} \min\limits_{\phi} & f^{(i)}(\nu) = \dfrac{a_0 e^{j\nu} + a_1 + a_2 e^{-j\nu}}{b_0 e^{j\nu} + b_1 + b_2 e^{-j\nu}} \\ s.t & \nu \in \Omega_\infty \text{ or } \Omega_L. \end{cases}$$

Consequently, the optimal phase of the code entry $x_{t,d}$ can be obtained by solving,

$$\nu^{\star(i)} = \arg\min_{\phi} \{ f^{(i)}(\nu) \,|\, \phi \in \Omega_\infty \text{ or } \Omega_L \}. \tag{3.5}$$

Subsequently, the variable $x_{t,d}$ will be updated by ${x^\star_{t,d}}^{(i)} = e^{j\nu^{\star(i)}}$. This procedure will continue until the stationary point is obtained. We consider $f(\boldsymbol{X}^{(i-1)}) - f(\boldsymbol{X}^{(i)}) < \zeta$, $(\zeta > 0)$ as stopping criterion of optimization. The proposed method is summarized in **Algorithm 4**. In the following we obtain the optimum solution under continuous and discrete phase.

Designing Continuous phase: As $f^{(i)}(\nu)$ is a real, differentiable and periodic function, it has at least two extrema. Therefore, its derivative has at least two real roots. By

[1] For the convenience we use ν instead of $\nu_{m,n}$ in the rest of the section.

Algorithm 4 : Transmit Beampattern Shaping for 4D-imaging radar

Input: Initial set of feasible sequences, $\boldsymbol{X}^{(0)}$.
Initialization: $i := 0$.
Optimization:

```
while (f(X^(i-1)) − f(X^(i))) > ζ do
    i := i + 1;
    for t = 1, ..., M do
        for d = 1, ..., N do
            Optimize x_{t,d}^{(i-1)} and obtain x*_{t,d};
            Update x_{t,d}^{(i)} = x*_{t,d};
            X^(i) = X^(i)_{-(t,d)}|_{x_{t,d}=x_{t,d}^(i)};
        end for
    end for
end while
```

Output: $\boldsymbol{X}^{\star} = \boldsymbol{X}^{(i)}$.

standard mathematical manipulations, the derivative of $f^{(i)}(\nu)$ can be obtained as,

$$f'^{(i)}(\nu) = \frac{c_0 e^{j\nu} + c_1 + c_2 e^{-j\nu}}{(b_0 e^{j\nu} + b_1 + b_2 e^{-j\nu})^2},$$

where, $c_0 = j(a_0 b_1 - a_1 b_0)$, $c_1 = j2(a_0 b_2 - a_2 b_0)$ and $c_2 = c_0^*$. Using the slack variable $z \triangleq e^{-j\nu}$, the critical points can be obtained by obtaining the roots of second degree polynomial of $f'^{(i)}(z) \triangleq c_2 z^2 + c_1 z + c_0 = 0$, which is equal to $z_{1,2}^{(i)} = \frac{-c_1 \pm \sqrt{c_1^2 - 4C_2C_0}}{2c_2}$. Therefore the extremum point of $f^{(i)}(\nu)$ is $\nu_{1,2}^{(i)} \triangleq j \ln(z_{1,2}^{(i)})$ and subsequently the optimized phase is,

$$\nu^{\star(i)} = \arg\min_{\nu} \left\{ f^{(i)}(\nu) \,|\, \nu \in \nu_{1,2}^{(i)} \right\}. \tag{3.6}$$

Designing Discrete phase: Since in discrete phase the phases are chosen from limited alphabet of length L, the objective function can be written with respect to the indices of Ω_L as, $f^{(i)}(l) = \sum_{n=0}^{2} a_n e^{-j\frac{2\pi nl}{L}} / \sum_{n=0}^{2} b_n e^{-j\frac{2\pi nl}{L}}$ where, $l = \{0, \ldots, L-1\}$. The summation term in the numerator and denominator in aforementioned equation is exactly the definition of $L-$point DFT of sequences $[a_0, a_1, a_2]$ and $[b_0, b_1, b_2]$ respectively. Therefore, $f^{(i)}(l)$ can be written as,

$$f^{(i)}(l) = \frac{\mathcal{F}_L\{a_0, a_1, a_2\}}{\mathcal{F}_L\{b_0, b_1, b_2\}}. \tag{3.7}$$

where, $\mathcal{F}_L$ is $L-$point DFT operator. The current function is only valid for $L > 2$. According to periodic property of DFT, $f^{(i)}(l)$ can be written as, $f^{(i)}(l) = \mathcal{F}_L\{a_0 + a_2, a_1\}/\mathcal{F}_L\{b_0 + b_2, b_1\}$ for $L = 2$. Therefore the optimum solution of (3.7) is, $l^{\star(i)} =$

$\arg \min_{l=1,\dots,L} \left\{ f^{(i)}(l) \right\}$. Subsequently, the optimum phase is,

$$\nu^{\star(i)} = \frac{2\pi(l^{\star(i)} - 1)}{L}. \tag{3.8}$$

3.1.3 Numerical Results

In this subsection we consider to evaluate the performance of the proposed and compare it with the state-of-the art counterparts. In this regards, we assume that the sequence length is $N = 128$ and the stopping condition for **Algorithm 4** is set at $\zeta = 10^{-6}$.

Beampattern shaping and convergence: We consider Uniform Linear Array (ULA) configuration for transmitters, whic are located in z axis ($p_{x_m} = p_{y_m} = 0$) with $M = 8$ transmitters and the antenna distance is set as $d_z = \frac{\lambda}{2}$. Figure 3.2a shows the beampattern response of the proposed method under C_1 and C_2 constraints with different alphabet size. In Figure 3.2a we assume that the desired and undesired angular regions are $\Psi_D = [30^o, 50^o]$ and $\Psi_U = [-90^o, 25^o] \cup [55^o, 90^o]$ with linear grid size of 5^o, respectively. In addition, the proposed method is initialized using random MPSK sequences with alphabet size $L = 4$. Here, every code entry is given by,

$$x_{m,n}^{(0)} = e^{j\frac{2\pi(l-1)}{L}}, \tag{3.9}$$

where l is the random integer variable uniformly distributed in $[1, L]$. As can be seen The proposed method steers the beampattern towards desired angles and minimizes the sidelobes level at undesired angles. Since the feasible set of problem under C_1 is greater than C_2, the performance of continuous phase is better than discrete phase. Besides, by increasing the alphabet size the beampattern under discrete phase tends to the beampattern of continuous phase constraint. Figure 3.2b shows the convergence behavior of the proposed method, corresponding to Figure 3.2a. As can be seen the objective function decreases monotonically in each iteration for both continuous and discrete phase. Similar to the behavior shown in Figure 3.2a, by increasing the alphabet size, the objective value under discrete phase tends to the value obtained under continuous phase constraint.

Beampattern shaping with binary sequences: Due to the simplicity of implementing of binary sequences, these kind of waveforms are attractive for radar designers. Here we assess the beampattern performance of proposed binary waveform design. Figure 3.3a shows the beampattern response of the proposed method, where we assume that $\Psi_D = [30^o, 50^o]$ and $\Psi_U = [-90^o, 25^o] \cup [55^o, 90^o]$ with linear grid size of 5^o. As can be seen, the beampattern response in binary case is symmetric about 0^o. Indeed, in a case when

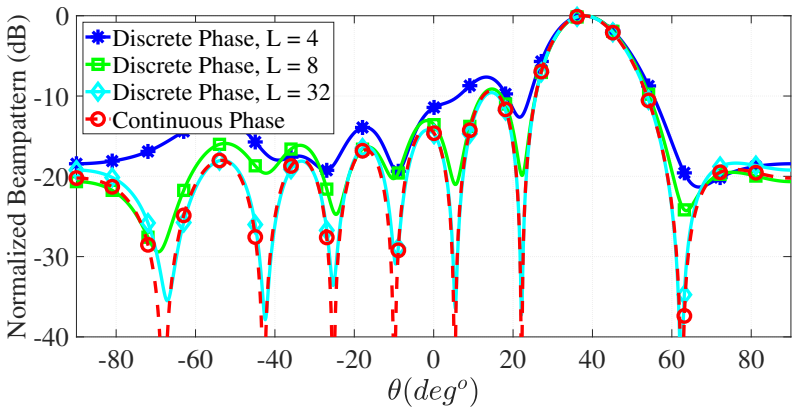

(A) Beampattern.

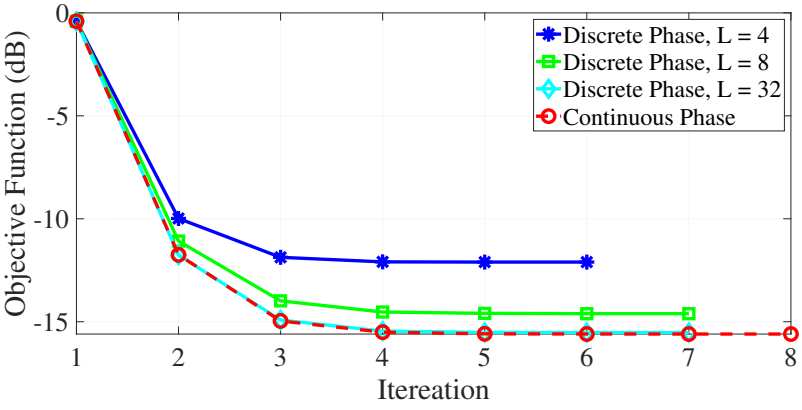

(B) Convergence behavior.

FIGURE 3.2: The linear array beampattern and convergence behavior of the proposed method ($M = 8$, $N = 128$ and $\Psi_D = [30^o, 50^o]$ and $\Psi_U = [-90^o, 25^o] \cup [55^o, 90^o]$)

the waveforms are real (binary sequences), the beampattern will be symmetric. In 4D-imaging application of automotive radar systems, the desired region for beampattern shaping can be limited to the angles around zero, where binary codes can be used. For instance a beampattern with $\Psi_D = [-10^o, 10^o]$ and $\Psi_U = [-90^o, -15^o] \cup [15^o, 90^o]$ as shown in Figure 3.3b can be used for automotive application.

Performance assessment in comparison with the counterparts: We compare the performance of the proposed method under C_1 and C_2 with MIA-CMC, MIA-CMC-AC[2] [45] and STTC [46] respectively. we assume that the target and the three interferers are located at 10^o, -5^o, 25^o and -60^o respectively. We set noise power -10 dB, and similar values of 30dB for target and clutter RCS. Since the proposed method and MIA-CMC does not consider the similarity constraint, for a fairness, we set the similarity threshold equal to 2, the maximum admissible similarity value in STTC. Figure 3.4a shows the normalized beampattern response of MIA-CMC, MIA-CMC-AC, STTC and the proposed method. Observe that in terms of null steering, the proposed method under C_1 constraint

[2] MIA-CMC-AC is the accelerated version of MIA-CMC.

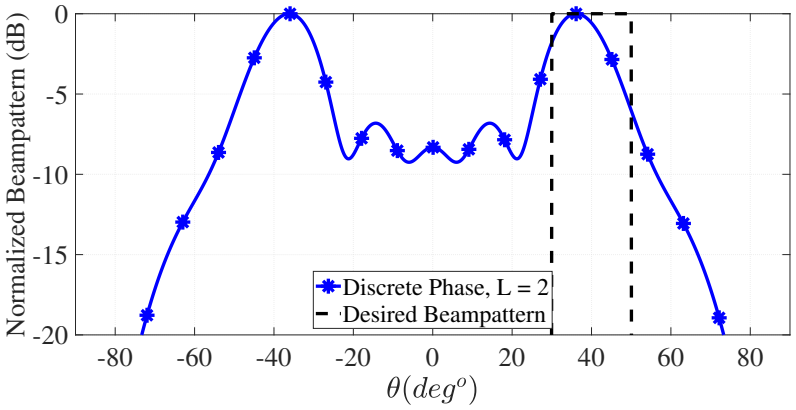

(A) $\Psi_D = (30^o, 50^o)$ and $\Psi_U = (-90^o, 25^o) \cup (55^o, 90^o)$.

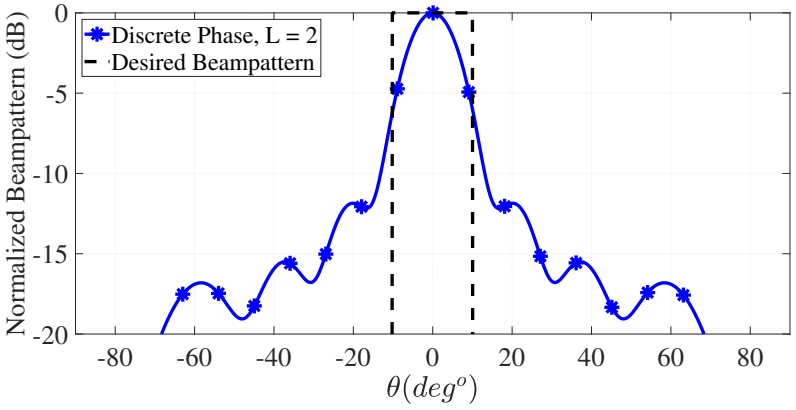

(B) $\Psi_D = (30^o, 50^o)$ and $\Psi_U = (-90^o, 25^o) \cup (55^o, 90^o)$.

FIGURE 3.3: The Beampattern of proposed method with binary set of sequences ($M = 8$ and $N = 128$)

outperforms MIA-CMC and has a similar performance under C_1 constraint compare with STTC.

Figure 3.4b compares the convergence time of the proposed method with MIA-CMC, STTC with different sequence length[3]. The highest convergence time belongs to the STTC method which is based on CD method. Note that STTC uses exhaustive search to find the optimum solution which is very expensive in terms of complexity. Although the proposed algorithm under C_2 constraint uses CD method as well, but due to the efficient formulation and using FFT, it has significantly lower computational time. Further, under C_1 constraint, the proposed method has lower convergence time in comparison with MIA-CMC.

Beampattern shaping for planar array: In this part we consider to evaluate the capability of beampattern shaping of the proposed method in case of planar array configuration. To this end we assume that the transmitters are laid on x and y plane in

[3]The reported values are obtained with a standard PC with Intel (R) Core (TM) i5-8250U CPU@ 1.60 GHz with installed memory (RAM) 8.00 GB.

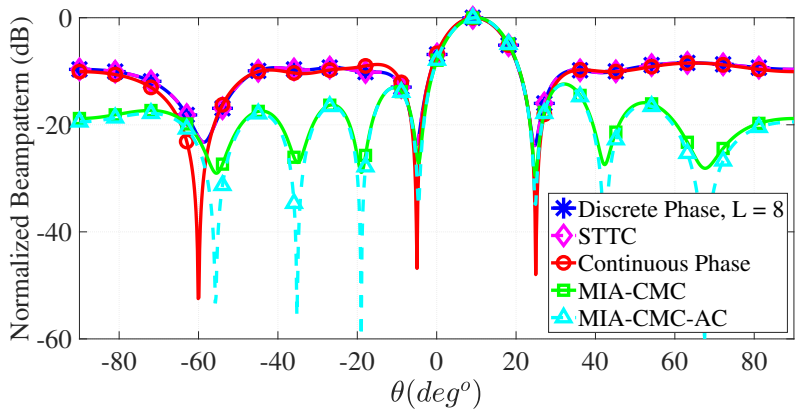

(A) Null steering ($N = 128$)

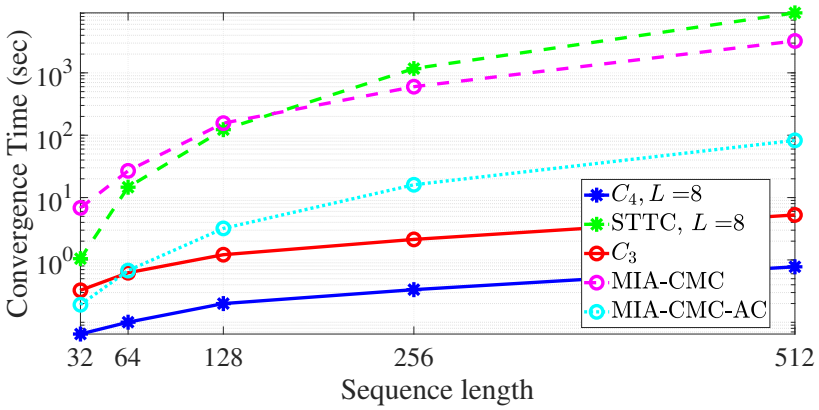

(B) Convergence Time.

FIGURE 3.4: Comparing the performance of the proposed method with MIA-CMC and STTC in terms of null steering and convergence time ($M = 8$, $\Psi_D = 10^o$ and $\Psi_U = \{-5^o, 25^o, -60^o\}$)

spherical coordinate systems i.e. $p_{z_m} = 0$. We assume the standard rectangular ULA configuration for transmitters, where the distance between the elements are $d_x = d_y = \frac{\lambda}{2}$. The number of transmitter is set as, $M = 4 \times 4$. For purpose of simulation, we consider an uniform sampling of regions $\theta = (0, \pi]$ and $\phi = (0, \pi]$ with a grid size of 5^o. We select the desired angular regions to be $\Psi_D = (\theta_k, \phi_k) | \theta_k = \phi_k \in [-50^o, -40^o] \cup [40^o, 50^o]$. Observe that the beampattern of discrete phase mimics the beampattern of continuous phase. However, since the feasible set of C_1 is greater than C_2 the continuous phase has greater gain when compared with the discrete phase.

3.2 MIMO Radar Transmit Beampattern Matching Based on Block Successive Upper-bound Minimization

Waveform design with considering discrete phase constraint at the design stage tends to be pertinent in the emerging radar designs, especially since the digital to analogue

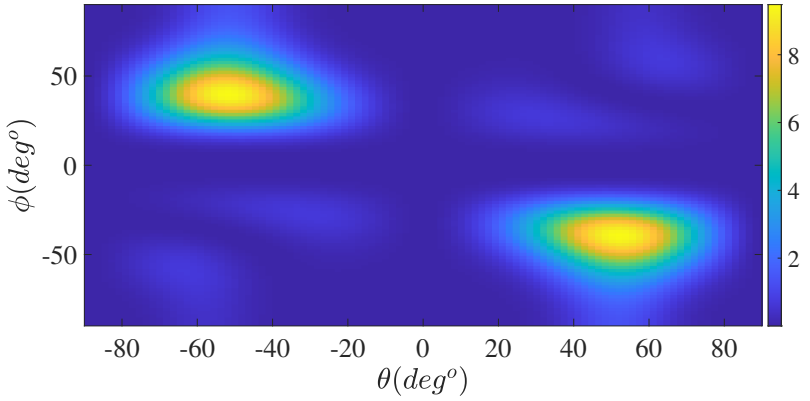

(A) Continuous Phase.

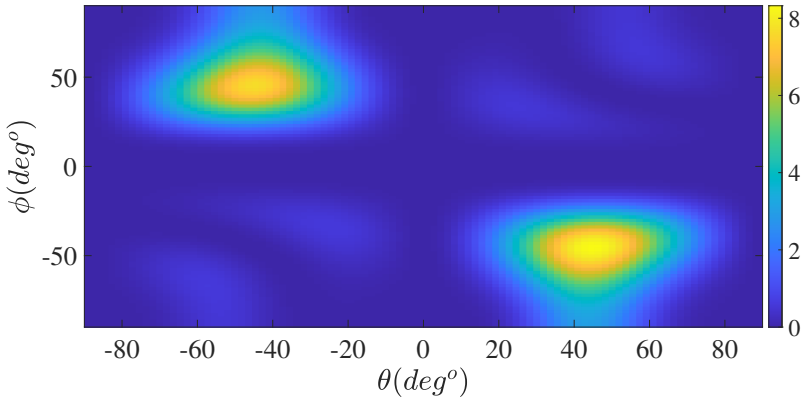

(B) Discrete Phase $L = 8$

FIGURE 3.5: The Beampattern of proposed method in case of planar array configuration ($M = 4 \times 4$, $N = 128$ and $\Psi_D = (\theta_k, \phi_k)|\theta_k = \phi_k \in [-50^o, -40^o] \cup [40^o, 50^o]$.)

converters are limited in the resolution. However, this constraint confines the degree of freedom to be only the waveform phase, which should be selected from a limited alphabet. In this section, we aim to approximate a desired beampattern closely by designing the transmit waveform while considering the discrete phase constraint at the design stage. To this end, we consider a novel ℓ_p-norm metric to achieve quasi-equiripple beampattern, which reduces the interference from the undesired directions. This problem leads to a NP-hard and non-convex optimization problem, where to efficiently solve it, we utilize the BSUM algorithm which successively optimizes the objective function by optimizing a certain upper bound of the original objective in a coordinate wise manner. In the numerical results, we show the performance of the proposed method and compare it with the state-of-the art.

Transmit beampattern shaping controls the directionality of the transmission on transmit antennas in MIMO radar systems. Beampattern shaping by providing a better SINR, improves the spectral-special efficiency, better detection probability, target identification, improved interference mitigation, etc. In this regards, adaptive waveform design, plays

important role to shape the beampattern effectively. Generally, there are two approaches for beampattern shaping via waveform design are exist, the indirect (two-step) and direct methods [26]. In indirect approach first, the waveform correlation matrix is designed and then the original waveform matrix is obtained through one of the decomposition methods [44]. While in direct method the waveform is designed directly [26]. Besides, there are several metrics (objective functions) to shape the beampattern, such as, beampattern matching, spatial-ISLR minimization and SINR maximization. In beampattern matching the goal is minimizing the difference of the beampattern response of MIMO radar with the desired beampattern [26–28, 41, 42]. In Spatial-ISLR minimization approach, the aim is minimizing the ratio of *summation of beampattern response on undesired over desired angles* [32, 37, 43]. In SINR optimization approaches, the problem does not deal with the beampattern directly. However, kind of beampattern will be shaped as a result of transmit waveform optimization [30, 31, 45, 46].

In this section, we consider the ℓ_p-norm beampattern matching problem under discrete phase, i.e. MPSK constraint. Considering the ℓ_p-norm metric for the beampattern matching problem was originally suggested in [42], and it has been shown that it provides quasi-equiripple beampattern comparing with the standard ℓ_2-norm metric. In [42], PAR and energy constraints were considered as the optimization constraints in the design stage. It is worth noting that in the aforementioned schemes, high-resolution digital-to-analog converters (DACs) are considered by default. However, it will cause massive power consumption and huge hardware cost when employing MIMO radars, especially for the 4D-imaging cases [43]. This motivates the use of low resolution DACs. Recently, in [103, 104], the low-resolution DACs is utilized to beampattern design. However, the aforementioned methods need several time approximation which can lead some performance loss. Different from the works in the literature, we directly solve the problem of ℓ_p-norm based beampattern matching considering the discrete phase constraint at the design stage. This scheme results in a non-convex, possibly NP-hard problem. Our approach is to design the waveform directly using BSUM which offers a low complexity methodology to a complex problem.

To this end, the section is organized as follow. Subsection 3.2.1 introduces the system model and describes the problem formulation. Subsection 3.2.2 presents the proposed BSUM based method whose performance is numerically assessed in subsection 3.2.3.

Notations: We adopt the notation of using lower case boldface for vectors ($\mathbf{a}$) and capital boldface for matrix ($\mathbf{A}$). The transpose, conjugate transpose, Frobenius norm absolute and Hadamard product operators are denoted by the $(.)^T$, $(.)^H$, $\| \, . \, \|_F$, $|.|$ and respectively. The letter j represents the imaginary unit (i.e., $j = \sqrt{-1}$), while the letter (i) is use as step of a procedure.

3.2.1 System Model and Problem Formulation

Let $\mathbf{X} \in \mathbb{C}^{M,N}$ be the transmitted waveform in the base-band of a MIMO radar system with M transmitters and the sequence length of N. At time sample n, the waveform transmitted through the M antennas is denoted by $\mathbf{x}_n$, where,

$$\mathbf{x}_n = [x_{1,n}, x_{2,n}, \ldots, x_{M,n}]^T \in \mathbb{C}^M. \tag{3.10}$$

In (3.10), $x_{m,n}$ denotes the n^{th} sample of the m^{th} transmitter. Let ULA be the configuration of the transmitter, where the distance between the elements are $d_t = \frac{\lambda}{2}$ and λ is the wavelength. Thus, the steering vector can be written as [105], $\mathbf{a}(\theta) = [1, e^{j\pi \sin(\theta)}, \ldots, e^{j\pi(M-1)\sin(\theta)}]^T \in \mathbb{C}^M$. In this case the transmit beampattern is given by [44],

$$r(\mathbf{X}, \theta) = \sum_{n=1}^{N} \left| \mathbf{a}^H(\theta)\mathbf{x}_n \right|^2 = \sum_{n=1}^{N} \mathbf{x}_n^H \mathbf{A}(\theta)\mathbf{x}_n, \tag{3.11}$$

where, $\mathbf{A}(\theta) \triangleq \mathbf{a}(\theta)\mathbf{a}^H(\theta)$.

Using the beampattern matching under discrete phase constraint leads us to solve the following optimization problem [42],

$$\begin{cases} \min\limits_{\mathbf{X},\mu} & f(\mathbf{X}, \mu) \triangleq \sum\limits_{k=1}^{K} |r(\mathbf{X}, \theta_k) - \mu q_k|^p \\ s.t. & x_{m,n} = e^{j\phi}, \quad \phi \in \Phi_L, \end{cases} \tag{3.12}$$

where, $p \geq 2$, q_k is the desired beampattern, μ is a scaling factor [26], and Φ_L indicates the discrete phase alphabet. Precisely, Φ_L indicates the MPSK alphabet, e.g. $\Phi_L = \left\{0, \frac{2\pi}{L}, \ldots, \frac{2\pi(L-1)}{L}\right\}$.

As can be seen the (3.12) is a multi-variable, non-convex and NP-hard optimization problem. In the following, we propose an algorithm based on BSUM to deal with (3.12).

3.2.2 Proposed Method

The BSUM algorithm generalizes the BCD methods and includes procedure that successively optimize particular upper-bounds or local approximation functions of the original objectives in a block by block manner [58, 106]. One possible choice for the approximation function is MM function. This choice is one of the condition which guarantees the convergence of the argument in optimization problem [107, 108]. In this section, we use the following lemma to obtain the majorizer function.

Lemma 3.1. *Let* $|x| \in [0, \tau]$*, for* $p \geq 2$*,* $|x|^p$ *can be majorized by* $\eta|x|^2 + \psi\Re\left\{x\frac{x^{(i)}}{|x^{(i)}|}\right\} + \nu$*, where,* $\psi \triangleq p|x^{(i)}|^{(p-1)} - 2\eta|x^{(i)}|$*,* $\eta \triangleq \frac{\tau^p + (p-1)|x^{(i)}|^p - p\tau|x^{(i)}|^{(p-1)}}{(\tau - |x^{(i)}|)^2}$*,* $\nu \triangleq \eta|x^{(i)}|^2 - (p-1)|x^{(i)}|^p$*.*

Proof. see [76]. □

Substituting $|r(\mathbf{X}, \theta_k) - \mu q_k|$ in lemma 3.1 and considering $r(\mathbf{X}, \theta_k) - \mu q_k$ is a real function, it can be shown that $f(\mathbf{X}, \mu)$ can be majorized by the following,

$$\begin{aligned} u(\mathbf{X}, \mu) = &\sum_{k=1}^{K} \eta_k (r(\mathbf{X}, \theta_k) - \mu q_k)^2 \\ &+ \sum_{k=1}^{K} \psi_k (r(\mathbf{X}, \theta_k) - \mu q_k) + \sum_{k=1}^{K} \nu_k. \end{aligned} \tag{3.13}$$

Defining $g_k^{(i)} \triangleq r(\mathbf{X}^{(i)}, \theta_k) - \mu^{(i)} q_k$ we have,

$$\begin{aligned} \eta_k &\triangleq \frac{\tau^p - |g_k^{(i)}|^p - p|g_k^{(i)}|^{p-1}(\tau - |g_k^{(i)}|)}{(\tau - |g_k^{(i)}|)^2} \\ \psi_k &\triangleq (p|g_k^{(i)}|^{p-2} - 2\eta_k) g_k^{(i)}, \nu_k \triangleq \eta_k |g_k^{(i)}|^2 - (p-1)|g_k^{(i)}|^p \end{aligned} \tag{3.14}$$

According to 3.1, in each iteration, τ should be chosen such that it is a upper bound of $|g_k|^p$. Therefore, one possible choice is $\tau = \left\|g_k^{(i)}\right\|_p$ [76].

The problem (3.13) depends on $\mathbf{X}$ and μ. One possible solution to tackle this problem is using *alternative optimization* technique [109]. Based on this technique, first we optimize the problem with respect to μ, then in the next step we optimize it with respect to $\mathbf{X}$.

3.2.2.1 Scaling factor optimization

The majorization function (3.13) has a quadratic form with respect to μ. In this case the problem is convex and the optimum value of μ can be obtain by finding the roots of the derivative of the objective function. It can be shown that the optimum value for μ is given by,

$$\mu^\star = \frac{\sum_{k=1}^{K} 2q_k\eta_k r(\mathbf{X}^{(i)}, \theta_k) + q_k\psi_k}{2\sum_{k=1}^{K} \eta_k q_k^2} \tag{3.15}$$

3.2.2.2 Waveform Optimization

The BSUM procedure consists of three steps as follows, 1) Select a block. 2) Find a local approximation function that locally approximates the objective function. 3) At every

iteration (i), a single block, is optimized by minimizing a approximation function of the selected block. In the smallest case each entry of matrix $\mathbf{X}$ can be considered as a block. In particular at i^{th} iteration, one entry of $\mathbf{X}^{(i)}$ is considered as the only variable while others are held fixed and with respect to this identified variable, the objective function is optimized. Such a methodology is efficient when the objective function can be written in a simplified form with respect to that variable. Let us assume that $x_{t,d}^{(i)} = e^{j\phi_{t,d}^{(i)}}$ is the only variable. Therefore the optimization problem with respect to $\phi_{t,d}^{(i)}$ can be written equivalently as [37],

$$\begin{cases} \min\limits_{\phi_{t,d}^{(i)}} & u(\mu^\star, \phi_{t,d}^{(i)}) = \sum\limits_{n=-2}^{2} c_n^{(i)} e^{jn\phi_{t,d}^{(i)}} \\ s.t. & \phi_{t,d}^{(i)} \in \Phi_L, \end{cases} \tag{3.16}$$

where the coefficients c_n are given in the Appendix B.2.

Since in discrete phase the phases are chosen from limited alphabet of length L, the objective function can be written with respect to the indices of Φ_L as,

$$u(\mu^\star, l) = e^{j\frac{4\pi l}{L}} \sum_{n=-2}^{2} c_n e^{j\frac{2\pi(n-2)l}{L}} \tag{3.17}$$

where $l \in \{0, \ldots, L-1\}$. As can be seen, the summation part of (3.17) is the definition of L-points DFT of sequence $[c_2, \ldots, c_{-2}]^T$. Therefore (3.17) can be written equivalently as,

$$u(\mu^\star, l) = \mathbf{h} \odot \mathcal{F}_L\{c_2, c_1, c_0, c_{-1}, c_{-2}\}, \tag{3.18}$$

where, $\mathbf{h} = [1, e^{j\frac{4\pi}{L}}, \ldots, e^{j\frac{4\pi(L-1)}{L}}]^T \in \mathbb{C}^L$ and $\mathcal{F}_L$ is $L-$point DFT operator. The current function is only valid for $L \geqslant 5$. According to periodic property of DFT, $u(\mu^\star, l)$ can be written as,

$$\begin{aligned} L = 4 &\Rightarrow u(\mu^\star, l) = \mathbf{h}_L \odot \mathcal{F}_L\{c_2 + c_{-2}, c_1, c_0, c_{-1}\}, \\ L = 3 &\Rightarrow u(\mu^\star, l) = \mathbf{h}_L \odot \mathcal{F}_L\{c_2 + c_{-1}, c_1 + c_{-2}, c_0\}, \\ L = 2 &\Rightarrow u(\mu^\star, l) = \mathbf{h}_L \odot \mathcal{F}_L\{c_2 + c_0 + c_{-2}, c_1 + c_{-1}\}. \end{aligned}$$

Therefore the optimum solution for discrete phase is, $l^\star = \arg\min\limits_{l=1,\ldots,L} \left\{u(\mu^\star, l)\right\}$. Subsequently, the optimum phase is, $\phi_d^\star = \frac{2\pi(l^\star - 1)}{L}$.

Proposed Algorithm: The proposed method is summarized in **Algorithm 5**. The inputs of this algorithm comprise $\mathbf{X}^{(0)}$ which is a set of random and feasible waveform, and the desired beampattern q_k. In the initialization step the optimization parameters will be initialized with proper values. Then in the first step we obtain the optimum value of μ, subsequently, the variable $x_{t,d}$ will be updated by $e^{j\phi_d^\star}$. This procedure will be continued until the stationary point is obtained. We consider to terminate the algorithm

procedure when the argument of the objective convergence to the optimum value, e.g., we consider $\Delta\mathbf{X}^{(i)} \triangleq \left\|\mathbf{X}^{(i)} - \mathbf{X}^{(i-1)}\right\|_F \leq \zeta$ as the stopping criterion.

Algorithm 5 : Waveform Design

Input: $\mathbf{X}^{(0)}$, q_k
Output: Optimized waveform, $\mathbf{X}^\star$

1. **Initialization**
   - Set $i := 0$, $t, d := 1$ and $\mu := 1$;
2. **Optimizing the scaling factor**
   - calculate the coefficients by (B.2)
   - Obtain the optimum μ by (3.15);
3. **Optimizing the waveform**
   - Calculate $u(\mu^\star, l)$, using (3.18);
   - Find the Optimum phase, using $\phi_d^\star = \frac{2\pi(l^\star - 1)}{L}$;
   - $\mathbf{X}^{(i)} = \mathbf{X}^{(i-1)}|_{x_{t,d}=e^{j\phi_d^\star}}$;
   - If $t = M$ then $t := 1$; otherwise $t := t + 1$;
   - If $d = N$ go to 4); otherwise $d := d + 1$ and go to 2);
4. **Stopping criterion**
   - If $\Delta\mathbf{X}^{(i)} = \left\|\mathbf{X}^{(i)} - \mathbf{X}^{(i-1)}\right\|_F \leq \zeta$, go to 5); otherwise $d := 1$ and go to 2);
5. **Output**
   - Set $\mathbf{X}^\star = \mathbf{X}^{(i)}$

3.2.3 Numerical results

In this subsection, we provide some representative numerical examples to illustrate the effectiveness of proposed method. We consider the following assumptions. For system parameters we consider ULA configuration with $M = 16$ transmitters with $N = 128$ pulses. For purpose of simulation, we consider an uniform sampling of the regions $\theta = [-90^o, 90^o]$ with a grid size of 5^o. For the **Algorithm 5**, we consider a random MPSK sequences as initial waveform and the stopping condition of algorithm 5 is set at $\zeta = 10^{-3}$.

3.2.3.1 Convergence Behavior

Figure 3.6 shows the convergence behavior of the proposed algorithm in two aspects, namely the objective function and the argument. For these figures, we assume that the desired angles are located at $[-15^o, 15^o]$ and the algorithm 5 is initialized with

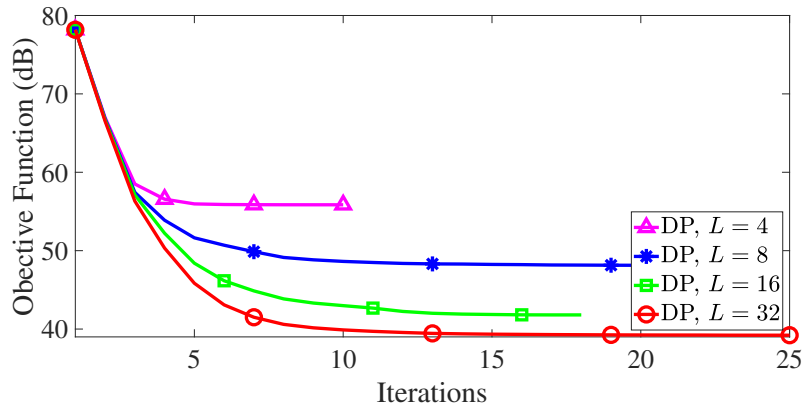

(A) objective function

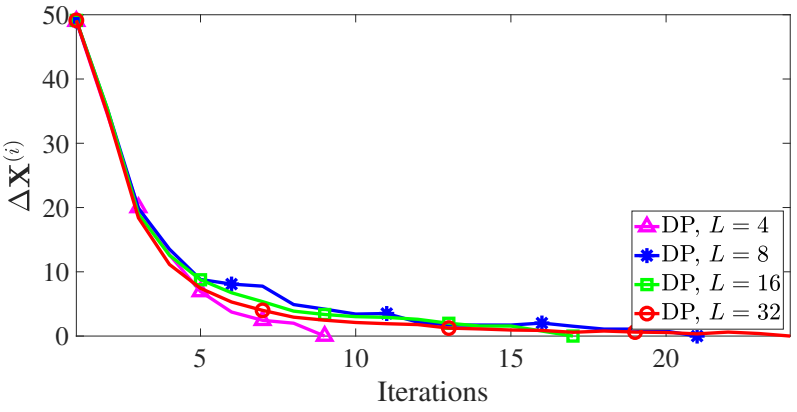

(B) argument

FIGURE 3.6: Convergence behavior of the proposed method with different alphabet size ($M = 16$, $N = 128$, $p = 3$ and $q_k \in [-15^o, 15^o]$)

random MPSK sequence with alphabet size of $L = 4$. Figure 3.6a shows the convergence behavior of the objective function with different alphabet sizes. As can be seen, in all cases the objective function decreases monotonically. By increasing the alphabet size of the waveform the feasible set of the problem increases, therefore the performance of the proposed method becomes better. Figure 3.6b shows the convergence behavior of the argument of the problem. Observe that in all cases the argument converges to the optimum value.

3.2.3.2 The impact of alphabet size

Here we investigate the impact of alphabet size of the waveform on beampattern response. Figure 3.7 shows the beampattern response of the proposed method with different alphabet sizes. In this figure, we consider similar simulation setup with Figure 3.6. Observe that, increasing the alphabet size cause better beampattern response in terms

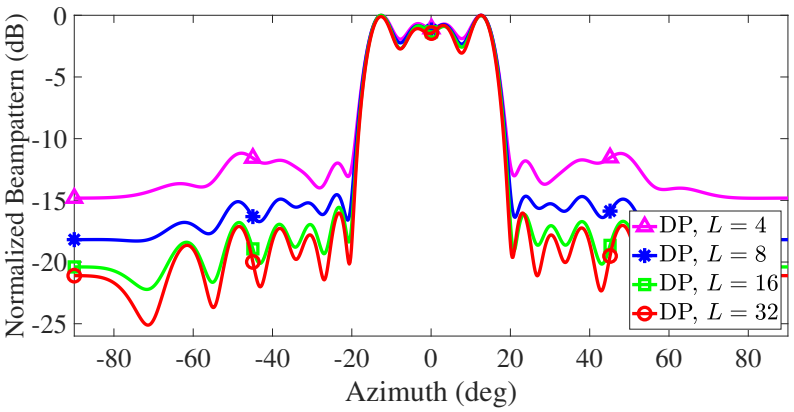

FIGURE 3.7: The impact of alphabet size on the beampattern response of the proposed method ($M = 16$, $N = 128$, $p = 3$ and $q_k \in [-15^o, 15^o]$).

of the side-lobes. This behavior was expected, because by increasing the alphabet size the feasible set will increase as well.

3.2.3.3 Beampattern Analysis

In this part we evaluate the performance of the proposed method in terms of beampattern response. Figure 3.8 compares the beampattern response of the proposed method with UNIQUE-C_4 [37] and the ADMM [26] methods. The UNIQUE-C_4 method proposed a CD-based method to solve the spatial-ISLR problem under discrete phase, while the authors in [26] solved the beampattern matching problem based on ADMM method under continuous phase constraint. Observe that UNIQUE offers the lowest sidelobes in both terms of spatial-ISLR and -PSLR among the methods. However, the beampattern response on the mainlobe is imperfect. The ADMM-based and proposed methods with ℓ_2- and ℓ_p-norm matching have the same mainlobe beampattern response. However, the advantage of the proposed method is designing a discrete phase waveform with finite alphabet size which is more attractive for radar engineers, due to the simplicity.

3.2.3.4 Computational Complexity

Figure 3.9 compares the convergence time of the proposed with UNIQUE-C_4 and ADMM, with different sequence length. As can be seen, the ADMM has the highest convergence time which indicates the the high computational complexity of it. The UNIQUE-C_4 method offers the lowest convergence time which shows the efficiency of the algorithm. However, convergence time of the ℓ_2-norm and ℓ_p-norm beampattern matching approach is some how between the two aforementioned methods. Since in the proposed method we do not directly deal with the original problem, this behavior is expected. Furthermore,

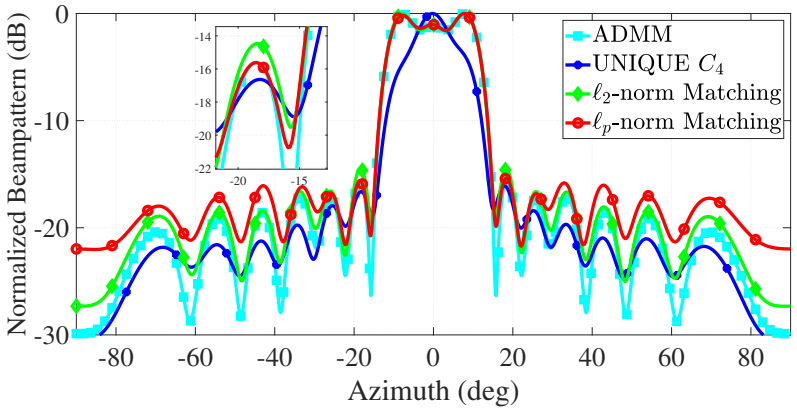

FIGURE 3.8: Comparing the beampattern response of the proposed method with UNIQUE-C_4 and ADMM ($M = 16$, $N = 32$ $p = 64$, $L = 16$ and $q_k \in [-10^o, 10^o]$).

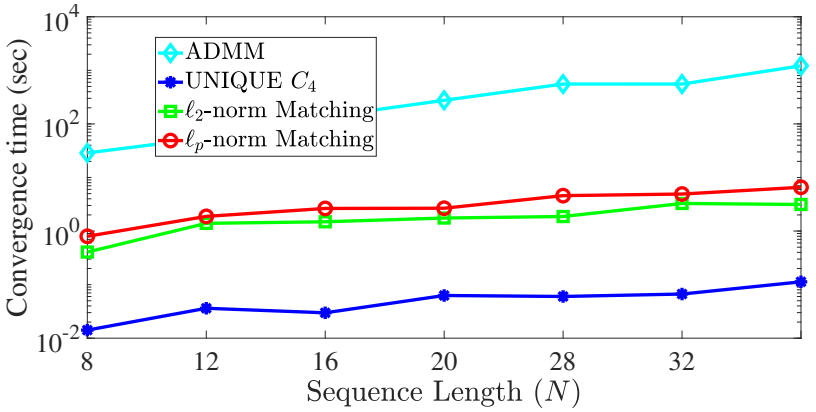

FIGURE 3.9: Comparing the convergence time of the proposed method with UNIQUE-C_4 and ADMM, with different sequence length ($M = 16$, $p = 64$, $L = 16$ and $q_k \in [-10^o, 10^o]$).

from Figure 3.9 it can be concluded that, approximately the UNIQUE-C_4 is 100 times faster than the ℓ_2-norm and ℓ_p-norm approaches. In similar way the ℓ_2-norm and ℓ_p-norm approach is 100 times faster than ADMM method.

3.3 Beampattern Shaping for Coexistence of Cognitive MIMO Radar and MIMO Communications

This section focuses on designing a set of transmit sequences for coexisting cognitive Multiple-Input Multiple-Output (MIMO) radar and MIMO communications (MRMC) systems. The aim is to shape the transmit beampattern to minimize the spatial Integrated Side-lobe Level (ISL) while having a good response on a desired direction in cognitive paradigm. The resulting non-convex, multi-variable optimization problem for the sequence design is addressed using the proposed Coordinate Descent (CD) framework under

constant modulus and discrete phase constraints. The CD method has the capability of directly designing M-ary Phase Shift Keying (MPSK), which is important in practical applications. Numerical results indicate the superior performance of the proposed method over solutions based on Semi-definite Relaxation (SDR).

Spectrum management between MIMO Radar and MIMO Communications (MRMC) is becoming crucial for next-generation active sensing and communications [110, 111]. Two approaches for spectrum management − co-design and coexistence − is pursued in MRMC systems [110]. In co-design, the radar and communications are designed jointly and a single unit is employed for both purposes [112–115]. On the other hand, in the coexistence approach, radar and communications exist as separate systems which adjust their transmitter parameters to mitigate the interference from each other adaptively [116, 117]. In the coexistence context, cognitive radars which continuously learn about the environment through experience gained from interactions with the environment [118, 119] play a key role in efficient spectrum management. Interestingly, radar waveform processing and signal recovery in cognitive MIMO radar systems enjoy a similar set of research opportunities, particularly in the emerging scenario of self-driving automotive applications [11, 120, 121].

We investigate radar beampattern shaping for a MRMC coexistence scenario comprising a cognitive radar. Specifically, it considers the emerging automotive scenario depicted in fig. 3.10 with the following guidelines for beampattern shaping,

- Steering nulls towards the direction of the base station and the communication user to enable coexistence.
- Minimizing the ISL on clutter region to mitigate the interference.
- Steering the beam toward the targets to enhance detection.

Clearly, the dynamic scenario necessitates an adaptive waveform design; this is enabled through the cognitive radar.

Two approaches for beampattern shaping via waveform design are prevalent [26]. In the *two-step method* the waveform correlation matrix is designed first and the waveform is then obtained through one of the decomposition methods [44]; the waveform *per-se* is designed in the *direct method* [26]. Due to implementation and technological considerations, considering constant modulus or discrete phase alphabet in the design stage tends to be pertinent in the emerging system designs, especially since finite energy constraints have become a norm [78, 86]. These constraints render the waveform design problem significantly more complex than the unconstrained version [1, 24, 122]. Several papers

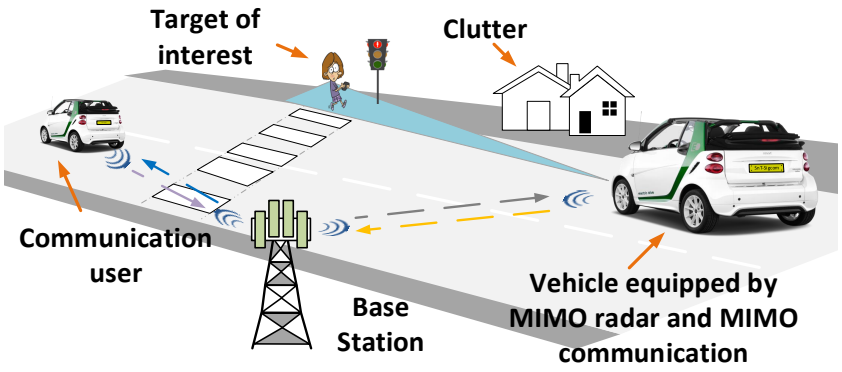

FIGURE 3.10: An illustration of MRMC system. The pedestrian is the target-of-interest for the MIMO radar deployed on a vehicle at the right. The buildings and ground cause clutter. At the same time, the car on the left is a MIMO communications user that communicates with the nearest BS.

have addressed beampattern design with constant modulus constraint; in [26] and [27] the authors present a method based on ADMM for beampattern matching and minimizing the spatial cross-correlation in narrow and wide band respectively, whereas [123] proposes a method based on Quasi-Newton iterations. However, these works do not consider the application to the cognitive MRMC coexistence scenario and the resulting shaping requirements.

This section address beampattern shaping for MRMC coexistence; it considers the *two-step approach* by using SDR [124] under energy constraint, and the *direct approach* using CD [92, 102] under constant modulus and discrete phase constraints. The latter is particularly novel in literature. In this context, the system model and problem statement in introduced in subsection 3.3.1, the different design approaches are detailed in subsection 3.3.2 and numerical results presented in subsection 3.3.5.

Notations: We use lower case boldface for vectors ($\boldsymbol{a}$) and uppercase boldface for matrices ($\boldsymbol{A}$). $\Re\{a\}$, $\Im\{a\}$ indicate the real, imaginary part of a respectively and $\mathrm{Tr}(\boldsymbol{A})$ is the trace of matrix $\boldsymbol{A}$. $\boldsymbol{A} \succeq 0$ means that is a positive semidefinite matrix. $(.)^H$ denotes Hermitian, the Frobenius and second order norms are denoted by $\| . \|_F$ and $\| . \|_2$ respectively, $j = \sqrt{-1}$, the letter (i) is use as step of a procedure and $\odot$ is the Hadamard product.

3.3.1 Problem Formulation

We consider a colocated narrow-band MIMO radar system, with M transmit antennas, each transmitting N pulses in the *fast-time* domain. Let the matrix $\boldsymbol{S}$ denote the transmitted waveform in the base-band, whose m^{th} row indicates the pulses from the m^{th} transmitter while the n^{th} column indicates the n^{th} pulse of all the transmitters. Let $\boldsymbol{s}_n$

and $\boldsymbol{a}(\theta)$ be the n^{th} sample of the waveform transmitted through the M antennas and the steering vector respectively. The transmit beampattern can be written as [28, 44, 125],

$$P(\boldsymbol{S},\theta) = \frac{1}{N}\sum_{n=1}^{N}\left|\boldsymbol{a}^H(\theta)\boldsymbol{s}_n\right|^2 = \frac{1}{N}\sum_{n=1}^{N}\boldsymbol{s}_n^H\boldsymbol{A}(\theta)\boldsymbol{s}_n \tag{3.19}$$

where $\boldsymbol{A}(\theta) \triangleq \boldsymbol{a}(\theta)\boldsymbol{a}^H(\theta)$. Let us denote by θ_t, θ_b, θ_v, and $\theta_q \in \{\theta_1, \theta_2, \ldots, \theta_Q\}$ the locations (directions in the spatial domain) of the target, base station, communication receiver and clutter patches, respectively. These are assumed to be known from an ideal cognitive process. We aim to minimize the beampattern gain at the undesired angles (θ_b, θ_v and θ_q) and simultaneously have a good gain at the desired angle (θ_t). Accordingly, we consider the following optimization problem,

$$\mathcal{P}_1\begin{cases}\min\limits_{\boldsymbol{S}} & w_bP(\boldsymbol{S},\theta_b) + w_vP(\boldsymbol{S},\theta_v) + w_c\sum_{q=1}^{Q}P(\boldsymbol{S},\theta_q)\\ \max\limits_{\boldsymbol{S}} & P(\boldsymbol{S},\theta_t)\\ s.t & \boldsymbol{S}\in C_1 \text{ or } C_2 \text{ or } C_3,\end{cases}$$

where, $w_u \geq 0$ ($u \in \{b, v, c\}$) denotes the weight corresponding to the beampattern response on the undesired angles. Further, $C_1 \triangleq \{\boldsymbol{S} \mid \|\boldsymbol{S}\|_F^2 \leq MN\}$ is the energy constraint, $C_2 \triangleq \{\boldsymbol{S} \mid s_{m,n} = e^{j\phi}, \phi \in \Phi_\infty\}, \Phi_\infty = [0, 2\pi)$ is constant modulus constraint and $C_3 \triangleq \{\boldsymbol{S} \mid s_{m,n} = e^{j\phi}, \phi \in \Phi_L\}, \Phi_L = \left\{0, \frac{2\pi}{L}, \ldots, \frac{2\pi(L-1)}{L}\right\}$ is discrete phase constraint. In fact, Φ_L indicates the MPSK with alphabet size L.

In Problem $\mathcal{P}_1$, the maximum of $P(\boldsymbol{S},\theta_t)$ is M^2, and occurs when $\boldsymbol{s}_n = \boldsymbol{a}(\theta_t)$, $n = 1, \ldots, N$. This limits the design flexibility and does not serve the shaping requirements for coexistence. To address this, we enlarge the set of feasible solutions by introducing the scaling coefficient, α, as,

$$\mathcal{P}_2\begin{cases}\min\limits_{\boldsymbol{S}} & w_bP(\boldsymbol{S},\theta_b) + w_vP(\boldsymbol{S},\theta_v) + w_c\sum_{q=1}^{Q}P(\boldsymbol{S},\theta_q)\\ s.t & P(\boldsymbol{S},\theta_t) = \alpha M^2\\ & \boldsymbol{S}\in C_1 \text{ or } C_2 \text{ or } C_3\end{cases}.$$

$\mathcal{P}_2$ is equivalent with $\mathcal{P}_1$ when $\alpha = 1$, but the former offers design flexibility through the adjustment of α. We adopt $\alpha \in [1/2, 1]$ to have a maximum 3 dB loss in the beampattern gain of the desired angle. Towards solving $\mathcal{P}_2$, we consider the constraint $P(\boldsymbol{S},\theta_t) = \alpha M^2$ as a penalty term to obtain,

$$\mathcal{P}_3\begin{cases}\min\limits_{\boldsymbol{S}} & \sum_{n=1}^{N}\boldsymbol{s}_n^H\boldsymbol{A}_U\boldsymbol{s}_n + \delta\left\|\frac{\sum_{n=1}^{N}\boldsymbol{s}_n^H\boldsymbol{A}_T\boldsymbol{s}_n - \alpha M^2}{M^2}\right\|_2^2,\\ s.t & \boldsymbol{S}\in C_1 \text{ or } C_2 \text{ or } C_3\end{cases}$$

where $\boldsymbol{A}_U \triangleq \frac{1}{N}\Big(w_1\boldsymbol{A}(\theta_b) + w_2\boldsymbol{A}(\theta_v) + w_3\sum_{q=1}^{Q}\boldsymbol{A}(\theta_q)\Big)$, $\boldsymbol{A}_T \triangleq \frac{1}{N}\boldsymbol{A}(\theta_t)$, and $\delta \geqslant 0$ is the penalty weight. In the next subsection, we introduce efficient algorithms to tackle $\mathcal{P}_3$ under different practical constraints.

3.3.2 Proposed Method

We now use SDR to tackle $\mathcal{P}_3$ under the constraint C_1, and then introduce CD to design the set of transmit sequences under constraints C_2 and C_3.

3.3.3 Energy constraint

$\mathcal{P}_3$ is a non-convex problem due to the penalty term. A possible solution is using the SDR technique by converting it to a convex problem [124]. Towards this, defining $\boldsymbol{X}_n = \boldsymbol{s}_n\boldsymbol{s}_n^H$, we obtain

$$\mathcal{P}_4 \begin{cases} \min\limits_{\boldsymbol{X}_n} & \sum\limits_{n=1}^{N}\mathrm{Tr}(\boldsymbol{A}_U\boldsymbol{X}_n) + \delta\left\|\dfrac{\sum_{n=1}^{N}\mathrm{Tr}(\boldsymbol{A}_T\boldsymbol{X}_n) - \alpha M^2}{M^2}\right\|_2^2 \\ s.t & \sum_{n=1}^{N}\mathrm{Tr}(\boldsymbol{X}_n) \leq MN \\ & \boldsymbol{X}_n \succeq 0, \end{cases}$$

where $\|\boldsymbol{S}\|_F^2 \leq MN \Leftrightarrow \sum_{n=1}^{N}\mathrm{Tr}(\boldsymbol{X}_n) \leq MN$. Solving $\mathcal{P}_4$ leads to obtain the optimum $\boldsymbol{X}_n^\star$ and there exist several methods to approximate $\boldsymbol{s}_n^\star$, e. g., eigen-decomposition and Gaussian randomization [124, 126, 127].

3.3.4 Constant modulus and discrete phase constraints

The problem $\mathcal{P}_3$ under C_2 and C_3 constraints is non-convex and multi-variable; we propose the CD framework to tackle it [92, 102]. The CD based methods are intuitively appealing and very simple to implement, yet they exhibit powerful performance in emerging radar waveform design applications [24, 78]. In particular, we consider one entry of $\boldsymbol{S}$ as being the only variable while keeping the others fixed; for this identified variable, we optimize the objective function. Such a methodology is efficient when the objective function can be written in a simplified form for that identified variable. In this regard, let us assume that $s_{t,d}$ is the only variable at $(i)^{th}$ iteration of the optimization procedure. The resulting single-variable objective function at $(i)^{th}$ iteration can be written as (see Appendix B.3),

$$f_{cd}(s_{t,d}, \boldsymbol{S}_{-(t,d)}^{(i)}) = c_0^{(i)}s_{t,d}^2 + c_1^{(i)}s_{t,d} + c_2^{(i)} + c_3^{(i)}s_{t,d}^* + c_4^{(i)}{s_{t,d}^*}^2.$$

Here, $\boldsymbol{S}^{(i)}_{-(t,d)} = \boldsymbol{S}^{(i)}|_{s_{t,d}=0}$ refers to the fixed entries. Considering the constraint $\phi \in \Phi_\infty$ or Φ_L, it would be straightforward to show that $f_{cd}(s_{t,d}, \boldsymbol{S}^{(i)}_{-(t,d)})$ depends only on the variable ϕ, where $s_{t,d} = e^{j\phi}$. By substituting $s_{t,d} = e^{j\phi}$, the objective function can be recast as follows,

$$f_o^{(i)}(\phi) = c_0^{(i)} e^{j2\phi} + c_1^{(i)} e^{j\phi} + c_2^{(i)} + c_3^{(i)} e^{-j\phi} + c_4^{(i)} e^{-j2\phi}, \tag{3.20}$$

and the optimization problem under constraints C_2 and C_3 at $(i)^{th}$ iteration can be written as,

$$\mathcal{P}_5^{(i)} \begin{cases} \min\limits_{\phi} & f_o^{(i)}(\phi) \\ s.t & \phi \in \Phi_\infty \text{ or } \Phi_L. \end{cases}$$

Consequently, the optimal phase of the code entry $s_{t,d}$ can be obtained by solving,

$$\phi^{\star(i)} = \arg\min_{\phi} \{ f_o^{(i)}(\phi) \,|\, \phi \in \Phi_\infty \text{ or } \Phi_L \}. \tag{3.21}$$

Subsequently, the variable $s_{t,d}$ will be updated by ${s^\star_{t,d}}^{(i)} = e^{j\phi^{\star(i)}}$. This procedure will continue until the stationary point is obtained. We consider $(f_o^{(i)}(\phi^{\star(i-MN)}) - f_o^{(i)}(\phi^{\star(i)})) < \zeta$, $(\zeta > 0)$ as stopping criterion of optimization. The proposed method is summarized in **Algorithm 6**.

Algorithm 6 :Transmit Beampattern design for MRMC

Input: Random-phase initial set $\boldsymbol{S}^{(0)}|_{s_{m,n} \in \Phi_\infty \text{ or } \Phi_L}$;
Output: Optimized set $\boldsymbol{S}^\star$;

1. **Initialization**.
   - Choose $\alpha \in [0, 1/2]$, and set $i := 0$, $t, d := 1$;
2. **Optimization**.
   - $i := i + 1$;
   - Obtain $\phi^{\star(i)}$ using (3.24) or (3.27);
   - ${s^\star_{t,d}}^{(i)} = e^{j\phi^{\star(i)}}$ then $\boldsymbol{S}^{(i)} = \boldsymbol{S}^{(i-1)}|_{s_{t,d}={s^\star_{t,d}}^{(i)}}$;
   - If $t = M$ then $t := 1$; else $t := t + 1$;
   - If $d = N$ go to 3); else $d := d + 1$ and go to 2);
3. **Stopping criterion**.
   - If $(f_o^{(i)}(\phi^{\star(i-MN)}) - f_o^{(i)}(\phi^{\star(i)}) < \zeta$, go to 4); otherwise $d := 1$ and go to 2);
4. **Output**.
   - Set $\boldsymbol{S}^\star = \boldsymbol{S}^{(i)}$;

In the sequel, we obtain $\phi^{\star(i)}$ under different constraints.

Optimal solution under continuous phase constraints: As $f_o^{(i)}(\phi)$ is a real, differentiable and periodic function, it has at least two extrema. Therefore, its derivative has at least two real roots. The derivative of $f_o^{(i)}(\phi)$ can be obtained by,

$$f_o'^{(i)}(\phi) = j\left(2c_0^{(i)}e^{j2\phi} + c_1^{(i)}e^{j\phi} - c_3^{(i)}e^{-j\phi} - 2c_4^{(i)}e^{-j2\phi}\right).$$

It can be seen from Appendix that $c_4 = c_1^*$ and $c_3 = c_1^*$ (details omitted). Then $f_o'^{(i)}(\phi)$ can be written as, $j\left(j4\Im\{c_0^{(i)}e^{j2\phi}\} + j2\Im\{c_1^{(i)}e^{j\phi}\}\right)$. Hence,

$$\begin{aligned} f_o'^{(i)}(\phi) = &-8c_{0r}\sin(\phi)\cos(\phi) - 4c_{0i}\left(\cos^2(\phi) - \sin^2(\phi)\right) \\ &- 2c_{1r}\sin(\phi) - 2c_{1i}\cos(\phi), \end{aligned}$$

where $c_{0r} \triangleq \Re\{c_0\}$, $c_{0i} \triangleq \Im\{c_0\}$, $c_{1r} \triangleq \Re\{c_1\}$ and $c_{0i} \triangleq \Im\{c_1\}$. Considering $\cos(\phi) = (1-\tan^2(\phi))/(1+\tan^2(\phi))$, $\sin(\phi) = 2\tan(\phi)/(1+\tan^2(\phi))$ and changing variable $z \triangleq \tan(\frac{\phi}{2})$, $f_o'^{(i)}(\phi)$ can be obtained by,

$$f_z'^{(i)}(z) = \frac{p_0^{(i)}z^4 + p_1^{(i)}z^3 + p_2^{(i)}z^2 + p_3^{(i)}z + p_4^{(i)}}{(1+z^2)^2} \tag{3.22}$$

where, $p_0, \ldots, p_4$ are real coefficient defined by $p_0 \triangleq 2\Im\{2c_0 - c_1\}$, $p_1 \triangleq 2\Re\{2c_1 - 8c_0\}$, $p_2 \triangleq -12\Im\{c_0\}$, $p_3 \triangleq 2\Re\{2c_1 + 8c_0\}$ and $p_4 \triangleq 2\Im\{2c_0 + c_1\}$. Since the denominator in $f_z'^{(i)}(z)$ is non-zero, the critical points can be obtained by obtaining the roots of

$$p_0^{(i)}z^4 + p_1^{(i)}z^3 + p_2^{(i)}z^2 + p_3^{(i)}z + p_4^{(i)}. \tag{3.23}$$

Let us assume that $z_k^{(i)}$ are the roots of (3.23), therefore the critical points of $f_o'^{(i)}(\phi)$ can be obtained by, $\phi_k^{(i)} = 2\ \tan^{-1}(z_k^{(i)})$, Notice that only the real roots of (3.23) represent the extremum of $f_o^{(i)}(\phi)$, therefore the optimized phase is,

$$\phi^{\star(i)} = \arg\min_{\phi_k^{(i)}} \left\{ f_o^{(i)}(\phi_k^{(i)}) \,|\, \Im\{\phi_k^{(i)}\} = 0 \right\}. \tag{3.24}$$

Optimized code entry under discrete phase constraints: It can be noted that

$$f_o^{(i)}(\phi) = e^{j2\phi}(c_0^{(i)} + c_1^{(i)}e^{-j\phi} + c_2^{(i)}e^{-j2\phi} + c_3^{(i)}e^{-j3\phi} + c_4^{(i)}e^{-4j\phi}).$$

Consequently, $f_o^{(i)}(\phi_k)$ can be formulated as,

$$f_o^{(i)}(\phi_k) = e^{j\frac{4\pi k}{L}} \sum_{n=0}^{4} c_n^{(i)} e^{-j\frac{2\pi nk}{L}}, \tag{3.25}$$

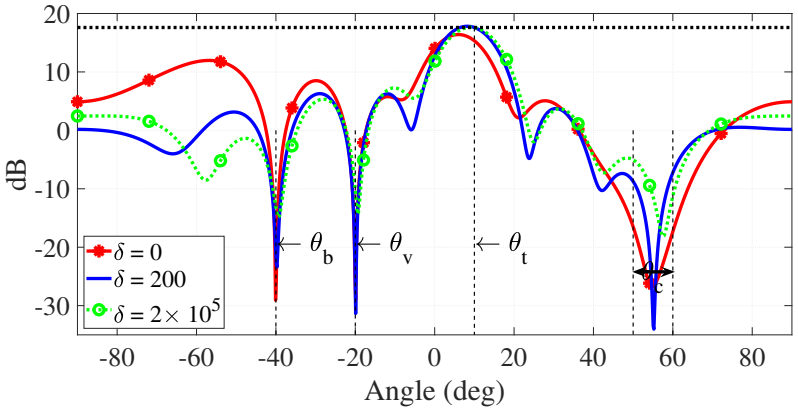

FIGURE 3.11: Beampattern of CD method, continuous phase constraint, different δ.

where, $k = \{0, \ldots, L-1\}$. Equation (3.25) is exactly the definition of $L-$point DFT of sequence $\{c_0, \ldots, c_4\}$. Therefore, $f_o^{(i)}(\phi_k)$ can be written as,

$$f_{o_d}^{(i)}(k) = \boldsymbol{h}_L \odot \mathcal{F}_L\{c_0^{(i)}, c_1^{(i)}, c_2^{(i)}, c_3^{(i)}, c_4^{(i)}\} \tag{3.26}$$

where, $\boldsymbol{h}_L = [1, e^{j\frac{4\pi}{L}}, \ldots, e^{j\frac{4\pi(L-1)}{L}}]^T \in \mathbb{C}^L$ and $\mathcal{F}_L$ is $L-$point DFT operator. The current function is only valid for $L \geqslant 5$. According to periodic property of DFT, $f_{o_d}^{(i)}(k)$ can be written as,

$$\begin{aligned}
L = 4 &\Rightarrow f_{o_d}^{(i)}(k) = \boldsymbol{h}_L \odot \mathcal{F}_L\{c_0^{(i)} + c_4^{(i)}, c_1^{(i)}, c_2^{(i)}, c_3^{(i)}\},\\
L = 3 &\Rightarrow f_{o_d}^{(i)}(k) = \boldsymbol{h}_L \odot \mathcal{F}_L\{c_0^{(i)} + c_3^{(i)}, c_1^{(i)} + c_4^{(i)}, c_2^{(i)}\},\\
L = 2 &\Rightarrow f_{o_d}^{(i)}(k) = \boldsymbol{h}_L \odot \mathcal{F}_L\{c_0^{(i)} + c_2^{(i)} + c_4^{(i)}, c_1^{(i)} + c_3^{(i)}\}.
\end{aligned}$$

Therefore the optimum solution of (3.26) is, $k^{\star(i)} = \arg\min_{k=1,\ldots,L} \{f_{o_d}(k)\}$. Subsequently, the optimum phase is,

$$\phi^{\star(i)} = \frac{2\pi(k^{\star(i)} - 1)}{L}. \tag{3.27}$$

3.3.5 Numerical results

We consider a ULA configuration with $M = 8$ transmitters and $N = 64$ pulses. Target, base station, vehicle and clutter patches are located at $\theta_t = 10^o$, $\theta_b = -40^o$, $\theta_v = -20^o$ and $\theta_c = [50^o, 60^o]$, respectively. We consider $\alpha = 0.9$ and $w_b = 0.45$, $w_v = 0.45$ and $w_c = 0.1$ respectively. For algorithm 8, the stopping condition is set at $\zeta = 10^{-3}$. Finally, the $\mathcal{P}_4$ is solved via the CVX toolbox with SDPT3 solver [128].

The impact of penalty factor (δ): Fig.3.11, shows the beampattern of proposed methods under C_2 with different penalty weights. We observe that a good ISL at the cost of a poor mainlobe response when the penalty is not considered. On the other hand, for a high penalty factor, despite the good mainlobe response, the algorithm is unable to minimize the sidelobes at undesired angles. However, by choosing a moderate penalty

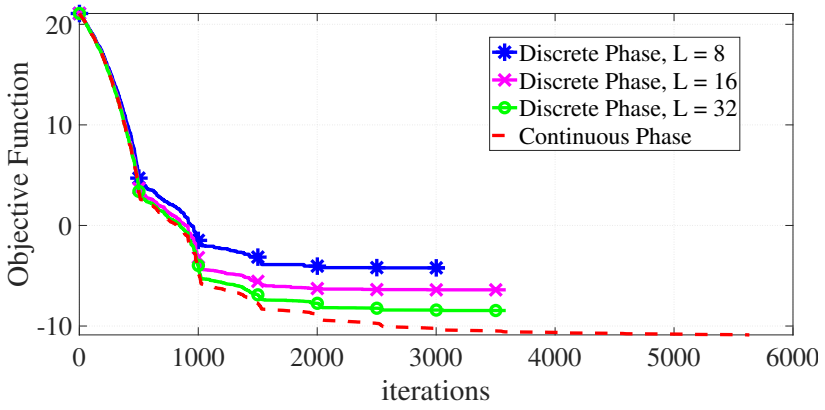

FIGURE 3.12: Convergence of CD method for different alphabet size.

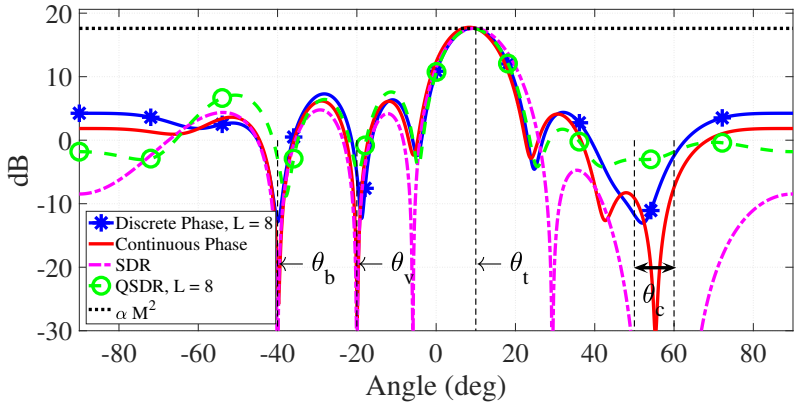

FIGURE 3.13: Comparison of beampattern obtained by CD, SDR and QSDR.

factor ($\delta = 200$), we can enforce an efficient trade off between mainlobe and ISL. Hence $\delta = 200$ in considered henceforth.

Convergence behavior: Fig.3.12 shows the convergence behavior CD method under C_2 and C_3 constraints when initialized using random MPSK sequences with alphabet size $L = 8$. As can be seen, the objective decreases monotonically and converges to a certain value. The continuous phase design obtains a better performance than the discrete phase due to higher degrees of freedom. Also, larger the alphabet size, better the performance in designing discrete phase sequences. This arises from the fact that increasing the alphabet size enlarges the feasibility set, thereby rendering the achievement of a lower objective at optimum.

Beampattern comparison: Fig.3.5 illustrates the beampattern of obtained from different optimization methods in this section, i.e., SDR under constraint C_1, and CD under constraints C_2, and C_3. Further, we map the obtained waveform of the SDR solution to the nearest MPSK sequence; calling it Quantized Semi-definite Relaxation (QSDR) and we use it as initial sequence for algorithm. Interestingly, the waveforms optimized through the proposed CD mimic the beampattern obtained via SDR, indicating

the efficiency of this approach in designing set of sequences with practical constraints. Notice that, there is a significant difference between the solution obtained via CD under constraint C_3, and that obtained by QSDR. This can be justified from the fact CD directly considers the constraints in the design, while quantizing the waveform to the nearest MPSK sequence does not guarantee an optimal solution.

3.4 Transmit Beampattern Shaping Via Waveform Design In Cognitive MIMO Radar

This section is focused on designing a set of constant modulus waveform for cognitive Multiple-Input Multiple-Output (MIMO) radar systems. The aim is to shape the beampattern in transmitter to minimize the Integrated Side-lobe Level (ISL) in spatial domain in a cognitive paradigm. This minimization leads to a NP-hard and non-convex optimization problem. To address this, the problem is formulated based on Coordinate Descent (CD) framework with constant modulus constraint. Subsequently, an low-complexity and fast method based on Discrete Fourier Transform (DFT) is proposed which monotonically decreases the spatial ISL. Finally, we show some numerical results and assess the performance of the proposed technique.

Cognitive radar systems are smart sensors which have a dynamic interaction with environment to enable optimal adaption of the transmit, receive and other parameters to the environment [11]. Cognitive beampattern shaping by controlling the spatial distribution of the transmit power can play an important role to improve radar performance through enhanced power efficiency, better detection probability, target identification, improved interference mitigation etc. Clearly, this necessitates an adaptive waveform design approach. Generally, there are two methods for beampattern shaping via waveform design, two-step and direct methods [26]. In two-step method first, the waveform correlation matrix is designed and then the original waveform matrix is obtained through one of the decomposition methods [44]. While in direct method the waveform is designed directly [26].

In this section, we consider minimizing the beampattern response in undesired directions while simultaneously achieving good response in desired directions. These directions can be driven by cognitive paradigm in response to the environmental situation [11]. Further, due to the need for higher power efficiency in mmWave radars and ease of hardware implementation. In this context we consider solving the problem under constant modulus discrete phase MPSK sequences [1, 99] which requires limited valued phase shifters. This scheme results in a non-convex, possibly NP-hard problem. Our approach is to design

the waveform directly using CD which offers a low complexity methodology to a complex problem while exhibiting gains. The section, thus considers a novel beampattern design problem in MIMO cognitive radars and offers a fast and efficient solution.

To this end, the section is organized as follow. Subsection 3.4.1 introduces the system model and describes the problem formulation. Subsection 3.4.2 presents the proposed CD based framework whose performance is numerically assessed in subsection 3.4.3.

Notations: We adopt the notation of using lower case boldface for vectors ($\boldsymbol{a}$) and capital boldface for matrix ($\boldsymbol{A}$). The transpose, conjugate transpose, Frobenius norm, absolute value and ceiling operators are denoted by the $(.)^T$, $(.)^H$, $\| \, . \, \|_F$, $|.|$ and $\lceil . \rceil$ respectively. $\mathrm{Tr}(\boldsymbol{A})$ indicates the trace of matrix $\boldsymbol{A}$ and $\boldsymbol{A} \succeq 0$ means that is a positive semidefinite matrix. The letter j represents the imaginary unit (i.e., $j = \sqrt{-1}$), while the letter (i) is use as step of a procedure. Finally $\odot$ denotes the Hadamard product.

3.4.1 System Model and Problem Formulation

We consider a colocated narrow-band MIMO radar system, with M transmitters, and each transmits N pulses in the fast-time domain. Let the matrix $\boldsymbol{S}$ denotes the transmitted waveform in the base-band, where the m^{th} row indicates the pulses of m^{th} transmitter while n^{th} column indicates the n^{th} pulse of the transmitters. At time sample n, the waveform transmitted through the M antennas is denoted by s_n, where:

$$\boldsymbol{s}_n = [s_{1,n}, s_{2,n}, \ldots, s_{M,n}]^T \in \mathbb{C}^M. \tag{3.28}$$

In (3.28), $s_{m,n}$ is the n^{th} pulse of m^{th} transmitter. We assume the standard ULA configuration for transmitters, where the distance between the elements are $d_t = \frac{\lambda}{2}$. Thus, the steering vector can be written as [105]:

$$\boldsymbol{a}(\theta) = [1, e^{j\pi sin(\theta)}, \ldots, e^{j\pi(M-1)sin(\theta)}]^T \in \mathbb{C}^M. \tag{3.29}$$

The transmit beampattern can be written as [28, 44, 125]:

$$P(\boldsymbol{S}, \theta) = \sum_{n=1}^{N} \left| \boldsymbol{a}^H(\theta)\boldsymbol{s}_n \right|^2 = \sum_{n=1}^{N} \boldsymbol{s}_n^H \boldsymbol{A}(\theta)\boldsymbol{s}_n \tag{3.30}$$

where, $\boldsymbol{A}(\theta) = \boldsymbol{a}(\theta)\boldsymbol{a}^H(\theta)$.

Let us denote $\boldsymbol{\theta}_d = [\theta_{d,1}, \theta_{d,2}, \ldots, \theta_{d,M_d}]$ and $\boldsymbol{\theta}_u = [\theta_{u,1}, \theta_{u,2}, \ldots, \theta_{u,M_u}]$ respectively, be the sets of desired and undesired angles in spatial domain and are obtained by cognitive paradigm. We are interested in minimizing the beampattern gain at the undesired angles while simultaneously have a good gains at the desired angles. In this regards, we define

$f_1(\boldsymbol{S}) \triangleq \sum_{p=1}^{M_u} P(\boldsymbol{S}, \theta_{u,p})$ as spatial ISL and $g_1(\boldsymbol{S}) \triangleq \sum_{p=1}^{M_d} P(\boldsymbol{S}, \theta_{d,p})$ as summation of beampattern on desired directions. In the point of view of radar designing the viable solution is minimizing the spatial ISL subject to, $g_1(\boldsymbol{S})$ is greater than a specific value under constant modulus with discrete phase constraint. To this regard, a relevant design metric is:

$$\mathcal{P}_1 \begin{cases} \min\limits_{\boldsymbol{S}} & f_1(\boldsymbol{S}) = \sum_{n=1}^{N} \boldsymbol{s}_n^H \boldsymbol{A}_u \boldsymbol{s}_n \\ s.t & g_1(\boldsymbol{S}) = \sum_{n=1}^{N} \boldsymbol{s}_n^H \boldsymbol{A}_d \boldsymbol{s}_n \geqslant \gamma \\ & s_{m,n} = e^{j\phi}, \quad \phi \in \Phi_L, \end{cases} \tag{3.31}$$

where, $\boldsymbol{A}_d = \sum_{p=1}^{M_d} \boldsymbol{A}(\theta_{d,k})$, $\boldsymbol{A}_u = \sum_{p=1}^{M_u} \boldsymbol{A}(\theta_{u,k})$, $m \in \{1, \ldots, M\}$, $n \in \{1, \ldots, N\}$ and Φ_L indicates the MPSK phases. Precisely, $\Phi_L = \left\{0, \frac{2\pi}{L}, \ldots, \frac{2\pi(L-1)}{L}\right\}$.

In $\mathcal{P}_1$, as the constraints are non-convex, therefore the problem is non-convex. But if we relax by replacing the second constraint with limited energy ($\|\boldsymbol{S}\|_F^2 \leq MN$) we encounter with a complex-valued separable Quadratic Constraint Quadratic Programming (QCQP) which is still non-convex [124]. In this case, a possible solution is SDR.The standard method is to let $\boldsymbol{R}_n = \boldsymbol{s}_n \boldsymbol{s}_n^H$, recast the problem using $\boldsymbol{R}_n$ and imposing the rank constraint on $\boldsymbol{R}_n$. This problem is further relaxed by omitting the rank constraint as,

$$\mathcal{P}_{SDR} \begin{cases} \min\limits_{\boldsymbol{R}_n} & \sum_{n=1}^{N} \mathrm{Tr}(A_u \boldsymbol{R}_n) \\ s.t & \sum_{n=1}^{N} \mathrm{Tr}(A_d \boldsymbol{R}_n) \geqslant \gamma \\ & \sum_{n=1}^{N} \mathrm{Tr}(\boldsymbol{R}_n) \leqslant MN \\ & \boldsymbol{R}_n \succeq 0, \end{cases} \tag{3.32}$$

where $\|\boldsymbol{S}\|_F^2 \leq MN \Leftrightarrow \sum_{n=1}^{N} \mathrm{Tr}(\boldsymbol{X}_n) \leq MN$. This problem is known as the SDR of QCQP. Solving $\mathcal{P}_{SDR}$ leads to obtain the optimum $\boldsymbol{R}_n^\star$ and there are several methods to approximate $\boldsymbol{s}_n^\star$ such as decomposition and Gaussian randomization [124, 126, 127].

3.4.2 Proposed Method

By standard mathematical manipulation, the problem $\mathcal{P}_1$ can be written as function of matrix $\boldsymbol{S}$ as follows:

$$\mathcal{P}_2 \begin{cases} \min\limits_{\boldsymbol{S}} & f_2(\boldsymbol{S}) = \mathrm{Tr}(\boldsymbol{A}_u \boldsymbol{S} \boldsymbol{S}^H) \\ s.t & g_2(\boldsymbol{S}) = \mathrm{Tr}(\boldsymbol{A}_d \boldsymbol{S} \boldsymbol{S}^H) \geqslant \gamma \\ & s_{m,n} = e^{j\phi}, \quad \phi \in \Phi_L, \end{cases} \tag{3.33}$$

Problem $\mathcal{P}_2$ can be tackled by CD framework [102]; in fact [129] solves a problem with similar objective but with different constraint. In CD method instead of the whole matrix $\boldsymbol{S}$, it is designed on an entry by entry basis in an iterative manner [24, 78]. In particular, one entry of $\boldsymbol{S}$ is considered as the only variable while others are held fixed. With respect to this identified variable, the objective function is optimized. Such a methodology is efficient when the objective function can be written in a simplified form with respect to that variable. In this regard, let us assume that $s_{t,d}$ is the only variable at i^{th} iteration of optimization procedure. Therefore $\mathcal{P}_2$ can be written equivalently as (see Appendix B.3):

$$\mathcal{P}_3^{(i)} \begin{cases} \min\limits_{s_{t,d}} & f_3(s_{t,d}, \boldsymbol{S}^{(i)}_{-(t,d)}) = a_0^{(i)} s_{t,d} + a_1^{(i)} + a_2^{(i)} s_{t,d}^* \\ s.t & g_3(s_{t,d}, \boldsymbol{S}^{(i)}_{-(t,d)}) = b_0^{(i)} s_{t,d} + b_1^{(i)} + b_2^{(i)} s_{t,d}^* \geqslant \gamma \\ & s_{t,d} = e^{j\phi}; \quad \phi \in \Phi_L, \end{cases} \tag{3.34}$$

where, $\boldsymbol{S}^{(i)}_{-(t,d)} = \boldsymbol{S}^{(i)}|_{s_{t,d}=0}$ and refers to the fixed entries.

Problem $\mathcal{P}_3^{(i)}$ depends only on parameter ϕ. By substituting $s_{t,d} = e^{j\phi}$, $\mathcal{P}_3^{(i)}$ can be recast as follows after some manipulations:

$$\mathcal{P}_4^{(i)} \begin{cases} \min\limits_{\phi} & f_4(\phi) = a_0^{(i)} e^{j\phi} + a_1^{(i)} + a_2^{(i)} e^{-j\phi} \\ s.t & g_4(\phi) = b_0^{(i)} e^{j\phi} + b_1^{(i)} + b_2^{(i)} e^{-j\phi} \geqslant \gamma \\ & \phi \in \Phi_L, \end{cases} \tag{3.35}$$

As $\phi \in \Phi_L$, one approach for solving the problem $\mathcal{P}_4^{(i)}$ is examining all the possible phases in the set Φ_L and choose the phase that minimizes $f_4(\phi)$ and satisfies $g_4(\phi) \geqslant \gamma$. It can be shown that $\mathcal{P}_4^{(i)}$ is equivalent to [24, 78]:

$$\mathcal{P}_5^{(i)} \begin{cases} \min\limits_{k} & f_5(k) = \boldsymbol{p}_L \odot \mathcal{F}_L\{a_0^{(i)}, a_1^{(i)}, a_2^{(i)}\} \\ s.t & g_5(k) = \boldsymbol{p}_L \odot \mathcal{F}_L\{b_0^{(i)}, b_1^{(i)}, b_2^{(i)}\} \geqslant \gamma, \end{cases} \tag{3.36}$$

where, $\boldsymbol{p}_L = \left[1, e^{j\frac{2\pi}{L}}, \ldots, e^{j\frac{2\pi(L-1)}{L}}\right]^T$, $\mathcal{F}_L$ is L points DFT operator and $k \in \{1, \ldots, L\}$. Problem $\mathcal{P}_5^{(i)}$ is valid when $L \geqslant 3$. In case of $L = 2$, $\mathcal{P}_5^{(i)}$ can be written as:

$$\mathcal{P}_6^{(i)} \begin{cases} \min\limits_{k} & f_6(k) = \boldsymbol{p}_L \odot \mathcal{F}_2\{a_0^{(i)} + a_2^{(i)}, a_1^{(i)}\} \\ s.t & g_6(k) = \boldsymbol{p}_L \odot \mathcal{F}_2\{b_0^{(i)} + b_2^{(i)}, b_1^{(i)}\} \geqslant \gamma. \end{cases} \tag{3.37}$$

The choice of γ to ensure feasibility is a tricky aspect. In our work, we assume that the γ is selected such that the problem has a feasible solution (e.g., by choosing $\gamma = g_1(\boldsymbol{S})$

for some initial sequence $\boldsymbol{S}$).

To tackle problems $\mathcal{P}_5^{(i)}$, our approach is to first find the feasible set from the constraint $(g_6(k) \geqslant \gamma)$ and then choose the phase from the feasible set which minimizes the objective function. Accordingly, algorithm 7[4] is proposed to optimize all MN pulses of matrix $\boldsymbol{S}$. In the following, the key steps of the algorithm are:

Finding the feasible set: In this step, the whole possible value for $g_5(k)$ is obtained, then by subtracting γ from $g_5(k)$, the feasible set can be derived. In particular, a negative k^{th} entry implies that, $g_5(k)$ is less than γ and hence the phase is infeasible; naturally, a non-negative entry implies feasibility. Subsequently the feasible and infeasible entries are mapped into 1 and $+\infty$ respectively in $\boldsymbol{k}_f$ of algorithm 1.

Optimization: In this step, the whole possible value for $f_5(k)$ is obtained. Subsequently, the infeasible entries in $\boldsymbol{h}$ of algorithm 7 are mapped to ∞ while the feasible entries are retained. Then, in $s_{t,d}^*$ the optimum pulse is obtained.

Stopping criterion: After optimizing the MN^{th} pulse, the algorithm examines the convergence metric for the spatial ISL. If the stopping criteria is not met the algorithm repeats the aforementioned steps for maximum $100MN$ iterations. We consider $\left(f_2(\boldsymbol{S}^{(i-MN)}) - f_2(\boldsymbol{S}^{(i)})\right) < \zeta$ as stopping criterion of optimization.

3.4.3 Numerical results

In this subsection, we provide some representative numerical examples to illustrate the effectiveness of proposed method. The reported values are obtained with a standard PC with Intel (R) Core (TM) i5-8250U CPU @ 1.60GHz with installed memory (RAM) 8.00 GB. Towards this end, unless otherwise explicitly stated, we consider the following assumptions. For system parameters we consider ULA configuration with $M = 8$ transmitters with $N = 64$ pulses. The desired angle is located in the interval of $[20^o, 60^o]$ and we consider γ corresponding to the initial sequence for both methods. For the CD method, we consider a random MPSK sequences as initial waveform and the stopping condition of algorithm 8 is set at $\zeta = 10^{-3}$. Finally the phase unconstrained problem in $\mathcal{P}_{SDR}$ is considered as the benchmark and is solved via the CVX toolbox [128].

3.4.3.1 Convergence Behavior

We investigate the convergence behavior of the proposed algorithm and we compare it with SDR solution. Since the SDR method designs a non constant modulus waveform, for fair comparison, we map the resulting waveform to the nearest MPSK sequence; we

[4]The procedure for $\mathcal{P}_6^{(i)}$ is similar to $\mathcal{P}_5^{(i)}$. In this regards we can replace functions $f_5(k)$ and $g_5(k)$ with $f_6(k)$ and $g_6(k)$ respectively.

Algorithm 7 : Waveform Design

Input: Initial set of random MPSK, $\boldsymbol{S}^{(0)}|s_{m,n} \in \Omega_d$ and L
Output: Optimized set of MPSK, $\boldsymbol{S}^{\star}$

1. **Initialization**.
   - Set $i := 0$, $t, d := 1$ and $\gamma := g_2(\boldsymbol{S}^{(0)})$;
2. **Find the feasible set**.
   - $i := i + 1$ then $g_5(k) = \boldsymbol{p}_L \odot \mathcal{F}_L\{b_0^{(i)}, b_1^{(i)}, b_2^{(i)}\}$;
   - $\boldsymbol{k}_f = \frac{2}{\lceil \text{sign}\left(g_5(k)-\gamma\right)+1 \rceil}$;
3. **Optimization**.
   - $f_5(k) = \boldsymbol{p}_L \odot \mathcal{F}_L\{a_0^{(i)}, a_1^{(i)}, a_2^{(i)}\}$;
   - $\boldsymbol{h} = f_5(k) \odot \boldsymbol{k}_f$;
   - $k^{(i)} = \arg \min_{k=1,\ldots,L} \{\boldsymbol{h}\}$;
   - $s_{t,d}^{\star} = e^{j\frac{2\pi\left(k^{(i)}-1\right)}{L}}$, $\boldsymbol{S}^{(i)} = \boldsymbol{S}^{(i-1)}|_{s_{t,d}=s_{t,d}^{\star}}$;
   - If $t = M$ then $t := 1$; otherwise $t := t + 1$;
   - If $d = N$ go to 4); otherwise $d := d + 1$ and go to 2);
4. **Stopping criterion**.
   - If $i = 100MN$ go to 5);
   - If $\left(f_2(\boldsymbol{S}^{(i-NM)}) - f_2(\boldsymbol{S}^{(i)})\right) < \zeta$, go to 5); otherwise $d := 1$ and go to 2);
5. **Output**.
   - Set $S^{\star} = S^{(i)}$

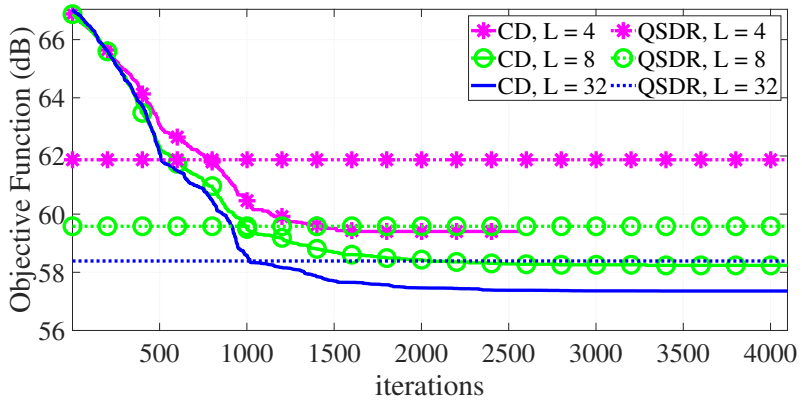

FIGURE 3.14: Convergence of CD method for different alphabet size with corresponding optimum objective function of QSDR.

term this as QSDR. Fig.3.14 shows the convergence of CD with different alphabet size with corresponding optimum objective function of QSDR.

As can be seen, the objective function decreases monotonically and converges to a certain value and by increasing alphabet size the performance becomes better. This result is reasonable, since increasing the alphabet size enlarges the feasibility set thereby rendering

TABLE 3.1: Comparison between the computational-time (s) of CD and SDR methods averaged over 10 independent trials, for different alphabet sizes.

CD			SDR
$L = 4$	$L = 8$	$L = 32$	
0.25	0.27	0.51	3.56

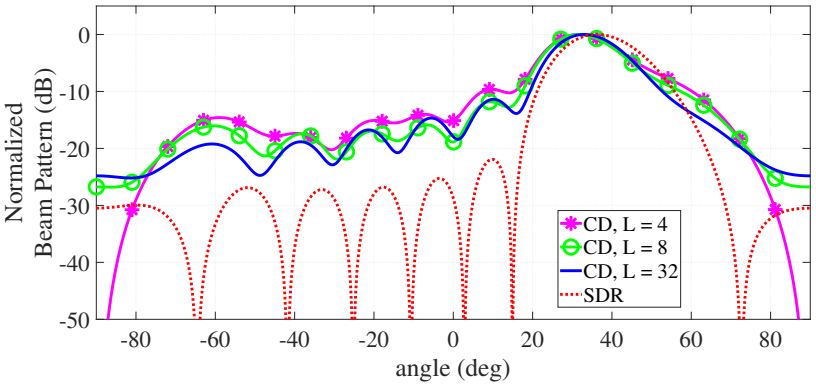

FIGURE 3.15: Beampattern of CD method for different alphabet size and SDR method.

the achievement of a lower objective at optimum. Besides, the performance of proposed method is much better than correspond QSDR. This can be justified from the fact that, there is no discrete phase constraint in SDR method and quantizing the waveform to the nearest MPSK sequence does not guarantee optimality. This does arise in the proposed method as it designs discrete phase sequences explicitly.

Besides, Table 3.1 shows the convergence time of CD for several alphabet sizes and SDR method averaged over 10 independent trials. It can be observed that, by increasing the alphabet size the convergence-time of CD method increases very slightly, while its beampattern matching ability improves. Further, on an average, CD is 10.37 times faster than SDR method.

3.4.3.2 Beampattern Analysis

Fig.3.15 shows the beampattern of both methods. Observe that the beampattern of SDR method has smaller sidelobes when compared with the CD method. This result is predictable because in SDR method is unconstrained unlike the proposed method. Therefore the feasible set of SDR method is much larger than CD and it can thus achieve better performance.

3.4.3.3 Power Efficiency

Fig.3.16 shows the constellation designed from the methods.

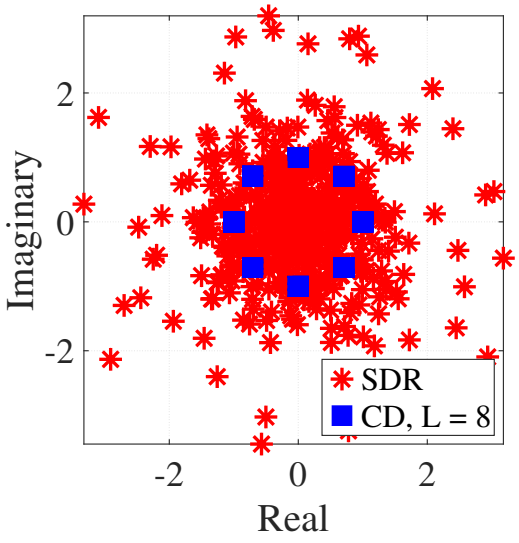

FIGURE 3.16: Constellation of CD method with $L = 8$ and SDR method.

As can be seen, the CD method designs a constant modulus waveform and is of interest to the radar system designers due to this property. While the optimum waveform designed by SDR is not constant modulus and each code should be transmitted with different power. Therefore, is not possible to transmit the code with maximum power this results in a loss in transmit power efficiency. This deviation can be assessed from the point of view of PAR criterion. For a given sequence PAR is [130]:

$$\text{PAR} = \frac{\max\limits_{\{m=1,\ldots,M\}\{n=1,\ldots,N\}} |s_{m,n}|^2}{\frac{1}{MN}\| \boldsymbol{S} \|_F^2}. \tag{3.38}$$

Due to the constant modulus the PAR of proposed method and QSDR is equal to 0 dB. However, the average PAR for benchmark scheme is 9.14 dB.

3.5 Conclusion

In this chapter, we look at several beampattern shaping problems for MIMO radar systems with continuous and discontinuous phase constraints. We use spatial-ISLR minimization and ℓ_p-norm beampattern matching as design metrics in this context. In most cases, the problems result in non-convex, multi-variable, and NP-Hard optimization problems. We proposed various efficient waveform design methods based on CD, SDR, BSUM and the penalty technique in order to get optimal solutions. The simulation results suggest that the proposed strategy improves the spatial domain performance of the MIMO radar system. When compared to state-of-the-art analogues in terms of

beampattern shaping and computing time, the proposed method outperforms or performs similarly.

Chapter 4

Spatial- and Range- ISLR Trade-off in MIMO Radar via Waveform Correlation Optimization

This chapter aims to design a set of transmit waveforms in cognitive colocated MIMO radar systems considering the simultaneous minimization of spatial- and the range- ISLR. The design problem is formulated as a bi-objective Pareto optimization under practical constraints on the waveforms, namely total transmit power, PAR, constant modulus, and discrete phase alphabet. A CD based approach, called UNIQUE, is proposed in which at every single variable update of the algorithm we obtain the solution of the uni-variable optimization problems. The novelty of the chapter comes from deriving a flexible waveform design problem applicable for the emerging 4D imaging MIMO radars with application to automotive radar systems. The simultaneous optimization leads to a trade-off between the two ISLRs and the simulation results illustrate significantly improved trade-off offered by the proposed methodologies.

4.1 Introduction

Transmit beampattern shaping and orthogonality have been the key waveform design aspects influencing the performance of colocated MIMO radar systems [17]. Beampattern shaping involves steering the radiation power in a spatial region of desired angles, while reducing interference from sidelobe returns to improve target detection [99]. There

exists a rich literature on waveform design for beampattern shaping following different approaches with regards to the choice of the variables, the objective function and the constraints; kindly refer to [28, 32, 40, 44–46] for details. An interesting approach to enhance detection of weak targets in the vicinity of strong ones is the design of waveforms with a small ISLR [32, 44] in the or spatial domain. This can be achieved by *imparting appropriate correlation among the waveforms* transmitted from the different antennas [131]. Waveform orthogonality, on the other hand, aims to enhance spatial resolution through the concept of virtual array. Similar to the beampattern design, there is a rich literature on orthogonal waveform design; kindly refer to [132] for details. Waveforms with low ISLR in time domain, also known as range-ISLR, are typically sought [21, 24], to enable an effective virtual array. This is achieved by designing a *set of waveforms that are uncorrelated* with each other (within and across antennas). Thus, a contradiction arises in achieving small spatial- and range-ISLR simultaneously, leading to a waveform design trade-off between spatial- and range-ISLR. This trade-off necessitates a dedicated waveform design approach [21], a subject pursued by the UNIQUE method proposed in this chapter.

Spatial-ISLR minimization: In the spatial-ISLR the approach is to maximize/ minimize the response of beampattern on desired/ undesired angles respectively. In [32], a waveform covariance design based on SDR under a constraint on the 3 dB main-beam is proposed to minimize the spatial-ISLR. In [44], the worst case transmit beampattern optimization is considered by minimizing the spatial-ISLR and -PSLR. Unlike the aforementioned methods, [40] proposes a direct design of the waveform entries based on ADMM to minimize the spatial-PSLR under constant modulus constraint. In [45], MIA approach was proposed based on MM for joint waveform and filter design under similarity, constant modulus and PAR constraints. In [46] a CD based method (STTC) was proposed to design space-time codes under similarity, uncertain steering matrices, continuous or discrete phase constraints. The authors propose a Dinkelbach based method and exhaustive search for continuous and discrete phase constraints, respectively.

Range-ISLR minimization: Unlike aforementioned spatially correlated designs, set of waveforms having low *auto- and cross-correlations* for all lags have been investigated in [2, 3, 21–24]. Low cross-correlations traditionally has been used as a metric to design set of approximately orthogonal sequences and exploiting the virtual array in a CDM-MIMO radar system. On the other hand, low auto-correlation level is a requirement in every radar system to avoid masking of the weak targets by the range sidelobes of a strong target, and to mitigate the harmful effects of distributed clutter returns close to the target of interest [20]. These two requirements naturally lead to the use of ISLR/ PSLR minimization as the metric which is pursued through several approaches including, CAN, MM, ADMM and CD. The authors in [2, 21] proposed the CAN algorithm to optimize

sequence with good ISL using the alternating minimization technique. However, instead of directly solving the ISL minimization, they solved its approximation. To solve the ISL minimization problem the authors in [3] proposed the MM-Corr algorithm and the authors in [22] proposed the ISL-NEW algorithm, both using the majorization-minimization technique. The authors in [23] used the ADMM technique to solve an approximation of the ISL minimization problem. The authors in [24] used the CD technique, to minimize a weighed sum of ISL and PSL under discrete phase constraint. They have reported superior performance comparing with the state-of-the art by using the CD approach.

Simultaneous range and spatial-ISLR designs: It is clearly evident that simultaneous minimization of range- and spatial-ISLR would be essential to achieve high performance in both range and spatial domains while minimizing the interfering radiation or clutter reflections. In addition, simultaneous minimization provides a new design perspective offering novel waveforms. In this context, there are a few works even on the general topic of waveform design considering simultaneous waveform orthogonality and beampattern shaping. The same holds for the case of spatial- and range-ISLR minimization. The authors in [131] bring out the contradictory nature of the orthogonality and beampattern shaping and propose a method for beampattern matching under particular constraints on the waveform cross-correlation matrix. In [133], the authors present an algorithm which, at first, minimizes the difference between desired and designed beampattern responses for one sub-pulse. Subsequently, other sub-pulses are obtained through random permutation. The waveforms obtained exhibit quasi-Dirac auto-correlation and the different waveforms are quasi-orthogonal. Since the spatial-ISLR is the ratio of beampattern response on undesired and desired angles, the approach in [133] is not equivalent to minimizing the spatial-ISLR. In [134], the authors introduce a beampattern matching by including orthogonality requirement as a penalty in the objective function and using the PDR approach for the solution. In [135], the authors propose a method based on ADMM to design a beampattern with good cross-correlation property but they do not consider the need for a good auto-correlation in their formulation. The aforementioned papers design constant modulus waveforms with continuous phase alphabets. However, they do not consider simultaneous minimization of range- and spatial-ISLR metrics in designing the waveform set; nor do they consider discrete-phase constraint.

Another approach considering both orthogonality and beampattern shaping is the phased-MIMO technique where the transmit array is divided into a number of sub-arrays and each sub-array coherently transmits a waveform which is orthogonal to those transmitted by the other sub-arrays. For instance, [136] considers designing a weight vector for each sub-array to form a beam in a desired direction. In order to obtain the orthogonality, [136] allocates non-overlapping bandwidth to each sub-array, where the bandwidth is greater than the Pulse Repetition Frequency (PRF) of the system (similar to DDMA technique).

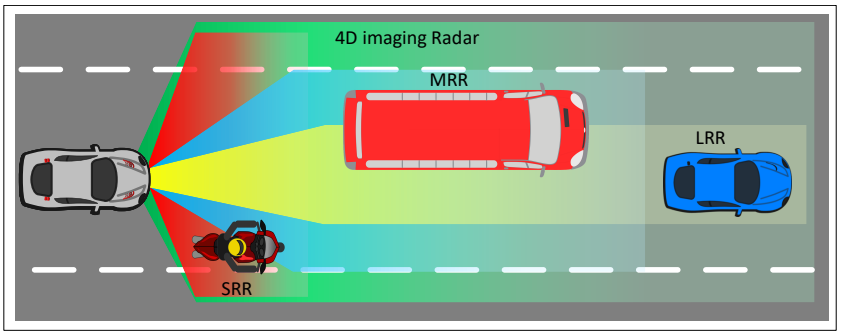

FIGURE 4.1: A comparison between the current automotive radars, and emerging 4D imaging MIMO radar systems, that can utilize UNIQUE waveforms in the transmission (SRR: Red, MRR: Blue, LRR: Yellow, 4D imaging Radar: Green).

In this case, the radar system may occupy large bandwidth leading to inefficient spectrum allocation. On the other hand, the authors in [137] first, generate correlated waveform to achieve arbitrary beampattern subsequently the matrix waveform is permuted to achieve a pseudo noise like quasi-orthogonal waveform. However, phased-MIMO radars tend to be effective for large antenna systems and may not be suitable for applications with few transmit antennas.

4.1.1 Contributions

In the emerging 4D-imaging automotive MIMO radar systems, the SRR, MRR, and LRR applications are planned to be merged, to provide unique[1] and high angular resolution in the entire radar detection range, as depicted in Figure 4.1. In this application, both long range property and fine angular resolution are required. To achieve the long range property, the MIMO radar system should have the capability of transmitting fully correlated waveforms to perform beampattern shaping and enhance the received SINR while the small cross-correlation is required to build the MIMO radar virtual array in the receiver and obtaining fine angular resolution.

The novel problem in this chapter is aimed to address the above practical requirements, by considering a CD framework subsuming the key objectives and constraints while offering an elegant design methodology. This motivation drives the following contributions of the chapter:

- *Use of both range- and spatial-ISLR:* Since these two aspects are important in MIMO radar systems, we exploit the well-known weighting to propose a flexible framework enabling a trade-off between spatial- and range-ISLR in a cognitive MIMO radar paradigm. This is considered by resorting to a scalarization of the

[1]The method proposed in this chapter called UNIQUE to point to this property of 4D-imaging radars.

multi-objective problem through its weighted sum. The weight offers a trade-off between spatial- and range- ISLR. This property is very useful for cognitive radars where the system can set the operation levels for the two ISLRs based on the scenario. The proposed optimization problem is then augmented with different sets of practical constraints, i.e., limited energy, PAR, constant modulus and discrete phase. This novel exercise of consolidation eases design and achieves higher design efficiency.

- *Optimization framework:* The problem formulation leads to an objective function comprising a weighted sum of fractional quadratic (spatial-ISLR) and quartic (range-ISLR) functions; together with the constraints, the formulation leads to a non-convex, multi-variable, and NP-hard optimization problem. The chapter proposes a unified framework based on the CD approach to solve the optimization problem under the different sets of constraints. An effective iterative algorithm based on CD, which minimizes the objective function monotonically, in each iteration is devised. While the CD approach is well-known [24, 38, 53, 60, 78, 92, 102, 138–141], challenges lie in deriving an efficient solution to each of the single variable optimization problems. A key analytical contribution of this chapter is to specialize the single variable objective functions and obtain closed-form or numerically efficient design methodologies based on the constraints. Particularly, the chapter considers the following approaches to derive the global optimum at each single variable update (i) gradient based approach for limited power and PAR constraints wherein the minimization problems are reformulated to enable derivation of gradients efficiently using real computations, (ii) a traditional calculus approach for continuous phase followed by simplification, (iii) solving the problem to yield an efficient FFT based solution for discrete phase problems.

- *Discrete Phase Design:* A systematic approach to the design of discrete phase sequences, generally not addressed in the literature, is considered in this chapter. The design of discrete phase sequences is important since it allows for the efficient utilization of the limited transmitter power. Further, the phases of these sequences are chosen from a limited alphabet, lending it attractive for radar engineers/designers from the point of view of hardware implementation. An FFT based methodology is considered to handle CD for such sequences.

- *Trade-off and Flexibility:* Extensive simulations comparing the proposed method with literature are provided to illustrate the superior trade-off obtained by the proposed solutions in minimizing the spatial- and range- ISLR. The flexibility of the framework is also illustrated by reporting superior performance when minimizing only the spatial-ISLR or the range-ISLR.

TABLE 4.1: The contribution of UNIQUE method in comparison with the literature.

Papers	[32, 40, 44–46]	[2, 3, 21–24]	[133–135]	UNIQUE
Beampattern Shaping	✓	×	✓	✓
Range-ISLR	×	✓	×	✓
Beampattern Shaping by orthogonal sets	×	×	✓	✓
Trade-off between Spatial & Range-ISLR	×	×	×	✓

Table 4.1 provides an overview of the contributions of this chapter in comparison with the literature.

4.1.2 Organization and Notations

The rest of this research is organized as follows. In Section 4.2, the system model and the design problem is formulated. We develop the CD framework to solve the problem in Section 4.3 and provide numerical experiments to verify the effectiveness of proposed algorithm in Section 4.4.

Notations This chapter uses lower-case and upper-case boldface for vectors ($\boldsymbol{a}$) and matrices ($\boldsymbol{A}$) respectively. The conjugate, transpose and the conjugate transpose operators are denoted by the $(.)^*$, $(.)^T$ and $(.)^H$ symbols respectively. Besides the Frobenius norm, l_2 norm, absolute value and round operator are denoted by $\|.\|_F$, $\|.\|_2$, $|.|$ and $\lfloor . \rceil$ respectively. For any complex number a, $\Re(a)$ and $\Im(a)$ denotes the real and imaginary part respectively. The letter j represents the imaginary unit (i.e., $j = \sqrt{-1}$), while the letter (i) is use as step of a procedure. Finally $\odot$ denotes the Hadamard product.

4.2 System Model and Problem Formulation

We consider a colocated narrow-band MIMO radar system, with M_t transmit antennas, each transmitting a sequence of length N in the fast-time domain. Let the matrix $\boldsymbol{S} \in \mathbb{C}^{M_t \times N}$ denotes the transmitted set of sequences in baseband as follows,

$$\boldsymbol{S} \triangleq \begin{bmatrix} s_{1,1} & s_{1,2} & \dots & s_{1,N} \\ s_{2,1} & s_{2,2} & \dots & s_{2,N} \\ \vdots & \vdots & \vdots & \vdots \\ s_{M,1} & s_{M,2} & \dots & s_{M,N} \end{bmatrix},$$

Let us assume that $\boldsymbol{S} \triangleq [\bar{\boldsymbol{s}}_1, \ldots, \bar{\boldsymbol{s}}_N] \triangleq [\tilde{\boldsymbol{s}}_1^T; \ldots; \tilde{\boldsymbol{s}}_{M_t}^T]^T$, where the vector $\bar{\boldsymbol{s}}_n \triangleq [s_{1,n}, s_{2,n}, \ldots, s_{M_t,n}]^T \in \mathbb{C}^{M_t}$ $(n = \{1, \ldots, N\})$ indicates the n^{th} time-sample across the M_t transmitters (the n^{th} column of matrix $\boldsymbol{S}$) while the $\tilde{\boldsymbol{s}}_m \triangleq [s_{m,1}, s_{m,2}, \ldots, s_{m,N}]^T \in \mathbb{C}^N$ $(m = \{1, \ldots, M_t\})$ indicates the N samples of m^{th} transmitter (the m^{th} row of matrix $\boldsymbol{S}$). In this chapter, we deal with the spatial- and range- related ISLR. To this end, in the following, we introduce the ISLR model in these domains.

4.2.1 System Model in Spatial Domain

We assume a ULA structure for the transmit array. The transmit steering vector takes the from [17],

$$\boldsymbol{a}(\theta) = [1, e^{j\frac{2\pi d_t}{\lambda}\sin(\theta)}, \ldots, e^{j\frac{2\pi d_t(M_t-1)}{\lambda}\sin(\theta)}]^T \in \mathbb{C}^{M_t}. \tag{4.1}$$

In (4.1), d_t is the distance between the transmitter antennas and λ is the signal wavelength. The power of transmitted signal (beampattern) in the direction θ can be written as [17, 28, 44],

$$P(\boldsymbol{S}, \theta) = \frac{1}{N}\sum_{n=1}^{N}\left|\boldsymbol{a}^H(\theta)\bar{\boldsymbol{s}}_n\right|^2 = \frac{1}{N}\sum_{n=1}^{N}\bar{\boldsymbol{s}}_n^H\boldsymbol{A}(\theta)\bar{\boldsymbol{s}}_n$$

where, $\boldsymbol{A}(\theta) = \boldsymbol{a}(\theta)\boldsymbol{a}^H(\theta)$. Let $\Theta_d = \{\theta_{d,1}, \theta_{d,2}, \ldots, \theta_{d,M_d}\}$ and $\Theta_u = \{\theta_{u,1}, \theta_{u,2}, \ldots, \theta_{u,M_u}\}$ denote the sets of M_d desired and M_u undesired angles in the spatial domain, respectively, where $\Theta_d \cap \Theta_u = \varnothing$ This information can be obtained from a cognitive paradigm. We define the spatial-ISLR, $\bar{f}(\boldsymbol{S})$, as the ratio of beampattern response on the undesired directions (sidelobes) to those on the desired angles (mainlobes) by the following equation,

$$\bar{f}(\boldsymbol{S}) \triangleq \frac{\frac{1}{M_u}\sum_{r=1}^{M_u}P(\boldsymbol{S}, \theta_{u,r})}{\frac{1}{M_d}\sum_{r=1}^{M_d}P(\boldsymbol{S}, \theta_{d,r})} = \frac{\sum_{n=1}^{N}\bar{\boldsymbol{s}}_n^H\boldsymbol{A}_u\bar{\boldsymbol{s}}_n}{\sum_{n=1}^{N}\bar{\boldsymbol{s}}_n^H\boldsymbol{A}_d\bar{\boldsymbol{s}}_n}, \tag{4.2}$$

where $\boldsymbol{A}_u \triangleq \frac{\sum_{r=1}^{M_u}\boldsymbol{A}(\theta_{u,r})}{NM_u}$ and $\boldsymbol{A}_d \triangleq \frac{\sum_{r=1}^{M_d}\boldsymbol{A}(\theta_{d,r})}{NM_d}$. Note that $\bar{f}(\boldsymbol{S})$ is a fractional quadratic function.

4.2.2 System Model in Fast-Time Domain

The aperiodic cross-correlation of $\tilde{\boldsymbol{s}}_m$ and $\tilde{\boldsymbol{s}}_l$ is defined as,

$$r_{m,l}(k) = \sum_{n=1}^{N-k} s_{m,n}s_{l,n+k}^*, \tag{4.3}$$

where $m, l \in \{1, \ldots, M_t\}$ are the transmit antennas indices and $k \in \{-N+1, \ldots, N-1\}$ denotes the lag of cross-correlation. If $m = l$, (4.3) represents the aperiodic auto-correlation of signal $\tilde{\boldsymbol{s}}_m$. The zero lag of auto-correlation represents the mainlobe of the

matched filter output and contains the energy of sequence, while the other lags ($k \neq 0$) are referred to the sidelobes. The range-ISL can therefore be expressed by [22, 24],

$$\sum_{\substack{m,l=1 \\ l\neq m}}^{M_t} \sum_{k=-N+1}^{N-1} |r_{m,l}(k)|^2 + \sum_{m=1}^{M_t} \sum_{\substack{k=-N+1 \\ k\neq 0}}^{N-1} |r_{m,m}(k)|^2, \tag{4.4}$$

where the first and second terms represent the cross- and auto-correlation sidelobes, respectively. For the sake of convenience, (4.4) can be written as,

$$\text{ISL} = \sum_{m,l=1}^{M_t} \sum_{k=-N+1}^{N-1} |r_{m,l}(k)|^2 - \sum_{m=1}^{M_t} |r_{m,m}(0)|^2. \tag{4.5}$$

The range-ISLR (time-ISLR) is the ratio of range-ISL over the mainlobe energy, i.e.,

$$\tilde{f}(\boldsymbol{S}) = \frac{\sum\limits_{m,l=1}^{M_t} \sum\limits_{k=-N+1}^{N-1} \left\| \tilde{\boldsymbol{s}}_m^H \boldsymbol{J}_k \tilde{\boldsymbol{s}}_l \right\|_2^2 - \sum\limits_{m=1}^{M_t} \left\| \tilde{\boldsymbol{s}}_m^H \tilde{\boldsymbol{s}}_m \right\|_2^2}{\sum\limits_{m=1}^{M_t} \left\| \tilde{\boldsymbol{s}}_m^H \tilde{\boldsymbol{s}}_m \right\|_2^2}, \tag{4.6}$$

where $\boldsymbol{J}_k = \boldsymbol{J}_{-k}^T$ donates the $N \times N$ shift matrix [142]. Note that, when the transmit set of sequences are unimodular, $\sum_{m=1}^{M_t} \left\| \tilde{\boldsymbol{s}}_m^H \tilde{\boldsymbol{s}}_m \right\|_2^2 = M_t N^2$, and $\tilde{f}(\boldsymbol{S})$ is a scaled version of the range-ISLR defined in [24]. As can be seen $\tilde{f}(\boldsymbol{S})$ is a fractional quartic function.

4.2.3 Problem Formulation

We aim to design sets of sequences that simultaneously possess good properties in terms of both spatial- and range-ISLR, under limited transmit power, bounded PAR, constant modulus and discrete phase constraints. The optimization problem can be represented as,

$$\begin{cases} \min\limits_{\boldsymbol{S}} & \bar{f}(\boldsymbol{S}), \tilde{f}(\boldsymbol{S}) \\ s.t & C \end{cases} \tag{4.7}$$

where $C \in \{C_1, C_2, C_3, C_4\}$, with

$$\begin{aligned} C_1 &: 0 < \|\boldsymbol{S}\|_F^2 \leqslant M_t N \\ C_2 &: 0 < \|\boldsymbol{S}\|_F^2 \leqslant M_t N, \ \frac{\max |s_{m,n}|^2}{\frac{1}{M_t N}\|\boldsymbol{S}\|_F^2} \leqslant \gamma_p \\ C_3 &: s_{m,n} = e^{j\phi_{m,n}}; \ \phi \in \Phi_\infty \\ C_4 &: s_{m,n} = e^{j\phi_{m,n}}; \ \phi \in \Phi_L \end{aligned} \tag{4.8}$$

where $m = \{1, \ldots, M_t\}$, and $n = \{1, \ldots, N\}$. In (4.8),

- C_1 represents the limited transmit power constraint.

- C_2 is the PAR constraint with limited power, and γ_p indicates the maximum admissible PAR.
- C_3 is the constant modulus constraint with $\Phi_\infty = [-\pi, \pi)$.
- C_4 is the discrete phase constraint with $\Phi_L = \{\phi_0, \phi_1, \ldots, \phi_{L-1}\} \in \left\{0, \frac{2\pi}{L}, \ldots, \frac{2\pi(L-1)}{L}\right\}$, and L is the alphabet size.

The first constraint (C_1) is convex while the second constraint (C_2) is non-convex due to the fractional inequality. Besides, the equality constraints C_3 and C_4 ($s_{m,n} = e^{j\phi}$ [2] or $|s_{m,n}| = 1$) are not affine. The aforementioned constraints can be sorted from the smallest to the largest feasible set as,

$$C_4 \subset C_3 \subset C_2 \subset C_1. \tag{4.9}$$

Problem (4.7) is a bi-objective optimization problem in which a feasible solution that minimizes the both the objective functions may not exist [24, 143]. Scalarization, a well known technique converts the bi-objective optimization problem to a single objective problem, by replacing a weighted sum of the objective functions. Using this technique, the following Pareto-optimization problem will be obtained,

$$\mathcal{P}\begin{cases} \min\limits_{\boldsymbol{S}} & f_o(\boldsymbol{S}) \triangleq \eta \bar{f}(\boldsymbol{S}) + (1-\eta)\tilde{f}(\boldsymbol{S}) \\ s.t & C, \end{cases} \tag{4.10}$$

The coefficient $\eta \in [0, 1]$ is a weight factor that effects trade-off between spatial- and range-ISLR. In (4.10), $\bar{f}(\boldsymbol{S})$ is a fractional quadratic function of $\bar{\boldsymbol{s}}_n$, and $\tilde{f}(\boldsymbol{S})$ is a fractional quartic function of $\tilde{\boldsymbol{s}}_m$. Hence, the objective is a non-convex and multi-variable function. Thus, we encounter a non-convex, multi-variable and NP-hard optimization problem [24, 78].

4.3 Proposed Waveform Design

To tackle the fractional optimization problems, several approaches including expanded SDR [32, 144], Dinkelbach [62, 145], polynomial optimization [146] and Grab-n-Pull [147] can be used. In this chapter, to solve (4.10) directly, we propose CD framework, which is applicable for both fractional quadratic and quartic problems under four different constraints, i.e., C_1, C_2, C_3, and C_4. Under this framework, the multi variable problem is solved as a sequence of single variable problems. Further this single variable problems admit a global solution.

[2] For the convenience we use ϕ instead of $\phi_{m,n}$ in the rest of the chapter.

4.3.1 CD based framework

The methodologies based on CD, generally start with a feasible matrix $\boldsymbol{S} = \boldsymbol{S}^{(0)}$ as the initial waveform set. Then, in each iteration, the waveform set is updated entry by entry several times [24, 38, 53, 60, 78, 92, 102, 138–140]. In particular, an entry of $\boldsymbol{S}$ is considered as the only variable while others are held fixed and then the objective function is optimized with respect to this identified variable. Let us assume that $s_{t,d}$ ($t \in \{1,\ldots,M_t\}$ and $d \in \{1,\ldots,N\}$) is the only variable. There are several rules to update the matrix $\boldsymbol{S}$: (a) randomized i.e., the entry ($s_{t,d}$) is chosen uniformly randomly at each single variable update, (b) cyclic i.e., iterate over all different $s_{t,d}$ entries and (c) Maximum Block Improvement (MBI) (greedy) i.e., optimizing the problem for each entry separately and choosing the best one. Note that in case of large number of variables, the use of MBI rule naturally increases the convergence time drastically. In this chapter, we consider cyclic rule to update the waveform. In this case, the fixed code entries are stored in the matrix $\boldsymbol{S}^{(i)}_{-(t,d)}$ as the following,

$$\boldsymbol{S}^{(i)}_{-(t,d)} \triangleq \begin{bmatrix} s^{(i)}_{1,1} & \cdots & \cdots & \cdots & \cdots & \cdots & s^{(i)}_{1,N} \\ \vdots & \vdots & \vdots & \vdots & \vdots & \vdots & \vdots \\ s^{(i)}_{t,1} & \cdots & s^{(i)}_{t,d-1} & 0 & s^{(i-1)}_{t,d+1} & \cdots & s^{(i-1)}_{t,N} \\ \vdots & \vdots & \vdots & \vdots & \vdots & \vdots & \vdots \\ s^{(i-1)}_{M_t,1} & \cdots & \cdots & \cdots & \cdots & \cdots & s^{(i-1)}_{M_t,N} \end{bmatrix},$$

where, the superscripts (i) and $(i-1)$ show the updated and non-updated entries at iteration i. This methodology is efficient when the problem in (4.10) is written in a simplified form with respect to that variable. In this regards, the optimization problem with respect to variable $s_{t,d}$ can be written as follows (see Appendix C.1 for details),

$$\mathcal{P}_{s_{t,d}} \begin{cases} \min\limits_{s_{t,d}} & f_o(s_{t,d}, \boldsymbol{S}^{(i)}_{-(t,d)}) \\ s.t & C \end{cases} \tag{4.11}$$

where, $f_o(s_{t,d}, \boldsymbol{S}^{(i)}_{-(t,d)})$ and the constraints are given by,

$$f_o(s_{t,d}, \boldsymbol{S}^{(i)}_{-(t,d)}) \triangleq \eta \bar{f}(s_{t,d}, \boldsymbol{S}^{(i)}_{-(t,d)}) + (1-\eta)\tilde{f}(s_{t,d}, \boldsymbol{S}^{(i)}_{-(t,d)}),$$

$$\bar{f}(s_{t,d}, \boldsymbol{S}^{(i)}_{-(t,d)}) \triangleq \frac{a_0 s_{t,d} + a_1 + a_2 s^*_{t,d} + a_3 |s_{t,d}|^2}{b_0 s_{t,d} + b_1 + b_2 s^*_{t,d} + b_3 |s_{t,d}|^2}, \tag{4.12}$$

$$\tilde{f}(s_{t,d}, \boldsymbol{S}^{(i)}_{-(t,d)}) \triangleq \frac{c_0 s_{t,d}^2 + c_1 s_{t,d} + c_2 + c_3 s_{t,d}^* + c_4 {s_{t,d}^*}^2 + c_5 |s_{t,d}|^2}{|s_{t,d}|^4 + d_1 |s_{t,d}|^2 + d_2}, \tag{4.13}$$

$$\begin{aligned} C_1 &: |s_{t,d}|^2 \leqslant \gamma_e, \\ C_2 &: |s_{t,d}|^2 \leqslant \gamma_e, \quad \gamma_l \leqslant |s_{t,d}|^2 \leqslant \gamma_u, \\ C_3 &: s_{t,d} = e^{j\phi}; \quad \phi \in \Phi_\infty, \\ C_4 &: s_{t,d} = e^{j\phi}; \quad \phi \in \Phi_L, \end{aligned} \tag{4.14}$$

Note: In (4.12), (4.13) and (4.14) the coefficients a_v, b_v, $(v \in \{0, \ldots, 3\})$, c_w $(w \in \{0, \ldots, 5\})$ and boundaries γ_l, γ_u and γ_e, depend on $\boldsymbol{S}^{(i)}_{-(t,d)}$ all of which are defined in Appendix C.1.

At i^{th} iteration, for $t = 1, \ldots, M_t$, and $d = 1, \ldots, N$, the $(t,d)^{th}$ entry of $\boldsymbol{S}$ will be updated by solving (4.11). After updating all the entries, a new iteration will be started, provided that the stopping criteria is not met. This procedure will continue until the objective function converges to an optimal value. A summary of the proposed method is reported (like a pseudo-code) in **Algorithm 8**.

To optimize the code entries, notice that the optimization variable is a complex number and can be expressed as $s_{t,d} = re^{j\phi}$, where $r \geqslant 0$ and $\phi \in [-\pi, \pi)$ are the amplitude and phase of $s_{t,d}$, respectively. By substituting $s_{t,d}$ with $re^{j\phi}$ and performing standard mathematical manipulations, the problem $\mathcal{P}_{s_{t,d}}$ can be rewritten with respect to r and ϕ as follows,

$$\mathcal{P}_{r,\phi} \begin{cases} \min\limits_{r,\phi} & f_o(r,\phi) \\ s.t & C \end{cases} \tag{4.15}$$

with $f_o(r,\phi) \triangleq \eta \bar{f}(r,\phi) + (1-\eta)\tilde{f}(r,\phi)$, where,

$$\bar{f}(r,\phi) \triangleq \frac{a_0 re^{j\phi} + a_1 + a_2 re^{-j\phi} + a_3 r^2}{b_0 re^{j\phi} + b_1 + b_2 re^{-j\phi} + b_3 r^2}, \tag{4.16}$$

$$\tilde{f}(r,\phi) \triangleq \frac{c_0 r^2 e^{j2\phi} + c_1 re^{j\phi} + c_2 + c_3 re^{-j\phi} + c_4 r^2 e^{-j2\phi} + c_5 r^2}{r^4 + d_1 r^2 + d_2}. \tag{4.17}$$

$$\begin{aligned} C_1 &: 0 \leqslant r \leqslant \sqrt{\gamma_e}, \\ C_2 &: 0 \leqslant r \leqslant \sqrt{\gamma_e}, \sqrt{\gamma_l} \leqslant r \leqslant \sqrt{\gamma_u}, \\ C_3 &: r = 1; \quad \phi \in \Phi_\infty, \\ C_4 &: r = 1; \quad \phi \in \Phi_L. \end{aligned} \tag{4.18}$$

Algorithm 8 : UNIQUE method for transmit waveform design

Input: Initial set of feasible sequences, $\boldsymbol{S}^{(0)}$.
Initialization: $i = 0$.
Optimization:

1. **while** $(f_o(\boldsymbol{S}^{(i-1)}) - f_o(\boldsymbol{S}^{(i)})) > \zeta$ **do**
2. $\quad i = i + 1$;
3. $\quad$ **for** $t = 1, \ldots, M_t$ **do**
4. $\quad\quad$ **for** $d = 1, \ldots, N$ **do**
5. $\quad\quad\quad$ Optimize $s_{t,d}^{(i-1)}$ and obtain $s_{t,d}^{\star}$;
6. $\quad\quad\quad$ Update $s_{t,d}^{(i)} = s_{t,d}^{\star}$;
7. $\quad\quad\quad$ $\boldsymbol{S}^{(i)} = \boldsymbol{S}_{-(t,d)}^{(i)}\big|_{s_{t,d}=s_{t,d}^{(i)}}$;
8. $\quad\quad$ **end for**
9. $\quad$ **end for**
10. **end while**

Output: $\boldsymbol{S}^{\star} = \boldsymbol{S}^{(i)}$.

Let $s_{t,d}^{\star} = r^{\star}e^{j\phi^{\star}}$ be the optimized solution of Problem $\mathcal{P}_{r,\phi}$. Towards obtaining this solution, **Algorithm 8** considers a feasible set of sequences as the initial waveforms. Then, for each update of single variable, it selects $s_{t,d}^{(i-1)}$ as the variable and updates it with the optimized $s_{t,d}^{(i)}$, denoted by $s_{t,d}^{\star}$. This procedure is repeated for other entries and is undertaken until all the entries are optimized at least once. After optimizing the M_tN^{th} entry, the algorithm examines the convergence metric for the objective function. If the stopping criteria is not satisfied, the algorithm will repeat the aforementioned steps. We consider $(f_o(\boldsymbol{S}^{(i)}) - f_o(\boldsymbol{S}^{(i-1)}) \leq \zeta$, ($\zeta$ is the stopping threshold, $\zeta > 0$) as the stopping criterion of the proposed method. With the defined methodology, it now remains to solve $\mathcal{P}_{r,\phi}$ for the different constraints. This is considered next.

4.3.2 Solution for limited power constraint

Problem $\mathcal{P}_{r,\phi}$ under C_1 constraint can be written as follows (see Appendix C.2 for details),

$$\mathcal{P}_e \begin{cases} \min\limits_{r,\phi} & f_o\left(r,\phi\right) \\ s.t & C_1 : 0 \leqslant r \leqslant \sqrt{\gamma_e}. \end{cases} \tag{4.19}$$

where $f_o\left(r,\phi\right) = \eta\bar{f}\left(r,\phi\right) + (1-\eta)\tilde{f}\left(r,\phi\right)$ and,

$$\bar{f}\left(r,\phi\right) = \frac{a_3 r^2 + 2(a_{0r}\cos\phi - a_{0i}\sin\phi)r + a_1}{b_3 r^2 + 2(b_{0r}\cos\phi - b_{0i}\sin\phi)r + b_1}, \tag{4.20}$$

$$\begin{aligned}\tilde{f}\left(r,\phi\right) = &[(2c_{0r}\cos 2\phi - 2c_{0i}\sin 2\phi + c_5)r^2 \\ &+ 2(c_{1r}\cos\phi - c_{1i}\sin\phi)r + c_2]\frac{1}{r^4 + d_1 r^2 + d_2}.\end{aligned} \tag{4.21}$$

The solution to $\mathcal{P}_e$ will be obtained by finding the critical points of the objective function and selecting the one that minimizes the objective. As $f_o(r,\phi)$ is a differentiable function, the critical points of $\mathcal{P}_e$ contain the solutions to $\nabla f_o(r,\phi) = 0$ and the boundaries $(0, \sqrt{\gamma_e})$, which satisfy the constraint $(0 \leqslant r \leqslant \sqrt{\gamma_e})$. To solve this problem, we use alternating optimization, where we first optimize for r keeping ϕ fixed and vice-versa.

4.3.2.1 Optimization with respect to r

Let us assume that the phase of the code entry $s_{t,d}^{(i-1)}$ is $\phi_0 = \tan^{-1}\left(\frac{\Im(s_{t,d}^{(i-1)})}{\Re(s_{t,d}^{(i-1)})}\right)$. By substituting ϕ_0 in $\frac{\partial f_o(r,\phi)}{\partial r}$, it can be shown that the solution to the condition $\frac{\partial f_o(r,\phi_0)}{\partial r} = 0$ can be obtained by finding the roots of the following degree 10 real polynomial (see Appendix C.3 for details),

$$\textstyle\sum_{k=0}^{10} p_k r^k = 0. \tag{4.22}$$

Further, since r is real, we seek only the real extrema points. Let us assume that the roots are r_v, $v = \{1,\ldots,10\}$; therefore the critical points of problem $\mathcal{P}_e$ with respect to r can be expressed as,

$$R_e = \left\{r \in \{0, \sqrt{\gamma_e}, r_1, \ldots, r_{10}\} | \Im(r) = 0, 0 \leqslant r \leqslant \sqrt{\gamma_e}\right\}. \tag{4.23}$$

Thus, the optimum solution for r will be obtained by,

$$r_e^\star = \arg\min_r \left\{f_o(r,\phi_0) | r \in R_e\right\}. \tag{4.24}$$

4.3.2.2 Optimization with respect to ϕ

Let us keep r fixed and optimize the problem with respect to ϕ. Considering $\cos(\phi) = (1-\tan^2(\frac{\phi}{2}))/(1+\tan^2(\frac{\phi}{2}))$, $\sin(\phi) = 2\tan(\frac{\phi}{2})/(1+\tan^2(\frac{\phi}{2}))$ and using the change of variable $z \triangleq \tan(\frac{\phi}{2})$, it can be shown that finding the roots of $\frac{\partial f_o(r_e^\star,\phi)}{\partial\phi}$ is equivalent finding the roots of the following 8-degree real polynomial (see Appendix C.4 for details),

$$\sum_{k=0}^{8} q_k z^k. \tag{4.25}$$

Similar to (4.22), we only admit real roots. Let us assume that z_v, $v = \{1, \ldots, 8\}$ are the roots of (4.25). Hence, the critical points of $\mathcal{P}_e$ with respect to ϕ can be expressed as,

$$\Phi = \left\{ 2 \arctan(z_v) | \Im(z_v) = 0 \right\}. \tag{4.26}$$

Therefore, the optimum solution for ϕ is,

$$\phi_e^\star = \arg\min_{\phi} \left\{ f_o(r_e^\star, \phi) | \phi \in \Phi \right\}. \tag{4.27}$$

Subsequently the optimum solution for $s_{t,d}$ is, $s_{t,d}^{(i)} = r_e^\star e^{j\phi_e^\star}$.

Remark 4.1. Since 0 and $\sqrt{\gamma_e}$ are members of R_e, hence, there are two critical points and R_e is not a null set. On the other hand, as $f_o(r_0, \phi)$ is function of $\cos\phi$ and $\sin\phi$, it is periodic, real and differentiable. Therefore, it has at least two extrema and its derivative has at least two real roots; thus Φ_e never becomes a null set. As a result in each single variable update, the problem has a solution and never becomes infeasible.

4.3.3 Solution for PAR constraint

Problem $\mathcal{P}_{r,\phi}$ under C_2 constraint is a special case of C_1 and the procedures in subsection 4.3.2 are valid for limited power and PAR constraint. The only difference lies in the boundaries and critical points with respect to r. Considering the C_2 constraint, the critical points can be expressed as the following,

$$\begin{aligned} R_p = \{ & r \in \{\max\{0, \sqrt{\gamma_l}\}, \min\{\sqrt{\gamma_u}, \sqrt{\gamma_e}\}, r_1, \ldots, r_{10}\} | \\ & \Im(r) = 0, \max\{0, \sqrt{\gamma_l}\} \leqslant r \leqslant \min\{\sqrt{\gamma_u}, \sqrt{\gamma_e}\}\}. \end{aligned} \tag{4.28}$$

Therefore, the optimum solution for r and ϕ is,

$$\begin{aligned} r_p^\star &= \arg\min_{r} \left\{ f_o(r, \phi_0) | r \in R_p \right\}, \\ \phi_p^\star &= \arg\min_{\phi} \left\{ f_o(r_p^\star, \phi) | \phi \in \Phi \right\}, \end{aligned} \tag{4.29}$$

and, the optimum entry can be obtained by, $s_{t,d}^{(i)} = r_p^\star e^{j\phi_p^\star}$.

4.3.4 Solution for Continuous Phase

The continuous phase constraint (C_3) is a special case of limited power (C_1) constraint. In this case $r = 1$, and the optimum solution for ϕ is,

$$\phi_c^\star = \arg\min_{\phi} \left\{ f_o(r, \phi) | \phi \in \Phi, r = 1 \right\}. \tag{4.30}$$

The optimum entry can be obtained by $s_{t,d}^{(i)} = e^{j\phi_c^\star}$.

4.3.5 Solution for discrete phase

We consider the design of a set of MPSK sequences for the discrete phase problem. In this case, $\mathcal{P}_{r,\phi}$ can be written as follows (see Appendix C.5 for details),

$$\mathcal{P}_d \begin{cases} \min\limits_{\phi} & f_d(\phi) = \dfrac{e^{j3\phi} \sum_{k=0}^{6} g_k e^{-jk\phi}}{e^{j\phi} \sum_{k=0}^{2} h_k^{-jk\phi}} \\ s.t & C_4 : \phi \in \Phi_L. \end{cases} \tag{4.31}$$

As the problem under C_4 constraint is discrete, the optimization procedure is different compared with other constraints. In this case all the discrete points lie on the boundary of the optimization problem; hence, all of them are critical points for the problem. Therefore, one approach for solving this problem is to obtain all the possibilities of the objective function $f_o(\phi)$ over the set $\Phi_L = \{\phi_0, \phi_1, \ldots, \phi_{L-1}\} \in \left\{0, \frac{2\pi}{L}, \ldots, \frac{2\pi(L-1)}{L}\right\}$ and choose the phase which minimizes the objective function. It immediately occurs that such an evaluation could be cumbersome; however, for MPSK alphabet, an elegant solution can be obtained as detailed below.

The objective function can be formulated with respect to the indices of Φ_L as follows,

$$f_d(\phi_l) = f_d(l) = \frac{e^{j3\frac{2\pi l}{L}} \sum_{k=0}^{6} g_k e^{-jk\frac{2\pi l}{L}}}{e^{j\frac{2\pi l}{L}} \sum_{k=0}^{2} h_k e^{-jk\frac{2\pi l}{L}}}, \tag{4.32}$$

where $l = \{0, \ldots, L-1\}$, and the summation terms on numerator and denominator exactly follow the definition of L-points DFT of sequences $\{g_0, \ldots, g_6\}$ and $\{h_0, h_1, h_2\}$ respectively. Therefore, the problem $\mathcal{P}_d$ can be written as,

$$\mathcal{P}_l \left\{ \min_{l} \quad f_d(\phi_l) = \frac{\boldsymbol{w}_{L,3} \odot \mathcal{F}_L\{g_0, g_1, g_2, g_3, g_4, g_5, g_6\}}{\boldsymbol{w}_{L,1} \odot \mathcal{F}_L\{h_0, h_1, h_2\}}, \right. \tag{4.33}$$

where, $\boldsymbol{w}_{L,\nu} = [1, e^{-j\nu\frac{2\pi}{L}}, \ldots, e^{-j\nu\frac{2\pi(L-1)}{L}}]^T \in \mathbb{C}^L$ and $\mathcal{F}_L$ is an L point DFT operator. Due to aliasing phenomena, when $L < 7$, the objective function would be changed.

Let N_{f_d} and D_{f_d} be the summation terms in nominator and denominator of $f_d(\phi_l)$ respectively, it can be shown that,

$$\begin{aligned}
L = 6 &\Rightarrow N_{f_d} = \mathcal{F}_L\{g_0 + g_6, g_1, g_2, g_3, g_4, g_5\} \\
L = 5 &\Rightarrow N_{f_d} = \mathcal{F}_L\{g_0 + g_5, g_1 + g_6, g_2, g_3, g_4\} \\
L = 4 &\Rightarrow N_{f_d} = \mathcal{F}_L\{g_0 + g_4, g_1 + g_5, g_2 + g_6, g_3\} \\
L = 3 &\Rightarrow N_{f_d} = \mathcal{F}_L\{g_0 + g_3 + g_6, g_1 + g_4, g_2 + g_5\},
\end{aligned}$$

and for $L = 2$, $N_{f_d} = \mathcal{F}_L\{g_0 + g_2 + g_4 + g_6, g_1 + g_3 + g_5\}$ and $D_{f_d} = \mathcal{F}_L\{h_0 + h_2, h_1\}$.

According to aforementioned discussion the optimum solution of (4.33) is,

$$l^\star = \arg \min_{l=1,\dots,L} \left\{ f_d(\phi_l) \right\}. \tag{4.34}$$

Hence, $\phi_d^\star = \frac{2\pi(l^\star - 1)}{L}$ and the optimum entry is $s_{t,d}^{(i)} = e^{j\phi_d^\star}$.

4.3.6 Convergence

The convergence of the proposed method can be discussed in two aspects, the convergence of objective function and the convergence of the waveform set $\boldsymbol{S}$. With regard to objective function, as $\bar{f}(\boldsymbol{S}) > 0$ and $\tilde{f}(\boldsymbol{S}) > 0$, therefore, $f_o(\boldsymbol{S}) > 0$, $\forall \boldsymbol{S} \neq 0$, and this expression is also valid for the optimum solution of **Algorithm 8** ($f_o(\boldsymbol{S}^\star) > 0$).

On the other hand, the **Algorithm 8** minimizes the objective function in each step leading to a monotonic decrease of the function value. Since the function value is lower bounded, it can be argued that the algorithm converges to a specific value. Particularly, if the algorithm starts with feasible $\boldsymbol{S}^{(0)}$ we have,

$$f_o(\boldsymbol{S}^{(0)}) \geqslant \cdots \geqslant f_o(\boldsymbol{S}^{(i)}) \geqslant \cdots \geqslant f_o(\boldsymbol{S}^\star) > 0.$$

Finally, the MBI updating rule (greedy), evaluates the new objective values by updating each entry separately and choosing the best one, ensures the convergence of argument [148–150] to stationary point. However, the MBI selection rule could be costly with large number of variables. In cyclic rule which is considered in this chapter, there are three key assumptions in convergence of the argument: (a) separable constraints, (b) differentiable objective, and (c) unique minimizer at each step [151].

In this chapter we consider the convergence of objective function and numerically observed that the problem converges under limited energy, PAR, continuous and discrete phase constraints.

4.3.7 Computational Complexity

In each single variable update, **Algorithm 8** needs to carry out the following steps:

- *Calculate the coefficient a_v, b_v and c_w in (4.15)*: Calculating a_v and b_v needs $M_t^2 N$ operations, while c_w needs $M_t^2 N \log_2(N)$ due to using fast convolution (see Appendix C.1 for details). Using a recursive relation, the computational complexity for the coefficients a_v and b_v can be reduced to M_t^2 and for c_w can be reduced to $M_t N \log_2(N)$. Typically, in most practical MIMO radar systems, $N >> M_t$. Hence, considering the fact that a_v and b_v can be obtained in parallel, the overall computational complexity of calculating the coefficients is $\mathcal{O}(M_t N \log_2(N))$.
- *Solve the optimization problem (4.15)*: Under C_1 and C_2 constraints, **Algorithm 8** needs finding the roots of 10 and 8-degree polynomials[3] in (4.22) and (4.25), which take an order of 10^3 and 8^3 operations respectively, while under C_3 the algorithm needs finding roots of (4.25) and takes an order of 8^3 operations. In case of C_4 constraint we obtain (4.32) using two L-point FFT, where each needs $L \log_2(L)$ operations.
- *Optimizing all the entries of matrix $\boldsymbol{S}$*: To this end we need to repeat the two aforementioned steps $M_t N$ times.

Let us assume that $\mathcal{K}$ iterations are required for convergence of the algorithm. Therefore, the overall computational complexity of **Algorithm 8** is $\mathcal{O}(\mathcal{K} M_t N(10^3 + 8^3 + M_t N \log_2(N)))$ under C_1 and C_2 constraints, while under C_3 is $\mathcal{O}(\mathcal{K} M_t N(8^3 + M_t N \log_2(N)))$. In case of C_4 the computational complexity is $\mathcal{O}(\mathcal{K} M_t N(L \log_2(L) + M_t N \log_2(N)))$.

4.4 Numerical Results

In this section, we provide some representative numerical examples to illustrate the effectiveness of the proposed algorithm. Towards this end, unless otherwise explicitly stated, we consider the following assumptions. For transmit parameters we consider an ULA configuration with $M_t = 8$ transmitters and the antenna distance is $d_t = \frac{\lambda}{2}$. We also consider an ULA configuration at the receive side with $M_r = 8$ antennas. We select the desired and undesired angular regions to be $\Theta_d = [-55^o, -35^o]$ and $\Theta_u = [-90^o, -60^o] \cup [-30^o, 90^o]$ respectively. For purpose of simulation, we consider an

[3]For finding the roots of polynomial we use "roots" function in MATLAB. This function is based on computing the eigenvalues of the companion matrix. Thus the computational complexity of this method is $\mathcal{O}(k^3)$, where k is the degree of the polynomial [95, 96]

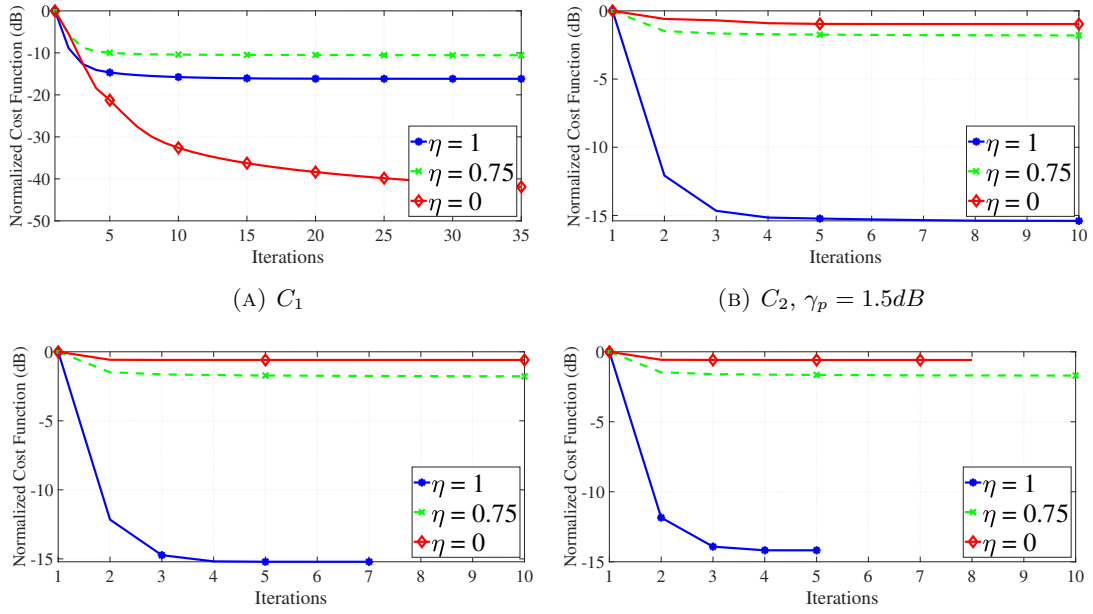

(A) C_1 (B) C_2, $\gamma_p = 1.5dB$

(C) C_3 (D) C_4, $L = 8$

FIGURE 4.2: Convergence behavior of the proposed algorithm for different constraint and values of η ($M_t = 8$, $N = 64$).

uniform sampling of these regions with a grid size of 5^o. The stopping condition for **Algorithm 8** is $\zeta = 10^{-6}$.

4.4.1 Convergence

Figure 4.2 depicts the convergence behavior of UNIQUE algorithm under C_1, C_2, C_3, and C_4 constraints under different scalarization coefficients η. Since MPSK sequences are feasible for the all constraints, we consider a set of random MPSK sequences ($\boldsymbol{S}_0 \in \mathbb{C}^{M_t \times N}$) with alphabet size $L = 8$ as an initial waveform. Here, every code entry is given by,

$$s_{m,n}^{(0)} = e^{j\frac{2\pi(l-1)}{L}}, \tag{4.35}$$

where l is the random integer variable uniformly distributed in $[1, L]$. According to Figure 4.2, the objective function decreases monotonically for all values of η and for all the constraints. Furthermore, for any η, the performance ordering of limited power, PAR, continuous and discrete phase can be predicted from the relation $C_4 \subset C_3 \subset C_2 \subset C_1$.

4.4.2 Trade-off between spatial- and range-ISLR

In this part we firstly assess the contradiction in waveform design for beampattern shaping and orthogonality; subsequently, we show the importance of making a trade-off

between spatial- and range-ISLR to obtain a better performance.

4.4.2.1 Relation between Beampattern Shaping and Orthogonality

Figure 4.3 shows the beampattern of the proposed algorithm under $C_1, \ldots, C_4$ constraints with different values of η. Setting $\eta = 0$ results in an almost omni directional beam. By increasing η, radiation pattern takes the shape of a beam with $\eta = 1$ offering the optimized pattern.

On the other hand, Table 4.2 shows a three-dimensional representation of the amplitude of correlation of a particular sequence with the other waveforms in the optimized set $\boldsymbol{S}^{\star}$[4]. The 4^{th} sequence shows the auto-correlation of that particular waveform. With $\eta = 1$ (first row in Table 4.2), yields an optimized beampattern, the cross-correlation with other sequences is rather large in all cases.

This shows the transmission of scaled waveforms (phase-shifted) from all antennas similar to traditional phased array. In this case, it would not be possible to separate the transmit signals at the receiver (by matched filter) and the MIMO virtual array will not be formed, thereby losing in the angular resolution. When $\eta = 0$ (last row in Table 4.2), an orthogonal set of sequences is obtained as their cross-terms (auto- and cross-correlation lags) are small under different design constraints. The resulting omnidirectional beampattern (see Figure 4.3), however, prevents steering of the transmit power towards the desired angles, while a strong signal from the undesired directions may saturate the radar receiver. The middle row in Table 4.2, depicts $\eta = 0.5$, a case when partially orthogonal waveforms are adopted, while some degree of transmit beampattern shaping can still be obtained (see Figure 4.3).

Figure 4.3 and Table 4.2 show that, having simultaneous beampattern shaping and orthogonality are contradictory, and the choice of η effects a trade-off between the two and enhance the performance of radar system. This is explored in the next part.

4.4.2.2 Beampattern nulling and target discrimination

To illustrate the effectiveness of choosing $0 < \eta < 1$, we consider a scenario where two desired targets (T_1 and T_2) with similar reflectivity, speed, and range are located in $\theta_{T_1} = -40^o$ and $\theta_{T_2} = -50^o$. The reason for selecting similar speed and range is to consider a worse case scenario where targets cannot be extracted from the range and

[4]In order to plot the auto- and cross-correlation, first we sort the optimized waveforms based on their energy, then we move the waveform which has the maximum energy at the middle of the waveform set ($\lfloor \frac{M_t}{2} \rceil$). By this rearrangement, the peak of auto-correlation will be located at the middle.

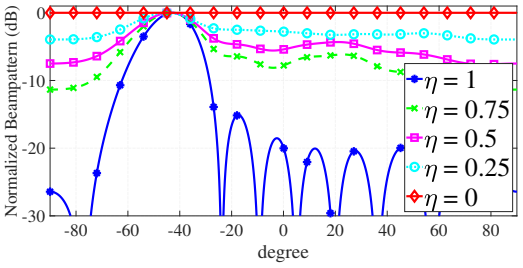

(A) C_1

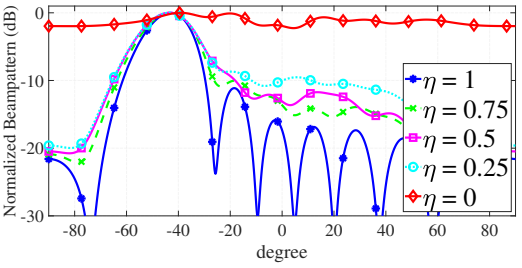

(B) C_2, $\gamma_p = 1.5dB$.

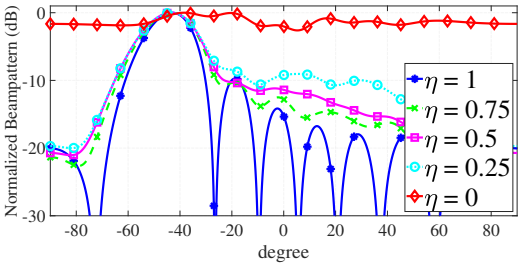

(C) C_3

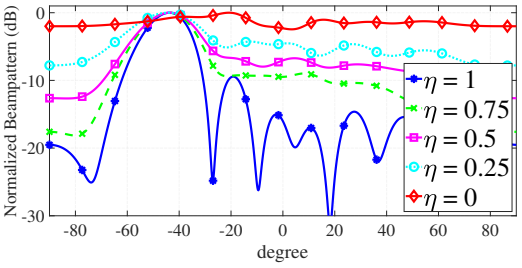

(D) C_4, $L = 8$

FIGURE 4.3: Transmit beampattern under different constraint and value of η ($M_t = 8$, $N = 64$, $\Theta_d = [-55^o, -35^o]$ and $\Theta_u = [-90^o, -60^o] \cup [-30^o, 90^o]$).

TABLE 4.2: Three-dimensional representation of the auto- and cross-correlation of proposed method ($M_t = 8$, $N = 1024$).

η	C_1	C_2, $\gamma_p = 1.5dB$	C_3	C_4 $(L = 8)$
1	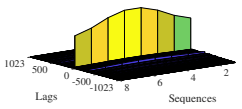	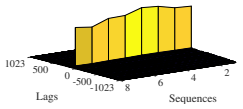	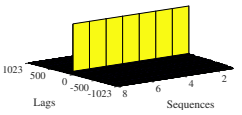	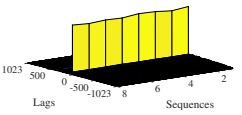
0.5	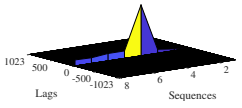	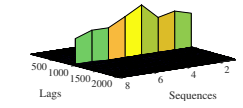	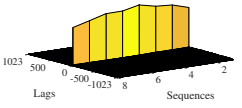	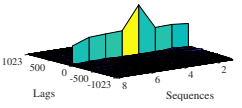
0	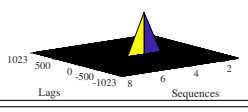	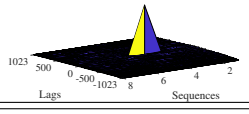	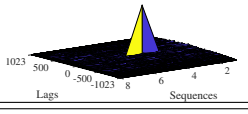	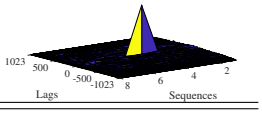

Doppler processing. Also, we assume that three more strong targets denoted as B_1, B_2 and B_3 (potentially can be clutter), are located in identical speed and range, but with different angles, $\theta_{B_1} = -9.5^o$, $\theta_{B_2} = 18.5^o$ and $\theta_{B_3} = 37^o$, we aim to design a set of transmit sequences to be able to discriminate the two desired targets, meanwhile avoiding interference from the undesired directions.

Figure 4.4 shows the range-angle profile of the above scenario under the representative C_4 constraint with $L = 8$. When $\eta = 1$, we consider the conventional phased array receiver processing for Figure 4.4a and use one matched filter to extract the range-angle profile. To this end we assume $\lambda/2$ spacing for transmit and receive antenna elements,

TABLE 4.3: Amplitude of the desired and undesired targets

η	T_1	T_2	B_1	B_2	B_3
1	9.54 dB	9.79 dB	-13.24 dB	-19.93 dB	-9.4 dB
0.5	8.78 dB	9.71 dB	-3.5 dB	-3.51 dB	-0.6 dB
0	-2.39 dB	-2.44 dB	3.68 dB	2.95 dB	2.87 dB

i.e., $d_t = d_r = \frac{\lambda}{2}$. Observe that, despite the mitigation of undesired targets, the two targets are not discriminated and are merged into a single target. The same scenario has been repeated in Figure 4.4b when $\eta = 0$. Since the optimized waveforms are orthogonal in this case, we consider MIMO processing to exploit the virtual array and improve the discrimination/identifiability. In this case, we use M_t matched filters in every receive chain, each corresponding to one of the M_t transmit sequences. The receive antennas have a sparse configuration with $d_r = M_t\frac{\lambda}{2}$ but the distance between transmit antennas is $d_t = \frac{\lambda}{2}$; this forms a MIMO virtual array with a maximum length. In this case, the optimized set of transmit sequences is able to discriminate the two targets, but it is contaminated by the strong reflections of the undesired targets. Also, some false targets (F_1, F_2 and F_3) have appeared due to the high side-lobe levels of the strong reflectors. By choosing $\eta = 0.5$, we are able to discriminate the two targets and mitigate the signal of the undesired reflections in a same time. This fact is shown in Figure 4.4c.

Table 4.3 shows the amplitude of the desired targets and undesired reflections in the scene (after the detection chain) at different Pareto-weights (η). As can be seen from Table 4.3, the performance of target enhancement and interference mitigation reduces from $\eta = 1$ to $\eta = 0$. Nevertheless by choosing $\eta = 0.5$ the waveform achieves a trade-off between spatial- and range-ISLR, it can discriminate the two targets and mitigate the interference from the undesired locations.

4.4.2.3 Pareto-front

Pareto-front or non-dominated solutions, is a curve which gives a set of optimal solutions and helps the radar designers to choose the best solution for the radar system according to the environment conditions, priorities and risks. To the best of our knowledge, there is no technique in literature trading off the two spatial- and range-ISLR functions considered in the chapter. In this regards, we consider to compare the performance of the proposed method with Non-Dominated Sorting Genetic Algorithm (NSGA)-II, a multi objective evolutionary algorithm [152]. We assume the following setup for NSGA-II, the number of population $n_p = 50$, crossover percentage $c_r = 70\%$, mutation percentage $m_p = 40\%$ and mutation rate $m_r = 0.05$.

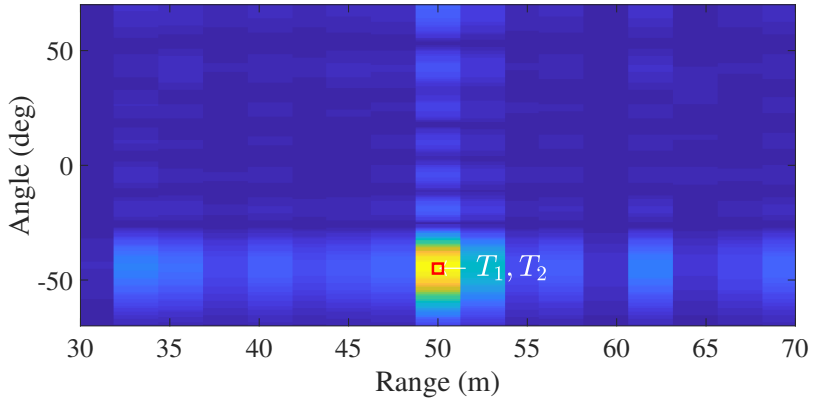

(A) Phased array processing $\eta = 1$.

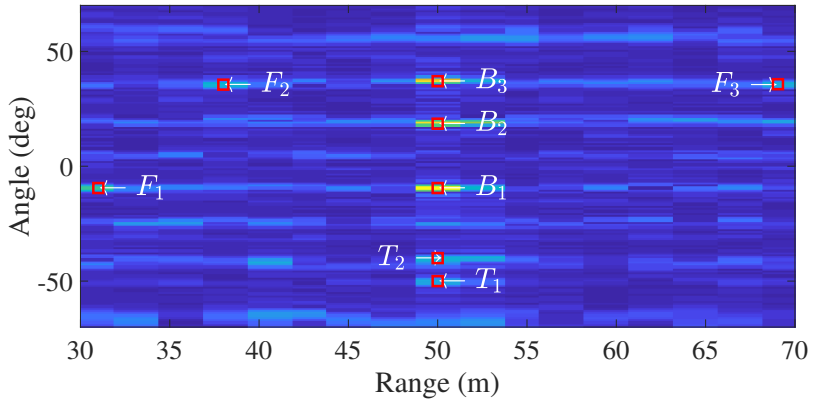

(B) MIMO processing $\eta = 0$.

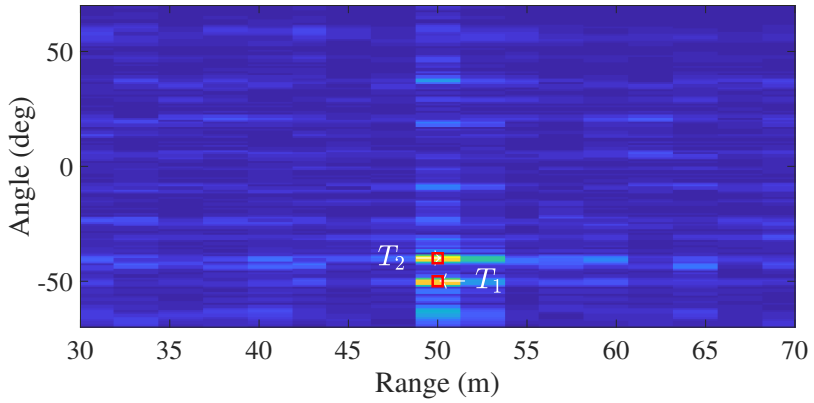

(C) MIMO processing $\eta = 0.5$.

FIGURE 4.4: Illustration of the centrality of η (C_4 constraint, $M_t = M_r = 8$, $N = 64$, $L = 8$, $\theta_{T_1} = -50^o$, $\theta_{T_2} = -40^o$, $\theta_{B_1} = -9.5^o$, $\theta_{B_2} = 18.5^o$ and $\theta_{B_3} = 37^o$).

Figure 4.5 shows the non-dominated (optimal) solutions of the proposed method under $C_1, \ldots, C_4$ constraints and NSGA-II method under discrete phase. As can be seen the solution obtained by NSGA-II cannot dominate the Pareto front of proposed method. Besides the proposed methods offers more diversity in compare with NSGA-II. In addition Figure 4.5 also depicts the performance of the solution corresponding to $\eta = 0.5$; this

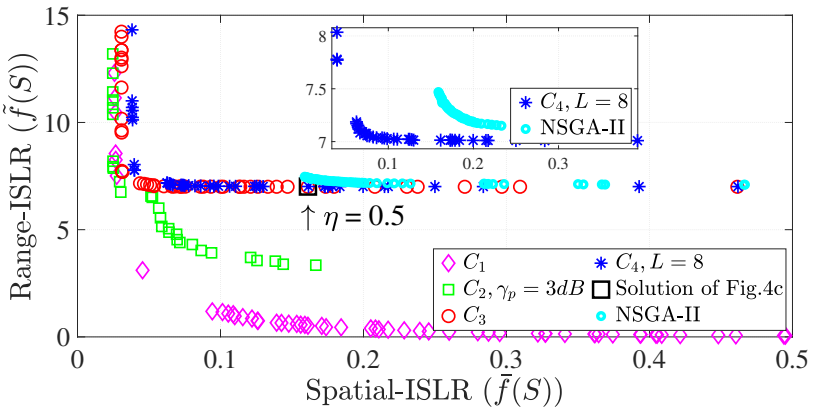

FIGURE 4.5: Solution for Pareto front obtained from NSGA-II and the proposed method ($N = 64$, $M_t = 8$).

solution is used to generate Figure 4.4c. It can be observed that the solution lies on the Pareto front.

The correct choice of η is essential to achieve the objectives and that, such a choice of η depends on the scenario. In the following, we provide an plausible method for selecting an appropriate η.

- **Training Step**: This is an offline procedure which contains the following steps,
  1. We consider different scenarios and obtain the optimized waveform set and its η value by using the Pareto front. Then, we store the corresponding results for every scenario in a database.
  2. We design an artificial neural networks and train it with the different scenarios and optimized waveforms corresponding to the best η value that are stored on the database, to offer the optimum solution based on the scenario.
- **Functional Step**: After training successfully the artificial neural network we can consider the following procedure,
  1. In order to form the virtual array at the receiver, at the first the MIMO radar system transmits an orthogonal set of sequences ($\eta = 0$). In this case, the MIMO radar system is able to estimate the angles of targets and interference with high discrimination (other parameters such as range and Doppler can be estimated as well).
  2. Based on the estimated parameters, the artificial neural network offers the optimized set of sequences by using the database.
  3. Using the chosen set of sequences, the environment parameters are estimated.
  4. We go to step 2.

As mentioned earlier, the training step is performed offline; similar sensor training is also typically undertaken in many commercial offerings. Further, the functional step does not involve optimization procedures but executes a neural network which is typically fast, thereby rendering the scheme practically is applicable. We consider a detailed study on this scheme for our future research.

4.4.3 Minimizing spatial-ISLR ($\eta = 1$)

By choosing $\eta = 1$, we focus on minimizing the spatial-ISLR. In this subsection, we compare the performance of proposed method under different constraints. In this regards, we compare with SDR based method [32] for C_1, MIA-PC for C_2, MIA-CMC [45] for C_3 and STTC [46] C_4 as a benchmark respectively.

To compare with the SDR method [32], we assume that the desired and undesired angular regions to be $\Theta_d = [-55^o, -35^o]$ and $\Theta_u = [-90^o, -60^o] \cup [-30^o, 90^o]$ respectively. In Figure 4.6a, we illustrate the beampattern of the optimized waveforms through different constraints and SDR method. In case of designing discrete phase sequences, we map the results of SDR to the nearest MPSK sequence and call it Quantized-SDR (Q-SDR). Interestingly, the optimized waveforms through the proposed method mimics the beampattern obtained via SDR, indicating the attractiveness of this approach in designing set of sequences with practical constraints. Notice that, there is a significant difference between the solution obtained via the proposed method under the discrete phase constraint and Q-SDR for identical alphabet sizes. This can be justified from the fact that we consider the constraint directly in the design problem, while quantizing the waveform to the nearest MPSK sequence does not guarantee an optimal solution.

In order to compare under PAR continuous and discrete phase, we assume that the target and the three interferers are located at 10^o, -5^o, 25^o and -60^o respectively. We set noise power at -10 dB, and similar values of 30dB for target and clutter RCS. For a fairness, we compare with MIA-PC and MIA-CMC in [32], where the similarity constraint is not considered. Also, in [46], we set the similarity threshold equal to 2, the maximum admissible similarity value in STTC. Figure 4.6(b),(c),(d) shows the normalized beampattern responses of MIA-PC, MIA-CMC, STTC and the proposed method. Observe that the proposed method outperforms MIA-PC and MIA-CMC in terms of null steering. Besides the performance of the proposed method and STTC under discrete phase are similar.

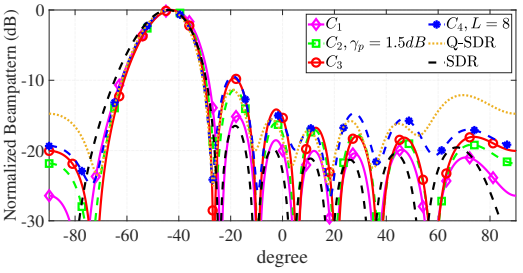

(A) Comparison of C_1 and SDR.

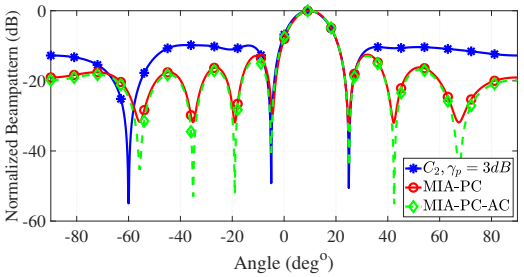

(B) Comparison of C_2 and MIA-PC.

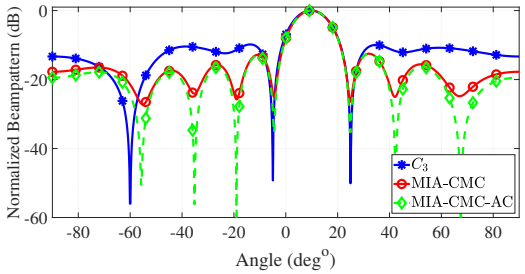

(C) Comparison of C_3 and MIA-CMC.

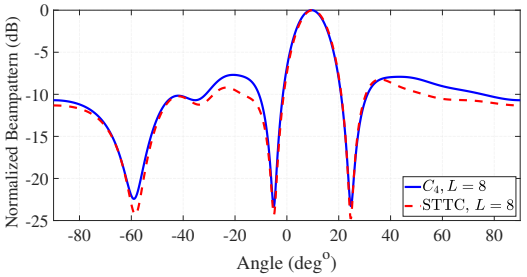

(D) Comparison of C_4 and STTC).

FIGURE 4.6: The comparison of beampattern shaping of proposed method with (a) SDR, (b) MIA-PC, (c) MIA-CMC and (d) STTC ($M_t = 8$ and $N = 64$).

4.4.4 Minimizing range-ISLR ($\eta = 0$)

We set $\eta = 0$ and evaluate the performance of the proposed method. Kindly refer to the last row of Table 4.2, which shows the three-dimensional representation of the auto- and cross-correlation (following the methodology in footnote 3 of section 4.4.2), under $C_1, \ldots, C_4$ constraints. In this case, the proposed method designs a waveform with good orthogonality under C_2, C_3 and C_4 constraints, and interestingly achieves a perfect orthogonality under the C_1 constraint. Figure 4.7 shows the absolute value of optimum sequence under C_1 constraint. As can be seen all the power is concentrated on one transmitter with no waveform from others. This is similar to TDM approach for orthogonality [132].

We choose Multi-CAN [2] and MM-Corr [3] as the benchmark and assess the range-ISLR under C_3 and C_4 (unimodular sequences) for a fair comparison. In this case, a lower bound on the scaled range-ISLR is $10\log(M_t - 1)$ dB [3]. Table 4.4 compares the average scaled range-ISLR of the proposed method with Multi-CAN, MM-Corr and the lower bound for different number of transmitters. Similar to the Multi-CAN and MM-Corr, the proposed method meets the lower bound under continuous phase constraint. Interestingly, even with discrete phase constraint where $L = 8$ and $L = 2$ (binary), the obtained set of sequences exhibits the scaled range-ISLR values quite close to the lower bound.

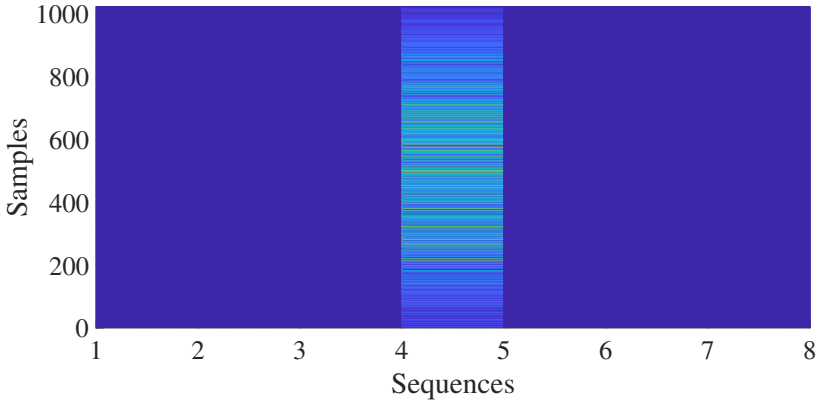

FIGURE 4.7: Optimized waveform of proposed method under C_1 constraints ($\eta = 0$, $M_t = 8$, $N = 1024$).

TABLE 4.4: Comparison between the average scaled range-ISLR (dB) of the proposed method under C_3 and C_4, Multi-CAN [2], MM-corr [3] and lower bound with different number of transmitters ($\eta = 0$, $N = 64$).

M_t	Lower bound	Multi-CAN	MM-Corr	C_3	C_4 ($L = 8$)	C_4 ($L = 2$)
2	0	0	0.0003	0	0.2583	0.5266
3	3.0103	3.0103	3.0104	3.0103	3.1045	3.2133
4	4.7712	4.7712	4.7712	4.7712	4.8080	4.8587
5	6.0206	6.0206	6.0206	6.0206	6.0411	6.0950
6	6.9897	6.9897	6.9897	6.9897	7.0024	7.0283
7	7.7815	7.7815	7.7815	7.7815	7.7891	7.8071
8	8.4510	8.4510	8.4510	8.4510	8.4581	8.4684

TABLE 4.5: The range-ISLR of the proposed method under the C_4 constraint with different sequence lengths ($\eta = 0$, $M_t = 8$).

N	32	64	128	256	512	1024
$L = 2$	8.4678	8.4688	8.4687	8.4684	8.4676	8.4675
$L = 8$	8.4569	8.458	8.4578	8.457	8.4568	8.4567

Table 4.5 shows the optimized scaled range-ISLR values under C_4, for $L = 8$ and $L = 2$ with different sequence lengths when $M_t = 8$. As can be seen the proposed method is capable to design large sequence length without degradation. Recalling the last row of Table 4.5, we observe that the optimized sequences have range-ISLR values quite close to the lower bound (less than 0.02 dB difference when $M_t = 8$).

4.4.5 Beampattern shaping with binary sequences

Due to the simplicity of implementing of binary sequences, these kind of waveforms are attractive for radar designers. Here we assess the beampattern performance of the proposed binary waveform design. Figure 4.8a shows the beampattern response of

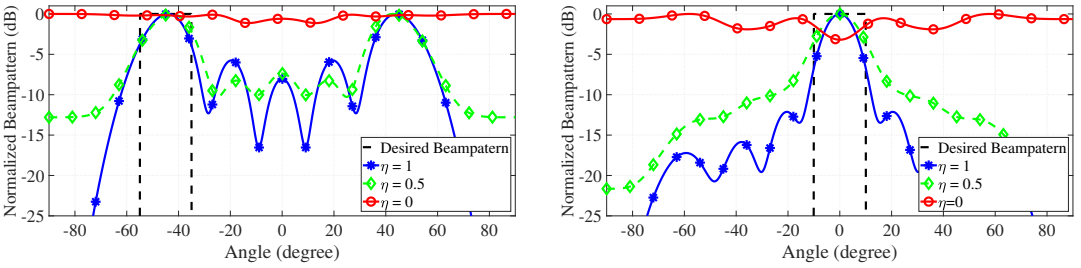

(A) $\Theta_d = (-55^o, -35^o)$ and $\Theta_u = (-90^o, -60^o) \cup (-30^o, 90^o)$.

(B) $\Theta_d = (-10^o, 10^o)$ and $\Theta_u = (-90^o, -15^o) \cup (15^o, 90^o)$.

FIGURE 4.8: The beampattern of optimized binary sequences ($M_t = 8$, $N = 1024$).

the proposed method in binary case with different value of η, where we assume that $\Theta_d = [-55^o, -35^o]$ and $\Theta_u = [-90^o, -60^o] \cup [-30^o, 90^o]$. As can be seen with $\eta = 1$ we obtain the optimum beampattern response and by decreasing the η the beampattern worsens. Besides, the beampattern response in binary case is symmetric about 0^o. Indeed, in a case when the waveforms are real (binary sequences), the beampattern will be symmetric.

In 4D-imaging application of automotive radar systems, the desired region for beampattern shaping can be limited to the angles around zero, where binary codes can be used. Figure 4.8b shows the beampattern response at $\Theta_d = [-10^o, 10^o]$ and $\Theta_u = [-90^o, -15^o] \cup [15^o, 90^o]$ for different η.

4.4.6 The impact of alphabet size and PAR

Figure 4.9 shows the impact of alphabet size and PAR in several aspects. In (a) and (b), the solution of C_4 approaches that of C_3 for large alphabet sizes. This behavior is expected since the feasible set of C_4 will be close to that of C_3, and the optimized solutions will behave the same. In (c), by increasing the PAR threshold, the feasible set under C_2 constraint converges to C_1. By decreasing the PAR threshold to 1, the feasible set will be limited to that specified in C_3. Part (d), shows the constellation of the optimized sequences under different constraints.

4.4.7 Computational Time

Table 4.6 shows a typical computational time[5] required to obtain the results of Table 4.2. To provide this table, we initialized the algorithm with 10 independent set of random sequences and performed Algorithm 8. The obtained run-times were averaged and

[5]The computational times in this section is reported based on running the algorithms on a desktop PC with Intel (R) Core (TM) i9-9900K CPU @ 3.60GHz and 64.00 GB installed memory (RAM).

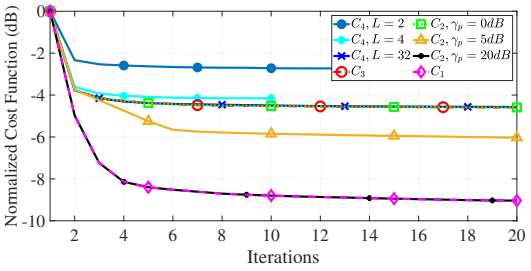

(A) Convergence ($\eta = 0.95$).

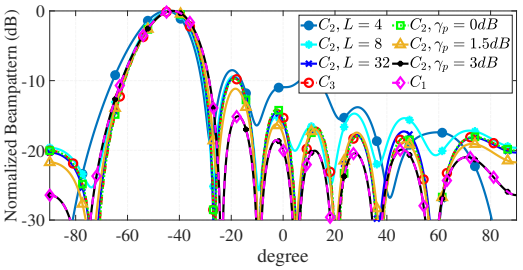

(B) Beampattern ($\eta = 1$, $\Theta_d = (-55^o, -35^o)$ and $\Theta_u = (-90^o, -60^o) \cup (-30^o, 90^o)$).

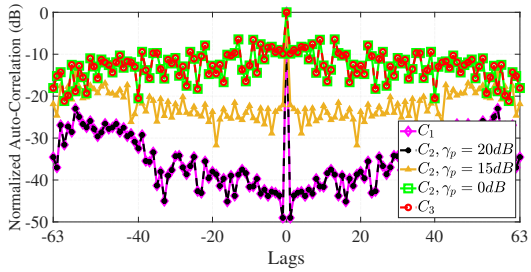

(C) Auto-correlation ($\eta = 0$).

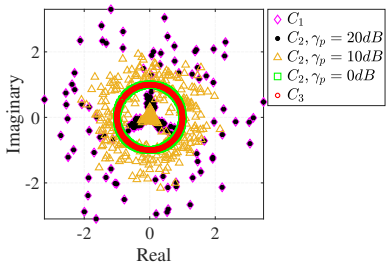

(D) Constellation ($\eta = 1$).

FIGURE 4.9: The impact of alphabet size ((a) and (b)) and PAR ((c) and (d)) ($M_t = 8$ and $N = 64$).

TABLE 4.6: Averaged computational time (sec) of Table 4.2 over 10 independent trails ($M_t = 8$ and $N = 1024$).

Constraint	C_1	C_2	C_3	C_4
$\eta = 0$	1124	270	694	1083
$\eta = 0.5$	756	277	25570	5809
$\eta = 1$	5.9	10.5	0.62	0.58

reported in Table 4.6. Note that depending to the objective and the approach used for updating the single variable, the proposed algorithm can have different computational time. In the following, we compare the computational time of the proposed method with the counterparts.

4.4.7.1 $\eta = 0$

Figure 4.10a compares the computational time of the proposed method with Multi-CAN [2, 21] and MM-Corr [3] with $M_t = 2$ at different sequence lengths. In this figure, we consider that all of the methods are initialized with the same set of random discrete phase sequences with alphabet size of $L = 8$. Note that the proposed method offers lower

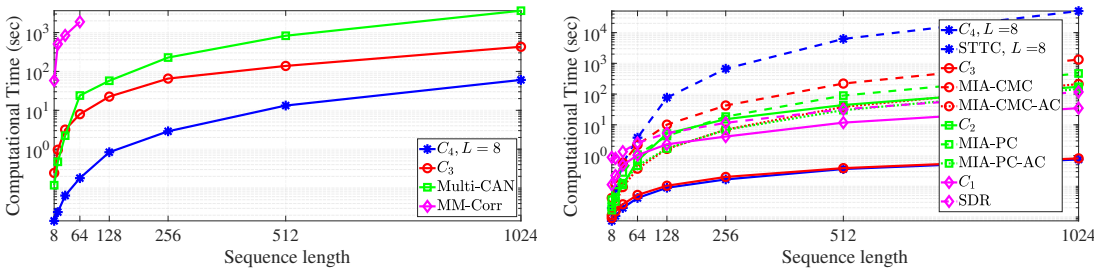

(A) Range-ISLR minimization ($\eta = 0$, $M_t = 2$)

(B) Spatial-ISLR minimization ($\eta = 1$, $M_t = 8$)

FIGURE 4.10: Averaged computational time over 10 independent trails.

computational time in comparison with Multi-CAN and MM-Corr under continuous and discrete phase constraints[6].

4.4.7.2 $\eta = 1$

Figure 4.10b compares the computational time of the proposed method with the the methods which are performing beampattern shaping, with $M_t = 8$ at different sequence lengths. Note that the highest computational time belongs to the STTC [46] method which is based on CD method. Note that STTC uses exhaustive search to find the optimum solution which is very expensive in terms of complexity. Although the proposed algorithm under discrete phase constraint uses CD method as well, but due to the efficient formulation and using FFT, it has significantly lower computational time. Further, under limited energy and continuous phase constraints, the proposed method has lower computational time in comparison with SDR [32] and MIA-CMC [45], respectively. Finally, in case of PAR constraint, the proposed method has lower run-time in comparison with MIA-PC, and its run-time is similar to MIA-PC-AC [45].

4.5 Conclusion

We used spatial- and range-ISLR as representative figures of merit in this chapter to achieve a trade-off between beampattern response and orthogonality. Accordingly, we introduced a bi-objective Pareto framework to minimize the two metrics simultaneously for MIMO radar systems, under power budget, PAR, continuous and discrete phase constraints. The problem formulation led to a non-convex, multi-variable and NP-hard optimization problem. To tackle the problem, we proposed an iterative method based on CD; in each of its steps we utilized an effective method to minimize the objective

[6]We have not reported the computational time of MM-Corr for $N > 64$, since it takes much more time than the counterparts.

function. Specifically, we used a gradient based method under energy budget, PAR and continuous phase constraints; an FFT-based method was used under the discrete phase constraint.

Simulation results have illustrated the monotonicity of the proposed method in minimizing the objective function as well as the contradiction in minimizing the two ISLRs. In this context, the proposed method is capable of effecting an optimal trade-off between the two. The chapter also provided a Pareto curve aided cognitive radar system to decide on the operating levels of the two ISLRs. Besides, the proposed framework also shows good performance in comparison to counterparts when used for minimizing the spatial- and range-ISLR individually; this indicates the flexibility offered by the framework.

Possible future research directions includes the consideration of Doppler filter bank and spectrum shaping for enhanced cognition in MIMO radar systems.

Chapter 5

MIMO Radar Transmit Beampattern Shaping for Spectrally Dense Environments

Designing unimodular waveforms with a desired beampattern, spectral occupancy and orthogonality level is of vital importance in the next generation MIMO radar systems. Motivated by this fact, in this chapter, we propose a framework for shaping the beampattern in MIMO radar systems under the constraints simultaneously ensuring unimodularity, desired spectral occupancy and orthogonality of the designed waveform. In this manner, the proposed framework is the most comprehensive approach for MIMO radar waveform design focusing on beampattern shaping. The problem formulation leads to a non-convex quadratic fractional programming. We propose an effective iterative to solve the problem, where each iteration is composed of a Semi-definite Programming (SDP) followed by eigenvalue decomposition. Some numerical simulations are provided to illustrate the superior performance of our proposed over the state-of-the-art.

5.1 Introduction

Transmit beampattern shaping by controlling the spatial distribution of the transmit power, can play an important role in improving the radar performance through enhanced power efficiency, better detection probability, target identification, improved interference mitigation, among others. The goal is to focus the transmit power on desired angles while minimizing it at undesired angles [25]. Recently, the beampattern shaping via waveform design in MIMO radar systems has been widely studied. From a waveform design perspective, there are two methods for beampattern shaping, indirect and direct methods

[26, 27]. The early works (two-step method) focus on the correlation matrix design and the waveform matrix is subsequently obtained through one of the decomposition methods [28–36], but the latest works is more about the direct waveform design. The drawback of the two-step method is, there is no guarantee to obtain a rank one solution. On the other hand, there are several metrics (objective functions) to obtain the optimum beampattern such as, beampattern matching, spatial-ISLR/PSLR minimization, and SINR maximization.

Beampattern Matching In beampattern matching, the aim is to minimize the difference between the desired and designed beampattern. For instance, the following papers have worked on designing the waveform covariance matrix employing beampattern matching. The authors in [28] devised a method to address the joint beampattern shaping and the cross-correlation minimization in spatial domain through SQP technique. In [29], CA is presented to shape the beampattern under low PAR constraint. In [34, 35], the authors propose a covariance matrix design method based on DFT coefficients and Toeplitz matrices. The DFT-based technique provides a well-match transmit beampattern at low complexity. However, the drawback of the DFT-based method is that, for small number of antennas, the performance of the DFT-based method is slightly poorer. On the other hand, several papers focus on designing directly the transmit waveforms for beampattern shaping. For example, in [26], two optimization algorithms based on ADMM are proposed under constant modulus constraint for the probing waveform. In [27], a method based in ADMM is proposed to design a beampattern in wide-band systems. In [41], a method for beampattern matching is addressed based on gradient decent which they term it PDR. In [42], the authors propose a method based on MM for beampattern matching under PAR constraint in two cases of wide- and narrow-band.

Spatial-ISLR and PSLR minimization In Spatial-ISLR and PSLR minimization approach, the aim is to minimize the ratio of *summation of beampattern response on undesired over desired angles*, and to minimize the ratio of *maximum beampattern response on undesired angles over minimum beampattern response on desired angles*, respectively. In [32], a method based on SDR under constant energy and 3 dB main beam-width constraint is proposed to minimize the spatial-ISLR. In [44], the robust designs of waveform covariance matrix through optimizing the worst case transmit beampattern are considered to minimize the spatial-ISLR and -PSLR of beampatterns, respectively. Unlike two aforementioned methods, [37, 40, 43] propose a direct waveform design solution. The authors in [37] propose the efficient UNIQUE algorithm based on CD method to minimize spatial- and range-ISLR under four different constraints, namely, limited energy, PAR, continuous and discrete phase constraints. The method proposed in

[43] is similar to UNIQUE without considering range-ISLR metric and PAR and limited energy constraints. A method based on ADMM is proposed in [40] to minimize the spatial-PSLR under constant modulus constraint.

SINR maximization In SINR optimization approaches, the problem does not deal with the beampattern directly. However, the beampattern is implicitly shaped as a result of transmit waveform optimization. For example [30, 31] address the problem of waveform design in the presence of signal dependence clutter. In these works, an iterative approach is presented to jointly optimize the transmit waveform and receive filter to maximize the output SINR. The authors in [45] propose MIA based on MM method for joint waveform and filter design under similarity, constant modulus (MIA-CMC) and PAR (MIA-PC) constraints. While STTC [46] is proposed based on CD to solve the problem under similarity, uncertain steering matrices, continuous or discrete phase constraints. In [46], a Dinkelbach based method and exhaustive search is proposed for continuous and discrete phase constraints respectively.

In order to form the virtual array and enhancing the angular resolution, the received signal in MIMO radar system should be separable (orthogonal) in receiver while a set of arbitrary waveforms are adopted in the transmit side. In order to obtain the orthogonality, the waveform should have small cross-correlation [17]. Also, small auto-correlation sidelobes is a requirement, to avoid masking weak targets within the range sidelobes of a strong target, and to mitigate the harmful effects of distributed clutter returns close to the target of interest. Recently, many optimization techniques, e.g., Multi-CAN [2, 21], Iterative Direct Search [85], ISL New [22, 153], MM-Corr [3], BiST [24], UNIQUE [37] and WeBEST [58] are proposed to design orthogonal sets of sequences, minimizing the ISL/PSL metrics. However, beampattern shaping in MIMO radar systems yield a correlated waveform which, is in contradiction with orthogonality [37, 131]. In this context there are few papers which addressed these two aspects in MIMO radar systems. For instance [131] proposes beampattern matching problem under particular constraints on the waveform cross-correlation matrix. In [133], the authors minimizes the difference between desired and undesired beampattern responses for one sub-pulse. Then the quasi-orthogonality of other sub-pulses are obtained by random permutation. In [134], the authors combine a beampattern matching by orthogonality requirement as a penalty in the objective function and use the PDR approach for the solution. In [135], the authors propose a method based on ADMM to design a beampattern with good cross-correlation. In [37], UNIQUE is proposed as a unified framework to minimize the spatial- and range-ISLR using weighted sum technique under limited energy, PAR, continuous and discrete phase constraints. By choosing an appropriate value for the

regularization parameter, UNIQUE is able to make trade-off between having a good orthogonality and beampattern shaping.

On the other hand, spectral shaping is an important aspect of resource management in cognitive[1] MIMO radar systems. Uing this approach, the cognitive radar system is able to utilize effectively the available bandwidth. One attractive application of spectral shaping is coexistence of communications and cognitive MIMO radar systems, which the whole bandwidth is shared between these two systems based on the priorities [47]. There are several methods for spectral shaping. For instance, in [1, 23, 48–51] spectral matching approach is proposed to shape the spectral of the transmit waveform. In [52, 53], the authors consider a waveform design approach to maximize SINR, while the spectral behaviour is considered as a constraint. In [54, 55], the ratio of the maximum stop-band level to the minimum pass-band level is considered as the objective function to shape the spectrum. SILR minimization approach is consider under continuous and discrete phase constraints in [47]. The design of constant modulus waveform for beampattern matching under spectral constraint are addressed in [50, 56]. To tackle the non-convex optimization problem the authors in [50] and [56] propose IBS and BIC methods respectively.

5.1.1 Contribution

In this chapter, we consider the spatial-ISLR as design metric similar to [43]. In [43], the authors proposed CD-based method to enhance the performance of the radar in spatial domain. However, in this chapter, we deal with the design of waveform considering the features in three domains: ISLR in the spatial and range domain and masking in the spectral domain. Particularly, we propose a waveform design framework to shape the beampattern with practical constraints, namely, spectral masking, 3 dB beam-width, constant modulus and similarity constraints. Spectral masking constraint plays an important role in cognitive MIMO radar systems in several scenarios, such as spectral sharing in coexistence of MIMO radar and MIMO communication. The 3 dB beam-width constraint ensures that the beampattern has a good response at the mainlobe. This constraint can be used in the emerging 4D-imaging automotive MIMO radar systems, wherein the SRR, MRR and LRR configurations are merged, to provide unique and high angular resolution in the entire radar detection range [37, 43]. Constant modulus waveforms are attractive for radar system designers due to efficient utilization of the limited transmitter power. Besides, since constant modulus is a kind of only phase-modulated sequence, implementing of constant modulus waveform is simple. As to the orthogonality, we incorporate the beampattern shaping optimization problem with

[1] Cognitive MIMO radar systems are smart sensors which interact with the environment to adapt the properties of the waveform with the environment to enhance their performance [11].

similarity constraints to make a trade-off between having a good beampattern response and orthogonality [37]. This constraint imposes that the optimize waveform inherit some properties of a reference waveform. In fact, we consider the designed waveform to be similar to a specific waveform which have a good orthogonality to form the virtual array in receivers and enhance its angular resolution.

It is desirable to include all these properties to improve radar performance in emerging applications and in the emerging scenario of crowded environments with interference from other radars or communication systems. In this context, the contributions of the work are listed below.

- *Incorporation of metrics from multiple domains:* Radar tasks are influenced by parameters in the spatial, temporal and spectral domain. Hence it is pertinent to consider quality metrics in all these domains to improve performance. Thus, while it is highly interesting to consider all the metrics in the waveform design, the existing works consider only a selection of these performance metrics. A problem set-up involving these key performance indicators in different domains is lacking in literature. In this context the proposed framework incorporating all the metrics is the most comprehensive approach for MIMO radar waveform design focusing on beampattern shaping; it subsumes existing works as special cases. The gains obtained by incorporating these metrics over the existing works bears testimony to their impact.

- *Novel optimization framework:* The incorporation of all the aforementioned quality metrics adds further complexity to the waveform optimization and these cannot be handled by the existing frameworks. In this context, the chapter also offers a novel optimization framework to obtain a local optimum solution of the non-convex multi-variable and NP-hard problem. In an attempt to solve this problem, we propose an indirect method based on SDP. We first recast the waveform-design problem as a rank-one constrained optimization problem. Then, unlike the conventional methods which drop the rank one constraint, we propose a new iterative algorithm for efficiently solving the resulting rank-one constrained optimization problem. Each iteration of the proposed iterative algorithm is composed of an SDP followed by an Eigenvalue Decomposition (ED). In every iteration, we force the second largest eigen value towards zero to obtain the rank one solution. We prove that the proposed iterative algorithm converges to a local minima of the rank-one constrained optimization problem. Further, we compute the computational complexity of the proposed iterative algorithm. In addition the proposed framework can be extended to apply other convex constraints.

5.1.2 Organization and Notation

The rest of this research is organized as follows. In Section 5.2, the system model and the design problem for minimizing the spatial-ISLR under constant modulus, 3 dB beam-width, similarity and spectral masking, constraints is formulated. We develop the iterative WISE framework based on SDP to obtain a rank-one solution in Section 5.3. Finally we provide numerical experiments to verify the effectiveness of proposed algorithm in Section 5.4.

Notations This chapter uses lower-case and upper-case boldface for vectors ($\mathbf{a}$) and matrices ($\mathbf{A}$) respectively. The conjugate, transpose and the conjugate transpose operators are denoted by the $(.)^*$, $(.)^T$ and $(.)^\dagger$ symbols respectively. Besides the Frobenius norm, ℓ_2 and ℓ_p norm, absolute value and round operator are denoted by $\|.\|_F$, $\|.\|_2$, $\|.\|_p$, $|.|$ and $\lfloor . \rceil$ respectively. For any matrix $\mathbf{A}$, $\mathrm{Tr}(\mathbf{A})$, $\mathrm{Diag}(\mathbf{A})$ and $\mathrm{Rank}(\mathbf{A})$ stand for the trace, diagonal vector and the rank of $\mathbf{A}$, respectively. The letter j represents the imaginary unit (i.e., $j = \sqrt{-1}$), while the letter (i) is use as step of a procedure. Finally $\mathbf{1}$ and $\mathbf{0}$ denote a matrix/vector with proper size which all the elements are equal to one and zero respectively.

5.2 System Model

We consider a colocated narrow-band MIMO radar system, with M transmit antennas, each transmitting a sequence of length N in the fast-time domain. Let the matrix $\mathbf{S} \in \mathbb{C}^{M\times N}$ denote the transmitted set of sequences as,

$$\mathbf{S} \triangleq \begin{bmatrix} s_{1,1} & s_{1,2} & \dots & s_{1,N} \\ s_{2,1} & s_{2,2} & \dots & s_{2,N} \\ \vdots & \vdots & \vdots & \vdots \\ s_{M,1} & s_{M,2} & \dots & s_{M,N} \end{bmatrix}.$$

Let us denote that $\mathbf{S} \triangleq [\bar{\mathbf{s}}_1, \dots, \bar{\mathbf{s}}_N] \triangleq [\tilde{\mathbf{s}}_1^T, \dots, \tilde{\mathbf{s}}_M^T]^T$, where the vector $\bar{\mathbf{s}}_n \triangleq [s_{1,n}, s_{2,n}, \dots, s_{M,n}]^T \in \mathbb{C}^M$ $(n = \{1, \dots, N\})$ indicates the n^{th} time-sample across the M transmitters (the n^{th} column of matrix $\mathbf{S}$) while the $\tilde{\mathbf{s}}_m \triangleq [s_{m,1}, s_{m,2}, \dots, s_{m,N}]^T \in \mathbb{C}^N$ $(m = \{1, \dots, M\})$ indicates the N samples of m^{th} transmitter (the m^{th} row of matrix $\mathbf{S}$). In this chapter, we deal with the design of $\mathbf{S}$ considering features in three domains: ISLR in the spatial and range domain and masking in the spectral domain. To this end, we now introduce

the system model to describe in spatial and spectral domains. Subsequently, we also introduce similarity constraints to impose the range-ISLR features.

5.2.1 System Model in Spatial Domain

Let assume a colocated MIMO radar system with an ULA structure for the transmit array characterized by the following steering vector[17],

$$\mathbf{a}(\theta) = [1, e^{j\frac{2\pi d}{\lambda}\sin(\theta)}, \ldots, e^{j\frac{2\pi d(M-1)}{\lambda}\sin(\theta)}]^T \in \mathbb{C}^M, \tag{5.1}$$

where d is the distance between the transmitter antennas and λ is the signal wavelength. The beampattern in the direction of θ can be written as [17, 28, 44],

$$P(\mathbf{S}, \theta) = \frac{1}{N}\sum_{n=1}^{N}\left|\mathbf{a}^\dagger(\theta)\bar{\mathbf{s}}_n\right|^2 = \frac{1}{N}\sum_{n=1}^{N}\bar{\mathbf{s}}_n^\dagger\mathbf{A}(\theta)\bar{\mathbf{s}}_n$$

where, $\mathbf{A}(\theta) = \mathbf{a}(\theta)\mathbf{a}^\dagger(\theta)$. Let Θ_d and Θ_u be the sets of desired and undesired angles in the spatial domain, respectively. These two sets satisfy, $\Theta_d \cap \Theta_u = \varnothing$ and $\Theta_d \cup \Theta_u \subset [-90^o, 90^o]$. In this regard the spatial-ISLR is given by the following expression [37],

$$f(\mathbf{S}) \triangleq \frac{\sum_{\theta\in\Theta_u} P(\mathbf{S}, \theta)}{\sum_{\theta\in\Theta_d} P(\mathbf{S}, \theta)} = \frac{\sum_{n=1}^{N}\bar{\mathbf{s}}_n^\dagger\mathbf{A}_u\bar{\mathbf{s}}_n}{\sum_{n=1}^{N}\bar{\mathbf{s}}_n^\dagger\mathbf{A}_d\bar{\mathbf{s}}_n}, \tag{5.2}$$

where $\mathbf{A}_u \triangleq \frac{1}{N}\sum_{\theta\in\Theta_u}\mathbf{A}(\theta)$ and $\mathbf{A}_d \triangleq \frac{1}{N}\sum_{\theta\in\Theta_d}\mathbf{A}(\theta)$.

5.2.2 System Model in Spectrum Domain

Let $\mathbf{F} \triangleq [\mathbf{f}_0, \ldots, \mathbf{f}_{\hat{N}-1}] \in \mathbb{C}^{\hat{N}\times\hat{N}}$ be the DFT matrix ($\hat{N} \geq N$), where,

$$\mathbf{f}_k \triangleq [1, e^{-j\frac{2\pi k}{\hat{N}}}, \ldots, e^{-j\frac{2\pi k(\hat{N}-1)}{\hat{N}}}]^T \in \mathbb{C}^{\hat{N}},\ k = \{0, \ldots, \hat{N}-1\}.$$

Let $\mathcal{U} = \cup_{k=1}^{K}(u_{k,1}, u_{k,2})$ be the K number of normalized frequency stop-bands, where $0 \leq u_{k,1} < u_{k,2} \leq 1$ and $\cap_{k=1}^{K}(u_{k,1}, u_{k,2}) = \varnothing$. Thus, the undesired discrete frequency bands are given by $\mathcal{V} = \cup_{k=1}^{K}(\lfloor\hat{N}u_{k,1}\rceil, \lfloor\hat{N}u_{k,2}\rceil)$. In this regards, the absolute value of the spectrum at undesired frequency bins can be expressed as $|\mathbf{G}\hat{\mathbf{s}}_m|$, where $\hat{\mathbf{s}}_m$ is $\hat{N}-N$ zero-pad version of $\hat{\mathbf{s}}_m$, and defined as,

$$\hat{\mathbf{s}}_m \triangleq [\tilde{\mathbf{s}}_m; \underbrace{0; \ldots; 0}_{\hat{N}-N}], \tag{5.3}$$

and, $\mathbf{G} \in \mathbb{C}^{K\times\hat{N}}$ contains the rows of $\mathbf{F}$ corresponding to the frequencies in $\mathcal{V}$, and K is the number of undesired frequency bins [47].

5.2.3 Problem Formulation

We aim to design a set of constant modulus sequences for MIMO radar such that the transmit beampattern is steered towards desired directions and has nulls at undesired directions simultaneously, with spectrum compatibility and similarity constraints. To this end, we can formulate the following optimization problem,

$$\begin{cases} \min\limits_{\mathbf{S}} & f(\mathbf{S}) = \dfrac{\sum_{n=1}^{N} \bar{\mathbf{s}}_n^{\dagger}\mathbf{A}_u\bar{\mathbf{s}}_n}{\sum_{n=1}^{N} \bar{\mathbf{s}}_n^{\dagger}\mathbf{A}_d\bar{\mathbf{s}}_n} & \text{(5.4a)} \\ s.t. & 0.5 \leq \dfrac{\sum_{n=1}^{N} \bar{\mathbf{s}}_n^{\dagger}\mathbf{A}(\theta_d)\bar{\mathbf{s}}_n}{\sum_{n=1}^{N} \bar{\mathbf{s}}_n^{\dagger}\mathbf{A}(\theta_0)\bar{\mathbf{s}}_n} \leq 1, & \text{(5.4b)} \\ & |s_{m,n}| = 1, & \text{(5.4c)} \\ & \max\left\{|\mathbf{G}\hat{\mathbf{s}}_m|\right\} \leq \gamma,\ m \in \{1,\ldots,M\}, & \text{(5.4d)} \\ & \dfrac{1}{\sqrt{MN}}\|\mathbf{S}-\mathbf{S}_0\|_F \leq \delta, & \text{(5.4e)} \end{cases}$$

where (5.4b) indicates the 3 dB beam-width constraint to guarantee the beampattern response at all desired angles is at least half the maximum power. In (5.4b), $\theta_d \in \{\theta|\forall\theta \in \Theta_d\}$ and θ_0, denotes the the angle with maximum power, which is usually chosen to be at the center point of Θ_d. The constraint (5.4c) indicates the constant modulus property; this is attractive for radar system designers since its allows for the efficient utilization of the limited transmitter power. The constraint (5.4d) indicates the spectrum masking and guarantees the power of spectrum in undesired frequencies not to be greater than γ. Finally, the constraint (5.4e) has been imposed on the waveform to control properties of the optimized code (such as orthogonality) similar to the reference waveform $\mathbf{S}_0$, for instance this helps controlling ISLR in range domain. If we consider $\mathbf{S}$ and $\mathbf{S}_0$ to be a constant modulus waveform, the maximum admissible value of the similarity constraint parameter would be $\delta = 2$ $(0 \leq \delta \leq 2)$.

In (5.4), the objective function (5.4a) is a fractional quadratic function, also (5.4b) is a non-convex inequality constraint. The (5.4c) is a non-affine equality constraint while, the inequality constraint (5.4e) yields a convex set. Therefore, we encounter a non-convex, multi-variable and NP-hard optimization problem [37]. In the following, we propose an iterative method based on SDP to obtain an efficient local optimum solution.

5.3 Proposed Method

The maximum of $P(\mathbf{S},\theta)$ is clearly M^2, and occurs when $\bar{\mathbf{s}}_n = \mathbf{a}(\theta)$ $n = \{1,\dots,N\}$. Therefore, the denominator of (5.4a) satisfies, $\sum_{n=1}^{N} \bar{\mathbf{s}}_n^{\dagger}\mathbf{A}_d\bar{\mathbf{s}}_n \leq K_d M^2$, where K_d is the number of desired angles. Thus, the problem (5.4) can be relaxed as [154],

$$
\begin{cases}
\min\limits_{\mathbf{S}} & \displaystyle\sum_{n=1}^{N} \bar{\mathbf{s}}_n^{\dagger}\mathbf{A}_u\bar{\mathbf{s}}_n & \text{(5.5a)}\\
s.t. & \displaystyle\sum_{n=1}^{N} \bar{\mathbf{s}}_n^{\dagger}\mathbf{A}_d\bar{\mathbf{s}}_n \leq K_d M^2, & \text{(5.5b)}\\
& \displaystyle\sum_{n=1}^{N} \bar{\mathbf{s}}_n^{\dagger}\mathbf{A}(\theta_d)\bar{\mathbf{s}}_n \leq \sum_{n=1}^{N} \bar{\mathbf{s}}_n^{\dagger}\mathbf{A}(\theta_0)\bar{\mathbf{s}}_n, & \text{(5.5c)}\\
& \displaystyle\sum_{n=1}^{N} \bar{\mathbf{s}}_n^{\dagger}\mathbf{A}(\theta_0)\bar{\mathbf{s}}_n \leq 2\sum_{n=1}^{N} \bar{\mathbf{s}}_n^{\dagger}\mathbf{A}(\theta_d)\bar{\mathbf{s}}_n, & \text{(5.5d)}\\
& |s_{m,n}| = 1, & \text{(5.5e)}\\
& \|\mathbf{G}\hat{\mathbf{s}}_m\|_{p\to\infty} \leq \gamma,\ m \in \{1,\dots,M\}, & \text{(5.5f)}\\
& \dfrac{1}{\sqrt{MN}}\|\mathbf{S}-\mathbf{S}_0\|_F \leq \delta & \text{(5.5g)}
\end{cases}
$$

In (5.5), constraints (5.5c) and (5.5d) are obtained by expanding (5.4b) constraint. Besides, we replace the constraint $\max\{|\mathbf{G}\hat{\mathbf{s}}_m|\}$ (5.4d) with $\|\mathbf{G}\hat{\mathbf{s}}_m\|_{p\to\infty}$ (5.5f), which is a convex constraint for each finite p.

Remark 5.1. Another possible solution to consider the constraint (5.4d) is direct implementation by individually bounding each frequency response at each undesired frequency bin. This reformulation makes the problem convex, but needs to consideration of $M \times K$ constraints in total, which increases the complexity of the Algorithm. As the alternative, in this chapter we replace this constraint with ℓ_p-norm and leveraging the stability of the algorithm, choose a large p value to solve the problem.

Problem (5.5) is still non-convex with respect to $\mathbf{S}$ due to (5.5c), (5.5d) and (5.5e). To cope with this problem, defining $\mathbf{X}_n \triangleq \bar{\mathbf{s}}_n \bar{\mathbf{s}}_n^{\dagger}$, we recast (5.5) as follows,

$$
\begin{cases}
\min\limits_{\mathbf{S},\mathbf{X}_n} & \sum\limits_{n=1}^{N} \mathrm{Tr}(\mathbf{A}_u \mathbf{X}_n) & \text{(5.6a)} \\
s.t. & \sum\limits_{n=1}^{N} \mathrm{Tr}(\mathbf{A}_d \mathbf{X}_n) \leq K_d M^2, & \text{(5.6b)} \\
& \sum\limits_{n=1}^{N} \mathrm{Tr}(\mathbf{A}(\theta_d) \mathbf{X}_n) \leq \sum\limits_{n=1}^{N} \mathrm{Tr}(\mathbf{A}(\theta_0) \mathbf{X}_n), & \text{(5.6c)} \\
& \sum\limits_{n=1}^{N} \mathrm{Tr}(\mathbf{A}(\theta_0) \mathbf{X}_n) \leq 2 \sum\limits_{n=1}^{N} \mathrm{Tr}(\mathbf{A}(\theta_d) \mathbf{X}_n), & \text{(5.6d)} \\
& \mathrm{Diag}(\mathbf{X}_n) = \mathbf{1}_M, & \text{(5.6e)} \\
& \text{(5.5f)}, \text{(5.5g)}, & \text{(5.6f)} \\
& \mathbf{X}_n \succcurlyeq \mathbf{0}, & \text{(5.6g)} \\
& \mathbf{X}_n = \bar{\mathbf{s}}_n \bar{\mathbf{s}}_n^{\dagger}, & \text{(5.6h)}
\end{cases}
$$

It is readily observed that, in (5.6), the objective function and all the constraints but (5.6h) are convex in $\mathbf{X}_n$ and $\mathbf{S}$. In the following, we first present an equivalent reformulation for (5.6), which paves the way for iteratively solving this non-convex optimization problem .

Theorem 5.1. *Defining* $\mathbf{Q}_n \triangleq \begin{bmatrix} 1 & \bar{\mathbf{s}}_n^{\dagger} \\ \bar{\mathbf{s}}_n & \mathbf{X}_n \end{bmatrix} \in \mathbb{C}^{(M+1)\times(M+1)}$ *and considering slack variables* $\mathbf{V}_n \in \mathbb{C}^{(M+1)\times M}$ *and* $b_n \in \mathbb{R}$. *The optimization problem* (5.6) *is equivalent to,*

$$
\begin{cases}
\min\limits_{\mathbf{S},\mathbf{X}_n,b_n} & \sum\limits_{n=1}^{N} Tr(\mathbf{A}_u \mathbf{X}_n) + \eta \sum\limits_{n=1}^{N} b_n & \text{(5.7a)} \\
s.t. & \text{(5.6b)}, \text{(5.6c)}, \text{(5.6d)}, \text{(5.6e)}, \text{(5.6f)}, \text{(5.6g)} & \text{(5.7b)} \\
& \mathbf{Q}_n \succcurlyeq 0, & \text{(5.7c)} \\
& b_n \mathbf{I}_M - \mathbf{V}_n^{\dagger} \mathbf{Q}_n \mathbf{V}_n \succcurlyeq \mathbf{0}, & \text{(5.7d)} \\
& b_n \geq 0, & \text{(5.7e)}
\end{cases}
$$

where η *is a regularization parameter.*

Proof. See Appendix D.1. □

The problem (5.7) can be solved iteratively by alternating between the parameters. Let, $\mathbf{V}_n^{(i)}$, $\mathbf{Q}_n^{(i)}$, $\mathbf{S}^{(i)}$, $\mathbf{X}_n^{(i)}$ and $b_n^{(i)}$ be the values of $\mathbf{V}_n$, $\mathbf{Q}_n$, $\mathbf{S}$, $\mathbf{X}_n$ and b_n at i^{th} iteration, respectively. Given $\mathbf{V}^{(i-1)}$ and $b_n^{(i-1)}$, the optimization problem with respect to $\mathbf{S}^{(i)}$, $\mathbf{X}_n^{(i)}$ and $b_n^{(i)}$ at the i^{th} iteration becomes,

$$
\begin{cases}
\min\limits_{\mathbf{S}^{(i)},\mathbf{X}_n^{(i)},b_n^{(i)}} & \sum\limits_{n=1}^{N}\mathrm{Tr}(\mathbf{A}_u\mathbf{X}_n^{(i)})+\eta\sum\limits_{n=1}^{N}b_n^{(i)} & \text{(5.8a)}\\
s.t. & \sum\limits_{n=1}^{N}\mathrm{Tr}(\mathbf{A}_d\mathbf{X}_n^{(i)})\le K_dM^2, & \text{(5.8b)}\\
& \sum\limits_{n=1}^{N}\mathrm{Tr}(\mathbf{A}(\theta_d)\mathbf{X}_n^{(i)})\le\sum\limits_{n=1}^{N}\mathrm{Tr}(\mathbf{A}(\theta_0)\mathbf{X}_n^{(i)}), & \text{(5.8c)}\\
& \sum\limits_{n=1}^{N}\mathrm{Tr}(\mathbf{A}(\theta_0)\mathbf{X}_n^{(i)})\le 2\sum\limits_{n=1}^{N}\mathrm{Tr}(\mathbf{A}(\theta_d)\mathbf{X}_n^{(i)}), & \text{(5.8d)}\\
& \mathrm{Diag}(\mathbf{X}_n^{(i)})=\mathbf{1}_M, & \text{(5.8e)}\\
& \left\|\mathbf{G}\hat{\mathbf{s}}_m^{(i)}\right\|_{p\to\infty}\le\gamma,\ m\in\{1,\dots,M\}, & \text{(5.8f)}\\
& \frac{1}{\sqrt{MN}}\left\|\mathbf{S}^{(i)}-\mathbf{S}_0\right\|_F\le\delta, & \text{(5.8g)}\\
& \mathbf{X}_n^{(i)}\succcurlyeq\mathbf{0}, & \text{(5.8h)}\\
& \mathbf{Q}_n^{(i)}\succcurlyeq\mathbf{0}, & \text{(5.8i)}\\
& b_n^{(i)}\mathbf{I}_M-{\mathbf{V}_n^{(i-1)}}^{\dagger}\mathbf{Q}_n^{(i)}\mathbf{V}_n^{(i-1)}\succcurlyeq\mathbf{0}, & \text{(5.8j)}\\
& b_n^{(i-1)}\ge b_n^{(i)}\ge 0, & \text{(5.8k)}
\end{cases}
$$

Once $\mathbf{X}_n^{(i)}$, $\mathbf{S}_n^{(i)}$ and $b_n^{(i)}$ are found by solving (5.8), $\mathbf{V}_n^{(i)}$ can be obtained by seeking an $(M+1)\times M$ matrix with orthonormal columns such that $b_n^{(i)}\mathbf{I}_M\succcurlyeq{\mathbf{V}_n^{(i)}}^{\dagger}\mathbf{Q}_n^{(i)}\mathbf{V}_n^{(i)}$. Choosing $\mathbf{V}_n^{(i)}$ to be equal to the matrix composed of the eigenvectors of $\mathbf{Q}_n^{(i)}$ corresponding to its M smallest eigenvalues, and following similar arguments provided after (D.1) in the Appendix, we have [155, Corollary 4.3.16],

$$
\begin{aligned}
{\mathbf{V}_n^{(i)}}^{\dagger}\mathbf{Q}_n^{(i)}\mathbf{V}_n^{(i)}&=\mathrm{Diag}([\rho_1^{(i)},\rho_2^{(i)},\cdots,\rho_M^{(i)}]^T)\\
&\preccurlyeq\mathrm{Diag}([\nu_1^{(i-1)},\nu_2^{(i-1)},\cdots,\nu_M^{(i-1)}]^T)\preccurlyeq b_n^{(i)}\mathbf{I}_M,
\end{aligned}
\tag{5.9}
$$

where, $\rho_1^{(i)}\le\rho_2^{(i)}\le\cdots\le\rho_{M+N}^{(i)}$ and $\nu_1^{(i-1)}\le\nu_2^{(i-1)}\le\cdots\le\nu_M^{(i-1)}$ denote the eigenvalues of $\mathbf{Q}_n^{(i)}$ and ${\mathbf{V}_n^{(i-1)}}^{\dagger}\mathbf{Q}_n^{(i)}\mathbf{V}_n^{(i-1)}$, respectively. It follows from (5.9) that the matrix composed of the eigenvectors of $\mathbf{Q}_n^{(i)}$ corresponding to its M smallest eigenvalues is the appropriate choice for $\mathbf{V}_n^{(i)}$.

Accordingly, at each iteration of the proposed algorithm which we term as WISE, we need to solve a SDP followed by an Eigenvalue Decomposition (EVD). **Algorithm 9** summarizes the steps of the WISE approach for solving (3.4). In order to initialize the algorithm, $\mathbf{V}_n^{(0)}$ can be found through the eigenvalue decomposition of $\mathbf{Q}_n^{(0)}$ obtained from solving (5.8) without considering (5.8j) and (5.8k) constraints. Further, we terminate the algorithm when $\bar{\mathbf{s}}_n\bar{\mathbf{s}}_n^{\dagger}$ converges to $\mathbf{X}_n$. In this regards, let us assume that,

$$
\xi_{n,1}\ge\xi_{n,2}\ge\cdots\ge\xi_{n,m}\ge\cdots\ge\xi_{n,M}\ge 0,
$$

Algorithm 9 :WISE in MIMO Radar Systems

Input: γ, δ, $\mathbf{S}_0, \mathcal{U}$ and $\hat{N}$.
Initialization:

1. $i := 0$;
2. Obtain $\mathbf{Q}_n^{(0)}$ by dropping (5.8j) and (5.8k) then solving (5.8);
3. $\mathbf{V}_n^{(0)}$ is the M eigenvectors of $\mathbf{Q}_n^{(0)}$, corresponding to the M lowest eigenvalues;
4. $b_n^{(0)}$ is the second largest eigenvalue of $\mathbf{Q}_n^{(0)}$;

Optimization:

1. **while**, $\xi \geq e_1$ and $\max\left\{\frac{\left\|\bar{\mathbf{s}}_n\bar{\mathbf{s}}_n^{\dagger}-\mathbf{X}_n\right\|_F}{\sqrt{MN}}\right\} \geq e_2$ **do**
2. $\quad i := i+1$;
3. $\quad$ Obtain $\mathbf{S}^{(i)}$, $\mathbf{X}_n^{(i)}$ and $b_n^{(i)}$ by solving (5.8);
4. $\quad \mathbf{V}_n^{(i)}$ is the M eigenvectors of $\mathbf{Q}_n^{(i)}$, by dropping the eigenvector correspond to the largest eigenvalue.
5. $\quad b_n^{(i)}$ is the second largest eigenvalue of $\mathbf{Q}_n^{(i)}$.
6. **end while**

Output: $\mathbf{S}^{\star} = \mathbf{S}^{(i)}$.

be the eigenvalues of $\mathbf{X}_n$, we consider $\xi \triangleq \frac{\max\{\xi_{n,2}\}}{\min\{\xi_{n,1}\}} < e_1$ $(e_1 > 0)$ as the termination condition. In this case the *second* largest eigenvalue of $\mathbf{X}_n$ is negligible comparing to its largest eigenvalue and can be concluded that the solution is rank one. In addition, we consider $\max\left\{\frac{\left\|\bar{\mathbf{s}}_n\bar{\mathbf{s}}_n^{\dagger}-\mathbf{X}_n\right\|_F}{\sqrt{MN}}\right\} < e_2$ $(e_2 > 0)$ as the second termination condition.

We note that the proposed algorithm, which is based on alternating optimization method, is guaranteed that the objective function converges to at least a local minimum of (5.7) [156].

5.3.0.1 Convergence

It readily follows from (5.8k) that $\lim_{k\to\infty} \frac{|b_n^{(i)}|}{|b_n^{(i-1)}|} \leq 1$. This implies that $b_n^{(i)}$ converges at least sub-linearly to zero [157]. Hence, there exists some $\mathcal{I}$ such that $b_n^{(i)} \leq \epsilon$ $(\epsilon \to 0)$ for $i \geq \mathcal{I}$. Making use of this fact, we can deduce from (5.8j) that,

$$\mathbf{V}_n^{(i-1)^{\dagger}}\mathbf{Q}_n^{(i)}\mathbf{V}_n^{(i-1)} \preccurlyeq \epsilon\mathbf{I}_M, \quad \epsilon \to 0, \tag{5.10}$$

for $i \geq \mathcal{I}$. Then, it follows from (5.10) and (5.9) that $\text{Rank}(\mathbf{Q}_n^{(i)}) \simeq 1$ for $i \geq \mathcal{I}$, thereby $\mathbf{X}_n^{(i)} = \bar{\mathbf{s}}_n^{(i)} \bar{\mathbf{s}}_n^{(i)\dagger}$ for $i \geq \mathcal{I}$. This implies that $\mathbf{X}_n^{(i)}$, for any $i \geq \mathcal{I}$, is a feasible point for the optimization problem (5.7). On the other hand, considering the fact that $b_n^{(i)} \leq \epsilon$ for $i \geq \mathcal{I}$, we conclude that $\mathbf{X}_n^{(i)}$ for $i \geq \mathcal{I}$ is also a minimizer of the function $\sum_{n=1}^{N} \text{Tr}(\mathbf{A}_u \mathbf{X}_n)$. These imply that $\mathbf{X}_n^{(i)}$ for $i \geq \mathcal{I}$ is at least a local minimizer of the optimization problem (5.7). The proves the convergence of the proposed iterative algorithm.

5.3.0.2 Computational Complexity

In each iteration, **Algorithm 9** needs to perform the following steps:

- *Solving* (5.8): Needs the solution of a SDP, whose computational complexity is $\mathcal{O}(M^{3.5})$ [124].
- *Obtaining* $\mathbf{V}_n^{(i)}$ *and* $b_n^{(i)}$: Needs the implementation of a Single Value Decomposition (SVD), whose computational complexity is $\mathcal{O}(M^3)$ [96].

Since we have N summation, the computational complexity of solving (5.8) is $\mathcal{O}(N(M^{3.5}+M^3))$. Let us assume that $\mathcal{I}$ iterations are required for convergence of the **Algorithm 9**. Therefore, the overall computational complexity of **Algorithm 9** is, $\mathcal{O}(\mathcal{I}N(M^{3.5}+M^3))$.

5.4 Numerical Results

In this section, numerical results are provided for assessing the performance of the proposed algorithm for beampattern shaping and spectral matching under constant modulus constraint. Towards this end, unless otherwise explicitly stated, we consider the following set-up. For transmit parameters, we consider ULA configuration with $M = 8$ transmitters, with the spacing of $d = \lambda/2$ and each antenna transmits $N = 64$ samples. We consider an uniform sampling of regions $\theta = [-90^o, 90^o]$ with a grid size of 5^o and the desired and undesired angels for beampattern shaping are $\Theta_d = [-55^o, -35^o]$ ($\theta_0 = -45^o$) and $\Theta_u = [-90^o, -60^o] \cup [-30^o, 90^o]$, respectively. The DFT point numbers is set as $\hat{N} = 5N$, the normalized frequency stop-band is set at $\mathcal{U} = [0.3, 0.35] \cup [0.4, 0.45] \cup [0.7, 0.8]$ and the absolute spectral mask level is set as $\gamma = 0.01\sqrt{\hat{N}}$. As to the reference signal for similarity constraint, we consider $\mathbf{S}_0$ be a set of sequences with a good range-ISLR property, which is obtained by the method in [37]. For the optimization problem we set $\eta = 0.1$ and $p = 1000$ to approximate the (5.5f) constraint. The convex optimization problems are solved via the CVX toolbox [158] and the stop condition for **Algorithm 9** are set at $e_1 = 10^{-5}$ and $e_2 = 10^{-4}$, with maximum iteration of 1000.

5.4.1 Convergence

Figure 2.1 depicts the convergence behavior of the proposed method in different aspects. In this figure, we consider the maximum admissible value for similarity parameter, i.e., $\delta = 2$. Figure 5.1a shows the convergence of ξ to zero. This indicates that the second largest eigenvalue of $\mathbf{X}_n$ is negligible in comparison with the largest eigenvalue, therefore resulting in a rank one solution for $\bar{\mathbf{s}}_n$. Figure 5.1b shows that the solution of $\mathbf{X}_n$ converges to $\bar{\mathbf{s}}_n$, which confirms our claim about obtaining a rank one solution.

To indicate the performance of the proposed method under constant modulus constraint, by defining

$$s_{max} \triangleq \max\{|s_{m,n}|\}, \quad s_{min} \triangleq \min\{|s_{m,n}|\}, \tag{5.11}$$

for $m \in \{1, \ldots, M\}$, and $n \in \{1, \ldots, N\}$, in Figure 5.1c we evaluate the maximum/minimum absolute values of the code entries in $\mathbf{S}$. The results indicate that the values of s_{max} and s_{min} are converging to a fixed value, which indicates the constant modulus solution of WISE.

In addition, Figure 5.1d depicts the proposed method's PAR convergence. In the first step, we have a high PAR value, and as the number of iterations increases, the PAR value converges to 1, indicating the constant modulus solution.

Please note that, the first iteration in Figure 5.1a, Figure 5.1b and Figure 5.1c shows the SDR solution of (5.8) by dropping (5.8j) and (5.8k). As can be seen the SDR method offers neither rank one nor constant modulus solution. Since in the initial step (SDR) we drop the constraints (5.8j) and (5.8k), we do not have lower bound or equality energy constraints on variable $\mathbf{S}$. By considering those two constraints (which are equivalent to (5h) constraint) in the next steps of the algorithm, we indeed impose the $\mathbf{X}_n = \bar{\mathbf{s}}_n \bar{\mathbf{s}}_n^{\dagger}$ constraints. On the other side we have the $\mathbf{Diag}\,\mathbf{X}_n = \mathbf{1}_M$ constraint which force the $\mathbf{S}$ variable to be constant modulus. Therefore in the first iteration the magnitude of the sequence in Figure 5.1c is close to zero.

5.4.2 Performance

Figure 5.2 compares the performance of the proposed method in terms of beampattern shaping and spectral masking with UNIQUE [37] method in spatial-ISLR minimization mode ($\eta = 1$) as a benchmark. Figure 5.2a shows the beampattern response of the proposed method and UNIQUE. In this figure, for fair comparison we drop the spectral masking (5.8f) and 3 dB main beam-width (5.8c) and (5.8d) constraints. As can be seen, in this case the proposed method offers almost similar performance (in some undesired

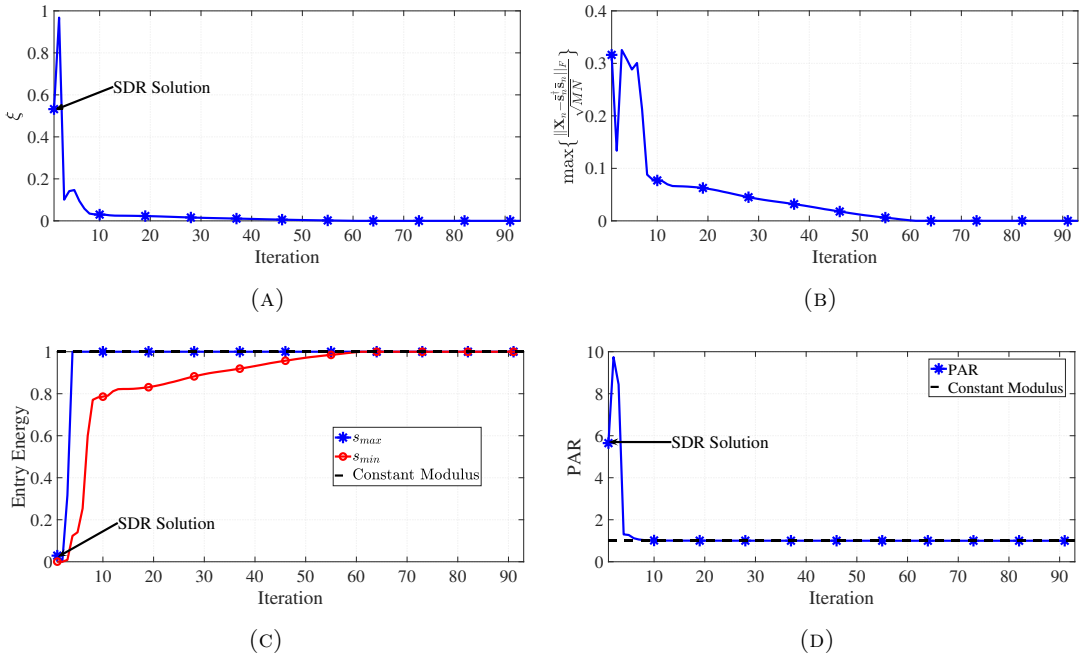

FIGURE 5.1: The convergence behavior of proposed method in different aspects, (a) $\xi = \frac{\max\{\xi_{n,2}\}}{\min\{\xi_{n,1}\}}$, (b) Constant modulus, (c) $\max\left\{\left\|\mathbf{X}_n - \mathbf{s}_n^{\dagger}\mathbf{s}_n\right\|_F\right\}$ and (d) PAR ($M = 8$, $N = 64$, $\hat{N} = 5N$, $\delta = 2$, $\Theta_d = [-55^o, -35^o]$, $\Theta_u = [-90^o, -60^o] \cup [-30^o, 90^o]$, $\mathcal{U} = [0.12, 0.14] \cup [0.3, 0.35] \cup [0.7, 0.8]$ and $\gamma = 0.01\sqrt{\hat{N}}$).

angles deeper nulls) as compared to UNIQUE method. However, considering the spectral masking (5.8f) and 3 dB main beam-width (5.8c) and (5.8d) constraints, the proposed method is able to steer the beam towards the desired and steer the nulls at undesired angles simultaneously.

The beampattern response of WISE at desired angles region and the spectrum response of the proposed method has better performance comparing to UNIQUE method. Figure 5.2b shows the main beam-width response of the proposed method and UNIQUE. Since UNIQUE does not have the 3 dB main beam-width constraint, it does not have a good main beam-width response. However, the 3 dB main beam-width constraint incorporated in our framework improves the main beam-width response. Besides, the maximum beampattern response is located at -45^o in the proposed method while there is a deviation in UNIQUE method. On the other hand Figure 5.2c shows the spectrum response of the proposed method. Observe that the waveform obtained by WISE masks the the spectral power in the stop-bands region ($\mathcal{U}$) below the γ value. However, since UNIQUE method is not spectral compatible, is unable to put notches on the stop-bands. Furthermore, as can be seen the spectral of the transmitters in UNIQUE are the same. On the other words in order to obtain a good beampattern response, the UNIQUE offers high correlated waveforms. This shows the contradiction of the steering beampattern with orthogonality.

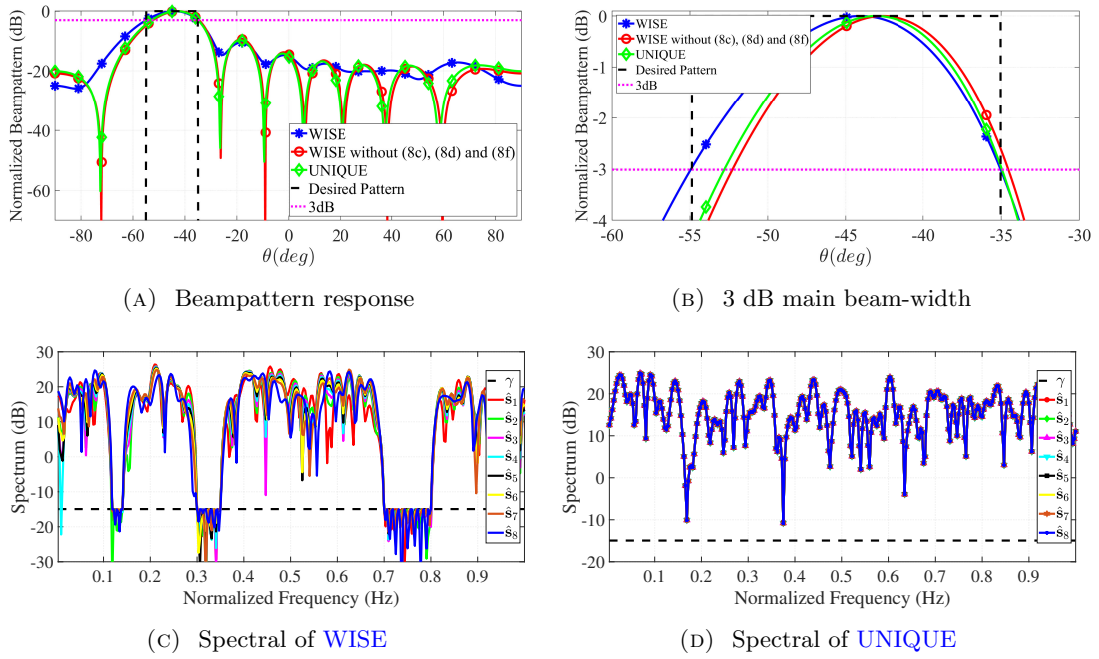

(A) Beampattern response

(B) 3 dB main beam-width

(C) Spectral of WISE

(D) Spectral of UNIQUE

FIGURE 5.2: Comparing the performance of WISE and UNIQUE methods in several aspects ($M = 8$, $N = 64$, $\hat{N} = 5N$, $\delta = 2$, $\Theta_d = [-55^o, -35^o]$, $\Theta_u = [-90^o, -60^o] \cup [-30^o, 90^o]$, $\mathcal{U} = [0.3, 0.35] \cup [0.4, 0.55] \cup [0.7, 0.85]$ and $\gamma = 0.01\sqrt{N}$).

5.4.3 The impact of similarity parameter

In this subsection, we evaluate the impact of choosing the similarity parameter δ on performance of the proposed method. When we consider the maximum admissible value for similarity parameter, i.e., $\delta = 2$, we do not include similarity constraint and by decreasing δ we have the degree of freedom to enforce properties similar to the reference waveform on the optimal waveform. As mentioned in section 5.4, we consider $\mathbf{S}_0$ be a set of sequences with a good range-ISLR property as the reference signal for similarity constraint, which is obtained by UNIQUE method [37]. Therefore, by decreasing the δ we obtain a waveform with good orthogonality, which leads to omni directional beampattern.

Figure 5.3 shows the beampattern response of the proposed method with different values of δ. As can be seen, with $\delta = 2$, yields an optimized beampattern and by decreasing δ the beampattern gradually tends to be omnidirectional.

On the other hand, Figure 5.4a, Figure 5.4c and Figure 5.4e show the correlation level of the 4^{th} transmitter of the proposed method with others transmitters with different values of δ. Observe that with $\delta = 2$ we a obtain fully correlated waveform and by decreasing δ the waveform gradually becomes uncorrelated. Therefore, having simultaneous beampattern shaping and orthogonality are contradictory, and the choice of δ effects a trade-off between the two and enhance the performance of radar system [37]. Besides Figure 5.4b, Figure 5.4d and Figure 5.4f show the spectrum of the proposed

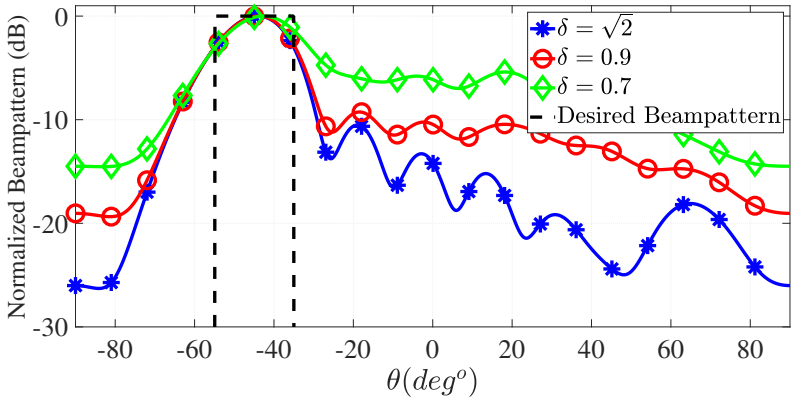

FIGURE 5.3: The impact of choosing δ in the proposed method on Beampattern response ($M = 8$, $N = 64$, $\hat{N} = 5N$, $\Theta_d = [-55^o, -35^o]$ and $\Theta_u = [-90^o, -60^o] \cup [-30^o, 90^o]$, $\mathcal{U} = [0.12, 0.14] \cup [0.3, 0.35] \cup [0.7, 0.8]$ and $\gamma = 0.01\sqrt{\hat{N}}$).

method with different values of δ. As can be seen in all cases the proposed method is able to perform the spectral masking. Furthermore observe that, in the desired frequency region (for instance in the region $[0.36, .069]$), when $\delta = 2$, the spectral responses of the transmitter waveforms are more similar than lower values of δ. This observation verifies that, the more similar spectral response leads to more obtain more correlated waveforms.

5.4.4 The impact of $\hat{N}$

Figure 5.5 shows the impact of choosing $\hat{N}$ on spectral response of the proposed method. In this figure we indicate the DFT points as N_{fft}. Figure 5.5a shows the spectrum response of WISE when we do not have zero padding ($\hat{N} = N$) and $N_{fft} = N$. In this case, the proposed method is able to mask the spectral response on undesired frequencies. When we increase the DFT point to $N_{fft} = 5N$, some spikes are appeared on $\mathcal{U}$ region (please see Figure 5.5b). However, as can be seen from Figure 5.5c and Figure 5.5d, when we apply the zero padding to $\hat{N} = 5N$, the proposed method is able to mask the spectral response on undesired frequencies for both $N_{fft} = 5N$ and $N_{fft} = 10N$ respectively.

5.4.5 The impact of Constant modulus in the IF band

In order to transmit the baseband waveform in radar system, it needs to be translated to Intermediate Frequency (IF) band. In this regards, in the first step the waveform passes through DUC to increase the sample rate and provide a real signal. Then the output of DUC passes through the DAC to generate the analog signal. Finally the analog signal passes the PA to do the amplification and become ready for next up-converting to the

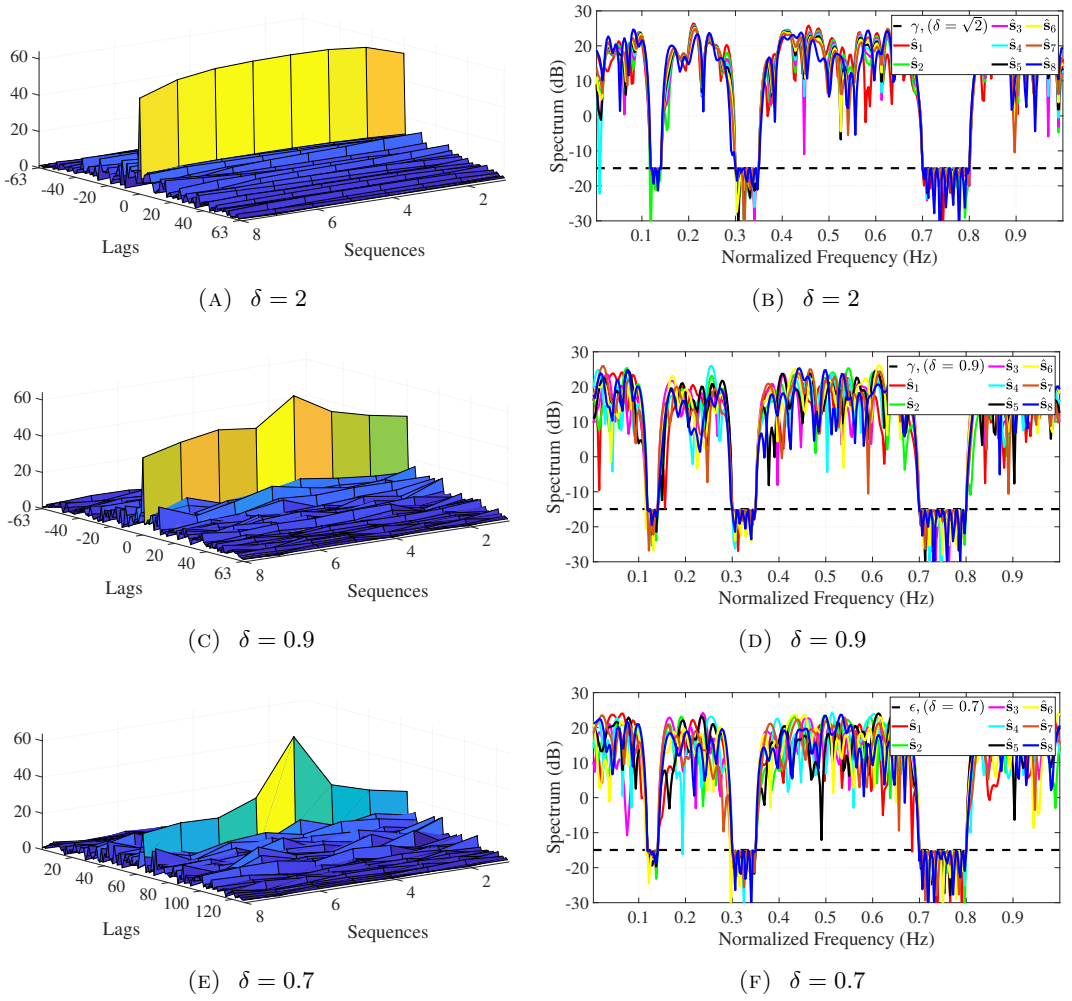

(A) $\delta = 2$ (B) $\delta = 2$

(C) $\delta = 0.9$ (D) $\delta = 0.9$

(E) $\delta = 0.7$ (F) $\delta = 0.7$

FIGURE 5.4: The impact of choosing δ on correlation level and spectral masking ($M = 8$, $N = 64$, $\hat{N} = 5N$, $\Theta_d = [-55^o, -35^o]$ and $\Theta_u = [-90^o, -60^o] \cup [-30^o, 90^o]$, $\mathcal{U} = [0.12, 0.14] \cup [0.3, 0.35] \cup [0.7, 0.8]$ and $\gamma = 0.01\sqrt{\hat{N}}$).

RF frequency. In this subsection we aim to evaluate the performance of the proposed method from the baseband till the PA.

In this regards, Figure 5.6a depicts the normalized constellation of the optimized waveforms obtained by two proposed methods in this chapter; say WISE and SDR. We pass these two optimized waveforms through DUC to obtain IF band in digital domain. Figure 5.6b compares the power level of the optimized waveforms obtained by WISE and SDR after DUC when the reference signal in similarity constraint was randomly chosen in 100 trials. In this figure, P_{WISE}, $\bar{P}_{WISE}$, σ_{WISE}, P_{SDR}, $\bar{P}_{SDR}$ and σ_{SDR} denotes the instant, mean and standard deviation of the power of WISE and SDR respectively. We normalized the maximum output power of DUC of the both waveforms to 30 dB. Besides, we assume the following setup,

- Signal bandwidth: $BW_s = 1MHz$.

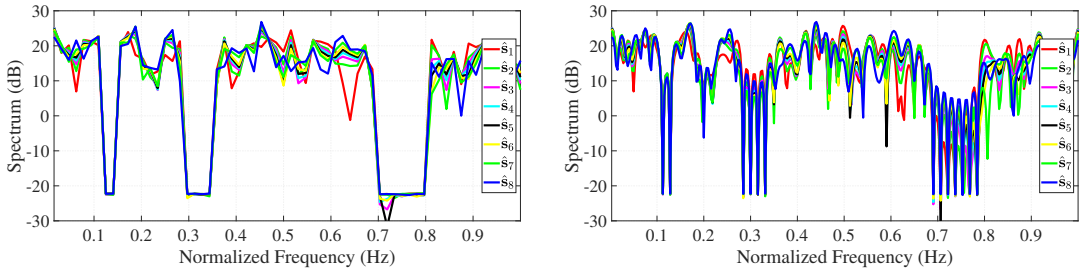

(A) ($\hat{N} = N$ and $N_{fft} = N$)

(B) $\hat{N} = N$ and $N_{fft} = 5N$

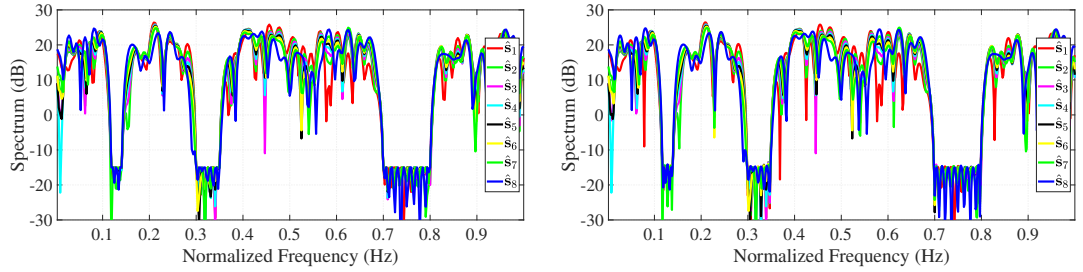

(C) $\hat{N} = 5N$ and $N_{fft} = 5N$

(D) $\hat{N} = 5N$ and $N_{fft} = 10N$

FIGURE 5.5: The impact of choosing $\hat{V}$ and N_{fft} on spectral response ($M = 8$, $N = 64$, $\Theta_d = [-55^o, -35^o]$ and $\Theta_u = [-90^o, -60^o] \cup [-30^o, 90^o]$, $\mathcal{U} = [0.12, 0.14] \cup [0.3, 0.35] \cup [0.7, 0.8]$ and $\gamma = 0.01\sqrt{\hat{N}}$).

- Sample rate: $f_s = 6MHz$.
- Interpolation factor: $N_{int} = 25$.
- Center frequency: $f_c = 50MHz$.
- Filter bandwidth: $BW_s = 2MHz$.

Based on this figure, two important facts can be concluded,

1. WISE offers higher average power rather than SDR waveform.
2. The standard deviation of WISE is less that SDR waveform.

The DUC output passes the DAC to convert the IF digital signal to analog domain. Subsequently it passes through the PA. In order to utilize the maximum power efficiency the input power of PA should be constant as much as possible [159] (see Appendix D.2). Hence, the Constant Modulus (CM) waveform is attractive for radar designers since they can drive the PAs at their maximum efficiency.

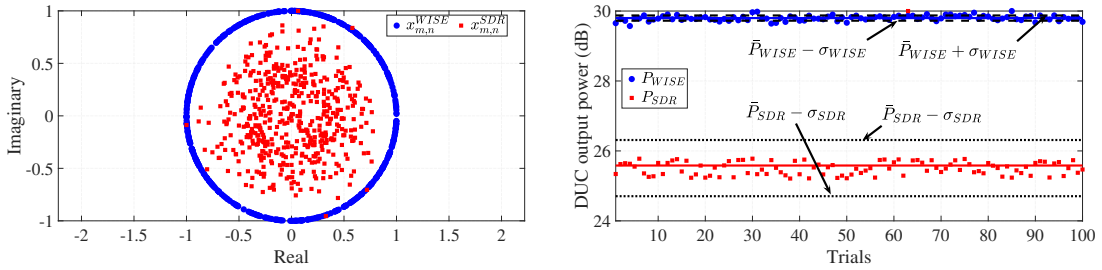

(A) ($\hat{N} = N$ and $N_{fft} = N$) (B) $\hat{N} = N$ and $N_{fft} = 5N$

FIGURE 5.6: Comparing the performance of WISE and SDR methods (a) Constellation (b) Power of the WISE and SDR after DUC for 100 number of trials ($M = 8$, $N = 64$, $\hat{N} = N$, $\delta = 2$, $\Theta_d = [-55^o, -35^o]$, $\Theta_u = [-90^o, -60^o] \cup [-30^o, 90^o]$, $\mathcal{U} = [0.3, 0.4]$ and $\gamma = 0.01\sqrt{\hat{N}}$).

5.4.6 Conclusion

In this chapter we discuss about the problem of beampattern shaping with practical constraints in MIMO radar systems namely, spectral masking, 3 dB beam-width, constant modulus and similarity constraints. Solving this problem, not considered hitherto, enables us to control the performance of MIMO radar in three domains namely, spatial, spectral and orthogonality (by similarity constraints). Accordingly, we consider a waveform design approach for beampattern shaping optimization problem under. The aforementioned problem leads to a non-convex and NP-hard optimization problem. In order to obtain a local optimum solution of the problem, first by introducing a slack variable we convert the optimization problem to a linear problem with a rank one constraint. Then to tackle the the we proposed an iterative method to obtain the rank one solution. Numerical results shows that the proposed method is able to manage the resources efficiently to obtain the best performance.

Chapter 6

SINR Maximization in Radar Systems

In this chapter we address the SINR maximization under discrete phase constraint in SISO radar system. To this end, we deal with general signal-dependent interfering scenario and devise an optimization procedure leading to sub-optimal solutions. Specifically, we focus on the joint waveform and the receive Doppler filter bank. We discuss two optimization approaches in this context. In the former, we assume that the target Doppler frequency is unknown and the worst-case SINR at the output of the filter bank as the design metric. To this end, we propose an CD-based iterative algorithm to design MPSK waveform. In the latter, we assume that the Doppler of the target is known and we consider to maximize the SINR of that specific Doppler. We propose an iterative ADMM-based method to solve the problem, where we obtain a closed form solution for the filter and we utilize CD method to design the waveform. We demonstrate the proposed approaches' performance and compare that to the state of the art using numerical results.

6.1 Designing MPSK Sequences and Doppler Filter Bank in Cognitive Radar Systems

Cognitive transmission is an emerging technique in the next-generation radar systems, where new levels of radar performance are needed. A cognitive radar system can design and transmit a waveform that adapts to the environment and provides a flexible framework with different trade-offs between a variety of performance objectives, including target detection [11]. In this context, the SINR at the receive side of every radar system determines the detection performance. Enhancing the SINR, therefore, improves the reliability of the radar system.

Enhancing the SINR through radar waveform design and Doppler filter banks is discussed in recent works [160, 161]. The authors in [160] consider the maximization of the minimum SINR at the output of a Doppler filter bank as the design metric under similarity (to other waveforms) and energy constraints. Similarity constraint can control some signal properties such as Doppler resolution, ISL and PSL. The problem leads to a non-convex optimization formulation which they tackle it with the GFP method based on Dinkelbach algorithm [162]. Subsequently, the design scope is enhanced to include the constant modulus sequences under budget energy and PAR constraint [161]. Authors in [161] represent ℓ_2-norm and ℓ_∞-norm for the energy budget and PAR level constraint, respectively. They propose two algorithms based on the Majorization Minimization or Minorization Maximization (MM) [163] to solve the problem.

Unimodular sequences is an important criterion in two aspects, first from the point of view of hardware implementation and second to allow for full utilization of the transmitter power. In order to achieve the best detection probability, radar systems generally transmit the signal with the maximum power. On the other hand, the maximum power of a radar transmitter is usually constant and unimodular sequences exploit this to output all sequences with maximum power. Therefore from the point of view of radar transmitter efficiency, unimodular sequences are attractive. In addition, in order to control the sidelobe levels of the phase changing points, discrete phase sequences whose phases are chosen from a small size alphabet, are typically preferred [78].

In this section, we tackle a problem similar to that addressed in [160, 161] under a more practically attractive constraint, namely the use of discrete phase MPSK sequences. We propose a method which is able to design MPSK sequences, to maximize the minimum SINR over a Doppler filter bank at the receiver under the assumption of unknown target Doppler shift and signal-dependent interference. Building on this method, the section presents a joint design of MPSK waveform and receiver Doppler filter bank to enhance worst case SINR in target Doppler domain. This approach leads to a multivariable, non-convex min-max optimization problem. Towards solving this, we propose an alternative algorithm based on CD framework [24, 102]. To this end, we sequentially optimize the objective function over one variable, keeping fixed the others.

We organized this section as follows. In subsection 6.1.1, we introduce the system model and problem statement, respectively. Subsection 6.1.2 presents the proposed CD based framework whose performance is numerically assessed in subsection 6.1.3.

6.1.1 System Model and Problem Statement

Let us assume a monostatic radar system which coherently transmits N pulses in the slow-time, each pulse denoted by s_i, $i = 1, \ldots, N$. The reflected signal from a moving target with the unknown-Doppler frequency f_{d_T} in a Coherent Pulse Interval (CPI) is contaminated by signal-independent interference (noise) and signal-dependent interference (clutter). For a given range gate, this signal can be written as [164],

$$\boldsymbol{r} = \alpha_R \boldsymbol{s} \odot \boldsymbol{v}(f_{d_T}) + \boldsymbol{r}_c + \boldsymbol{r}_n, \tag{6.1}$$

where α_R is proportional to the RCS of the target and free space path loss, $\boldsymbol{v}(f_{d_T})$ is the target steering vector which can be expressed as,

$$\boldsymbol{v}(f_{d_T}) = [1, e^{j2\pi f_{d_T}}, \ldots, e^{j2\pi(N-1)f_{d_T}}]^T \in \mathbb{C}^N. \tag{6.2}$$

In (6.2) f_{d_T} is the unknown target Doppler shift, and $\boldsymbol{r}_c$, $\boldsymbol{r}_n \in \mathbb{C}^N$ are signal-dependent and signal-independent interference, respectively.

6.1.1.1 Interference Model

In (6.1) the vector $\boldsymbol{r}_n$ is related to thermal noise which is modelled as zero-mean white Gaussian noise ($\mathbb{E}[\boldsymbol{r}_n] = 0$) and with autocorrelation matrix of $\mathbb{E}\left[\boldsymbol{r}_n \boldsymbol{r}_n{}^\dagger\right] = \boldsymbol{R}_n = \sigma_n^2 \boldsymbol{I}$. The vector $\boldsymbol{r}_c$ is related to the superposition of reflected signal from different uncorrelated scatterers and can be expressed as [160],

$$\boldsymbol{r}_c = \sum_{r=0}^{N_r} \sum_{l=0}^{N_a} \alpha_{(r,l)} \boldsymbol{J}_r \left(\boldsymbol{s} \odot \boldsymbol{v}(f_{d_{(r,l)}}) \right). \tag{6.3}$$

In (6.3) N_r and N_a are the numbers of the range-bin and azimuth-bin of clutter patches, $\alpha_{(r,l)}$ and $f_{d_{(r,l)}}$ are the received scatterer power and shift Doppler of the scatterer in r^{th} range and l^{th} azimuth bin, respectively and $\boldsymbol{J}_r$ denotes the shift matrix.

$$\boldsymbol{J}_r(p,q) = \begin{cases} 1 & p - q = r \\ 0 & p - q \neq r \end{cases} \qquad (p,q) \in \{1, \ldots, N\}^2.$$

From a statistical point of view, the mean RCS of each clutter patch is $\mathbb{E}\left[|\alpha(r,l)|^2\right] = \sigma^2_{(r,l)}$. The Doppler shift is uniformly distributed in the interval $f_{d_{(r,l)}} \in \left[\bar{f}_{d_{(r,l)}} - \frac{\epsilon_{d_{(r,l)}}}{2}, \bar{f}_{d_{(r,l)}} + \frac{\epsilon_{d_{(r,l)}}}{2}\right]$, where $\bar{f}_{d_{(r,l)}}$ and $\epsilon_{(r,l)}$ are the mean and variance shift Doppler of each clutter patch,

respectively. The covariance matrix of $\boldsymbol{r}_c$ can be expressed as [160],

$$\boldsymbol{R}_c(\boldsymbol{s}) = \mathbb{E}\left[\boldsymbol{r}_c \boldsymbol{r}_c{}^{\dagger}\right] = \sum_{r=0}^{N_r}\sum_{l=0}^{N_a} \sigma^2_{(r,l)} \boldsymbol{J}_r \boldsymbol{\Xi}\left(\boldsymbol{s},(r,l)\right)\boldsymbol{J}_r^{\dagger}, \tag{6.4}$$

where $\boldsymbol{\Xi}\left(\boldsymbol{s},(r,l)\right) = \mathbf{Diag}\left\{\boldsymbol{s}\right\}\boldsymbol{\Upsilon}^{\bar{f}_{d_{(r,l)}}}_{\epsilon_{d_{(r,l)}}}\mathbf{Diag}\left\{\boldsymbol{s}\right\}^{\dagger}$ and $\boldsymbol{\Upsilon}^{\bar{f}_{d_{(r,l)}}}_{\epsilon_{d_{(r,l)}}}$ is the covariance matrix of clutter steering vector $\left(\boldsymbol{v}(f_{d_{(r,l)}})\right)$ taking the form,

$$\boldsymbol{\Upsilon}^{\bar{f}_{d_{(r,l)}}}_{\epsilon_{(r,l)}}(p,q) = e^{j2\pi\bar{f}_{d_{(r,l)}}(p-q)}\frac{sin[\pi\epsilon_{(r,l)}(p-q)]}{\pi\epsilon_{(r,l)}(p-q)}.$$

6.1.1.2 SINR Formulation

The SINR at the output of k^{th} filter bank can be expressed as,

$$\mathrm{SINR}_k = \frac{|\alpha_R|^2\left|\boldsymbol{w}_k^{\dagger}\left(\boldsymbol{s}\odot\boldsymbol{v}(f^k_{d_T})\right)\right|^2}{\boldsymbol{w}_k^{\dagger}\boldsymbol{R}_c(\boldsymbol{s})\boldsymbol{w}_k + \boldsymbol{w}_k^{\dagger}\boldsymbol{R}_n\boldsymbol{w}_k}, \tag{6.5}$$

where $\boldsymbol{R}_c(\boldsymbol{s})$, $\boldsymbol{R}_n$ and $\boldsymbol{w}_k$ are the covariance matrices of clutter, noise and the coefficients of k^{th} filter, respectively.

The value of SINR is related to the statistical characterization of interference, and their knowledge is vital to optimized designs. As to the clutter it is necessary to measure the statistical parameter, such as $\sigma^2_{(r,l)}$, $\bar{f}_{d_{(r,l)}}$ and $\epsilon_{(r,l)}$. Cognitive radar is a system which estimates these parameters by interactions with the surrounding environment, using dynamic database and some clutter models [164]. In this regard, we consider using cognitive radar to derive the clutter statistical parameters.

6.1.1.3 Problem Statement

We assume a bank of K filters, each tuned to a specific Doppler shift to reveal the target radial velocity (see [160] for more details). In such a case, a relevant design metric is the maximization of the minimum SINR over the filter bank outputs [160, 161], i.e.,

$$\max_{\boldsymbol{s},\boldsymbol{w}_1,\ldots,\boldsymbol{w}_K} \min_{k=1,\ldots,K} \mathrm{SINR}_k \tag{6.6}$$

where $\boldsymbol{w}_k \in \mathbb{C}^N$ indicates the k^{th} filter coefficients tuned at Doppler shift f_d^k. If the filter bank covers the entire region of Doppler shifts, the worst case SINR is then related to signal-dependent interference (clutter) Doppler region. In this situation, maximizing the worst case SINR is not attractive since Doppler filter is not efficient for clutter processing

[160]. Hence many radar systems use other effective procedure to tackle this problem, such as Moving Target Indicator (MTI) and cluttering map. Consequently, we design the filter bank such that it doesn't overlap with the domain of considered clutter Doppler shifts.

Let us define,

$$\boldsymbol{\Omega}_M = \{\boldsymbol{s} | s_i \in \boldsymbol{\Psi}_M, i = 1, \ldots, N\}, \tag{6.7}$$

and $\boldsymbol{\Psi}_M = \{1, e^{j\frac{2\pi}{M}}, e^{j\frac{4\pi}{M}}, \ldots, e^{j\frac{2(M-1)\pi}{M}}\}$, where M is the alphabet size. The constrained optimization problem can be formulated as,

$$\begin{array}{ll} \max\limits_{\boldsymbol{s}, \boldsymbol{w}_1, \ldots, \boldsymbol{w}_K} & \min\limits_{k=1,\ldots,K} \text{SINR}_k \\ \text{s.t.} & \boldsymbol{s} \in \boldsymbol{\Omega}_M \end{array}. \tag{6.8}$$

This is a multi-variable non-convex constrained optimization and a sub-optimal approach to solving this is presented next.

6.1.2 Joint MPSK And Doppler filter bank design

A viable means to jointly design Doppler filter bank and the transmit sequence is to maximize the SINR output in the worse case [160, 161], i.e.,

$$\mathcal{P} = \begin{cases} \max\limits_{\boldsymbol{s}, \boldsymbol{w}_1, \ldots, \boldsymbol{w}_K} & \min\limits_{k=1,\ldots,K} \dfrac{|\alpha_R|^2 \left| \boldsymbol{w}_k^\dagger \left(\boldsymbol{s} \odot \boldsymbol{v}(f_{d_T}^k) \right) \right|^2}{\boldsymbol{w}_k^\dagger \boldsymbol{R}_c(s) \boldsymbol{w}_k + \boldsymbol{w}_k^\dagger \boldsymbol{R}_n \boldsymbol{w}_k} \\ \text{s.t.} & \boldsymbol{s} \in \boldsymbol{\Omega}_M \end{cases}, \tag{6.9}$$

which is a max-min non-convex constrained optimization problem. Note that the Doppler frequencies are considered outside the domain of clutter Doppler. Alternative optimization is a general framework to tackle this family of problems, where the optimization problem can be alternatively solved [92]. In particular, let the worst case SINR at step (n) be defined as,

$$h\left(\boldsymbol{s}^{(n)}, \boldsymbol{W}^{(n)}\right) = \min_{k=1,\ldots,K} \frac{|\alpha_R|^2 \left| \boldsymbol{w}_k^\dagger \left(\boldsymbol{s}^{(n)} \odot \boldsymbol{v}(f_{d_T}^k) \right) \right|^2}{\boldsymbol{w}_k^{(n)\dagger} \left[\boldsymbol{R}_c\left(\boldsymbol{s}^{(n)}\right) + \boldsymbol{R}_n \right] \boldsymbol{w}_k^{(n)}}, \tag{6.10}$$

where $\boldsymbol{W} \triangleq \left[\boldsymbol{w}_1^{(n)} | \boldsymbol{w}_2^{(n)} | \ldots | \boldsymbol{w}_K^{(n)} \right]$ denotes the matrix of filter bank coefficients. We alternatively tackle the following problems of sequence design given a filter bank ($\mathcal{P}_{\boldsymbol{s}^{(n)}}$) and design of a filter bank given a MPSK sequence ($\mathcal{P}_{\boldsymbol{w}^{(n)}}$),

$$\mathcal{P}_{\boldsymbol{s}^{(n)}} = \begin{cases} \max\limits_{\boldsymbol{s}} & h\left(\boldsymbol{s}^{(n-1)}, \boldsymbol{W}^{(n)}\right) \\ \text{s.t.} & \boldsymbol{s} \in \boldsymbol{\Omega}_M \end{cases}, \tag{6.11}$$

and,

$$\mathcal{P}_{\boldsymbol{w}}{}^{(n)} = \begin{cases} \max\limits_{\boldsymbol{w}_1,\ldots,\boldsymbol{w}_K} & h\left(\boldsymbol{s}^{(n)}, \boldsymbol{W}^{(n)}\right) . \end{cases} \tag{6.12}$$

Notice that, (6.12) is the well-known Minimum Variance Distortionless Response (MVDR) problem [165], and its solution can be directly obtained as [160, 161],

$$\boldsymbol{w}_k^{(n)} = \frac{(\boldsymbol{R}_c(\boldsymbol{s}^{(n)}) + \boldsymbol{R}_n)^{-1}\left(\boldsymbol{s}^{(n)} \odot \boldsymbol{v}(f_{d_T}^k)\right)}{\|(\boldsymbol{R}_c(\boldsymbol{s}^{(n)}) + \boldsymbol{R}_n)^{-1/2}\left(\boldsymbol{s}^{(n)} \odot \boldsymbol{v}(f_{d_T}^k)\right)\|^2}. \tag{6.13}$$

To tackle Problem $\mathcal{P}_{\boldsymbol{s}}{}^{(n)}$, instead of designing the entire vector $\boldsymbol{s}$, we consider designing it's entries consecutively. CD framework enables such an optimization by assuming one entry of the code vector $\boldsymbol{s} \in \mathbb{C}^N$ as the variable and keeping the others fixed. Subsequently, by examining all possible alphabet of MPSK for the chosen variable, we select the alphabet which leads to the best SINR [78].

Therefore to solve problem $\mathcal{P}_{\boldsymbol{s}}{}^{(n)}$, we propose Algorithm 10 to optimize all N pulses. In this algorithm we assume that the optimum entry, $s_d^\star$, the corresponding optimum filters, $\boldsymbol{W}_d^\star$, can be derived from the knowledge of the other using the CD framework, details of which will be presented later. Algorithm 10 optimizes the vector $\boldsymbol{s}$ entry by entry until all N pulses become optimized at least once. After optimizing the N^{th} pulse, the algorithm examines the convergence metric for the worst case SINR. The algorithm repeats the aforementioned steps if the stopping criteria is not met. We consider $\left(\text{SINR}_{\text{worst}}^{(n)} - \text{SINR}_{\text{worst}}^{(n-N)}\right) < \zeta$ for stopping criterion of optimization, where ζ, $\text{SINR}_{\text{worst}}^{(n)}$ and $\text{SINR}_{\text{worst}}^{(n-N)}$ are a positive threshold, the worst case of SINR in step n and step $n-N$, respectively.

To illustrate CD framework let us assume that s_d is the d^{th} transmitted pulse ($d = 1,\ldots,N$) and is the only variable, while the other $N-1$ entries are fixed; these are stacked into the $\boldsymbol{s}_{-d}$ vector as,

$$\boldsymbol{s}_{-d} = [s_1,\ldots,s_{d-1},s_{d+1},\ldots,s_N]^T \in \mathbb{C}^{N-1}. \tag{6.14}$$

The design Problem $\mathcal{P}_{\boldsymbol{s}}{}^{(n)}$ with respect to the variable s_d can be expressed as,

$$\mathcal{P}_{s_d}^{(n)} = \begin{cases} \max\limits_{s_d} & h\left(s_d, \boldsymbol{s}_{-d}, \boldsymbol{W}^{(n)}\right) \\ \text{s.t.} & s_d \in \boldsymbol{\Omega}_M \end{cases}, \tag{6.15}$$

which is still a non-convex constrained max-min optimization problem; however, unlike the earlier formulation, it involves only one variable. Towards solving this, we calculate the worst case SINR across the filter bank using (6.10) for each possible alphabet of s_d

Algorithm 10 : Joint waveform and filter bank design

Input: Initial waveform $\boldsymbol{s}^{(0)} | s_i \in \boldsymbol{\Psi}_M, i = 1, \ldots, N$
Output: Optimized waveform $\boldsymbol{s}^{\star}$ and filter bank $\boldsymbol{w}_k^{\star}$

1. **Initialization**.
   - Set $n := 0$, $\boldsymbol{s} := \boldsymbol{s}^{(n)}$ and $d := 1$;
   - Obtain $\boldsymbol{R}_c(\boldsymbol{s}^{(0)})$ from Eq (6.4)
   - Obtain $\boldsymbol{W}^{(0)}$ from Eq (6.13)
   - $\text{SINR}_{\text{worst}}^{(0)} = h\left(\boldsymbol{s}^{(0)}, \boldsymbol{W}^{(0)}\right)$
2. **Optimization**.
   - $n := n + 1$
   - Obtain $s_d^{\star}$, $\boldsymbol{W}_d^{\star}$ and $\text{SINR}_{\text{d,worst}}^{\star}$ from CD framework (see below)
   - $\boldsymbol{s}^{(n)} = \left[s_1^{(n-1)}, \ldots, s_d^{\star}, \ldots, s_N^{(n-1)}\right]^T$
   - $\boldsymbol{W}^{(n)} = \boldsymbol{W}_d^{\star}$
   - $\text{SINR}_{\text{worst}}^{(n)} = \text{SINR}_{\text{d,worst}}^{\star}$
   - if $d = N$ then go to 3); otherwise $d := d + 1$ and go to 2);
3. **Stopping Criterion**.
   - If $\left(\text{SINR}_{\text{worst}}^{(n)} - \text{SINR}_{\text{worst}}^{(n-N)}\right) < \zeta$, go to 4); otherwise $d := 1$ and go to 2);
4. **Output**.
   - Set $\boldsymbol{s}^{\star} = \boldsymbol{s}^{(n)}$ and $\boldsymbol{W}^{\star} = \boldsymbol{W}^{(n)}$

and choose the one that results in the best minimum SINR. In the next step, we perform this procedure for the next pulse (s_{d+1}) and the process is repeated till all pulses are optimized at least once. This optimization procedure is shown in (6.16) for vector $\boldsymbol{s}$.

$$
\begin{aligned}
s_1^{\star(n-d+1)} &= \arg\max_{s_1} \; h\left(s_1, \boldsymbol{s}_{-1}^{(n-d)}, \boldsymbol{W}^{(n-d)}\right) \\
s_2^{\star(n-d+2)} &= \arg\max_{s_2} \; h\left(s_2, \boldsymbol{s}_{-2}^{(n-d+1)}, \boldsymbol{W}^{(n-d+1)}\right) \\
&\vdots \\
s_d^{\star(n)} &= \arg\max_{s_d} \; h\left(s_d, \boldsymbol{s}_{-d}^{(n-1)}, \boldsymbol{W}^{(n-1)}\right) \\
&\vdots \\
s_N^{\star(n+N-d)} &= \arg\max_{s_N} \; h\left(s_N, \boldsymbol{s}_{-N}^{(n+N-d-1)}, \boldsymbol{W}^{(n+N-d-1)}\right),
\end{aligned}
\tag{6.16}
$$

CD framework

Input: Optimized waveform at step $n-1$ ($\boldsymbol{s}^{(n-1)}$), alphabet size M and pulse index d
Output: Optimum code ($s_d^\star$), optimum filter bank coefficients ($\boldsymbol{W}^\star$) and optimum worst case SINR ($\text{SINR}^\star_{\text{worst}}$)

1. **Initialization**.
   - set set $i := 1$ and $\boldsymbol{s} := \boldsymbol{s}^{(n-1)}$
2. **Optimization**.
   - $s_d = e^{j\frac{j2\pi(i-1)}{M}}$
   - $\boldsymbol{s} = [s_1, \ldots, s_d, \ldots, s_N]^T$
   - Obtain $\boldsymbol{R}_c(\boldsymbol{s})$ from Eq (6.4)
   - Obtain $\boldsymbol{W}$ from Eq (6.13) and $\boldsymbol{W}_i = \boldsymbol{W}$
   - $h_i = h\left(\boldsymbol{s}, \boldsymbol{W}_i\right)$
   - if $i = M$ go to 3); otherwise $i := i + 1$ and go to 2);
3. **Output**.
   - $m = \arg \max_{i=1,\ldots,M} \left\{h_i\right\}$
   - $s_d^\star = e^{j\frac{j2\pi(m-1)}{M}}$
   - $\boldsymbol{W}_d^\star = \boldsymbol{W}_m$
   - $\text{SINR}^\star_{\text{d,worst}} = h_m$

where $s_d^{\star(n)}$ denotes the optimum value of s_d at the step n of the optimization procedure. Therefore the optimized vector $\boldsymbol{s}$ can be obtained by,

$$\boldsymbol{s}^{(n)} = [s_1^{(n-1)}, \ldots, s_{d-1}^{(n-1)}, s_d^{\star(n)}, s_{d+1}^{(n-1)}, \ldots, s_N^{(n-1)}]^T. \tag{6.17}$$

Based on the aforementioned discussion, we propose CD framework waveform design to derive optimum $s_d^\star$ under the assumption of signal-dependent interference. Due to the iterative improvement, this framework guarantees that the worst case SINR converges to the local optimum value.

6.1.3 Performance Analysis

In this subsection, we provide some numerical examples to illustrate the effectiveness of the proposed method. Towards this end, unless otherwise explicitly stated, we consider the following assumptions. Note that all Doppler shift are normalized to PRF.

Waveform Parameters For the waveform characteristic, we consider a coherent stationary radar transmitting a burst of $N = 32$ pulses, while the alphabet size of the MPSK sequence is assuming $M = 8$. The energy transmitted is $e_s = \| s \|^2$. Besides, we consider a random alphabet MPSK sequence for the initial waveform.

Interference Parameters A white Gaussian noise is considered with $\sigma_n^2 = 1$. For signal-dependent interference (clutter) we assume $N_r = 2$ as interfering range rings, and $N_a = 100$ as azimuth sectors. We consider a homogeneous clutter which means $\sigma_{(r,l)}^2 = \sigma^2; \quad r \in \{1, \ldots, N_r\}, l \in \{1, \ldots, N_a\}$. The CNR can be calculated by [166],

$$\text{CNR} = \frac{\sigma_{(r,l)}^2}{\sigma_n^2} e_s,$$

which is adjusted to be equal to 30 dB. The normalized mean and variance shift Doppler are $\bar{f}_{d_{(r,l)}} = 0$ Hz and $\epsilon_{(r,l)} = 0.13$ Hz, respectively. Therefore the Doppler shifts of the clutter scatterers are uniformly distributed over the interval $\Omega_c = [\bar{f}_d - \frac{\epsilon}{2}, \bar{f}_d + \frac{\epsilon}{2}] = [-0.065, 0.065]$.

Target Parameters The SNR of received signal is [166],

$$\text{SNR} = \frac{|\alpha_R|^2}{\sigma_n^2} e_s.$$

which is adjusted to be 10 dB. In addition, we assume that the normalized target Doppler shift belongs to the interval $\Omega_T = [-0.5, -0.34] \cup [0.34, 0.5]$, in other words, we consider that there is no overlapping on target and clutter Doppler region. Besides, the normalized bandwidth of each filter is assumed to be $1/300$ Hz.

Finally, the stopping condition of the proposed algorithm is set at $\zeta = 10^{-4}$.

6.1.3.1 Convergence behavior of proposed algorithm

In this part, we investigate the convergence behavior of the proposed algorithm. Fig. 6.1 shows the worst case SINR versus the number of iterations for $N = 32$ and $M = 8$.

Note that, the upper bound for the SINR value is the case when there is no interference, equivalent to the SNR value therefore, the optimized SINR is bounded by 10 dB. Furthermore, in each iteration, the worst case SINR monotonically increases and converges to a certain value close to the upper bound.

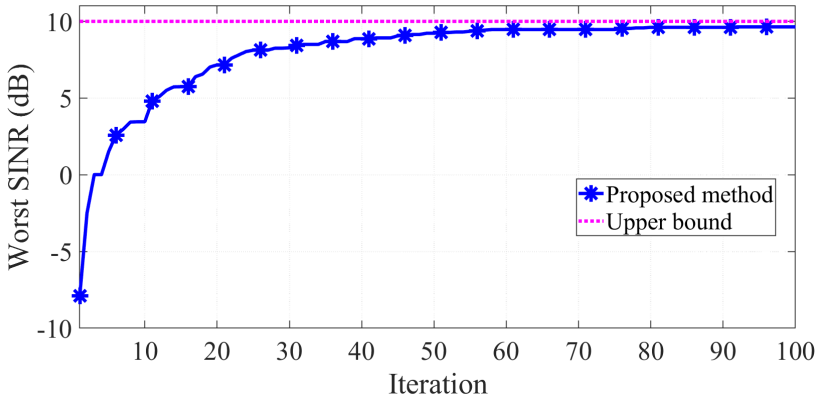

FIGURE 6.1: Convergence of worst-case SINR over the all filters ($N = 32$, $M = 8$, SNR = 10 dB, CNR = 30 dB).

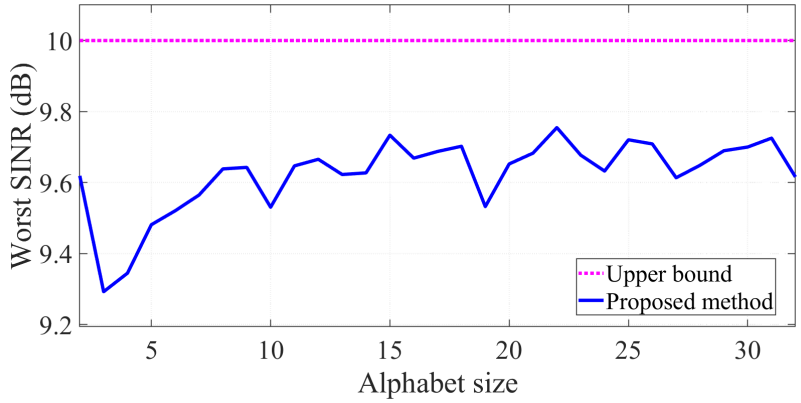

FIGURE 6.2: Robust worst case SINR convergence behavior versus different alphabet size ($N = 32$, SNR = 10 dB, CNR = 30 dB).

This behavior is investigated for different alphabet sizes. Fig.6.2 shows the optimized worst case SINR versus alphabet sizes, from $M = 2$ to $M = 32$. In this simulation, we assume that the initial waveform is a random MPSK sequence. Subsequently by performing the CD optimization procedure, we achieve the optimized SINR very close to the upper bound. On the other hand, the variation of the optimized SINR values for different alphabet sizes are very small. In this case the value of the optimized SINR is on $[9.74, 9.34]$ dB interval, so the maximum variation is 0.4 dB. This means that the proposed algorithm is capable to maximize the minimum SINR through filter bank for various alphabet sizes.

6.1.3.2 Receiver Operating Characteristic

Radar performance highly depends on detection and false alarm probability. Receiver Operating Characteristic (ROC) evaluates the variation of the detection probability (P_d) with false alarm probability (P_{fa}). In this part, we consider the worst-detection

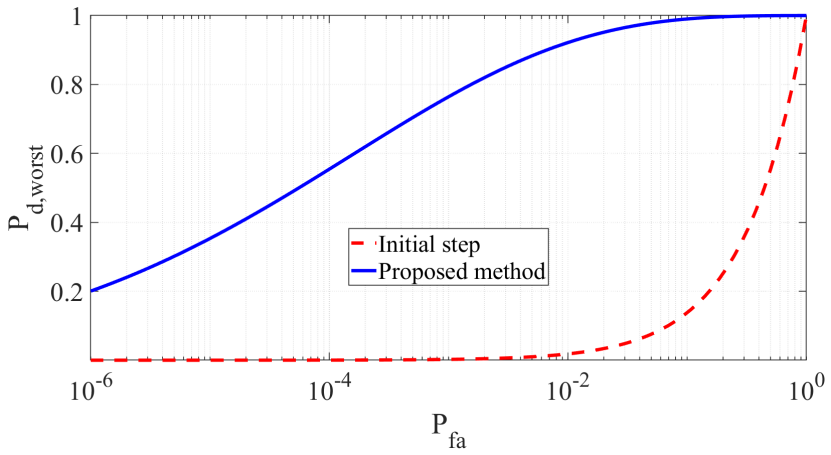

FIGURE 6.3: ROC of optimized and initial step waveform and filter bank ($N = 32$, $M = 8$, SNR = 10 dB, CNR = 30 dB).

probability which is given by [130, 167],

$$P_{d,worst} = Q\left(\sqrt{2\text{SINR}_{min}}, \sqrt{-2\log(P_{fa})}\right). \tag{6.18}$$

In (6.18) the $\text{SINR}_{min} = \min_{i\in\{1,\ldots,K\}} \text{SINR}_i$ is the minimum SINR through all filters, P_{fa} is the probability of false alarm and $Q(.,.)$ is the generalized Marcum-Q function.

Fig.6.3 shows the ROC curve related to the non-optimized and optimized waveform and their corresponding filter banks. Observe that, the proposed algorithm significantly enhances the detection performance.

6.1.3.3 Comparison With Existing Method

We now compare the performance of our method with the method proposed in [160], where we term it as the GFP method. In this regard, we assume a similar scenario addressed in [160]. With number of pulses is $N = 20$, and for the similarity constraint we consider a generalized Barker code with $\delta = 0.5$ and $\delta = 0.2$.

The GFP method designs a waveform which is not unimodular with a continuous phase. Therefore for a fair comparison, we map the optimum GFP waveform to the nearest MPSK sequence and term it quantized GFP. Fig.6.4 shows the constellation of the optimized waveform related to the proposed method, GFP and quantized GFP for two values of δ. The proposed waveform is unimodular by design and is of interest to the radar system designers due to this property. But the optimum waveform designed by GFP is not unimodular and this means that radar should transmit each code with different power and in this case, is not possible to transmit the code with maximum power in each Pulse Repetition Interval (PRI). Therefore, in this case, the power transmission is

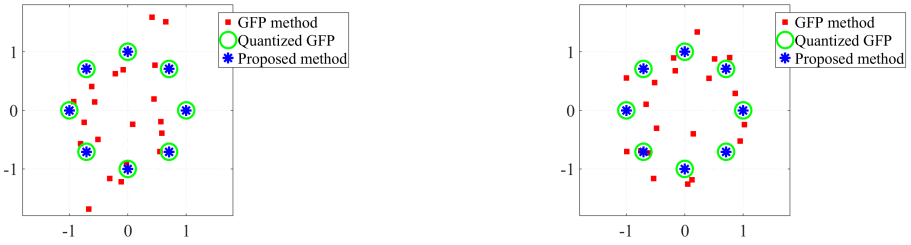

(A) $\delta = 0.5$ (B) $\delta = 0.2$

FIGURE 6.4: Convergence comparison between proposed method, GFP and Quantized GFP for different value of similarity constraint ($N = 20$, $M = 8$, SNR $= 10$ dB, CNR $= 30$ dB).

not efficient. However, using smaller δ leads to smaller deviation from the unimodular sequence. This deviation can be assessed from the point of view of PAR criterion. For a given sequence PAR is [130],

$$\text{PAR} = \frac{\max\limits_{i=1,\ldots,N} |s_i|^2}{\frac{1}{N}\| \boldsymbol{s} \|^2}. \tag{6.19}$$

Due to the unimodularity the PAR of proposed method and quantized GFP is equal to 0 dB. Whereas that value for GFP method is 2.65 dB and 5.16 dB for $\delta = 0.2$ and $\delta = 0.5$, respectively.

Fig.6.5 shows the worst-case SINR of three methods. As can be seen, the GFP method has a better performance in comparison to the proposed method in case of $\delta = 0.5$ and similar performance in case of $\delta = 0.2$. But if we quantize it to nearest MPSK code, the performance is decreased. Indeed, the obtained SINR value of the proposed method is 9.05 dB whereas, in quantized GFP that is 7.44 dB and 8.18 dB in case of $\delta = 0.5$ and $\delta = 0.2$, respectively. Therefore the proposed method improves the worst case SINR by 1.61 dB and 0.87 dB in case of $\delta = 0.5$ and $\delta = 0.2$, respectively. Besides, in quantized GFP, the behavior of the worst case SINR doesn't increase monotonically. This drawback can be justified that, there is no discrete phase constraint in GFP method and if we quantize it in nearest MPSK code, there is no guarantee to obtain the optimum waveform. But in the proposed method we tackle the optimization problem with discrete phase constraint directly.

Fig.6.5 shows that the proposed method converges in fewer iterations compared to the GFP. Table 6.1 shows the convergence time for several alphabet sizes and different CNR averaged over 10 independent trials. The reported values are obtained with a standard PC with Intel (R) Core (TM) i5-8250U CPU @ 1.60GHz with installed memory (RAM)

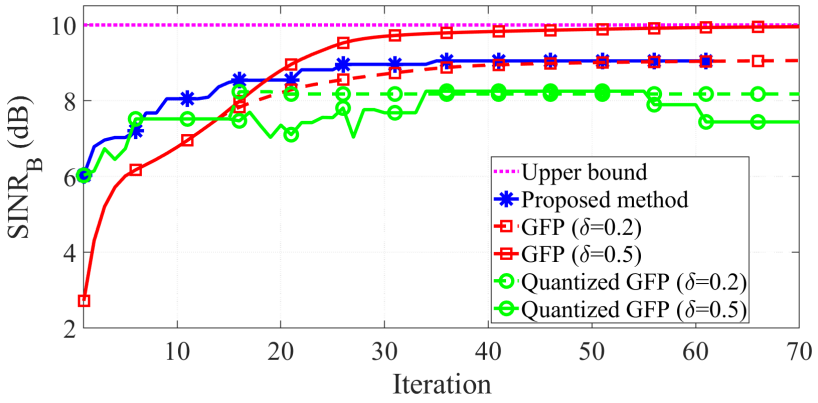

FIGURE 6.5: Convergence comparison between proposed method, GFP and Quantized GFP for different value of similarity constraint ($N = 20$, $M = 8$, SNR $= 10$ dB, CNR $= 30$ dB).

8.00 GB. Observe that with specific CNR, by increasing the alphabet size the convergence-time of proposed method increases, while those of GFP method and quantized GFP are almost constant. This behavior is expected, since the proposed method uses entry by entry search strategy to find the optimum solution; increasing the alphabet size naturally increases the convergence time.

On the other hand, the GFP method finds an optimum solution considering all the entries at once. For a given alphabet size, by increasing CNR the convergence time of CD method is almost constant. This is because the search region for the proposed method is independent of the CNR. However, in this scenario, the convergence time of GFP method increases. and this means that converge-time in GFP method depends on the value of CNR. This behavior is expected. Since the GFP method uses a sequential procedure, if the CNR is increased, the algorithm would start at lower SINR. Therefore GFP needs more time for converging to the optimum value.

TABLE 6.1: Comparison between the convergence-time (s) of proposed method and Quantized GFP averaged over 10 independent trials, for different alphabet sizes and different CNR.

M	CD		Quantized GFP	
	CNR 20 dB	CNR 30 dB	CNR 20 dB	CNR 30 dB
2	2.67	2.20	218.27	253.47
4	5.01	4.46	239.07	266.04
8	10.66	8.40	226.06	267.53
16	26.14	29.37	227.80	387.26
32	58.96	68.13	224.14	331.23

6.2 ADMM Based Transmit Waveform and Receive Filter Design in Cognitive Radar Systems

In this section, we aim to tackle the maximization of SINR by jointly optimizing the Doppler filter and waveform under the assumption of signal-dependent interference and MPSK sequences. The importance of designing a MPSK sequence can be discussed in two aspects. First, MPSK is an uni-modular sequence and allows the radar system for full utilization of the transmitter power. Second, the MPSK is a discrete phase sequences whose phases are chosen from a small size alphabet [78]. This property is attractive for radar designers in the point of view of hardware implementation.

This approach leads to a multi-variable, non-convex optimization problem. Towards solving this, we propose an algorithm based on ADMM [168]. According to this method we split the problem into two sub-optimization problem, specifically with respect to the Doppler filter and waveform, then we optimize the Doppler filter and waveform alternatively. This powerful approach simplifies the problem and offers an efficient and fast solution. Accordingly, the problem with respect to Doppler filter is a convex optimization problem and we find a closed-form solution for it. However the problem with respect to waveform is non-convex and we propose an iterative algorithm based on CD framework [24, 38, 39, 102, 149, 169] to design the waveform. Numerical results show that the proposed method has better performance in terms of computational time and reducing the sidelobe with its counterpart.

We organize this section as follows. In subsection 6.2.1, we introduce the system model and problem statement, respectively. Subsection 6.2.2 presents the proposed ADMM based framework whose performance is numerically assessed in subsection 6.2.3.

Notations: The following notations is adopted. Bold lowercase letters for vectors and bold uppercase letters for matrices. $\mathbf{Diag}\{\boldsymbol{a}\}$, $(.)^T$, $(.)^*$, $(.)^\dagger$, $\Re\{.\}$, $|.|$, $\mathbb{E}[.]$ and $\odot$ denote the diagonal matrix of vector $\boldsymbol{a}$, transpose, conjugate, conjugate transpose, real part, absolute value, statistical expectation and Hadamard product respectively. The letters j, (k) and (i) represent the imaginary unit (i.e., $j = \sqrt{-1}$) and the step of a procedure respectively.

6.2.1 System Model and Problem Formulation

Let $\boldsymbol{s} = \{s_1, \ldots, s_N\} \in \mathbb{C}^N$ be the slow-time transmitted signal in a mono-static radar system. The received signal at any CPI is,

$$\boldsymbol{r} = \alpha_t \boldsymbol{P}(f_d)\boldsymbol{s} + \boldsymbol{r}_c + \boldsymbol{r}_n \in \mathbb{C}^N, \tag{6.20}$$

where α_t is proportional to the RCS of the target and free space path loss. $\boldsymbol{r}_c$, $\boldsymbol{r}_n$ are signal-dependent and signal-independent interference, respectively. In (6.20) f_d denotes the Doppler shift and $\boldsymbol{P}(f_d) = \text{Diag}(\boldsymbol{v}(f_d)) \in \mathbb{C}^{N\times N}$, where $\boldsymbol{v}(f_d)$ is the target steering vector which can be expressed as, $\boldsymbol{v}(f_d) = [1, e^{j2\pi f_d}, \ldots, e^{j2\pi(N-1)f_d}]^T \in \mathbb{C}^N$.

Interference Model The signal-dependent interference is modelled as [160],

$$\boldsymbol{r}_c = \sum_{r=0}^{N_r}\sum_{l=0}^{N_a}\alpha_{(r,l)}\boldsymbol{J}_r\left(\boldsymbol{s}\odot\boldsymbol{v}(f_{d_{(r,l)}})\right), \tag{6.21}$$

where, $\alpha_{(r,l)}$ and $f_{d_{(r,l)}}$ are the received scatterer power and shift Doppler in the r^{th} range and l^{th} azimuth bin, respectively. N_r and N_a are the number of the range-bin and azimuth-bin of clutter patches and $\boldsymbol{J}_r$ denotes the shift matrix [160]. From the statistical point of view, the covariance matrix of $\boldsymbol{r}_c$ can be expressed as [160],

$$\boldsymbol{R}_c(\boldsymbol{s}) = \sum_{r=0}^{N_r}\sum_{l=0}^{N_a}\sigma^2_{(r,l)}\boldsymbol{J}_r\boldsymbol{\Xi}\left(\boldsymbol{s},(r,l)\right)\boldsymbol{J}_r^{\dagger}, \tag{6.22}$$

where, $\mathbb{E}\left[|\alpha(r,l)|^2\right] = \sigma^2_{(r,l)}$ is the mean RCS of each clutter patch and $\boldsymbol{\Xi}\left(\boldsymbol{s},(r,l)\right) = \textbf{Diag}\left\{\boldsymbol{s}\right\}\boldsymbol{\Upsilon}^{\bar{f}_{d_{(r,l)}}}_{\epsilon_{d_{(r,l)}}}\textbf{Diag}\left\{\boldsymbol{s}\right\}^{\dagger}$. $\bar{f}_{d_{(r,l)}}$ and $\epsilon_{(r,l)}$ are the mean and standard deviation shift Doppler of each clutter patch, and $\boldsymbol{\Upsilon}^{\bar{f}_{d_{(r,l)}}}_{\epsilon_{d_{(r,l)}}}$ is the covariance matrix of clutter steering vector $(\boldsymbol{v}(f_{d_{(r,l)}}))$ taking the form,

$$\boldsymbol{\Upsilon}^{\bar{f}_{d_{(r,l)}}}_{\epsilon_{(r,l)}}(p,q) = e^{j2\pi\bar{f}_{d_{(r,l)}}(p-q)}\frac{\sin(\pi\epsilon_{(r,l)}(p-q))}{\pi\epsilon_{(r,l)}(p-q)}.$$

The signal-independent interference is modelled as zero-mean white Gaussian noise ($\mathbb{E}\left[\boldsymbol{r}_n\right] = 0$), with autocorrelation matrix of $\mathbb{E}\left[\boldsymbol{r}_n{\boldsymbol{r}_n}^{\dagger}\right] = \boldsymbol{R}_n = \sigma_n^2\boldsymbol{I}$.

SINR Formulation Let $\boldsymbol{w}$ be the coefficients of Doppler filter, the output SINR of the Doppler filter can be expressed as,

$$\text{SINR} = \frac{|\alpha_t|^2\left|\boldsymbol{w}^{\dagger}\boldsymbol{P}(f_d)\boldsymbol{s}\right|^2}{\boldsymbol{w}^{\dagger}\boldsymbol{R}_i(\boldsymbol{s})\boldsymbol{w}}, \tag{6.23}$$

where $\boldsymbol{R}_i(\boldsymbol{s}) = \boldsymbol{R}_c(\boldsymbol{s}) + \boldsymbol{R}_n$.

The knowledge of the statistical characterization of interference such as $\sigma^2_{(r,l)}$, $\bar{f}_{d_{(r,l)}}$, $\epsilon_{(r,l)}$ and σ_n^2 are crucial for optimization design. Cognitive radar can estimate these parameters by interactions with the environment, using dynamic database and some clutter models [164]. In this regard, we consider using cognitive paradigm to derive the interference statistical parameters.

Problem Statement Assume a Doppler filter which is tuned to f_d. In such a case, a relevant design metric is the maximization of the output SINR under uni-modular and discrete phase constraint (e.g., MPSK). As SINR is a fractional function, one approach for maximizing (6.23) is,

$$\mathcal{P}_1 \begin{cases} \min\limits_{\boldsymbol{w},\boldsymbol{s}} & \boldsymbol{w}^\dagger \boldsymbol{R}_i(\boldsymbol{s})\boldsymbol{w} \\ s.t & \boldsymbol{w}^\dagger \boldsymbol{P}(f_d)\boldsymbol{s} = \kappa \\ & \boldsymbol{s} \in \Omega_M, \end{cases} \tag{6.24}$$

In $\mathcal{P}_1$ the first constraint is the well known Capon constraint with $\kappa \in \mathbb{R}$ [170, 171], and the second constraint indicates the uni-modular and discrete phase constraint. In $\mathcal{P}_1$, $\Omega_M = \{\boldsymbol{s} | s_n = e^{j\phi}, \phi \in \Psi_M, n = 1, \ldots, N\}$ is MPSK sequence set and $\Psi_M = \{0, \frac{2\pi}{M}, \frac{4\pi}{M}, \ldots, \frac{2(M-1)\pi}{M}\}$, where M is the alphabet size.

Problem $\mathcal{P}_1$ is a multi-variable non-convex constrained optimization and a solution is presented next.

6.2.2 Proposed Method

By straightforward mathematical manipulation problem (6.24) equivalently can be written as follow,

$$\mathcal{P}_2 \begin{cases} \min\limits_{\boldsymbol{w},\boldsymbol{s}} & \boldsymbol{w}^\dagger \boldsymbol{R}_i(\boldsymbol{s})\boldsymbol{w} \\ s.t & g(\boldsymbol{w}, \boldsymbol{s}) = 0 \\ & s_n = e^{j\phi}, \phi \in \Psi_M, \end{cases} \tag{6.25}$$

where, $g(\boldsymbol{w}, \boldsymbol{s}) = \boldsymbol{h}(\boldsymbol{w})\boldsymbol{s} - \kappa = \boldsymbol{h}'(\boldsymbol{s})\boldsymbol{w} - \kappa \in \mathbb{R}$ and,

$$\boldsymbol{h}(\boldsymbol{w}) = \boldsymbol{w}^\dagger \boldsymbol{P}(f_d) \in \mathbb{C}^{1\times N}, \tag{6.26}$$

$$\boldsymbol{h}'(\boldsymbol{s}) = \boldsymbol{s}^\dagger \boldsymbol{P}^\dagger(f_d) \in \mathbb{C}^{1\times N}. \tag{6.27}$$

As (6.25) depends on $\boldsymbol{w}$ and $\boldsymbol{s}$, problem $\mathcal{P}_2$ can be optimized alternatively using ADMM [168]. In this regards the augmented Lagrangian of (6.25) can be written as,

$$\mathcal{L}_\rho(\boldsymbol{w}, \boldsymbol{s}, \lambda) = \boldsymbol{w}^\dagger \boldsymbol{R}_i(\boldsymbol{s})\boldsymbol{w} + \Re\{\lambda(g(\boldsymbol{w}, \boldsymbol{s}))\} + \frac{\rho}{2}\left\|g(\boldsymbol{w}, \boldsymbol{s})\right\|^2, \tag{6.28}$$

where λ is Lagrangian multiplier and ρ is penalty parameter and can be adjusted according to the design requirements. Hence the ADMM procedure at step $(k+1)$ is summarize

as,

$$\boldsymbol{w}^{(k+1)} = \arg\min_{\boldsymbol{w}} \left\{ \mathcal{L}_\rho \left(\boldsymbol{w}, \boldsymbol{s}^{(k)}, \lambda^{(k)} \right) \right\}, \tag{6.29a}$$

$$\boldsymbol{s}^{(k+1)} = \arg\min_{\boldsymbol{s}} \left\{ \mathcal{L}_\rho \left(\boldsymbol{w}^{(k+1)}, \boldsymbol{s}, \lambda^{(k)} \right) | \boldsymbol{s} \in \Omega_M \right\}, \tag{6.29b}$$

$$\lambda^{(k+1)} = \lambda^{(k)} + \rho g \left(\boldsymbol{w}^{(k+1)}, \boldsymbol{s}^{(k+1)} \right). \tag{6.29c}$$

In order to solve (6.29a), inserting (6.28) and (6.27) in (6.29a) we have,

$$\begin{aligned} \mathcal{L}_\rho \left(\boldsymbol{w}, \boldsymbol{s}^{(k)}, \lambda^{(k)} \right) &= \boldsymbol{w}^\dagger \boldsymbol{R}_i(\boldsymbol{s}^{(k)}) \boldsymbol{w} \\ &+ \Re\{\lambda^{(k)} (\boldsymbol{h}'(\boldsymbol{s}^{(k)}) \boldsymbol{w} - \kappa)\} + \frac{\rho}{2} \left\| \boldsymbol{h}'(\boldsymbol{s}^{(k)}) \boldsymbol{w} - \kappa \right\|^2. \end{aligned} \tag{6.30}$$

By combining the linear and quadratic terms, (6.30) can be written in more compact form as the following,

$$\begin{aligned} \mathcal{L}_\rho \left(\boldsymbol{w}, \boldsymbol{s}^{(k)}, u^{(k)} \right) &= \boldsymbol{w}^\dagger \boldsymbol{R}_i(\boldsymbol{s}^{(k)}) \boldsymbol{w} \\ &+ \frac{\rho}{2} \left\| \boldsymbol{h}'(\boldsymbol{s}^{(k)}) \boldsymbol{w} - \kappa + u^{(k)} \right\|^2, \end{aligned} \tag{6.31}$$

where $u^{(k)} = \frac{1}{\rho} y^{(k)}$ is a scaled dual variable [168]. Therefore $\boldsymbol{w}^{(k+1)}$ can be obtained by solving the following problem,

$$\boldsymbol{w}^{(k+1)} = \arg\min_{\boldsymbol{w}} \left\{ \mathcal{L}_\rho \left(\boldsymbol{w}, \boldsymbol{s}^{(k)}, u^{(k)} \right) \right\}. \tag{6.32}$$

Similarly $\mathcal{L}_\rho \left(\boldsymbol{w}^{(k+1)}, \boldsymbol{s}, \lambda^{(k)} \right)$ can be recast as,

$$\begin{aligned} \mathcal{L}_\rho \left(\boldsymbol{w}^{(k+1)}, \boldsymbol{s}, u^{(k)} \right) &= \boldsymbol{w}^{(k+1)^\dagger} \boldsymbol{R}_i(\boldsymbol{s}) \boldsymbol{w}^{(k+1)} \\ &+ \frac{\rho}{2} \left\| \boldsymbol{h}(\boldsymbol{w}^{(k+1)}) \boldsymbol{s} - \kappa + u^{(k)} \right\|^2, \end{aligned} \tag{6.33}$$

In order to simplify (6.33), $\boldsymbol{w}^\dagger \boldsymbol{R}_c(\boldsymbol{s}) \boldsymbol{w}$ can be written as $\boldsymbol{w}^\dagger \boldsymbol{R}_c(\boldsymbol{s}) \boldsymbol{w} = \boldsymbol{s}^\dagger \boldsymbol{T}_c(\boldsymbol{w}) \boldsymbol{s}$ [160], where,

$$\begin{aligned} &\boldsymbol{T}_c(\boldsymbol{w}) = \\ &\textstyle\sum_{r=0}^{N_r} \sum_{l=0}^{N_a} \sigma^2_{(r,l)} \mathbf{Diag}\{\boldsymbol{J}_{-r} \boldsymbol{w}\} (\boldsymbol{\Upsilon}^{\bar{f}_{d_{(r,l)}}}_{\epsilon_{d_{(r,l)}}})^* \mathbf{Diag}\{\boldsymbol{J}_{-r} \boldsymbol{w}^*\}. \end{aligned} \tag{6.34}$$

In this case, $\boldsymbol{w}^\dagger \boldsymbol{R}_i(\boldsymbol{s}) \boldsymbol{w} = \boldsymbol{s}^\dagger \boldsymbol{T}_c(\boldsymbol{w}) \boldsymbol{s} + \boldsymbol{w}^\dagger \boldsymbol{R}_n \boldsymbol{w}$ and (6.33) can be written equivalently as follows,

$$\begin{aligned} \mathcal{L}_\rho \left(\boldsymbol{w}^{(k+1)}, \boldsymbol{s}, u^{(k)} \right) &= \boldsymbol{s}^\dagger \boldsymbol{T}_c(\boldsymbol{w}^{(k+1)}) \boldsymbol{s} \\ &+ \frac{\rho}{2} \left\| \boldsymbol{h}(\boldsymbol{w}^{(k+1)}) \boldsymbol{s} - \kappa + u^{(k)} \right\|^2, \end{aligned} \tag{6.35}$$

Therefore the equivalent problem of (6.29b) is,

$$\boldsymbol{s}^{(k+1)} = \arg\min_{\boldsymbol{s}} \left\{ \mathcal{L}_\rho \left(\boldsymbol{w}^{(k+1)}, \boldsymbol{s}, u^{(k)} \right) | \boldsymbol{s} \in \Omega_M \right\}, \tag{6.36}$$

With regard to $u^{(k+1)}$ the update rule is,

$$u^{(k+1)} = u^{(k)} + \boldsymbol{h}(\boldsymbol{s}^{(k+1)})\boldsymbol{w}^{(k+1)} - \kappa. \tag{6.37}$$

6.2.2.1 Optimizing $\boldsymbol{w}^{(k+1)}$

Problem (6.32) is a convex optimization problem, hence there is a closed-form solution for (6.32) by taking derivative from $\mathcal{L}_\rho \left(\boldsymbol{w}, \boldsymbol{s}^{(k)}, u^{(k)} \right)$ with respect to $\boldsymbol{w}$ and subsequently finding the roots,

$$\begin{aligned} &\nabla_{\boldsymbol{w}} \mathcal{L}_\rho \left(\boldsymbol{w}, \boldsymbol{s}^{(k)}, u^{(k)} \right) = 2\boldsymbol{R}_i^\dagger(\boldsymbol{s}^{(k)})\boldsymbol{w} \\ &+ \rho \boldsymbol{h}'^\dagger(\boldsymbol{s}^{(k)})\boldsymbol{h}'(\boldsymbol{s}^{(k)})\boldsymbol{w} - \rho \boldsymbol{h}'^\dagger(\boldsymbol{s}^{(k)}) \left(\kappa - u^{(k)} \right) = 0. \end{aligned} \tag{6.38}$$

Therefore the closed-form solution is,

$$\boldsymbol{w}^{(k+1)} = \boldsymbol{A}^{-1}\boldsymbol{a}. \tag{6.39}$$

where,

$$\boldsymbol{A} = 2\boldsymbol{R}_i^\dagger(\boldsymbol{s}^{(k)})\boldsymbol{w} + \rho \boldsymbol{h}'^\dagger(\boldsymbol{s}^{(k)})\boldsymbol{h}'(\boldsymbol{s}^{(k)}), \tag{6.40}$$

$$\boldsymbol{a} = \rho \boldsymbol{h}'^\dagger(\boldsymbol{s}^{(k)}) \left(\kappa - u^{(k)} \right). \tag{6.41}$$

6.2.2.2 Optimizing $\boldsymbol{s}^{(k+1)}$

Problem (6.36) is a multi-variable and non-convex optimization problem and we propose an iterative procedure based on CD framework [102] to solve it. CD is an iterative optimization method which starts with an initial feasible vector $\boldsymbol{x} = \boldsymbol{s}^{(0)}$, then $\boldsymbol{x}$ is updated by optimizing entry by entry basis in an iterative manner [24, 78]. In particular, one entry of $\boldsymbol{x}$ is considered as the only variable while others are held fixed. Subsequently, with respect to this identified variable, we optimize the problem (6.36). Let us assume that s_d is the d^{th} transmitted pulse ($d = 1, \ldots, N$) and is the only variable, while the other $N-1$ entries are fixed. We define $\boldsymbol{x}_{-d}^{(i)}$ as a vector at the i^{th} iteration of CD which

the d^{th} entry is undergone of the optimization procedure as,

$$\boldsymbol{x}_{-d}^{(i)} \triangleq [s_1^{(i)}, \ldots, s_{d-1}^{(i)}, s_d, s_{d+1}^{(i-1)}, \ldots, s_N^{(i-1)}]^T \in \mathbb{C}^N. \tag{6.42}$$

At iteration (i) of the CD procedure, the variable $s_d^{(i)}$ is updated by solving the following sub-problem,

$$s_d^{(i)} = \arg\min_{s_d} \left\{ \mathcal{L}_\rho \left(\boldsymbol{w}^{(k+1)}, \boldsymbol{x}_{-d}^{(i)}, u^{(k)} \right) | \boldsymbol{x}_{-d}^{(i)} \in \Omega_M \right\}, \tag{6.43}$$

Each iteration is completed when all of the entries are updated. At the end of each iteration the algorithm examines the convergence metric for the objective function. If the stopping criteria is not met another iteration is started to optimize the waveform. Let $\boldsymbol{x}^{(i)} \triangleq [s_1^{(i)}, \ldots, s_N^{(i)}]^T \in \mathbb{C}^N$ be the optimized vector at i^{th} iteration. We consider the following condition as stopping criterion of optimization,

$$\mathcal{L}_\rho \left(\boldsymbol{w}^{(k+1)}, \boldsymbol{x}^{(i-1)}, u^{(k)} \right) - \mathcal{L}_\rho \left(\boldsymbol{w}^{(k+1)}, \boldsymbol{x}^{(i)}, u^{(k)} \right) < \zeta \tag{6.44}$$

where, $\zeta > 0$.

In order to enhance the efficiency of the proposed method, problem (6.43) can be simplified by rewriting that with respect to s_d as follows (see Appendix E.1 for details),

$$\mathcal{P}_1 \begin{cases} \min\limits_{s_d} & c_0 s_d + c_1 + c_2 s_d^* \\ s.t & s_d = e^{j\phi}, \phi \in \Psi_M \end{cases}. \tag{6.45}$$

Replacing $s_d = e^{i\phi}$, the problem (6.45) can be recast as,

$$\mathcal{P}_2 \begin{cases} \min\limits_{\phi} & f(\phi) = e^{j\phi} \left(c_0 + c_1 e^{-j\phi} + c_2 e^{-2j\phi} \right) \\ s.t & \phi \in \Psi_M \end{cases}. \tag{6.46}$$

As ϕ is chosen over finite alphabet, the objective function can be written with respect to the index of Ψ_M as, $f(\phi_m) = e^{j\frac{2\pi m}{L}} \sum_{n=0}^{2} c_n e^{-j\frac{2\pi nm}{M}}$, where, $m = \{0, \ldots, M-1\}$. The summation term is the definition of $M-$point DFT of sequence $\{c_0, c_1, c_2\}$. Hence, $f(\phi_m)$ can be written as,

$$f(m) = \boldsymbol{h}_M \odot \mathcal{F}_M\{c_0, c_1, c_2\} \tag{6.47}$$

where, $\boldsymbol{h}_M = [1, e^{j\frac{2\pi}{L}}, \ldots, e^{j\frac{2\pi(L-1)}{L}}]^T \in \mathbb{C}^M$ and $\mathcal{F}_M$ is the $M-$point DFT operator. Therefore the optimum solution of (6.47) is, $m^\star = \arg\min_{m=1,\ldots,M} \{f(m)\}$. Subsequently, the optimum phase is,

$$\phi^\star = \frac{2\pi(m^\star - 1)}{M}. \tag{6.48}$$

To this end, based on the aforementioned discussion, we propose Algorithm 11 based on CD to solve (6.43).

Subroutine Procedure 11 : CD Framework

Input: $\boldsymbol{w}^{(k+1)}$, $\boldsymbol{s}^{(k)}$

Output: Optimized waveform $\boldsymbol{s}^{(k+1)}$.

1. **Initialization**.
   - Set $i := 0$, $\boldsymbol{x}^{(i)} := \boldsymbol{s}^{(k)}$ and $d := 1$;
2. **Optimization**.
   - $i := i + 1$;
   - Obtain $\phi^{\star}$ using (6.48), then $s_d^{(i)} = e^{j\phi^{\star}}$;
   - If $d = N$ go to 3); else $d := d + 1$ and go to 2);
3. **Stopping Criterion**.
   - $\boldsymbol{x}^{(i)} = [s_1^{(i)}, \ldots, s_N^{(i)}]^T$ and $d := 1$;
   - If (6.44) is satisfied, go to 4), otherwise go to 2);
4. **Output**.
   - Set $\boldsymbol{s}^{(k+1)} = \boldsymbol{x}^{(i)}$;

6.2.2.3 Termination Criteria of ADMM method

The authors in [168] suggest the two following criteria for ADMM termination at the k^{th} step,

$$\left\| r^{(k)} \right\|_2 < \epsilon^{\text{pri}}, \quad \left\| v^{(k)} \right\|_2 < \epsilon^{\text{dual}}, \tag{6.49}$$

where, $r^{(k)}$ and $v^{(k)}$ are known as primal and dual residual at iteration k, and $\epsilon^{\text{pri}} > 0$ and $\epsilon^{\text{dual}} > 0$ are tolerances for the primal and dual residual, respectively. Here, the primal and dual residual are,

$$r^k = \boldsymbol{h}'(\boldsymbol{s}^{(k)})\boldsymbol{w} - \kappa, \tag{6.50}$$

$$v^k = \rho \boldsymbol{h}(\boldsymbol{w}^{(k)}) \left(\boldsymbol{s}^{(k)} - \boldsymbol{s}^{(k-1)} \right), \tag{6.51}$$

and the tolerances for primal residuals are,

$$\epsilon^{\text{pri}} = \epsilon^{\text{abs}} \sqrt{N} + \epsilon^{\text{rel}} \max \left\{ \left\| \boldsymbol{h}(\boldsymbol{w}^{(k)}) \boldsymbol{s}^{(k)} \right\|, \left\| \boldsymbol{h}'(\boldsymbol{s}^{(k)}) \boldsymbol{w}^{(k)} \right\|, \kappa \right\}, \tag{6.52}$$

$$\epsilon^{\text{dual}} = \epsilon^{\text{abs}}\sqrt{N} + \epsilon^{\text{rel}}\left\|\rho\left(\boldsymbol{h}(\boldsymbol{w}^{(k)})\boldsymbol{s}^{(k)}\right)^{\dagger} u^{(k)}\right\|. \tag{6.53}$$

In (6.52) and (6.53) $\epsilon^{\text{abs}} > 0$ and $\epsilon^{\text{rel}} > 0$ are absolute and relative tolerance respectively and they are selected depending on the application.

6.2.2.4 ADMM algorithm

Algorithm 12 summarizes the joint Doppler filter and waveform design based on ADMM.

Subroutine Procedure 12 : Joint Doppler filter and waveform design

Input: $\boldsymbol{w}^{(0)}$, $\boldsymbol{s}^{(0)}$, $u^{(0)}$, ρ, ϵ^{dual} and ϵ^{rel}
Output: Optimized waveform $\boldsymbol{s}^{\star}$.

1. **Initialization**.
   - Set $k := 0$;
2. **Optimization**.
   - Obtain $\boldsymbol{w}^{(k+1)}$ using (6.39);
   - Obtain $\boldsymbol{s}^{(k+1)}$ using Algorithm 11;
   - $u^{(k+1)} := u^{(k)} + \boldsymbol{h}(\boldsymbol{s}^{(k+1)})\boldsymbol{w}^{(k+1)} - \kappa$;
   - $k := k + 1$;
3. **Stopping Criterion**.
   - If (6.49) is satisfied, go to 4), otherwise go to 2);
4. **Output**.
   - Set $\boldsymbol{w}^{\star} = \boldsymbol{w}^{(k+1)}$ and $\boldsymbol{s}^{\star} = \boldsymbol{s}^{(k+1)}$;

6.2.3 Numerical Results

In this subsection, we provide some simulation results to evaluate the effectiveness of the proposed method. Towards this end, unless otherwise explicitly stated, we consider the following assumptions. Note that all Doppler shifts are normalized to PRF.

Waveform Parameters We design a MPSK sequence with length and alphabet size of $N = 32$ and $M = 8$ respectively. The energy transmitted is $e_s = \| s \|^2$.

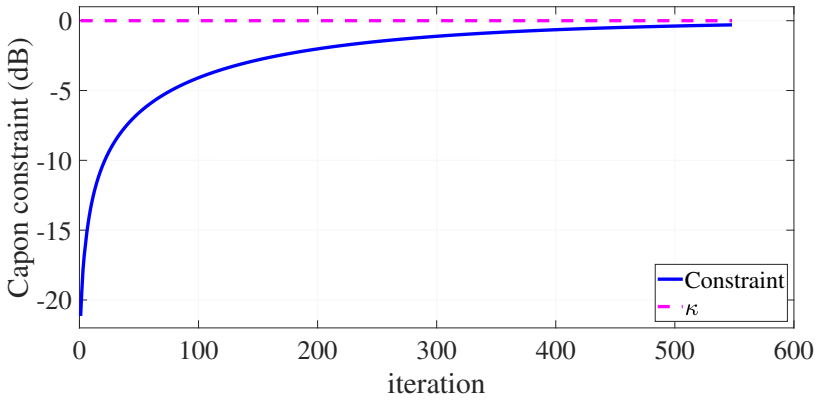

FIGURE 6.6: Convergence behavior of Capon constraint.

Interference Parameters We consider $\sigma_n^2 = 1$ for signal-independent interference. For signal-dependent interference (clutter) we assume $N_r = 2$ as interfering range rings, and $N_a = 100$ as azimuth sectors. We consider a homogeneous clutter which means $\sigma^2_{(r,l)} = \sigma^2$; $r \in \{1, \ldots, N_r\}, l \in \{1, \ldots, N_a\}$. The CNR can be calculated by $\text{CNR} = \frac{\sigma^2_{(r,l)}}{\sigma_n^2} e_s$, [166], which is equal to 30 dB. The normalized mean and variance shift Doppler are $\bar{f}_{d_{(r,l)}} = 0$ Hz and $\epsilon_{(r,l)} = 0.1$ Hz, respectively.

Target Parameters The SNR of received signal is, $\text{SNR} = \frac{|\alpha_t|^2}{\sigma_n^2} e_s$, [166], which is adjusted to be 10 dB. In addition, we assume that the normalized target Doppler shift is equal to $f_d = 0.35$ Hz.

Algorithm Parameters For problem (6.24), we set $\kappa = 1$. For Algorithm 12, we initialize $u^{(0)} = 0$ and $\boldsymbol{w}^{(0)}$ to be a zero vector while for $\boldsymbol{s}^{(0)}$ we consider a random MPSK sequence. We set the penalty $\rho = 100$, and the absolute tolerance and relative tolerance are $\epsilon^{\text{abs}} = 10^{-2}$ and $\epsilon^{\text{rel}} = 10^{-4}$. Finally, for Algorithm 11 the stopping condition is set at $\zeta = 10^{-3}$.

6.2.3.1 Convergence behavior of proposed algorithm

In this part, we investigate the convergence behavior of the proposed algorithm. Figure 6.6 shows the convergence behavior of the Capon constraint of (6.24). As we expected in Figure 6.6 the Capon constraint converges to κ.

Figure 6.7 shows the convergence behavior of the SINR of the proposed method. As can be seen in the SINR converges to the optimum value close to the upper bound.

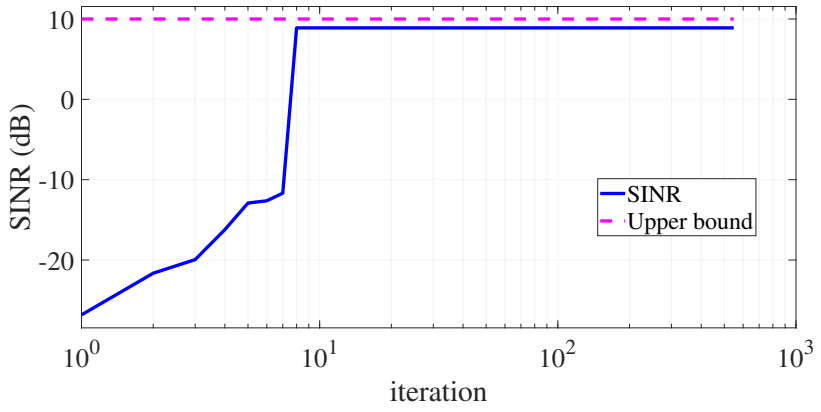

FIGURE 6.7: Convergence behavior of SINR.

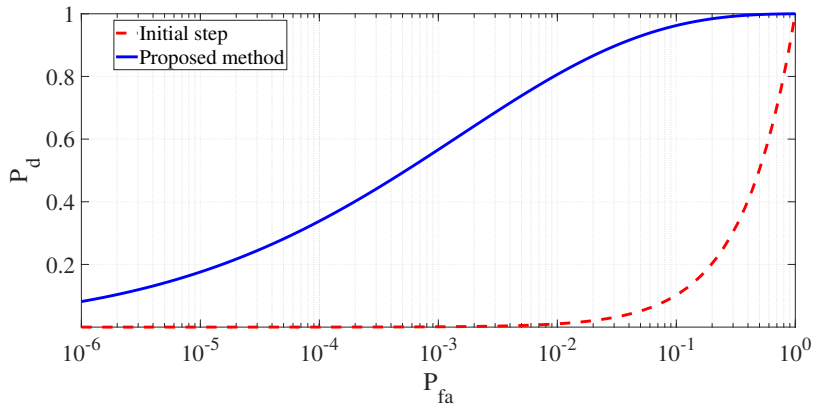

FIGURE 6.8: ROC improvement of proposed method.

Note that, the upper bound for the SINR value is the case when there is no clutter interference, equivalent to the SNR value therefore, the optimized SINR is bounded by 10 dB.

6.2.3.2 Receiver Operating Characteristic

The detection performance of radar system can be evaluate by ROC which plots the variation of the detection probability (P_d) with false alarm probability (P_{fa}). The detection probability is given by $P_d = Q\left(\sqrt{2\text{SINR}}, \sqrt{-2\log(P_{fa})}\right)$ [130, 167], where P_{fa} is the probability of false alarm and $Q(.,.)$ is the generalized Marcum-Q function.

Figure 6.8 shows the ROC of the proposed method in the first and the last iteration (optimized waveform and the corresponding Doppler filter). As can be seen, the detection performance is significantly enhanced by proposed method.

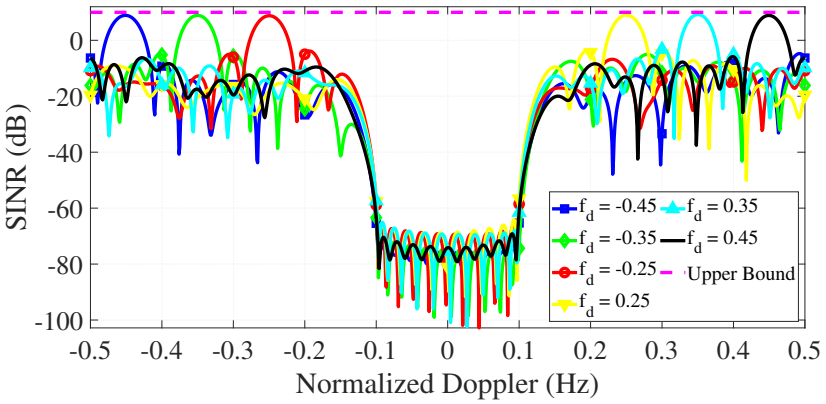

FIGURE 6.9: Doppler filter Response of proposed method with different f_d.

6.2.3.3 Filter Response

The Doppler filter response associated with different f_d are plotted in Figure 6.9. It can be observed that the proposed method enhances the output SINR of Doppler filter yielding a value close to the upper bound with different central frequencies.

6.2.3.4 Comparison with another method

In this part, we compare the performance the proposed method with GFP method in [160] in different aspects. To this end, we assume a similar simulation setup, where the number of pulses is $N = 20$, and for the similarity constraint we consider a generalized Barker code with different δ.

Frequency Response As [160] designs a Doppler filter bank, we choose one of them and we compare it with the proposed method with the same central Doppler frequency. Figure 6.10 shows the Doppler filter response of GFP and proposed method with $f_d = 0.425$ Hz. Observe that although GFP method provides a slightly better SINR in central frequency, it has higher spectrum sidelobes compared to the proposed method. This enables superior discrimination capability of the proposed approach.

Power Efficiency The optimum waveform obtained by GFP is not uni-modular and each code has different power, leading to inefficient power transmission. However due to the uni-modular sequence the proposed method has a better performance in compare with GFP method. The power efficiency can be assessed from the PAR criterion as [130],

$$\text{PAR} = \frac{\max\limits_{i=1,\dots,N} |s_i|^2}{\frac{1}{N}\| \boldsymbol{s} \|^2}. \tag{6.54}$$

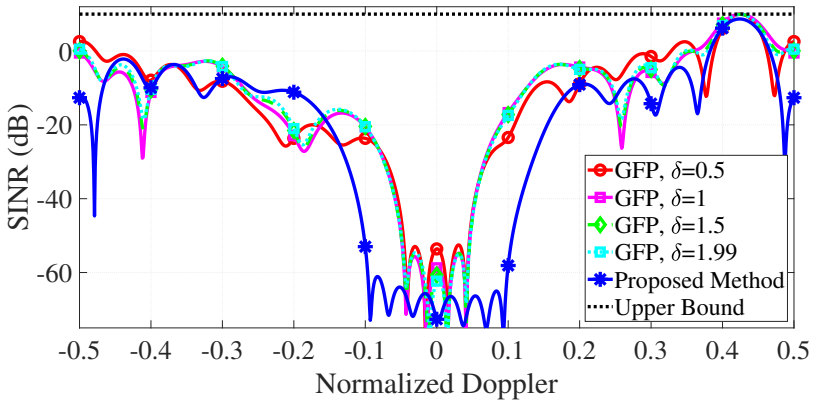

FIGURE 6.10: Comparison the filter Response between proposed method and GFP ($N = 20$, $M = 8$, $f_d = 0.425$ Hz, SNR = 10 dB and CNR = 30 dB).

TABLE 6.2: The convergence-time (s) of proposed method averaged over 10 independent trials, for different sequence length.

N	16	32	64	128	256
Convergence	0.69	1.04	1.93	5.05	19.75

The PAR of GFP method is equal to 4.35 dB whereas, it is equal to 0 dB in the proposed method due to the uni-modular sequence.

Computational Complexity Table 3.1 shows the convergence time of the proposed method with different sequence lengths over 10 independent trials. The reported values are obtained with a standard PC with Intel (R) Core (TM) i5-8250U CPU @ 1.60GHz with installed memory (RAM) 8.00 GB. By increasing the sequence length, the convergence-time of proposed method increases. This behavior is expected; increasing the sequence length increases the problem dimension and naturally increases the convergence time. However the average convergence time of GFP method is 119.97 seconds and table 3.1 shows that the proposed method is faster than GFP method.

6.3 Conclusion

In this chapter, we have considered a maximization of SINR by joint design the Doppler filter and waveform under assumption of presence of signal-dependent interfering. In addition, in order to achieve a good power efficiency and efficient hardware implementation, we consider discrete phase sequences. In this chapter We consider two design metric. First we consider maximizing the worst-case SINR at the output of the filter bank target Doppler frequency is unknown. Second we consider SINR maximization with known Doppler. To obtain a sub-optimal solution, we propose CD-based and ADMM-based

methods. Through the numerical results we evaluate the performance of the proposed methods and compare it with the state of the art.

Chapter 7

Joint spectral shaping and waveform orthogonality in MIMO radar systems implementation

In this chapter we address the joint spectral shaping and orthogonality problem in MIMO radar system. To this end, we deal with spectral nulling problem (on undesired frequency), while having a good orthogonality. In this regards we present two studies. In the first study, we consider the range-ISL as design metric, then we express the problem in frequency domain using Parseval theorem. In this step, the spectral shaping (nulling) can be achieved by incorporating some weights in the objective function in frequency domain. In this approach, the two metrics (orthogonality and spectral shaping) are integrated in one objective functions which makes tackling easier. In order to solve the problem, we proposed an algorithm based on CD method. In the second study, we introduce the SILR and ICCL as design metrics for spectral shaping and orthogonality, respectively. We formulate the problem as weighted sum of these two metrics, which ables us to make a trade-off between SILR and ICCL. In order to solve the problem we use CD method. Finally, we implement the framework using a custom built SDR based prototype developed on USRP from NI to demonstrate the performance of the proposed method in real application.

7.1 Waveform Design for Range-ISL Minimization with Spectral Compatibility in MIMO Radars

Cognitive radar systems are smart sensors which have a dynamic interaction with environment. These radars optimally adapt their transmit, receive and other parameters to the environment to enhance its performance [11]. Resource management in cognitive MIMO radar is becoming crucial for next-generation of active sensing and communications [111]. In general, there are three important resources, the time (range), spectral and spatial [57]. In time (range) domain, low auto and cross-correlation sidelobes level are required, to avoid masking weak targets within the range sidelobes of a strong target and to obtain orthogonality, respectively [17, 37, 58]. In Spatial domain, transmit beampattern shaping is used to control the spatial distribution of the transmit power [26, 39, 44]. In spectral domain, spectral shaping has a key role in spectral sharing for coexistence between MIMO radar and other RF systems [110, 114, 172, 173].

In this section we consider the range-ISL minimization problem in time (range) domain with spectral compatibility. We consider solving the problem under discrete phase MPSK sequences which requires limited valued phase shifters. In general, there are two approaches to tackle this problem. First, solving an optimization problem where, the range-ISL minimization and spectral compatibility as objective function and constraint, respectively [90]. Another approach is solving a bi objective optimization problem of range-ISL and spectral shaping with weighted sum method [97]. However, in this section we consider one objective function to tackle the problem. To this end, we express the range-ISL function in frequency domain using the Parseval theorem. Then we incorporate weights to the objective function to control the spectral response of the waveform. To solve the problem we proposed an iterative algorithm based on CD method which decreases the objective function monotonically in each iteration. In the numerical results we show the performance of the proposed method and we compare it with its counterpart.

We organize this section as follows. In subsection 7.1.1, we introduce the system model and problem statement. Subsection 7.1.2 presents the proposed CD based framework whose performance is numerically assessed in subsection 7.1.3

Notations: The following notations is adopted. Bold lower and uppercase letters for vectors matrices, respectively. $\mathbf{Diag}\{\mathbf{a}\}$, $(.)^T$, $(.)^*$, $(.)^r$, $|.|$, $\lfloor . \rceil$ and $\odot$ denote the diagonal matrix of vector $\mathbf{a}$, transpose, sequence reversal, conjugate, absolute value, round and Hadamard product respectively. The letter j represents the imaginary unit (i.e., $j = \sqrt{-1}$).

7.1.1 System Model and Problem Formulation

Let $\mathbf{X} \in \mathbb{C}^{M,N}$ be the transmitted sequence in MIMO radar system with M transmitters and the sequence length of N. At time sample n, the waveform transmitted through the M antennas is denoted by $\mathbf{x}_n$, where,

$$\mathbf{x}_n = [x_{1,n}, x_{2,n}, \dots, x_{M,n}]^T \in \mathbb{C}^M. \tag{7.1}$$

In (7.1), $x_{m,n}$ denotes the n^{th} sample of the m^{th} transmitter. The aperiodic cross-correlation of $\mathbf{x}_m$ and $\mathbf{x}_{m'}$ is defined as,

$$r_{m,m'}(k) \triangleq \sum_{n=1}^{N-k} x_{m,n} x^*_{m',n+k}, \tag{7.2}$$

where $m, m' \in \{1, \dots, M\}$ are the transmit antennas indices and $l \in \{-N+1, \dots, N-1\}$ is the lag of cross-correlation. If $m = m'$, (7.2) represents the aperiodic auto-correlation of signal $\mathbf{x}_m$. The zero lag of auto-correlation represents the peak of the matched filter output and contains the energy of sequence, while the other lags ($l \neq 0$) are referred to the sidelobes. The range-ISL can therefore be expressed by [39],

$$\text{ISL} = \sum_{m,m'=1}^{M} \sum_{l=-N+1}^{N-1} |r_{m,m'}(k)|^2 - MN^2. \tag{7.3}$$

Please note that, the MN^2 term in (7.3) is the peak of the matched filters output, where is a constant value for constant modulus waveforms ($\sum_{m=1}^{M} |r_{m,m}(0)|^2 = MN^2$). Therefore the range-ISL as objective function can be equivalently written as $f(\mathbf{X}) \triangleq \sum_{m,m'=1}^{M} \sum_{l=-N+1}^{N-1} |r_{m,m'}(l)|^2$.

Based on Parseval theorem the range-ISL minimization problem can be written in the frequency domain as, $f(\mathbf{X}) = \frac{1}{2N-1} \sum_{m,m'=1}^{M} \sum_{k=-N+1}^{N-1} |R_{m,m'}(k)|^2$, where, $R_{m,m'}(k)$ indicates the Fourier transform of $r_{m,m'}(l)$. Let $\mathbf{F} \triangleq [\mathbf{f}_0, \dots, \mathbf{f}_{2N-2}] \in \mathbb{C}^{(2N-1)\times(2N-1)}$ be the DFT matrix, where, $\mathbf{f}_k \triangleq [1, e^{-j\frac{2\pi k}{2N-1}}, \dots, e^{-j\frac{2\pi k(2N-2)}{2N-1}}]^T \in \mathbb{C}^{2N-1}$, $k = \{0, \dots, 2N-2\}$. Hence, we have, $R_{m,m'}(k) = \mathbf{F}\bar{\mathbf{x}}_m \odot \mathbf{F}\bar{\mathbf{x}_m^r}^*$, where, $\bar{\mathbf{x}}_t \in \mathbb{C}^{(2N-1)}$ is the $N-1$ zero pad version of $\mathbf{x}_t$, i.e. $\bar{\mathbf{x}}_t \triangleq [\mathbf{x}_t; \underbrace{0; \dots; 0}_{N-1}]$. In this regards, we consider the following optimization problem,

$$\begin{cases} \min\limits_{\mathbf{X}} & f(\mathbf{X}) = \sum_{m,m'=1}^{M} \left\| \mathbf{w} \odot \mathbf{F}\bar{\mathbf{x}}_m \odot \mathbf{F}\bar{\mathbf{x}_m^r}^* \right\|_2^2 \\ s.t. & x_{m,n} \in \mathcal{X}_L, \end{cases} \tag{7.4}$$

where, $\mathcal{X}_L$ indicates the discrete phase sequence with L alphabet size. More precisely, $\mathcal{X}_L = \{e^{j\phi} | \phi \in \Omega_L\}$, where $\Omega_L \triangleq \{0, \frac{2\pi}{L} \dots, \frac{2\pi(L-1)}{L}\}$; and, $\mathbf{w} = [w_0, \dots, w_{2N-2}]^T$, $0 \leq w_k \leq 1$, $k \in \{0, \dots, 2N-2\}$. Please note that, choosing $w_k = 1$, leads to range-ISL

minimization. Besides, by choosing appropriate value for $\mathbf{w}$ the spectral response can be shaped. In this regards, let $\mathcal{U} = \cup_{k=1}^{K}(u_{k,1}, u_{k,2})$ be the K number of normalized frequency stop-bands ($K \leq 2N-1$), where $0 \leq u_{k,1} < u_{k,2} \leq 1$ and $\cap_{k=1}^{K}(u_{k,1}, u_{k,2}) = \varnothing$. Thus, the undesired discrete frequency bins are given by $\mathcal{V} = \cup_{k=1}^{K}(\lfloor (2N-1)u_{k,1} \rceil, \lfloor (2N-1)u_{k,2} \rceil)$. Therefore the weights $\mathbf{w}$ can be obtained by,

$$w_k = \begin{cases} 1 & k \in \mathcal{V} \\ 0 & k \notin \mathcal{V} \end{cases}, \quad k \in \{1, \ldots, 2N-1\}. \tag{7.5}$$

Problem (7.4) is a multi-variable, non-convex and NP-hard optimization problem. In the following we proposed a CD-based method to obtain a local optimum solution.

7.1.2 Proposed Method

In CD based methods we need to consider one entry of $\mathbf{X}$ as being the only variable while keeping the others fixed; for this identified variable, we optimize the objective function. This methodology is efficient when the objective function can be written in a simplified form for that identified variable [24]. To this end, First we express the problem with respect to t^{th} transmitter, then we express it with the d^{th} sample. Let $\mathbf{x}_t$ be the only variable block, while other blocks are held fixed and stored in the matrix $\mathbf{X}_{-t} \triangleq [\mathbf{x}_1^T; \ldots; \mathbf{x}_{t-1}^T; \mathbf{x}_{t+1}^T; \ldots; \mathbf{x}_M^T] \in \mathbb{C}^{(M-1)\times N}$. In this case, the function $f(\mathbf{X})$ can be decomposed to a term independent of the optimization variable $\mathbf{x}_t$, and two other terms, one indicating the auto-correlation of $\mathbf{x}_t$, and the other is its cross-correlation with the other sequences of the set $\mathbf{X}_{-t}$. Precisely,

$$f(\mathbf{X}) = f_m(\mathbf{X}_{-t}) + f_{au}(\mathbf{x}_t) + f_{cr}(\mathbf{x}_t, \mathbf{X}_{-t}). \tag{7.6}$$

Since, $f_m(\mathbf{X}_{-t})$ does not depend on $\mathbf{x}_t$, therefore it can be ignored in the objective function. Thus, it can be shown that,

$$\begin{aligned} f_{au}(\mathbf{x}_t) &= \left\| \mathbf{w} \odot \mathbf{F}\bar{\mathbf{x}}_t^{r\,*} \odot \mathbf{F}\bar{\mathbf{x}}_t \right\|_2^2, \\ f_{cr}(\mathbf{x}_t, \mathbf{X}_{-t}) &= \sum_{\substack{m=1 \\ m\neq t}}^{M} \left\| \mathbf{w} \odot \mathbf{F}\bar{\mathbf{x}}_m^{r\,*} \odot \mathbf{F}\bar{\mathbf{x}}_t \right\|_2^2, \end{aligned} \tag{7.7}$$

Let us assume that $x_{t,d}$ is the only variable at $(i)^{th}$ iteration of the optimization procedure. In this regards $f(\mathbf{X})$ can be written with respect to $x_{t,d}$ as (see Appendix F.1),

$$f(x_{t,d}, \mathbf{X}_{-(t,d)}^{(i)}) = a_0 x_{t,d}^2 + a_1 x_{t,d} + a_2 + a_3 x_{t,d}^* + a_4 {x_{t,d}^*}^2, \tag{7.8}$$

where the coefficients are given in the Appendix F.1. Here, $\mathbf{X}^{(i)}_{-(t,d)} \triangleq \mathbf{X}^{(i)}|_{x_{t,d}=0}$ refers to the fixed entries. By substituting $x_{t,d} = e^{j\phi}$, (7.8) depends only on parameter ϕ [1]. In this case, since $\phi \in \mathcal{X}_L$ is chosen from a limited alphabet of length L, the objective function can be written with respect to the indices of $\mathcal{X}_L$ as, $f^{(i)}(\ell) = e^{j\frac{4\pi\ell}{L}} \sum_{n=0}^{4} a_n e^{j\frac{2\pi n\ell}{L}}$, where, $\ell = \{0, \ldots, L-1\}$. The summation term in the aforementioned equation is exactly the definition of $L-$point DFT of sequences $[a_0, a_1, a_2, a_3, a_4]$. Therefore we have,

$$f^{(i)}(\ell) = \mathbf{h} \odot \mathcal{F}_L\{a_0, a_1, a_2, a_3, a_4\}, \tag{7.9}$$

where, $\mathbf{h} \triangleq [1, e^{j\frac{4\pi}{L}}, \ldots, e^{j\frac{4\pi(L-1)}{L}}]^T \in \mathbb{C}^L$ and $\mathcal{F}_L$ is $L-$point DFT operator. Please note that the current function is only valid for $L \geqslant 5$. According to periodic property of DFT, $f^{(i)}(\ell)$ can be written as,

$$\begin{aligned}
L = 4 &\Rightarrow f^{(i)}(\ell) = \mathbf{h} \odot \mathcal{F}_L\{a_0 + a_4, a_1, a_2, a_3\},\\
L = 3 &\Rightarrow f^{(i)}(\ell) = \mathbf{h} \odot \mathcal{F}_L\{a_0 + a_3, a_1 + a_4, a_2\},\\
L = 2 &\Rightarrow f^{(i)}(\ell) = \mathbf{h} \odot \mathcal{F}_L\{a_0 + a_2 + a_4, a_1 + a_3\}.
\end{aligned}$$

Therefore the optimum solution of (7.9) is, $\ell^{\star(i)} = \arg \min_{\ell=1,\ldots,L-1} \left\{ f^{(i)}(\ell) \right\}$, then the optimum phase is,

$$\phi^{\star(i)} = \frac{2\pi\ell^{\star(i)}}{L}. \tag{7.10}$$

Subsequently, the variable $x_{t,d}$ will be updated by ${x^{\star}_{t,d}}^{(i)} = e^{j\phi^{\star(i)}}$. This procedure will continue for other entries until the stationary point is obtained. We consider $\frac{1}{\sqrt{MN}} \left\| \mathbf{X}^{(i)} - \mathbf{X}^{(i-1)} \right\|_F < \zeta$, $(\zeta > 0)$ as stopping criterion of optimization. The proposed method is summarized in **Algorithm 13**.

7.1.3 Numerical Results

In this subsection we consider to evaluate the performance of the proposed method and compare it with the state-of-the art counterparts. In this regards, we assume that the stopping condition for **Algorithm 8** is set at $\zeta = 10^{-5}$.

7.1.3.1 Convergence

Figure 7.1 shows the convergence behavior the objective function and the argument. For these figures, we assume that the undesired normalized frequency are located at $\mathcal{U} = [0.3, 0.35] \cup [0.4, 0.45] \cup [0.7, 0.8]$ and the algorithm 8 is initialized with random MPSK

[1] For the convenience we use ϕ instead of $\phi_{t,d}$ in the rest of the section.

Subroutine Procedure 13 : Spectral Compatible Range-ISL minimization.

Input: $\mathbf{X}^{(0)}$ and $\mathbf{w}$.
Initialization: $i := 0$.
Optimization:

1. **while** $\frac{1}{\sqrt{MN}}\left\|\mathbf{X}^{(i)} - \mathbf{X}^{(i-1)}\right\|_F < \zeta$ **do**
2. $\quad i := i + 1$;
3. $\quad$ **for** $t = 1, \ldots, M$ **do**
4. $\quad\quad$ **for** $d = 1, \ldots, N$ **do**
5. $\quad\quad\quad$ Optimize $x_{t,d}^{(i-1)}$ and obtain $x_{t,d}^{\star}$;
6. $\quad\quad\quad$ Update $x_{t,d}^{(i)} = x_{t,d}^{\star}$;
7. $\quad\quad\quad$ $\mathbf{X}^{(i)} = \mathbf{X}_{-(t,d)}^{(i)}\big|_{x_{t,d}=x_{t,d}^{(i)}}$;
8. $\quad\quad$ **end for**
9. $\quad$ **end for**
10. **end while**

Output: $\mathbf{X}^{\star} = \mathbf{X}^{(i)}$.

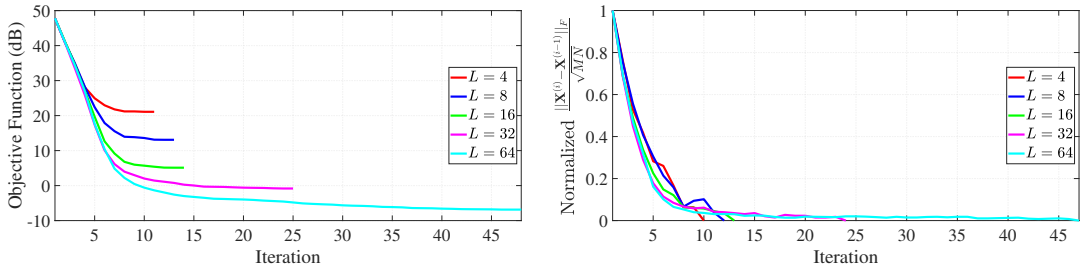

(A) Objective function (B) Argument

FIGURE 7.1: Convergence behavior of the proposed method with different alphabet size ($M = 4$, $N = 128$, and $\mathcal{U} = [0.3, 0.35] \cup [0.4, 0.45] \cup [0.7, 0.8]$)

sequence with alphabet size of $L = 4$. Figure 7.1a shows the convergence behavior of the objective function with different alphabet sizes. As can be seen, in all cases the objective function decreases monotonically. By increasing the alphabet size of the waveform the feasible set of the problem increases, therefore the performance of the proposed method becomes better. Figure 7.1b shows the convergence behavior of the argument of the problem. Observe that in all cases the argument converges to the optimum value.

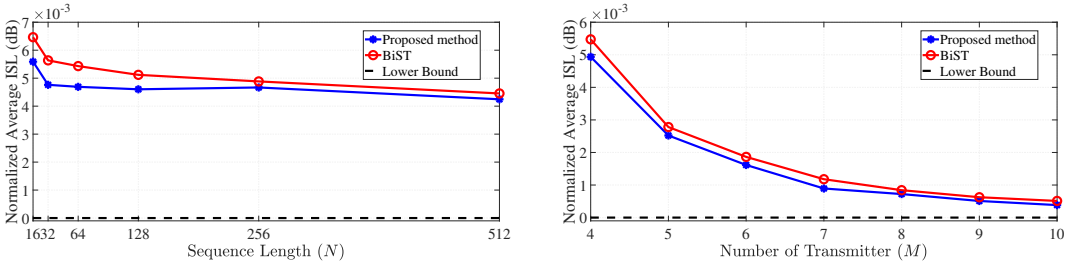

(A) Different sequence length ($M = 4$)

(B) Different number of transmitters ($N = 128$)

FIGURE 7.2: Comparison of average range-ISL of the proposed method with BiST and the lower bound with 10 number of trials ($L = 32$).

7.1.3.2 Range-ISL Minimization

The range-ISL minimization can be obtained by setting $w_k = 1, k \in \{1, \ldots, 2N-1\}$. Figure 7.2a and Figure 7.2b compare the average range-ISL of the proposed method with BiST and the lower bound which is given by, $N^2M(M-1)$, with different sequence length and number of transmitters, respectively. As can be seen in both cases the proposed method offers lower range-ISL compared to BiST.

7.1.3.3 Spectral Shaping

Figure 7.3 compares the performance of the proposed method with [174] in terms of spectral shaping. The authors in [174], address the spectral shaping and orthogonality in MIMO radar systems under discrete and continuous phase constraint. They proposed a weighted sum approach to make a trade off between spectral shaping and orthogonality. By choosing $\theta = 1$, [174] offers the optimum spectral response. As can be seen, the performance of the proposed method is similar to [174]. However, the range-ISL of the proposed method and [174] are 341767 and 355793, respectively. This indicates that the proposed method offers lower range-ISL rather than [174].

7.2 Cognitive Radar Prototype for Coexistence with Communications

Spectrum congestion has become an imminent problem with multitude of radio services like wireless communications, active RF sensing and radio astronomy vying for the scarce usable spectrum. Within this conundrum of spectrum congestion, radars need to cope with simultaneous transmissions from other RF systems. Spectrum sharing with

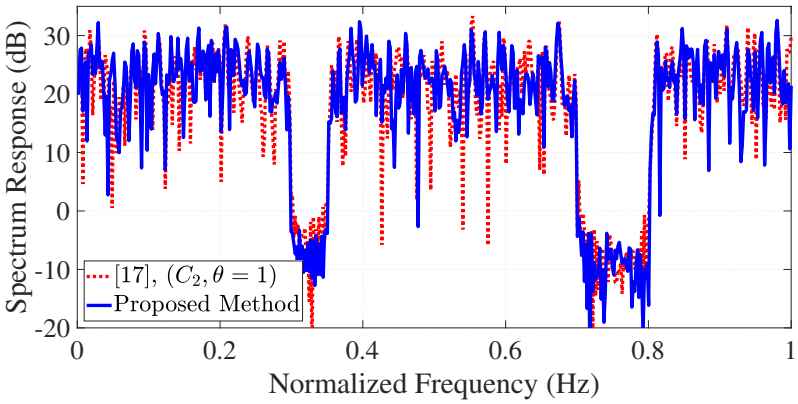

FIGURE 7.3: Comparison of spectrum response of the proposed method with [174] ($M = 4$, $N = 256$, $L = 64$ and $\mathcal{U} = [0.3, 0.35] \cup [0.7, 0.8]$)

communications being the highly plausible scenario given the need for high bandwidth in both systems [110, 114, 172]. While elaborate allocation policies are in place to regulate the spectral usage, the rigid allocations result in inefficient spectrum utilization when the subscription is sparse. In this context, smart spectrum utilization offers a flexible and a fairly promising solution for improved system performance in the emerging smart sensing systems [175].

Two paradigms, *Cognition* and *MIMO* have been central to the prevalence of smart sensing systems. Herein, the former concept offers ability to choose intelligent transmission strategies based on prevailing environmental conditions and a prediction of the behaviour of the emitters in the scene, in addition to the now ubiquitous receiver adaptation [69–72, 119, 176–179]. The second concept, offers a canvas of transmission strategies to the cognition manager to select from; these strategies exploit waveform diversity and the available degrees of freedom [180, 181]. Smart sensing opens up the possibility of coexistence of radar systems with incumbent communication systems in the earlier mentioned spectrum sharing instance. A representative coexistence scenario is illustrated in Figure 7.4, where an understanding of the environment is essential for seamless operation of radar systems while opportunistically using the spectrum allocated to communication [117, 182, 183].

In this chapter, we design a cognitive MIMO radar system towards fostering coexistence with communications; it involves spectrum sensing and transmission strategies adapted to the sensed spectrum while accomplishing the radar tasks and without degrading the performance of communications. Particularly, a set of transmit sequences is designed to focus the emitted energy in the bands suggested by the spectrum sensing module while limiting the out-of-band interference. The waveforms, along with the receive processing, are designed to enhance the radar detection performance. The designed system is then demonstrated for the representative scenario of Figure 3.10 using a custom built SDR

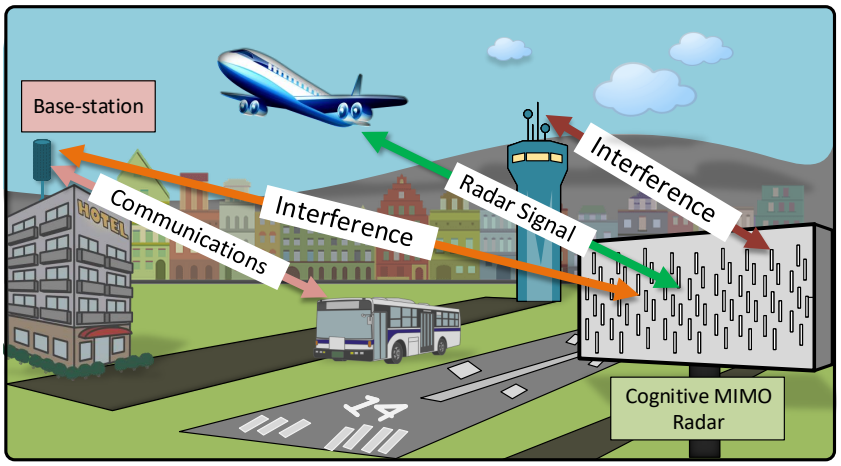

FIGURE 7.4: An illustration of coexistence between radar and communications. The radar aims to detect the airplane, without creating interference to the communication links, and similarly avoiding interference from the communication links.

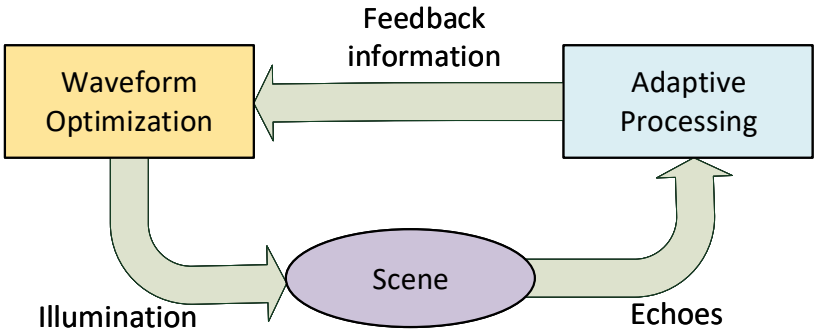

FIGURE 7.5: Sequence of operation in a cognitive radar system, including scanning of the environment, estimating the environmental parameters, and adapting the transceiver accordingly.

based prototype developed on USRPs[2] from NI [184, 185]. These USRPs operate at sub-6 GHz frequencies with a maximum instantaneous bandwidth of 160 MHz.

Notations: This section uses lower-case and upper-case boldface for vectors ($\boldsymbol{a}$) and matrices ($\boldsymbol{A}$), respectively. The conjugate, transpose and the conjugate transpose operators are denoted by $(.)^*$, $(.)^T$, and $(.)^\dagger$, respectively. The Frobenius norm, l_2 norm, absolute value and round operator are denoted by $\|.\|_F$, $\|.\|_2$, $|.|$ and $\lfloor . \rceil$ respectively.

7.2.1 Cognitive Radar

The scenario under consideration in this chapter is one where a radar system desires to operate in the presence of interfering signals that are generated by communication systems. The radar system will benefit from using as much bandwidth as possible. This

[2]USRPs are inexpensive programmable radio platforms used in wireless communications and sensing prototyping, teaching and research.

will improve the systems range resolution and accuracy, but requires the radar system to avoid the frequency band occupied by communication signals for two reasons:

[A] - *To enhance the performance of the communications, that requires the radar system does not interfere with the communication signals.*

[B] - *To improve the sensitivity of the radar system for detecting targets with very small SINR values. Indeed, by removing the communications interference, the radar SINR will be enhanced and thus the sensitivity of the radar system will be improved.*

Given the scenario under consideration, the cognitive radar requires to scan the environment; estimate the environmental parameters; and adapt the transceiver accordingly. These three steps are the high level structure for a cognitive loop or Perception/Action Cycle (PAC) that are indicated in Figure 7.5.

Thus, the first important step is to sense the RF spectrum. Once RF spectral information has been collected, then the interfering signals needs to be characterized and some specifications such as their center frequencies and bandwidths needs to be extracted. After that, radar must choose how to adapt given the obtained information from the interference. In this step, waveform optimization can be a solution, which provides the optimal solution for the given constraints, provided that it can be performed before any new change in the environmental parameters.

7.2.2 The Prototype Architecture

The prototype consists of three application frameworks as depicted in Figure 7.6; a) LTE Application Framework, b) Spectrum sensing application, and c) Cognitive MIMO radar application. A photograph of the proposed coexistence prototype is depicted in Figure 7.7. The hardware (HW) consists of three main modules: 1) USRP 2974 for LTE communications 2) USRP B210 for spectrum sensing, and 3) USRP 2944R for cognitive MIMO radar with specifications given in Table 7.1. USRPs are used for the transmission and reception of the wireless RF signals and the Rohde and Schwarz spectrum analyzer is used for the validation of the transmission.

7.2.2.1 LTE Application Framework

The LabVIEW LTE Application Framework (Figure 7.6a) is an add-on software that provides a real-time physical layer LTE implementation in the form of an open and modifiable source-code [186]. The framework complies with a selected subset of the 3GPP LTE which includes a closed-loop Over-The-Air (OTA) operation with channel state and

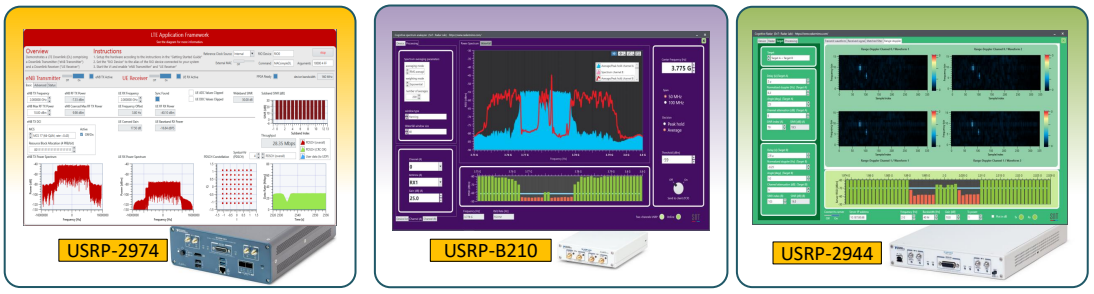

(A) LTE Application (B) Spectrum Sensing (C) MIMO Radar

FIGURE 7.6: Application frameworks forming the prototype: LTE application developed by NI, spectrum sensing and cognitive MIMO radar applications developed in this section.

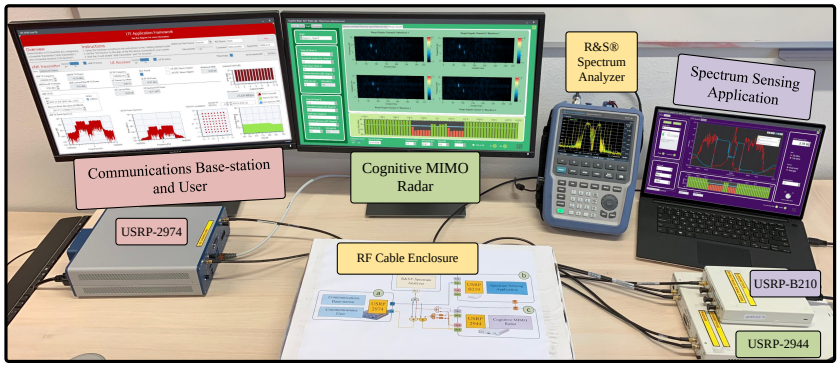

FIGURE 7.7: A photograph of the proposed coexistence prototype. The photo shows communication BS and user, spectrum sensing, and cognitive MIMO radar systems.

TABLE 7.1: Hardware characteristics of the proposed prototype

Parameters	**2974/2944R**	**B210**
Frequency range	10 MHz −6 GHz	70 MHz −6 GHz
Max. output power	20 dBm	10 dBm
Max. input power	+10 dBm	−15 dBm
Noise figure	5 − 7 dB	8 dB
Bandwidth	160 MHz	56 MHz
DACs	200 MS/s, 16 bits	61.44 MS/s, 12 bits
ADCs	200 MS/s, 14 bits	61.44 MS/s, 12 bits

ACK/ NACK feedback, 20 MHz bandwidth, PDSCH and Physical Downlink Control Channel (PDCCH), up to 75 Mbps data throughput, FDD and TDD configuration 5-frame structure, QPSK, 16-QAM, and 64-QAM modulation, channel estimation and zero-forcing channel equalization. The framework also has a basic MAC implementation to enable packet-based data transmission along with a MAC adaptation framework for rate adaptation. Since the NI-USRP 2974 has two independent RF chains and the Application Framework supports single antenna links, we emulated both the BS and communications user on different RF chains of the same USRP.

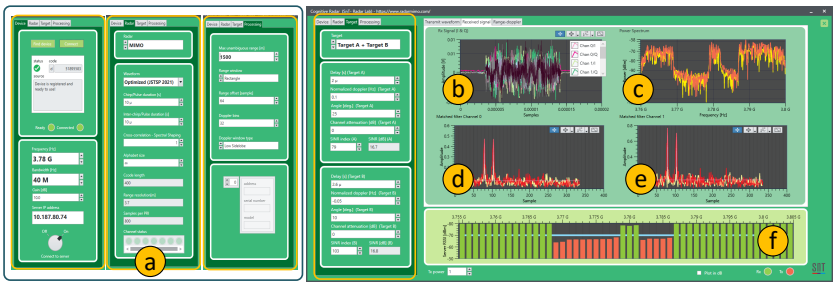

FIGURE 7.8: A snapshot of the developed cognitive MIMO radar application. (a) Settings for device, radar, and processing parameters. (b) I and Q signals of two receive channels. (c) Spectrum of the received signals in two receive channels. (d) Matched filters to two transmitting waveforms at the first receive channel. (e) Matched filters to two transmitting waveforms at the second receive channel. (f) Received information from the energy detector of the spectrum sensing application.

7.2.2.2 Spectrum Sensing Application

To perform the cognition and continuously sensing the environment, we developed an application based on LabView NXG 3.1 that connects to Ettus USRP B2xx (Figure 7.6b). The developed application is flexible in terms of changing many parameters on the fly, e.g., averaging modes, window type, energy detection threshold, and the USRP configurations (gain, channel, start frequency, etc.). In the developed application, the center frequency can be adjusted to any arbitrary value in the interval 70 MHz to 6 GHz, and the span bandwidth can be selected from the two values of 50 MHz, and 100 MHz[3]. The obtained frequency chart is being transferred through a network connection (LAN/Wi-Fi) to the cognitive MIMO radar application.

7.2.2.3 MIMO Radar Prototype

Figure 7.8 depicts a snapshot of the developed cognitive MIMO radar application framework, when the licensed band 3.78 GHz with 40 MHz bandwidth was used for transmission[4]. All the parameters related to the radar waveform, processing units, and targets can be changed and adjusted during the operation of the radar system. The MIMO radar application was developed based on LabView NXG 3.1, and was connected to the HW platform NI-USRP 2944R. This USRP consists of a 2×2 MIMO RF transceiver with a programmable Kintex-7 field programmable gate array (FPGA). The developed application is flexible in terms of changing the transmit waveform on the fly, such that it can adapt with the environment. Table 7.2 details the features and flexibilities of the developed application. The center frequency can be adjusted to any arbitrary value in

[3]Note that USRP B2xx provides 56 MHz of real-time bandwidth by using AD9361 RFIC direct-conversion transceiver. However, the developed application can analyze larger bandwidths by sweeping the spectrum with efficient implementation.

[4]SnT has experimental licence to use 3.75 - 3.8 GHz for 5G research in Luxembourg.

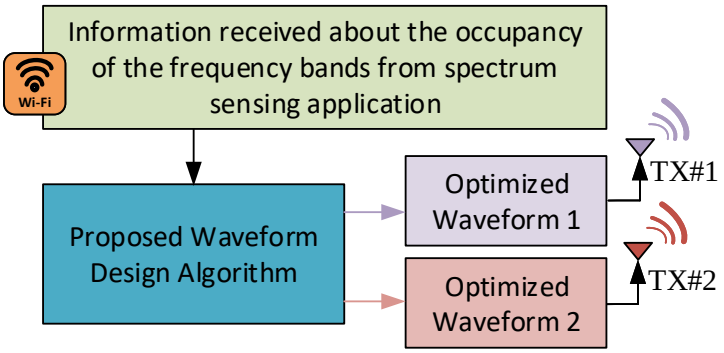

FIGURE 7.9: Block diagram of the transmitter in the developed cognitive MIMO radar application. A list of occupied frequency bands will determined by the spectrum sensing application. Based on this information, the proposed design algorithm optimizes the transmitting waveforms.

the interval 70 MHz to 6 GHz, and the radar bandwidth can be adjusted to any arbitrary value in the interval 1 MHz to 80 MHz.

TABLE 7.2: Characteristics of the developed cognitive MIMO radar

Parameters	**MIMO radar**
Bandwidth	$1 - 80$ MHz
Window type	Rectangle, Hamming, Blackman, etc.
Averaging mode	Coherent integration (FFT)
Processing units	Matched filtering, range-Doppler processing
Transmitting waveforms	Random-polyphase, Frank, Golomb, Random-Binary, Barker, m-Sequence, Gold, Kasami, Up-LFM, Down-LFM, and the optimized sequences

The block diagram of the transmit units of the developed cognitive MIMO radar is depicted in Figure 7.9. Note that the application is connected through a network (LAN/Wi-Fi) to the spectrum sensing application to receive a list of occupied frequency bands. Based on this information, the radar optimizes the transmitting waveforms. The design algorithm for the waveform optimization is described next.

7.2.2.4 Waveform Optimization

To perform waveform optimization in our developed cognitive radar prototype, we utilize the CD framework wherein a multi variable optimization problem can be sequentially solved as a sequence of (potentially easier) single variable optimization problems (see Chapter 5 for more details). The benefits of using CD framework for this prototype are listed below:

[A] - CD provides a sequential solution for the optimization problem which typically converges fast (comparing with the other optimization frameworks). Further, initial iterations of the CD algorithm, generally provide deep decrement in the objective value. Consequently, based on the limited available time for having a stationary environment, CD can be terminated after a few number of iterations.

[B] - CD converts a multivariable objective function to a sequence of single variable objective functions. As a result, the solutions of single variable problems are generally less complex than the original problem. This is helpful for real-time implementation of the optimization algorithm, where the algorithm does not need to do complex operations in every iteration.

Using the advantages of CD framework, we perform the waveform optimization given the limited time available for the scene to be remained stationary. This time in principle can be as small as one CPI time, or can be adjusted depending to the dynamic of the scene and the decision of the designer.

Let us now discuss in details the waveform design problem related to the scenario we pursued in this chapter. We consider a colocated narrow-band MIMO radar system, with M transmit antennas, each transmitting a sequence of length N in the fast-time domain. Let the matrix $\boldsymbol{X} \in \mathbb{C}^{M\times N} \triangleq [\mathbf{x}_1^T, \ldots, \mathbf{x}_M^T]^T$ denotes the transmitted set of sequences in baseband, where the vector $\mathbf{x}_m \triangleq [x_{m,1}, \ldots, x_{m,N}]^T \in \mathbb{C}^N$ indicates the N samples of the m^{th} transmitter ($m \in \{1, \ldots, M\}$). We aim to design a transmit set of sequences which have small cross-correlation among each others, while each of the sequences have a desired spectral behaviour. To this end, in the following, we introduce the SILR and ICCL metrics and subsequently the optimization problem to handle them.

Let $\boldsymbol{F} \triangleq [\mathbf{f}_0, \ldots, \mathbf{f}_{N-1}] \in \mathbb{C}^{N\times N}$ be the DFT matrix, where, $\mathbf{f}_k \triangleq [1, e^{j\frac{2\pi k}{N}}, \ldots, e^{j\frac{2\pi k(N-1)}{N}}]^T \in \mathbb{C}^N$, $k = \{0, \ldots, N-1\}$. Let $\mathcal{V}$ and $\mathcal{U}$ be the desired and undesired discrete frequency bands for MIMO radar, respectively. These two sets satisfy $\mathcal{V} \cup \mathcal{U} = \{0, \ldots, N-1\}$ and $\mathcal{V} \cap \mathcal{U} = \emptyset$. We define SILR as,

$$g_s(\boldsymbol{X}) \triangleq \frac{\sum_{m=1}^{M} \left\| \mathbf{f}_k^\dagger \mathbf{x}_m \right\|^2 | k \in \mathcal{U}}{\sum_{m=1}^{M} \left\| \mathbf{f}_k^\dagger \mathbf{x}_m \right\|^2 | k \in \mathcal{V}} \tag{7.11}$$

which is the energy of the radar waveform interfering with other incumbent services (like communications) relative to the energy of transmission in the desired bands. Optimizing the above objective function may shape the spectral-power of the transmitting sequence and satisfy a desired mask in the spectrum. However, in a MIMO radar it is necessary to separate the transmitting waveforms in the receiver to investigate the waveform diversity, which ideally requires orthogonality among the transmitting sequences. To make this

orthogonality feasible by CDM, we need to transmit a set of sequences which have small cross-correlations among each other. The aperiodic cross-correlation[5] of $\mathbf{x}_m$ and $\mathbf{x}_{m'}$ is defined as,

$$r_{m,m'}(l) = \sum_{n=1}^{N-l} x_{m,n} x^*_{m',n+l}, \tag{7.12}$$

where $m \neq m' \in \{1, \ldots, M\}$ are indices of the transmit antennas and $l \in \{-N+1, \ldots, N-1\}$ denotes the cross-correlation lag. We define ICCL as,

$$\widetilde{g}_c(\boldsymbol{X}) \triangleq \sum_{m=1}^{M} \sum_{\substack{m'=1 \\ m' \neq m}}^{M} \sum_{l=-N+1}^{N-1} |r_{m,m'}(l)|^2, \tag{7.13}$$

which can be used to promote the orthogonality among the transmitting sequences.

Problem Formulation We aim to design set of sequences with small SILR and ICCL values. To this end, we consider the following optimization problem,

$$\begin{cases} \min\limits_{\boldsymbol{X}} & g_s(\boldsymbol{X}), g_c(\boldsymbol{X}) \\ s.t. & C_1 \text{ or } C_2 \end{cases} \tag{7.14}$$

where $g_c(\boldsymbol{X}) = \frac{1}{(2MN)^2}\widetilde{g}_c(\boldsymbol{X})$ is the scaled version of the ICCL, defined in (7.13). By defining $\Omega_\infty = [0, 2\pi)$, and $\Omega_L = \left\{0, \frac{2\pi}{L}, \ldots, \frac{2\pi(L-1)}{L}\right\}$, then

$$C_1 \triangleq \{\boldsymbol{X} \mid x_{m,n} = e^{j\phi_{m,n}}, \phi_{m,n} \in \Omega_\infty\}, \tag{7.15}$$

and

$$C_2 \triangleq \{\boldsymbol{X} \mid x_{m,n} = e^{j\phi_{m,n}}, \phi_{m,n} \in \Omega_L\}, \tag{7.16}$$

indicate constant modulus constraint and discrete phase constraints, respectively.

Problem (7.14) is a bi-objective optimization problem in which a feasible solution that minimizes both objective functions may not exist [24, 143]. Scalarization is a well known technique that converts the bi-objective optimization problem to a single objective problem by replacing a weighted sum of the objective functions. Using this technique, the following Pareto-optimization problem will be obtained,

$$\mathcal{P} \begin{cases} \min\limits_{\boldsymbol{X}} & g(\boldsymbol{X}) \triangleq \theta g_s(\boldsymbol{X}) + (1-\theta) g_c(\boldsymbol{X}) \\ s.t. & C_1 \text{ or } C_2, \end{cases} \tag{7.17}$$

[5] In this chapter, we provide the solution to the design of sequences with good aperiodic correlation functions. However, following the same steps as indicated in [86], the design procedure can be extended to obtain sequences with good periodic correlation properties.

The coefficient $\theta \in [0,1]$ is a weight factor that effects trade-off between SILR and ICCL. In (7.17), $g_s(\boldsymbol{X})$ is a fractional quadratic function while $g_c(\boldsymbol{X})$ is quartic function, both with multiple variables. Further, both C_1 and C_2 constraints are not an affine set, besides C_2 is non-continuous and non-differentiate set. Therefore, we encounter a non-convex, multi-variable optimization problem [24, 78].

The Optimization Method Let us assume that $x_{t,d}$ is the only variable in code matrix $\mathbf{X}$ at $(i)^{th}$ iteration of CD algorithm, where the other entries are kept fixed and stored in the matrix $\boldsymbol{X}^{(i)}_{-(t,d)}$ defined by,

$$\boldsymbol{X}^{(i)}_{-(t,d)} \triangleq \begin{bmatrix} x^{(i)}_{1,1} & \dots & \dots & \dots & \dots & \dots & x^{(i)}_{1,N} \\ \vdots & \vdots & \vdots & \vdots & \vdots & \vdots & \vdots \\ x^{(i)}_{t,1} & \dots & x^{(i)}_{t,d-1} & 0 & x^{(i-1)}_{t,d+1} & \dots & x^{(i-1)}_{t,N} \\ \vdots & \vdots & \vdots & \vdots & \vdots & \vdots & \vdots \\ x^{(i-1)}_{M_t,1} & \dots & \dots & \dots & \dots & \dots & x^{(i-1)}_{M_t,N} \end{bmatrix}$$

The resulting single-variable objective function can be written as (see Appendix A),

$$g(x_{t,d}, \boldsymbol{X}^{(i)}_{-(t,d)}) = \theta \frac{a_0 x_{t,d} + a_1 + a_2 x^*_{t,d}}{b_0 x_{t,d} + b_1 + b_2 x^*_{t,d}} + (1-\theta)\left(c_0 x_{t,d} + c_1 + c_2 x^*_{t,d}\right) \tag{7.18}$$

where, the coefficients a_i, b_i and c_i depend on $\boldsymbol{X}^{(i)}_{-(t,d)}$ ($t \in \{1,\dots,M\}$ and $d \in \{1,\dots,N\}$) and are specified in Appendix A. By considering $g(x_{t,d}, \boldsymbol{X}^{(i)}_{-(t,d)})$ as the objective function of the single variable optimization problem, and substituting[6] $x_{t,d} = e^{j\phi}$, the optimization problem at i^{th} iteration of CD algorithm is

$$\mathcal{P}^{(i)}_{\phi} \begin{cases} \min\limits_{\phi} & \theta \dfrac{a_0 e^{j\phi} + a_1 + a_2 e^{-j\phi}}{b_0 e^{j\phi} + b_1 + b_2 e^{-j\phi}} + (1-\theta)\left(c_0 e^{j\phi} + c_1 + c_2 e^{-j\phi}\right) \\ s.t. & C_1 \text{ or } C_2, \end{cases} \tag{7.19}$$

Let us assume that $\phi^\star$ is the optimized phase value of $(t,d)^{th}$ entry of $\boldsymbol{X}$. This value can be found by solving (7.19), and consequently we obtain $x^\star_{t,d} = e^{j\phi^\star}$. After optimizing all the code entries ($t = 1,\dots,M$, and $d = 1,\dots,N$), a new iteration will be started, provided that the stopping criteria is not met. A summary of the devised optimization method is reported in **Algorithm 14**.

[6] For the sake of notational simplicity, we use ϕ instead of $\phi_{t,d}$ in the rest of this chapter.

Subroutine Procedure 14 The proposed method for designing set of sequences that avoid reserved frequency bands, and in the same time have small cross-correlation among each other.

Input: Initial set of feasible sequences, $\boldsymbol{X}^{(0)}$.
Initialization: $i := 0$.
Optimization:

- **while** the stopping criteria is not met, **do**
- $i := i + 1$;
- **for** $t = 1, \ldots, M$ **do**
- **for** $d = 1, \ldots, N$ **do**
- Optimize $x_{t,d}^{(i-1)}$ and obtain $x_{t,d}^{\star}$;
- Update $x_{t,d}^{(i)} = e^{j\phi^{\star}}$;
- $\boldsymbol{X}^{(i)} = \boldsymbol{X}_{-(t,d)}^{(i)}\big|_{x_{t,d}=x_{t,d}^{(i)}}$;
- **end for**
- **end for**
- **end while**

Output: $\boldsymbol{X}^{\star} = \boldsymbol{X}^{(i)}$.

Solution under continuous phase constraint Next step to finalize the waveform design part is to provide a solution to Problem $\mathcal{P}_{\phi}^{(i)}$. Let us define

$$g(\phi) = \theta \frac{a_0 e^{j\phi} + a_1 + a_2 e^{-j\phi}}{b_0 e^{j\phi} + b_1 + b_2 e^{-j\phi}} + (1-\theta)\left(c_0 e^{j\phi} + c_1 + c_2 e^{-j\phi}\right). \tag{7.20}$$

Since $g(\phi)$ is a differentiable function with respect to the variable ϕ, the critical points of (7.19) contain the solutions to $\frac{d}{d\phi} g(\phi) = 0$. By standard mathematical manipulations, the derivative of $g(\phi)$ can be obtained as,

$$g'(\phi) = \frac{e^{j3\phi} \sum_{p=0}^{6} q_p e^{jp\phi}}{(b_0 e^{j\phi} + b_1 + b_2 e^{-j\phi})^2}, \tag{7.21}$$

where, the coefficients q_p are given in Appendix B. Using the slack variable $z \triangleq e^{-j\phi}$, the critical points can be obtained by obtaining the roots of six degree polynomial of $g'(z) \triangleq \sum_{p=0}^{6} q_p z^p = 0$. Let us assume that z_p, $p = \{1, \ldots, 6\}$ are the roots of $g'(z)$. Hence, the critical points of (7.19) can be expressed as, $\phi_p = j \ln z_p$. Since ϕ is a real variable, we seek only the real extrema points. Therefore, the optimum solution for ϕ is,

$$\phi_c^{\star} = \arg\min_{\phi} \left\{ g(\phi) | \phi \in \phi_p, \Im(\phi_p) = 0 \right\}. \tag{7.22}$$

Subsequently, the optimum solution for is $x_{t,d} = e^{j\phi_c^\star}$[7].

Solution under discrete phase constraint In this case, the feasible set is limited to a set of L phases. Thus, the objective function with respect to the indices of Ω_L can be written as,

$$g(l) = \theta \frac{\sum_{n=0}^{2} a_n e^{-j\frac{2\pi nl}{L}}}{\sum_{n=0}^{2} b_n e^{-j\frac{2\pi nl}{L}}} + (1-\theta) e^{\frac{j2\pi l}{L}} \sum_{n=0}^{2} c_n e^{-j\frac{2\pi nl}{L}} \tag{7.23}$$

where, $l = \{0, \ldots, L-1\}$. The summation term in the numerator and denominator in Equation (7.23) is exactly the definition of $L-$point DFT of sequences $[a_0, a_1, a_2]$, $[b_0, b_1, b_2]$ and $[b_0, b_1, b_2]$ respectively. Therefore, $g(l)$ can be written as,

$$g(l) = \theta \frac{\mathcal{F}_L\{a_0, a_1, a_2\}}{\mathcal{F}_L\{b_0, b_1, b_2\}} + (1-\theta)\boldsymbol{h} \odot \mathcal{F}_L\{c_0, c_1, c_2\}. \tag{7.24}$$

where $\boldsymbol{h} = [1, e^{-j\frac{2\pi}{L}}, \ldots, e^{-j\frac{2\pi(L-1)}{L}}]^T \in \mathbb{C}^L$ and $\mathcal{F}_L$ is $L-$point DFT operator. The current function is valid only for $L > 2$. According to periodic property of DFT, for binary $g(l)$ can be written as,

$$g(l) = \theta \frac{\mathcal{F}_L\{a_0 + a_2, a_1\}}{\mathcal{F}_L\{b_0 + b_2, b_1\}} + (1-\theta)\boldsymbol{h} \odot \mathcal{F}_L\{c_0 + c_2, c_1\}. \tag{7.25}$$

Finally $l^\star = \arg\min_{l=1,\ldots,L} \{g(l)\}$, and $\phi_d^\star = \frac{2\pi(l^\star-1)}{L}$.

7.2.2.5 Adaptive Receive Processing

The block diagram of the receive units of the developed cognitive MIMO radar is depicted in Figure 7.10. The receiver starts sampling by a trigger that is received by transmitter, indicating the start of transmission (possibility of working in Continuous Wave (CW) mode is supported). In each receive channel, two filters matched to each of the transmitting waveforms is implemented using the fast convolution technique. Four range-Doppler plots corresponding to the receive channels and transmitting waveforms are obtained by implementing FFT in the slow-time dimension.

[7]Since $g(\phi)$ is a function of $\cos\phi$ and $\sin\phi$, it is periodic, real and differentiable. Therefore, it has at least two extrema, and hence its derivative has at least two real roots. Thus, Ω is never a null set. As a result in each single variable update, the problem has a solution and never becomes infeasible.

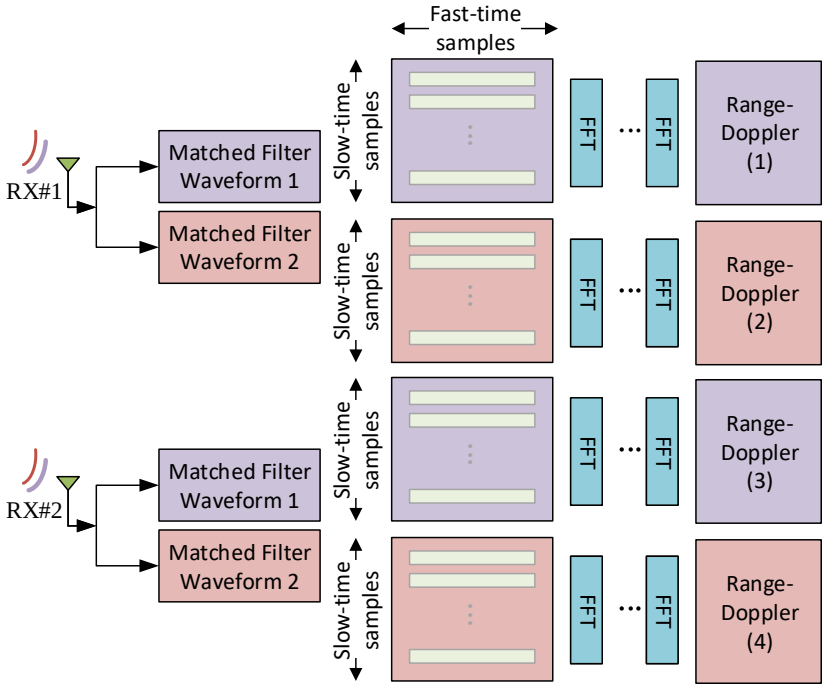

FIGURE 7.10: Block diagram of the receiver of the developed cognitive MIMO radar application. The coefficients of the matched filter will be updated for appropriate matched filtering in the fast-time dimension. Consequently, the modulus of the range-Doppler plots will be calculated after taking FFT in the slow-time dimension.

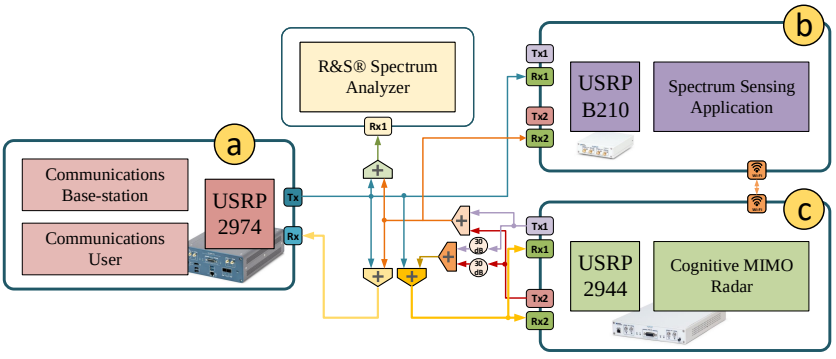

FIGURE 7.11: The connection diagram of the proposed coexistence prototype.

7.2.3 Experiments and Results

In this subsection, we present present experiments conducted using the developed prototype and analyze the HW results. For the practical applicability of our methods and verification of the simulation, we established all the connections shown in Figure 7.11 using RF cables and splitters/ combiners, and measured the performance in a controlled environment.

Passing the transmitting waveforms through the 30 dB attenuators as indicated in Figure 7.11, a reflection will be generated; this will be used to generate the targets, contaminated with the communications interference. The received signal in this way will

be further shifted in time, frequency and spatial direction to create the simulated targets. These targets will be detected after calculating the absolute values of the range-Doppler maps.

The transmitting waveforms can be selected based on the options in Table 7.2 or obtained based on **Algorithm 14**. When executing the application, input parameters to optimize the waveforms pass from the Graphical User Interface (GUI) to MATLAB, and the optimized set of sequences are passed to the application through the GUI. The other processing blocks of the radar system including matched filtering, Doppler processing, and scene generation are developed in the LabView G dataflow application. Table 7.3 and Table 7.4 summarize the parameters used for radar and targets in this experiment.

TABLE 7.3: Radar experiment parameters

Parameters	**Value**
Center frequency	2 GHz
Real-time bandwidth	40MHz
Transmit and receive channels	2×2
Transmit power	10 dBm
Duty cycle	50%
Transmit code length	400
Pulse repetition interval	20μs

For the LTE communications, we established the downlink between a BS and one user. Nonetheless, the experiments can be also be performed with uplink LTE as well as bi-directional LTE link. LabVIEW LTE framework offers the possibility to vary the MCS of PDSCH from 0 to 28 where the constellation size goes from QPSK to 64QAM [187]. LTE uses PDSCH for the transport of data between the BS and the user. Table 7.5 indicates the experimental parameters used in our test set-up for the communications.

In Figure 7.12, we assess the convergence behaviour of the proposed algorithm in case $M = 4$, and $N = 64$ for the first 100 iterations. It can be observed that given a few number of iterations, the objective value decreases significantly. This behaviour is the same for different values of θ, and also under C_1 or C_2 constraints. Note that the optimized solution under C_1 constraints obtain lower objective values comparing to the solution of C_2 constraint, due to a more degree of freedom in selecting the alphabet size.

Let us now, terminate the optimization procedure at iteration 10, and see the performance of the obtained waveform at this iteration, comparing with SHAPE [1] which is an algorithm for shaping the spectrum of the waveforms using spectral-matching framework. Figure 7.13 shows spectral behaviour and cross-correlation levels of the optimized waveforms in case $M = 2$, $N = 400$, and $\mathcal{S} = [0.25, 0.49] \cup [0.63, 0.75]$ Hz.

TABLE 7.4: Target experiment parameters

Parameters	**Target 1**	**Target 2**
Range delay	2μs	2.6μs
Normalized Doppler	0.2 Hz	-0.25 Hz
Angle	25 deg	15 deg
Attenuation	30 dB	35 dB

TABLE 7.5: Communications experiment parameters

Parameters	**Value**
Communication MCS	MCS0 (QPSK 0.12) MCS10 (16QAM 0.33) MCS17 (64QAM 0.43)
Center frequency (Tx and Rx)	2 GHz
Bandwidth	20 MHz

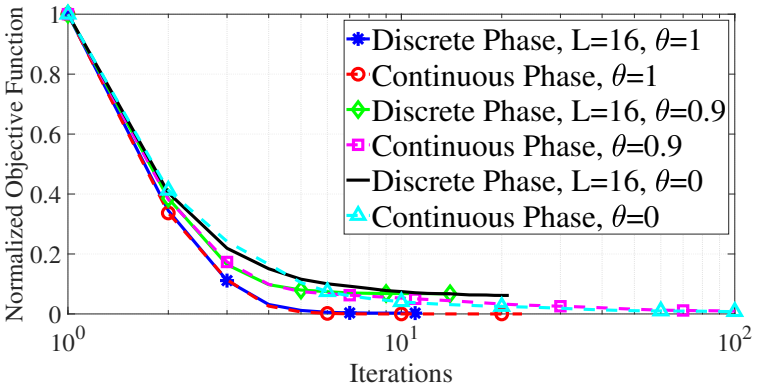

FIGURE 7.12: Convergence behaviour of the proposed method under continuous and discrete phase constraints for different θ values ($M = 4$, $N = 64$ and $L = 16$).

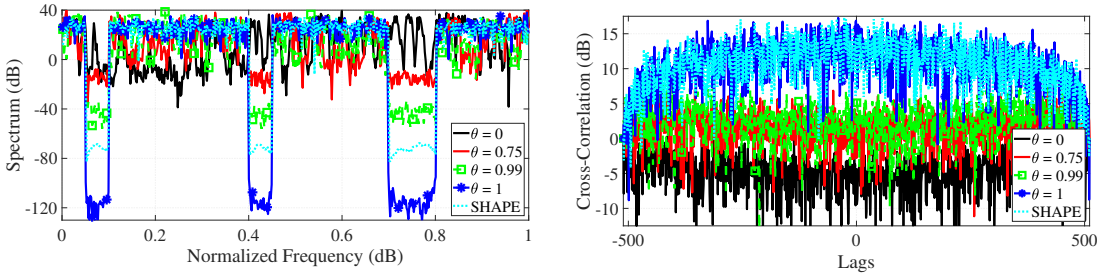

(A) Spectrum of the proposed method for different values of θ.

(B) Cross-correlation of the proposed method for different values of θ .

FIGURE 7.13: The impact of θ value on trade-off between (a) spectral shaping and (b) cross-correlation levels in comparison with SHAPE [1] ($M = 2$ and $N = 512$).

It is observable that by choosing $\theta = 0$, the optimized waveforms are not able to put notches on the undesired frequencies. By increasing θ, the notches will appear gradually

and in case of $\theta = 1$, we obtain the deepest notches. However, when $\theta = 1$ the cross-correlation is at the highest level which decreases with θ. In case $\theta = 0$, we obtain the best orthogonality. Therefore, by choosing an appropriate value of θ, one can make a good trade-off between spectral shaping and orthogonality. For instance, choosing $\theta = 0.75$ is able to put a null level around 50 dB (see Figure 7.13a), while having relatively good cross-correlation level (see Figure 7.13b).

Based on the aforementioned analysis, we set $\theta = 0.75$, and always terminate the algorithm after 10 iterations, for optimizing radar waveform. In this case, we show the impact of optimized radar waveform on a coexistence with communications scenario with the experiment. We use the experiment parameters reported in Table 7.3 and Table 7.5 for radar and communications, respectively. According to these tables, we utilize the radar with a 50% duty cycle. By transmitting a set of $M = 2$ waveforms with length $N = 400$, radar transmissions will occupy a bandwidth of 40 MHz with some nulls which will be obtained adaptively based on the received feedback from the spectrum sensing application. On the other side, the LTE communications framework utilizes 20 MHz bandwidth for transmission. To have some nulls that can be utilized by radar in the spectrum of communications, we select the allocation 111111111110000000111111 for the LTE resource blocks (4 physical resource blocks/bit), where the entry "1" indicates the use of the corresponding time-bandwidth resources in the LTE application framework. The spectrum of this LTE downlink is measured with the developed spectrum sensing application as depicted in Figure 7.14. This figure serves two purposes, (i) focusing on the LTE downlink spectrum, it validates the spectrum analyzer application with a commercial product, and (ii) it clearly indicates that the desired objective of spectrum shaping is met. The impact of this matching on performance of radar and communications are presented next.

When the radar is not aware of the presence of communications, it transmits optimized sequences when $\theta = 0$. In this case, radar utilizes the entire bandwidth and the two system mutually interfere. In fact, the operations of both radar and communications are disrupted as depicted in Figure 7.15 (a and c), thereby creating difficulties for their coexistence. In this case, by utilizing the optimized waveforms obtained by $\theta = 0.75$, the performance of both systems are enhanced as indicated pictorially in Figure 7.15 (b and d).

7.2.4 Performance Analysis

To measure the performance of the proposed prototype, we calculate the SINR of the two targets for radar while on the communication side, we report the PDSCH throughput

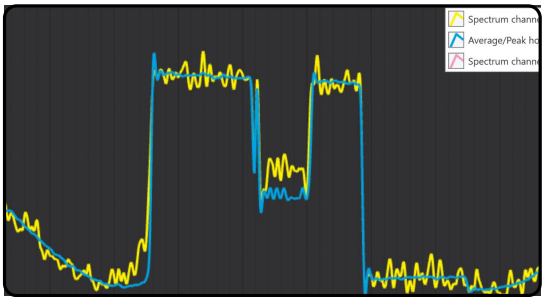

(A) LTE spectrum at developed application.

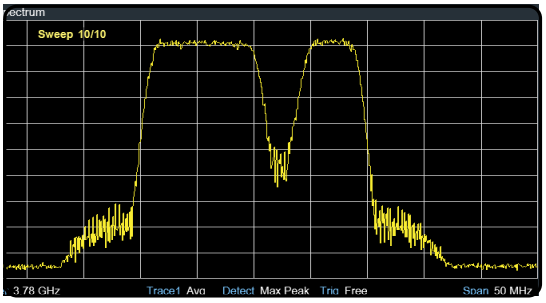

(B) LTE spectrum at R&H spectrum analyzer.

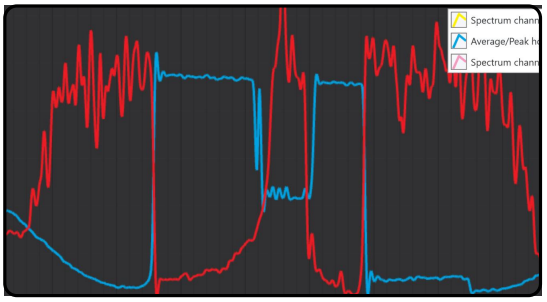

(C) Radar and LTE spectrum at the developed 2 channels spectrum sensing application.

FIGURE 7.14: Screen captures of the resulting spectrum occupied by the LTE communications and optimized radar signals ($\theta = 0.75$) at the developed two-channel spectrum sensing application and R&H spectrum analyzer. The spectrum of the LTE downlink in (a) is validated by a commercial product in (b), and (c) indicates the the resulting spectrum of both communications (blue) and radar (red) at the developed two-channel spectrum sensing application.

calculated by the LTE application framework. We perform our experiments in following steps:

- Step-1: In the absence of radar transmission, we collect the LTE PDSCH throughput for MCS0, MCS10 and MCS 17. For each MCS, we use LTE transmit power of 5 dBm, 10 dBm, 15 dBm and 20 dBm.
- Step-2: In the absence of LTE transmission, we obtain the received SNR for the two targets. In this case, radar utilizes its optimized waveform by setting $\theta = 0$. The SNR is calculated as the ratio of the peak power of the detected targets to the average power of the cells close to the target location in the range-Doppler map.
- Step-3: We transmit a set of optimized radar waveforms by setting $\theta = 0$. At the same time, we transmit the LTE waveform and let the two waveforms interfere with each other. We log the PDSCH throughput as well as the SINR of Target-1 and Target-2. We perform this experiment for MCS0, MCS10 and MCS17 and for each MCS, we increase the LTE transmit power from 5 dBm to 20 dBm in

steps of 5 dBm. Throughout the experiment we keep the radar transmit power fixed. For each LTE MCS and LTE transmit power combination, we average over 5 experiments before logging the PDSCH throughput and target SINRs.

- Step-4: We repeat step-3, but using the optimized waveforms with $\theta = 0.75$ at the radar transmitter.

To evaluate the performance of the communication data rate we reported PDSCH throughput in Figure 7.16. Indeed, the PDSCH throughput value matches the theoretical data rate for the combination of MCS and resource block allocation set for the UE TX. This value indicates the number of payload bits per received transport block that could be decoded successfully in every second. Mathematically it can be written as,

$$\text{throughput} = \sum_{1\text{second}} n_{\text{payload bits}}. \tag{7.26}$$

In Figure 7.16, we first notice that in the presence of radar interference, the link's throughput degrades. Because the SINR requirement for obtaining a clean constellation for larger modulations is also high, the degradation becomes more noticeable at higher MCS. Subsequently, the LTE throughput improves when the radar optimizes its waveform with $\theta = 0.75$. Again we see that the improvement is prominent in the higher MCS. This is because, after a certain SINR, the lower MCS show no symbol error because the constellation points are already well separated. However, as the distance between the constellation points decreases, even a small increase in SINR leads to improved Error Vector Magnitude (EVM), which leads to improved decoding and thus a significant increase in throughput.

In Figure 7.17, in the presence of LTE interference, we observe that the SINRs of Target-1 and Target-2 degrade. These quantities improve when the radar optimizes the transmitting waveforms by setting $\theta = 0.75$. Interestingly, when the LTE transmission power is high (15 dBm, and 20 dBm), higher improvement results from the avoidance of the used LTE bands. Precisely, when the communication system is transmitting with a power of 20 dBm, use of the optimized waveforms enhances the SINR of Target-1, and Target-2 in excess of 7 dB in all the MCS values. Note that, due to the different attenuation paths that is considered for the two targets (see Table 7.3), the measured SINRs for these targets are different. Also, in the absence of the LTE interference, the achieved SINR of Target-1, and Target-2 is 22 dB and 17 dB, respectively, which is the upper bound for the achievable SINR through the optimized waveforms in presence of the communications interference.

7.3 Conclusion

In section 7.1 we address the range-ISL minimization with spectral compatibility problem. In this regards, we express the range-ISL function in spectral domain, then incorporating the weights on spectral domain gives us the ability of controlling the spectral response. In order to design the waveform, we propose an algorithm based on CD and we utilize the FFT to implement the algorithm efficient. The simulation results shows the monotonicity decreasing of the objective function and better performance of the proposed method rather than the state of the art, in terms of range-ISL minimization and spectral shaping.

In section 7.2, we developed a SDR based cognitive MIMO radar prototype using USRP devices that coexist with LTE communications. To enable seamless operation of incumbent LTE links and smart radar sensing, the chapter relied on cognition achieved through the implementation of a spectrum sensing followed by the development of a MIMO waveform design process. An algorithm based on CD approach is considered to design a set of sequences, where the optimization is based on real-time feedback received from the environment through the spectrum sensing application. The developed prototype is tested both in controlled environment to validate its functionalities. The experimental results indicating adherence to system requirements and performance enhancement are noted.

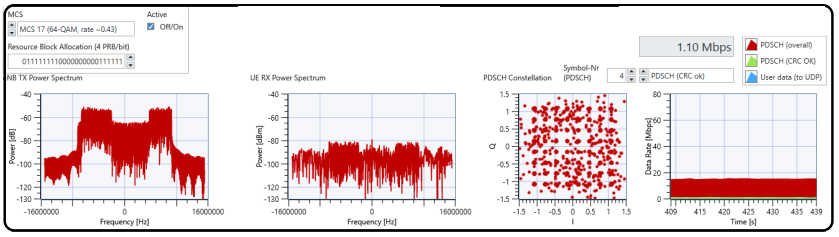

(A) LTE in the presence of radar interference that occupies entire band by utilizing optimized sequences ($\theta = 0$).

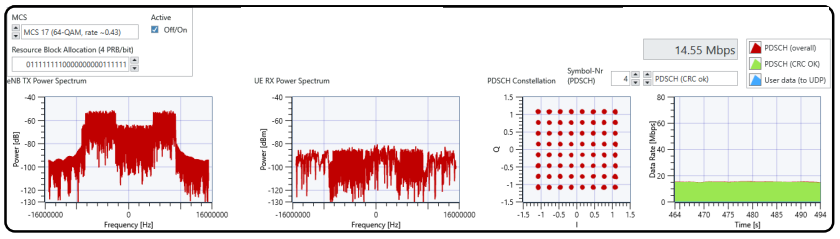

(B) LTE in the presence of optimized sequences for the coexistence scenario ($\theta = 0.75$).

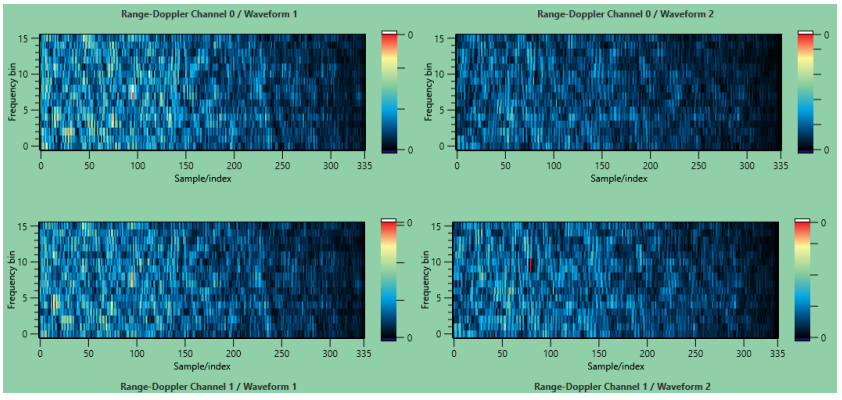

(C) MIMO radar utilizing optimized waveforms without considering the presence of communications ($\theta = 0$).

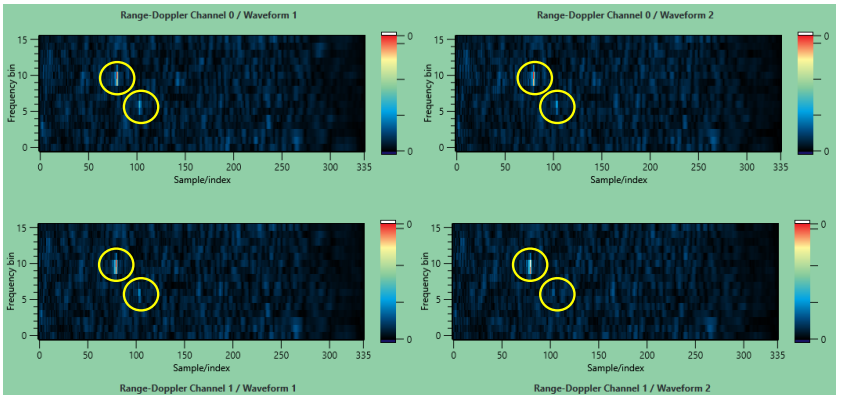

(D) MIMO radar utilizing optimized sequences for the coexistence scenario ($\theta = 0.75$).

FIGURE 7.15: LTE application framework in the presence of radar signal. In case of transmitting random-phase sequences in radar at the same frequency band of communications, the throughput of communications decreases drastically which is depicted in (a). In this case, radar also cannot detect targets as depicted in (c). In case of transmitting the optimized waveforms, the performance of both radar and communications enhances (b and c).

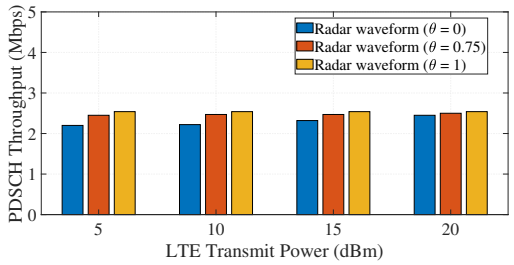

(A) MCS 0 (QPSK 0.12)

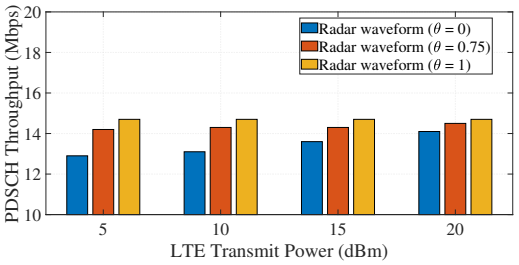

(B) MCS 10 (16QAM 0.33)

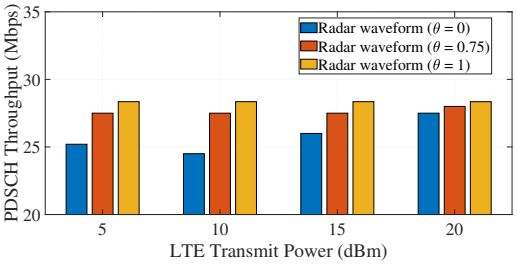

(C) MCS 17 (64QAM 0.43)

FIGURE 7.16: PDSCH throughput of LTE under radar interference. We observe that with radar interference reduces the PDSCH throughput but with cognitive spectrum sensing followed by spectral shaping of the radar waveform PDSCH throughput improves for all the LTE MCS.

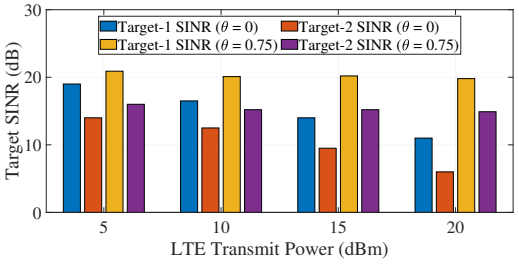

(A) MCS 0 (QPSK 0.12)

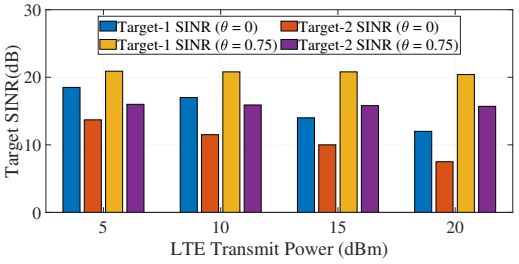

(B) MCS 10 (16QAM 0.33)

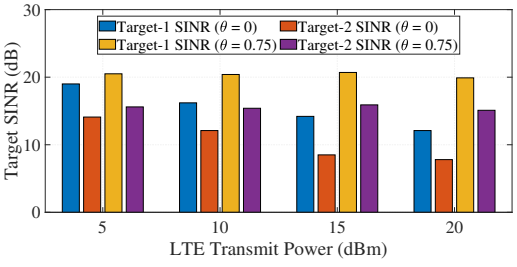

(C) MCS 17 (64QAM 0.43)

FIGURE 7.17: SINR of targets under interference from downlink LTE link. We observe that by optimizing the transmitting waveforms, the SNR of both the targets improves. Note that in this experiment the SNR upper-bound for the first and the second target in the absence of communications interference was 22 dB, and 17 dB, respectively.

Chapter 8

Conclusions and Future Work

8.1 Summary and conclusions

In this chapter, the main conclusions of the thesis are summarized, and also the possible research directions for the future works are identified and discussed. Broadly speaking, this thesis has looked into the problems of resource management in three primary domains (time (range), spatial, and spectral) using waveform design. In general, for each work we start with defining a specific problem and motivate that how solving the problem can enhance the performance of radar systems. Then by surveying the literature, we indicate the drawbacks of the state of the art and also the problems which are not addressed. Subsequently, we choose or define the appropriate design metrics and formulate it accordingly. The works in this thesis go beyond the state of the art the area of waveform design for cognitive radar by defining proposing novel algorithms. Moreover, the performance of the proposed algorithms has been analyzed and then assessed through comparing them with with the state-of-the-art and conventional algorithms.

In chapter 2, we focus on a time (range) management problem by considering the ℓ_p-norm of weighted auto- and cross-correlation under discrete and continuous phase constraints. We proposed WeBEST as a flexible BSUM-based framework to design waveform. By choosing appropriate value for the weights and p, the framework is able to design waveform with different properties, such as good ISL, PSL and sparse auto- and cross-correlation level. Through the numerical results we show that the proposed method meets the lower bound in case of ISL minimization, and decreases the PSL gap with the Welch lower bound. In chapter 3 we address several spatial management approaches for MIMO radar systems, such as spatial-ISLR minimization and ℓ_p-norm beampattern matching. In this regards we proposed various efficient waveform design methods based on CD, SDR, BSUM and the penalty technique in order to get optimal solutions and

we evaluated their performance in numerical results. In chapter 4 we addressed the attractive joint time (range) and spatial management. In this chapter we illustrated the inherent incompatibility of orthogonality and beampattern steering in MIMO radar systems. The key point of enhancing the performance is making an efficient trade-off between these two metrics. In this regards, we choose the weighted sum approach to solve the problem which the weight plays the role of trade-off parameter. In order to solve the problem we proposed an iterative method based on CD and we named it UNIQUE. Through the numerical results we reported the performance of UNIQUE to make a good trade-off between orthogonality and beampattern shaping. In chapter 5 we discussed about the problem of beampattern shaping with practical constraints in MIMO radar systems namely, spectral masking, 3 dB beam-width, constant modulus and similarity constraints. Solving this problem, enables us to control the performance of MIMO radar in three domains namely, spatial, spectral and orthogonality (by similarity constraints). Accordingly, we proposed WISE method to solve the problem, first by introducing a slack variable and convert the optimization problem to a linear problem with a rank one constraint. Then we proposed an iterative method to obtain the rank one solution. Numerical results shows that the proposed method is able to manage the resources efficiently to obtain the best performance. We considered maximizing of SINR by joint design of the Doppler filter and transmit waveform in chapter 6 under the assumption of signal-dependent interference. To obtain a sub-optimal solution, we proposed CD-based and ADMM-based methods. Through the numerical results we evaluated the performance of the proposed methods and compared it with the state of the art. In chapter 7, we considered the joint spectral shaping (nulling) and orthogonality problems in the MIMO radar system to handle the joint temporal (range) and spectral management challenge. The range-ISL problem was initially defined in frequency domain using the Parseval theorem, and then spectral shaping (nulling) was performed by including some weights. In the second study, we introduced the SILR and ICCL as design metrics for spectral shaping and orthogonality, respectively. To make a trade-off between these two metrics, we phrased the problem as a weighted sum of these two criteria. In order to solve the problem we used CD method. Finally, we implemented the framework using a custom built SDR based prototype developed on USRP to demonstrate the performance of the proposed method in real practical applications.

8.2 Future Directions

The research presented in this thesis can be expanded in a multiple ways. The following are the primary problems that need to be addressed in the future:

- **Trade-off between the design metrics:** Due to the contradictory of the metrics in time (range), spatial and spectral, obtaining solution which simultaneously optimize the waveform in these three domains, is impossible. In this regards making a trade-off between these metrics is crucial. Along this thesis we show the impact of trade-off in the performance of MIMO radar systems. But, more importantly, what is the best trade-off between these metrics? Finding answers to this topic opens up new possibilities for cognitive MIMO radar systems, such as those used in automotive. The following guidelines can be considered in this regard:

  1. In general current modern vehicles are equipped with three types of radar, namely, LRR (for adaptive cruise control), MRR (for cross traffic alert and lane change assist) and SRR (for parking aid, obstacle/pedestrian detection). The aim of 4D-imaging radar is merging all of these radars into one radar. This approach decreases the hardware price and complexity. However, on the signal processing point of view this brings up several requirements and challenges. This radars should be able to provide high angular resolution in the entire radar operation range. This necessities to have a good orthogonality and beampattern shaping simultaneously. Based on our study in chapter 4 these two are inherently incompatible and the trade-off between these two aspects is the key of enhancing the performance of the radar. However, since the scenario is dynamically changed in automotive application making trade-off is complicated. One possible approach for this study is *"reinforcement learning"*, which is able to predict the next state in dynamic environment and act based on that.
  2. Because an integrated radar and communication system is being investigated for the next generation of automotive technology, techniques for performing resource management is becoming increasingly important in this field. In this case, radar systems must have full control (management) over the use of available resources. We examine resource management in three domains (time (range), spatial, and spectral) in chapter 5. By suppressing the unwanted frequency bins, we maximize beampattern shaping with high spectral control. However, because we use a similarity constraint to provide time management, we don't have complete control over the waveform's orthogonality. In this case, it would be advantageous to have complete control over the correlation level by considering orthogonality as a problem constraint.
  3. Most of the literature are focused on far filed scenario, however in 4D-imaging the impact of *near field* waveform is challenging. This challenge is more critical when we use a large number of antenna to enhance the angular resolution. In

this regards, one possible study can be designing a waveform considering the near field phenomena.

- All of the developed waveform design procedures in this work were carried out without taking into account the negative impacts of PA. A further expansion of the current work might be the non-linearity behavior of PA on a designed waveform and consideration of it as a constraint in the design stage. The following activities can be considered as part of this study:
  - Investigate the effects of PA's non-linearity behavior on a waveform based on the literature.
  - Define and formulate a problem to reduce to waveform's cross-correlation with the PA output. Propose a solution to the problem based on existing methods such as CD.
  - For demonstrative purposes, implement the proposed method in USRP and using Field Programmable Gate Array (FPGA) implementation for real-time operation.
- The computer-based simulation works in this thesis, can be evaluated in a real-world setting. The first step in this direction is to demonstrate the algorithm's validity using USRP. Following that, setup the FPGA implementation to run in real-time mode.
- This study focuses on colocated MIMO radar systems. The resource management problems can be extended to the other MIMO configurations, such as widely separated MIMO radars.

Part I

Appendices

Appendix A

Appendices of Chapter 2

A.1

The BSUM algorithm includes algorithms that successively optimize particular upper-bounds or local approximation functions of the original objectives in a block by block manner [106, 139, 188, 189]. Let $\mathbf{X} \triangleq [\mathbf{x}_1^T; \ldots; \mathbf{x}_M^T] \in \mathbb{C}^{M \times N}$, where $\mathbf{x}_m, m = 1, \ldots, M$ is the transmitted signal from m^{th} transmitter. The following optimization problem,

$$\begin{cases} \min\limits_{\mathbf{x}} & f(\mathbf{x}_1, \mathbf{x}_2, \ldots, \mathbf{x}_M), \\ \text{s.t.} & \mathbf{x}_m \in \Psi_m, \ m = 1, \ldots, M. \end{cases} \tag{A.1}$$

can be iteratively obtained using BSUM by solving,

$$\begin{cases} \min\limits_{\mathbf{x}_m} & u_m(\mathbf{x}_m; \mathbf{x}_{-m}^{(i)}) \\ \text{s.t.} & \mathbf{x}_m \in \Psi_m, \quad m = 1, 2, \ldots, M \end{cases} \tag{A.2}$$

where u_m is *local approximation* of the objective function and $\mathbf{x}_{-m}^{(i)}$ represent the variable blocks that are kept fixed in the current iteration. If at some point, the objective is not decreasing at every coordinate direction, then we have obtained the optimum $\mathbf{X}^\star \equiv \mathbf{X}^{(i+1)} \triangleq [\mathbf{x}_1^{(i+1)^T}; \mathbf{x}_2^{(i+1)^T}; \ldots; \mathbf{x}_M^{(i+1)^T}]$. The above framework is rather general, and leaves us the freedom of how to choose the index m at i-th iteration (see [106, 149, 190] for more details).

The local approximation functions play an important role to simplify and efficiently solve the optimization problem. In the following, we introduce some local approximation functions which reduce the weighted ℓ_p-norm problem of (2.3) to simpler quadratic forms for $0 < p \leq 1$ and $p \geq 2$.

A.1.0.1 local approximation Function for $p \geq 2$

In this case, one choice for local approximation function is using majorization function [106]. Let $u(\mathbf{x})$ be a majorization (minorization) function of $f(\mathbf{x})$ and $\mathbf{x}^{(i)}$ be the variable at $i^{(th)}$ iteration. This function must satisfy the following conditions [161],

$$u(\mathbf{x}^{(i)}) = f(\mathbf{x}^{(i)});\ \forall \mathbf{x}^{(i)} \in \mathcal{X} \tag{A.3a}$$

$$u(\mathbf{x}) \geq f(\mathbf{x}) \text{ (minorize: } u(\mathbf{x}) \leq f(\mathbf{x}));\ \forall \mathbf{x}, \in \mathcal{X} \tag{A.3b}$$

$$\nabla u(\mathbf{x}^{(i)}) = \nabla f(\mathbf{x}^{(i)});\ \forall \mathbf{x}^{(i)} \in \mathcal{X} \tag{A.3c}$$

$$u(\mathbf{x}) \text{ is continuous } \forall \mathbf{x}, \in \mathcal{X}. \tag{A.3d}$$

Lemma A.1. *Let $f(x) = |x|^p$ and $|x| \in [0, \tau]$ be a real-valued function with $p \geq 2$. Then $u(x) = \eta|x|^2 + \psi|x| + \nu$ is a majorization function of $f(x)$ where, $\eta = \frac{\tau^p + (p-1)|x^{(i)}|^p - p\tau|x^{(i)}|^{p-1}}{(\tau - x^{(i)})^2}$, $\psi = p|x^{(i)}|^{p-1} - 2\eta|x^{(i)}|$ and $\nu = \eta|x^{(i)}|^2 - (p-1)|x^{(i)}|^p$.*

Proof. See [76]. □

Therefore when $p \geq 2$, $|w_k r_{m,l}(k)|^p$ can be majorized by the following function,

$$\eta_{mlk}|w_k r_{m,l}(k)|^2 + \psi_{mlk}|w_k r_{m,l}(k)| + \nu_{mlk}, \tag{A.4}$$

where,

$$\begin{aligned} \eta_{mlk} &\triangleq \frac{\tau^p + (p-1)|w_k r_{m,l}^{(i)}(k)|^p - p\tau|w_k r_{m,l}^{(i)}(k)|^{p-1}}{(\tau - |w_k r_{m,l}^{(i)}(k)|)^2}, \\ \psi_{mlk} &\triangleq p|w_k r_{m,l}^{(i)}(k)|^{p-1} - 2\eta_{mlk}|w_k r_{m,l}^{(i)}(k)|, \\ \nu_{mlk} &\triangleq \eta_{mlk}|w_k r_{m,l}^{(i)}(k)|^2 - (p-1)|w_k r_{m,l}^{(i)}(k)|^p, \end{aligned} \tag{A.5}$$

and

$$\tau \triangleq \left(\sum_{-N-1}^{N-1} |w_k r_{m,l}^{(i)}(k)|^p \right)^{\frac{1}{p}}. \tag{A.6}$$

A.1.0.2 local approximation Function for $0 < p \leq 1$

$f(\mathbf{X})|_{p \to 0}$ denotes the number of non-zero elements of auto- and cross-correlation.

Lemma A.2. *Let $f(x) = |x|^p$ be a real-valued function with $0 < p \leq 1$. The function $f(x)$ can be majorized by $\eta|x|^2 + \nu$ where, η and ν are determined by the following two conditions,*

$$f(x^{(i)}) = \eta(x^{(i)})^2 + \nu, \quad f'(x^{(i)}) = 2\eta x^{(i)}$$

Proof. See [93]. □

In this regard $|w_k r_{m,l}(k)|^p$ with $0 < p \leq 1$ can be majorized with the following simpler quadratic function,

$$u(w_k r_{m,l}(k)) \triangleq \eta_{mlk}|w_k r_{m,l}(k)|^2 + \nu_{mlk}, \tag{A.7}$$

where, the coefficients η_{mlk} and ν_{mlk} can be obtained by solving the following system of equation [93],

$$\begin{aligned} f(w_k r_{m,l}^{(i)}(k)) =& u(w_k r_{m,l}^{(i)}(k)) \\ \frac{\partial f(w_k r_{m,l}^{(i)}(k))}{\partial |w_k r_{m,l}^{(i)}(k)|} =& 2\eta_{mlk}|w_k r_{m,l}^{(i)}(k)|, \end{aligned} \tag{A.8}$$

resulting in,

$$\begin{aligned} \nu_{mlk} &= f(w_k r_{m,l}^{(i)}(k)) - \eta_{mlk}|w_k r_{m,l}^{(i)}(k)|^2 \\ \eta_{mlk} &= \frac{\partial f(w_k r_{m,l}^{(i)}(k))}{\partial |w_k r_{m,l}^{(i)}(k)|} \times \frac{1}{2|w_k r_{m,l}^{(i)}(k)|}. \end{aligned} \tag{A.9}$$

According to (A.9) the quadratic functions in (A.7), (A.9) are non-differentiable and singular when $w_k r_{m,l}(k) = 0$. A possible solution is to incorporate a small $\epsilon > 0$ that avoids this singularity issue and use the smooth approximation functions $f^{\epsilon}(w_k r_{m,l}(k))$ as follow [93],

$$f^{\epsilon}(w_k r_{m,l}(k)) = \begin{cases} \frac{p}{2}\epsilon^{p-2}|w_k r_{m,l}(k)|^2 & |w_k r_{m,l}(k)| \leqslant \epsilon \\ |w_k r_{m,l}(k)|^p - (1 - \frac{1}{p})\epsilon^p & |w_k r_{m,l}(k)| > \epsilon \end{cases} \tag{A.10}$$

Substituting (A.10) in (A.9) we have,

$$\eta_{mlk} = \begin{cases} \frac{p\epsilon^{(p-2)}}{2} & |w_k r_{m,l}(k)| \leqslant \epsilon \\ \frac{p|w_k r_{m,l}(k)|^{(p-2)}}{2} & |w_k r_{m,l}(k)| > \epsilon \end{cases} \tag{A.11}$$

A.2

The auto- and cross-correlation of t^{th} transmitter can be written as d^{th} entry as, [24, 78, 86],

$$\begin{aligned} r_{t,t}(k) &\triangleq \bar{c}_{ttdk} + \bar{a}_{ttdk} x_{t,d} + \bar{b}_{ttdk} x_{t,d}^* \\ r_{t,l}(k) &\triangleq \bar{c}_{tldk} + \bar{a}_{tldk} x_{t,d} \end{aligned} \tag{A.12}$$

where,

$$\begin{aligned}
&\bar{c}_{tldk} \triangleq \sum_{\substack{n=1 \\ n\neq d}}^{N-k} x_{t,n} x^*_{l,n+k}, \bar{a}_{tldk} \triangleq x^*_{l,d+k} I_A(d+k) \\
&\bar{c}_{ttdk} \triangleq \sum_{\substack{n=1 \\ n\neq d, n\neq d-k}}^{N-k} x_{t,n} x^*_{t,n+k} \\
&\bar{a}_{ttdk} \triangleq x^*_{t,d+k} I_A(d+k), \bar{b}_{ttdk} \triangleq x_{t,d-k} I_A(d-k)
\end{aligned} \tag{A.13}$$

where, $I_A(p)$ is the indicator function of set $A = \{1, \ldots, N\}$, i.e, $I_A(p) \triangleq \begin{cases} 1, & p \in A \\ 0, & p \notin A \end{cases}$. Please note that the coefficients $\bar{c}_{tldk}$ and $\bar{c}_{ttdk}$ are depend on $\mathbf{x}_{t,-d}$ while $\bar{a}_{tldk}$, $\bar{a}_{ttdk}$ and $\bar{b}_{ttdk}$ are depend on $x_{t,d}$. Therefore the weighted auto- and cross-correlation of t^{th} transmitter becomes,

$$\begin{aligned}
w_k r_{t,t}(k) &= c_{ttdk} + a_{ttdk} x_{t,d} + b_{ttdk} x^*_{t,d} \\
w_k r_{t,l}(k) &= c_{tldk} + a_{tldk} x_{t,d}
\end{aligned} \tag{A.14}$$

where

$$\begin{aligned}
&a_{ttdk} \triangleq w_k \bar{a}_{ttdk},\ b_{ttdk} \triangleq w_k \bar{b}_{ttdk},\ c_{ttdk} \triangleq w_k \bar{c}_{ttdk}, \\
&a_{tldk} \triangleq w_k \bar{a}_{tldk},\ c_{tldk} \triangleq w_k \bar{c}_{tldk},
\end{aligned} \tag{A.15}$$

A.3

Substituting (2.11) in (2.4) and expanding $u(w_k r_{t,t}(k,\phi))$ and $u(w_k r_{t,l}(k,\phi))$ for $0 < p \leq 1$, we have,

$$\begin{aligned}
u(w_k r_{t,t}(k,\phi)) &= \sum_{n=-2}^{2} \bar{v}_n e^{jn\phi}, \\
u(w_k r_{t,l}(k,\phi)) &= \sum_{n=-1}^{1} \tilde{v}_n e^{jn\phi},
\end{aligned} \tag{A.16}$$

where,

$$\bar{v}_{-2} \triangleq \sum_{k=-N+1}^{N-1} \eta_{ttk} (a^*_{ttdk} b_{ttdk}), \quad \bar{v}_2 \triangleq \bar{v}^*_{-2},$$

$$\bar{v}_{-1} \triangleq \sum_{k=-N+1}^{N-1} \eta_{ttk} (a^*_{ttdk} c_{ttdk} + c^*_{ttdk} b_{ttdk}),\ \bar{v}_1 \triangleq \bar{v}^*_{-1},$$

$$\bar{v}_0 \triangleq \sum_{k=-N+1}^{N-1} (\eta_{ttk} (|c_{ttdk}|^2 + |a_{ttdk}|^2 + |b_{ttdk}|^2) + \nu_{ttk}).$$

$$\tilde{v}_{-1} \triangleq 2\sum_{\substack{l=1\\l\neq t}}^{M}\sum_{k=-N+1}^{N-1}\eta_{tlk}a^{*}_{tldk}c_{tldk}, \quad \tilde{v}_{1} \triangleq \tilde{v}^{*}_{-1},$$

$$\tilde{v}_{0} \triangleq 2\sum_{\substack{l=1\\l\neq t}}^{M}\sum_{k=-N+1}^{N-1}(\eta_{tlk}(|c_{tldk}|^2+|a_{tldk}|^2)+\nu_{tlk}).$$

For $p \geq 2$, (A.4) can be majorized by [76],

$$\begin{aligned} u(w_k r_{m,l}(k)) &\triangleq \eta_{mlk}|w_k r_{m,l}(k)|^2 + \\ &\psi_{mlk}\Re\left\{w^{*}_k r^{*}_{m,l}(k)\frac{w_k r^{(i)}_{m,l}(k)}{|w_k r^{(i)}_{m,l}(k)|}\right\} + \nu_{mlk} \end{aligned} \tag{A.17}$$

Like wise, substituting (2.11) in (A.17) and expanding $u(w_k r_{t,t}(k,\phi))$ and $u(w_k r_{t,l}(k,\phi))$ for $p \geq 2$, we have,

$$u(w_k r_{t,t}(k,\phi)) = \sum_{n=-2}^{2}\bar{u}_n e^{jn\phi} + \Re\left\{\sum_{n=-1}^{1}\hat{u}_n e^{jn\phi}\right\},$$

$$u(w_k r_{t,l}(k,\phi)) = \sum_{n=-1}^{1}\tilde{u}_n e^{jn\phi} + \Re\left\{\sum_{n=-1}^{1}\check{u}_n e^{jn\phi}\right\},$$

Defining $\psi'_{ttk} \triangleq \frac{\psi_{ttk}}{|w_k r^{(i)}_{t,t}(k)|}$ and $\psi'_{tlk} \triangleq \frac{\psi_{tlk}}{|w_k r^{(i)}_{t,l}(k)|}$, it can be shown that,

$$\bar{u}_{-2} \triangleq \sum_{k=-N+1}^{N-1}\eta_{ttk}a^{*}_{ttdk}b_{ttdk}, \quad \bar{u}_{2} \triangleq \bar{u}^{*}_{-2},$$

$$\bar{u}_{-1} \triangleq \sum_{k=-N+1}^{N-1}\eta_{ttk}(a^{*}_{ttdk}c_{ttdk}+c^{*}_{ttdk}b_{ttdk}), \quad \bar{u}_{1} \triangleq \bar{u}^{*}_{-1},$$

$$\bar{u}_{0} \triangleq \sum_{k=-N+1}^{N-1}(\eta_{ttk}(|c_{ttdk}|^2+|a_{ttdk}|^2+|b_{ttdk}|^2)+\nu_{ttk})$$

$$\hat{u}_{-1} \triangleq \sum_{k=-N+1}^{N-1}\psi'_{ttk}(|c_{ttdk}|^2+c^{*}_{ttdk}a_{ttdk}e^{j\phi^{(i)}}+c^{*}_{ttdk}b_{ttdk}e^{-j\phi^{(i)}})$$

$$\hat{u}_{0} \triangleq \sum_{k=-N+1}^{N-1}\psi'_{ttk}(|b_{ttdk}|^2e^{-j\phi^{(i)}}+b^{*}_{ttdk}a_{ttdk}e^{j\phi^{(i)}}+b^{*}_{ttdk}c_{ttdk})$$

$$\hat{u}_{1} \triangleq \sum_{k=-N+1}^{N-1}\psi'_{ttk}(|a_{ttdk}|^2e^{j\phi^{(i)}}+a^{*}_{ttdk}b_{ttdk}e^{-j\phi^{(i)}}+a^{*}_{ttdk}c_{ttdk})$$

$$\tilde{u}_{-1} \triangleq 2\sum_{\substack{l=1\\l\neq t}}^{M}\sum_{k=-N+1}^{N-1}\eta_{tlk}c_{tldk}a^{*}_{tldk}, \quad \tilde{u}_{1} \triangleq \tilde{u}^{*}_{-1}$$

$$\tilde{u}_{0} \triangleq 2\sum_{\substack{l=1\\l\neq t}}^{M}\sum_{k=-N+1}^{N-1}(\eta_{tlk}(|c_{tldk}|^2+|a_{tldk}|^2)+\nu_{tldk}))$$

$$\check{u}_{-1} \triangleq 2\sum_{\substack{l=1\\l\neq t}}^{M}\sum_{k=-N+1}^{N-1}\psi'_{tlk}(|c_{tldk}|^2+c^{*}_{tldk}a_{tldk}e^{j\phi^{(i)}})$$

$$\check{u}_{0} \triangleq 2\sum_{\substack{l=1\\l\neq t}}^{M}\sum_{k=-N+1}^{N-1}\psi'_{tlk}(|c_{tldk}|^2+c^{*}_{tldk}a_{tldk}e^{j\phi^{(i)}})$$

$$\check{u}_{1} \triangleq 2\sum_{\substack{l=1\\l\neq t}}^{M}\sum_{k=-N+1}^{N-1}\psi'_{tlk}(|a_{tldk}|^2e^{j\phi^{(i)}}+a^{*}_{tldk}c_{tldk})$$

In this regard, readily it can be shown that the problem (2.12) can be written as (2.13), where the coefficients are,

$$v_{n;\in\{-2,2\}} \triangleq \begin{cases}\bar{v}_n & 0<p\leq 1\\ \bar{u}_n & p\geq 2\end{cases} \tag{A.18}$$

$$v_{n;\in\{-1,0,1\}} \triangleq \begin{cases}\bar{v}_n+\tilde{v}_n & 0<p\leq 1\\ \bar{u}_n+\tilde{u}_n+\hat{u}_n+\check{u}_n & p\geq 2\end{cases} \tag{A.19}$$

A.4

Substituting $e^{jn\phi}=\cos(n\phi)+j\sin(n\phi)$ in $u'(\phi)$ and separating the real and imaginary part, $u'(\phi)$ becomes,

$$\begin{aligned}u'(\phi) = {}& \xi_0\cos^2(\phi)+\xi_1\sin^2(\phi)+\xi_2\sin(\phi)\cos(\phi)\\ & +\xi_3\cos(\phi)+\xi_4\sin(\phi)\end{aligned} \tag{A.20}$$

where, $\xi_0 \triangleq 2\Im\{v_{-2}-v_2\}$, $\xi_1 \triangleq 2\Im\{v_2-v_{-2}\}$, $\xi_2 \triangleq -4\Re\{v_2+v_{-2}\}$, $\xi_3 \triangleq \Im\{v_{-1}-v_1\}$ and $\xi_4 \triangleq -\Re\{v_{-1}+v_1\}$. Using the change variable $z \triangleq \tan(\frac{\phi}{2})$ and substituting $\cos(\phi)=(1-z^2)/(1+z^2)$, $\sin(\phi)=2z/(1+z^2)$ in $u'(\phi)$, it can be written as, $u'(z)=\frac{\sum_{k=0}^{4}s_kz^k}{(1+z^2)^2}$, where,

$$\begin{aligned} &s_0 \triangleq \xi_0 + \xi_3,\ s_1 \triangleq 2(\xi_2 + \xi_4),\ s_2 \triangleq 2(2\xi_1 - \xi_0), \\ &s_3 \triangleq 2(\xi_4 - \xi_2),\ s_4 \triangleq \xi_0 - \xi_3 \end{aligned} \tag{A.21}$$

A.5

Let assume that $l' = \{1, 2, \ldots, L\}$ be the indices of alphabet Ω_L. Therefore the objective function can be written as,

$$\begin{aligned} f(l') = f(\mathbf{X}_{-t}) + 2\sum_{\substack{l=1 \\ l\neq t}}^{M} \sum_{k=-N+1}^{N-1} |a_{tldk} + c_{tldk} e^{-j2\pi \frac{l'-1}{L}}|^p \\ + \sum_{k=-N+1}^{N-1} |a_{ttdk} + c_{ttdk} e^{-j2\pi \frac{l'-1}{L}} + b_{ttdk} e^{-j4\pi \frac{l'-1}{L}}|^p \end{aligned} \tag{A.22}$$

Let assume that $\mathbf{y} \in \mathbb{C}^N$ be a vector and $\mathcal{F}_L\{\mathbf{y}\} \triangleq \sum_{n=1}^{N} y(n) e^{j2\pi \frac{(n-1)(l'-1)}{L}}$ be the L point DFT operator of $\mathbf{y}$. Therefore, it can be shown that all the possible values of $a_{tldk} + c_{tldk} e^{-j2\pi \frac{l'-1}{L}}$ and $a_{ttdk} + c_{ttdk} e^{-j2\pi \frac{l'-1}{L}} + b_{ttdk} e^{-j4\pi \frac{l'-1}{L}}$ for $l' = \{1, 2, \ldots, L\}$, can be obtained by $\mathcal{F}_L\{a_{tldk}, c_{tldk}\}$ and $\mathcal{F}_L\{a_{ttdk}, c_{ttdk}, b_{ttdk}\}$ respectively. Therefore, the optimum index can be can be obtained as (2.19).

Appendix B

Appendices of Chapter 3

B.1

The beampattern response on undesired angles can be written as $\sum_{n=1}^{N} \mathbf{x}_n^{\dagger} \boldsymbol{A}_U \mathbf{x}_n = \sum_{m=1}^{M} \sum_{l=1}^{M} \sum_{n=1}^{N} x_{m,n}^{*} U_{m,l} x_{l,n}$ where, $U_{m,l}$ are the elements of matrix $\boldsymbol{A}_U$. By a few mathematical manipulations it can be shown that, $\sum_{n=1}^{N} \mathbf{x}_n^{\dagger} \boldsymbol{A}_U \mathbf{x}_n = a_0 x_{t,d} + a_1 + a_2 x_{t,d}^{*}$, where,

$$a_0 = \sum_{\substack{m=1 \\ m \neq t}}^{M} s_{m,d}^{*} a_{U_{m,t}},\ a_2 = a_0^{*},\ a_1 = \sum_{\substack{n=1 \\ n \neq d}}^{N} \sum_{m,l=1}^{M} x_{m,n}^{*} U_{m,l} x_{l,n} + \sum_{\substack{m,l=1 \\ m,l \neq t}}^{M} x_{m,n}^{*} U_{m,t} x_{t,n} + U_{t,t}.$$

Likewise, $\sum_{n=1}^{N} \mathbf{x}_n^{\dagger} \boldsymbol{A}_D \mathbf{x}_n = b_0 x_{t,d} + b_1 + b_2 x_{t,d}^{*}$, where b_i's are obtained similar to a_i with $D_{m,t}$ and $D_{m,l}$ replacing $U_{m,t}$ and $U_{m,t}$ respectively, and $D_{m,l}$ are the elements of matrix $\boldsymbol{A}_D$.

B.2

The function $r(\mathbf{X}, \theta_k)$ can be written with respect to $x_{t,d}$ as $r(\mathbf{X}, \theta_k) = b_{1,k} e^{j\phi_{t,d}} + b_{0,k} + b_{-1,k} e^{-j\phi_{t,d}}$ [37], where,

$$\begin{aligned} b_{1,k} &\triangleq \sum_{\substack{m=1 \\ m \neq t}}^{M} x_{m,d}^{*} a_{k_{m,t}}, \quad b_{-1,k} \triangleq b_{1,k}^{*}, \\ b_{0,k} &\triangleq a_{k_{t,t}} + \sum_{\substack{n=1 \\ n \neq d}}^{N} \mathbf{x}_n^{H} \mathbf{A}(\theta_k) \mathbf{x}_n + \sum_{\substack{m=1 \\ m \neq t}}^{M} \sum_{\substack{l=1 \\ l \neq t}}^{M} x_{m,d}^{*} a_{k_{m,l}} x_{l,d}, \end{aligned} \tag{B.1}$$

and $a_{k_{m,l}}$ is the $(m,l)^{th}$ entry of matrix $\mathbf{A}(\theta_k)$. By substituting (B.1) in (3.13) and some mathematics manipulation the objective function in (3.33) can be obtained, as,

$$\begin{aligned} &c_2 \triangleq \sum_{k=1}^{K} \eta_k b_{1,k}, c_1 \triangleq \sum_{k=1}^{K} 2\eta_k b_{1,k}(b_{0,k} - \mu q_k) + \psi_k b_{1,k}, \\ &c_0 \triangleq \sum_{k=1}^{K} 2\eta_k(|b_{1,k}|^2 + (b_{0,k} - \mu q_k)^2) + \psi_k(b_{0,k} - \mu q_k) + \nu_k, \\ &c_{-1} \triangleq c_1^*, c_{-2} \triangleq c_2^*. \end{aligned} \tag{B.2}$$

B.3

The beampattern response on undesired angles can be written as $\sum_{n=1}^{N} \boldsymbol{s}_n^H \boldsymbol{A}_U \boldsymbol{s}_n = \sum_{m=1}^{M}\sum_{l=1}^{M}\sum_{n=1}^{N} s_{m,n}^* U_{m,l} s_{l,n}$ where, $U_{m,l}$ are the elements of matrix $\boldsymbol{A}_U$. By some mathematical manipulation it can be shown that, $\sum_{n=1}^{N} \boldsymbol{s}_n^H \boldsymbol{A}_U \boldsymbol{s}_n = a_0 s_{t,d} + a_1 + a_2 s_{t,d}^*$, where,

$$\begin{aligned} &a_0 = \textstyle\sum_{\substack{m=1 \\ m\neq t}}^{M} s_{m,d}^* a_{U_{m,t}}, \quad a_2 = a_0^*, \quad a_1 = \\ &\sum_{\substack{n=1 \\ n\neq d}}^{N}\sum_{m=1}^{M}\sum_{l=1}^{N} s_{m,n}^* U_{m,l} s_{l,n} + \sum_{\substack{m=1 \\ m\neq t}}^{M}\sum_{\substack{l=1 \\ l\neq t}}^{M} s_{m,n}^* U_{m,t} s_{t,n} + U_{t,t}. \end{aligned}$$

Likewise, $\sum_{n=1}^{N} \boldsymbol{s}_n^H \boldsymbol{A}_T \boldsymbol{s}_n = b_0 s_{t,d} + b_1 + b_2 s_{t,d}^*$, where b_i's are obtained similar to a_i with $T_{m,t}$ replacing $U_{m,t}$ and $T_{m,l}$ are the elements of matrix $\boldsymbol{A}_T$. It can be shown that the objective function of problem $\mathcal{P}_3$ is equal to $c_0 s_{t,d}^2 + c_1 s_{t,d} + c_2 + c_3 s_{t,d}^* + c_4 {s_{t,d}^*}^2$, where

$$\begin{aligned} &c_0 \triangleq \frac{\delta b_0^2}{M^4}, c_1 \triangleq \frac{2\delta b_0(b_1 - \alpha M^2)}{M^4}, c_4 = c_0^*, c_3 = c_1^* \\ &c_2 \triangleq \frac{2\delta|b_0|^2 + \delta(b_1 - \alpha M^2)^2 + a_1}{M^4}. \end{aligned} \tag{B.3}$$

B.4

Let $a_{u_{m,l}}$ be the elements of matrix $\boldsymbol{A}_u$. The spatial ISL can be written as, $f_1(\boldsymbol{S}) = \sum_{m=1}^{M}\sum_{l=1}^{M}\sum_{n=1}^{N} s_{m,n}^* a_{u_{m,l}} s_{l,n}$. By some mathematical manipulation $f_1(\boldsymbol{S})$ can be written with respect to $s_{t,d}$ entry as, $a_0 s_{t,d} + a_1 + a_2 s_{t,d}^*$, where $a_0 = \sum_{\substack{m=1 \\ m\neq t}}^{M} s_{m,d}^* a_{u_{m,t}}$,

$a_2 = a_0^*$ and:

$$a_1 = \sum_{\substack{m=1\\m\neq t}}^{M}\sum_{\substack{l=1\\l\neq t}}^{M}\sum_{n=1}^{N} s_{m,n}^* a_{u_{m,l}} s_{l,n} + \sum_{\substack{m=1\\m\neq t}}^{M}\sum_{\substack{n=1\\n\neq d}}^{N} s_{m,n}^* a_{u_{m,t}} s_{t,n} + \sum_{\substack{l=1\\l\neq t}}^{M}\sum_{\substack{n=1\\n\neq d}}^{N} s_{t,n}^* a_{u_{t,l}} s_{l,n} + \sum_{\substack{n=1\\n\neq d}}^{N} s_{t,n}^* a_{u_{t,t}} s_{t,n} + a_{u_{t,t}}.$$

Likewise $g_1(\boldsymbol{S})$ can be written as, $b_0 s_{t,d} + b_1 + b_2 s_{t,d}^*$, where, $a_{d_{m,l}}$ are the elements of matrix $\boldsymbol{A}_d$, $b_0 = \sum_{\substack{m=1\\m\neq t}}^{M} s_{m,d}^* a_{d_{m,t}}$, $b_2 = b_0^*$ and:

$$b_1 = \sum_{\substack{m=1\\m\neq t}}^{M}\sum_{\substack{l=1\\l\neq t}}^{M}\sum_{n=1}^{N} s_{m,n}^* a_{d_{m,l}} s_{l,n} + \sum_{\substack{m=1\\m\neq t}}^{M}\sum_{\substack{n=1\\n\neq d}}^{N} s_{m,n}^* a_{d_{m,t}} s_{t,n} + \sum_{\substack{l=1\\l\neq t}}^{M}\sum_{\substack{n=1\\n\neq d}}^{N} s_{t,n}^* a_{d_{t,l}} s_{l,n} + \sum_{\substack{n=1\\n\neq d}}^{N} s_{t,n}^* a_{d_{t,t}} s_{t,n} + a_{d_{t,t}}$$

Appendix C

Appendices of Chapter 4

C.1

Writing (4.10) with respect to $s_{t,d}$ has the following parts.

Spatial-ISLR coefficients Beampattern of undesired angles can be written as,

$$\sum_{n=1}^{N} \bar{\boldsymbol{s}}_n^H \boldsymbol{A}_u \bar{\boldsymbol{s}}_n = \sum_{\substack{n=1 \\ n\neq d}}^{N} \bar{\boldsymbol{s}}_n^H \boldsymbol{A}_u \bar{\boldsymbol{s}}_n + \bar{\boldsymbol{s}}_d^H \boldsymbol{A}_u \bar{\boldsymbol{s}}_d,$$

where the second term can be expanded as,

$$\sum_{m=1}^{M_t} \sum_{l=1}^{M_t} s_{m,d}^* a_{u_{m,l}} s_{l,d} = \sum_{\substack{m=1 \\ m\neq t}}^{M_t} \sum_{\substack{l=1 \\ l\neq t}}^{M_t} s_{m,d}^* a_{u_{m,l}} s_{l,d}$$
$$+ s_{t,d} \sum_{\substack{m=1 \\ m\neq t}}^{M_t} s_{m,d}^* a_{u_{m,t}} + s_{t,d}^* \sum_{\substack{l=1 \\ l\neq t}}^{M_t} a_{u_{t,l}} s_{l,d} + s_{t,d}^* a_{u_{t,t}} s_{t,d},$$

with $a_{u_{m,l}}$ indicating $\{m, l\}$ entries of matrix $\boldsymbol{A}_u$. Defining,

$$a_0 \triangleq \sum_{\substack{m=1 \\ m\neq t}}^{M_t} s_{m,d}^* a_{u_{m,t}}, \quad a_3 \triangleq a_{u_{t,t}}, \quad a_2 \triangleq a_0^*,$$
$$a_1 \triangleq \sum_{\substack{n=1 \\ n\neq d}}^{N} \bar{\boldsymbol{s}}_n^H \boldsymbol{A}_u \bar{\boldsymbol{s}}_n + \sum_{\substack{m=1 \\ m\neq t}}^{M_t} \sum_{\substack{l=1 \\ l\neq t}}^{M_t} s_{m,d}^* a_{u_{m,l}} s_{l,d},$$

the beampattern response on undesired angles is equivalent to,

$$\sum_{n=1}^{N} \bar{\boldsymbol{s}}_n^H \boldsymbol{A}_u \bar{\boldsymbol{s}}_n = a_0 s_{t,d} + a_1 + a_2 s_{t,d}^* + a_3 s_{t,d}^* s_{t,d}. \tag{C.1}$$

Like wise the beampattern at desired angles is:

$$\sum_{n=1}^{N} \bar{\boldsymbol{s}}_n^H \boldsymbol{A}_d \bar{\boldsymbol{s}}_n = b_0 s_{t,d} + b_1 + b_2 s_{t,d}^* + b_3 s_{t,d}^* s_{t,d}, \tag{C.2}$$

$$b_0 \triangleq \sum_{\substack{m=1 \\ m\neq t}}^{M_t} s_{m,d}^* a_{d_{m,t}}, \quad b_3 \triangleq a_{d_{t,t}}, \quad b_2 \triangleq b_0^*,$$
$$b_1 \triangleq \sum_{\substack{n=1 \\ n\neq d}}^{N} \bar{\boldsymbol{s}}_n^H \boldsymbol{A}_d \bar{\boldsymbol{s}}_n + \sum_{\substack{m=1 \\ m\neq t}}^{M_t} \sum_{\substack{l=1 \\ l\neq t}}^{M_t} s_{m,d}^* a_{d_{m,l}} s_{l,d},$$

where $a_{d_{m,l}}$ are the $\{m,l\}$ entries of $\boldsymbol{A}_d$. (4.12).

Range-ISLR coefficients (4.5) can be written as,

$$\begin{aligned}\text{ISL} &= \gamma_t + \textstyle\sum_{k=-N+1}^{N-1} |r_{t,t}(k)|^2 + |r_{t,t}(0)|^2 \\ &+ \textstyle\sum_{\substack{l=1\\l\neq t}}^{M_t} \sum_{k=-N+1}^{N-1} |r_{t,l}(k)|^2 + \sum_{\substack{m=1\\m\neq t}}^{M_t} \sum_{k=-N+1}^{N-1} |r_{m,t}(k)|^2.\end{aligned}$$

where,

$$\gamma_t \triangleq \textstyle\sum_{\substack{m=1\\m\neq t}}^{M_t} \sum_{\substack{l=1\\l\neq t}}^{M_t} \sum_{k=-N+1}^{N-1} |r_{m,l}(k)|^2 - \sum_{\substack{m=1\\m\neq t}}^{M_t} |r_{m,m}(0)|^2$$

Also,

$$\begin{aligned} r_{m,t}(k) &= \textstyle\sum_{\substack{n=1\\n\neq d-k}}^{N-k} s_{m,n} s_{t,n+k}^* + s_{m,d-k} s_{t,d}^* I_A(d-k) \\ r_{t,l}(k) &= \textstyle\sum_{\substack{n=1\\n\neq d}}^{N-k} s_{t,n} s_{l,n+k}^* + s_{t,d} s_{l,d+k}^* I_A(d+k) \\ r_{t,t}(k) &= \textstyle\sum_{\substack{n=1\\n\neq d,n\neq d-k}}^{N-k} s_{t,n} s_{t,n+k}^* + s_{t,d} s_{t,d+k}^* I_A(d+k) \\ &\quad + s_{t,d}^* s_{t,d-k} I_A(d-k) \end{aligned}$$

where, $I_A(p)$ is the indicator function of set $A = \{1,\ldots,N\}$, i.e, $I_A(p) \triangleq \begin{cases} 1, & p \in A \\ 0, & p \notin A \end{cases}$.

Let us define [1],

$$\begin{aligned} \gamma_{mtdk} &\triangleq \textstyle\sum_{\substack{n=1\\n\neq d-k}}^{N-k} s_{m,n} s_{t,n+k}^*, \beta_{mtdk} \triangleq s_{m,d-k} I_A(d-k) \\ \gamma_{tldk} &\triangleq \textstyle\sum_{\substack{n=1\\n\neq d}}^{N-k} s_{t,n} s_{l,n+k}^*, \alpha_{tldk} \triangleq s_{l,d+k}^* I_A(d+k) \\ \gamma_{ttdk} &\triangleq \textstyle\sum_{\substack{n=1\\n\neq d,n\neq d-k}}^{N-k} s_{t,n} s_{t,n+k}^*, \alpha_{ttdk} \triangleq s_{t,d+k}^* I_A(d+k) \\ \beta_{ttdk} &\triangleq s_{t,d-k} I_A(d-k) \end{aligned}$$

Thus, we obtain,

$$\text{ISL} = c_0 s_{t,d}^2 + c_1 s_{t,d} + c_2 + c_3 s_{t,d}^* + c_4 {s_{t,d}^*}^2 + c_5 |s_{t,d}|^2 \tag{C.3}$$

with,

$c_0 \triangleq \sum_{\substack{k=-N+1\\k\neq 0}}^{N-1} \alpha_{ttdk} \beta_{ttdk}^*, \quad c_4 \triangleq c_0^*,$

$c_3 \triangleq c_1^*, \quad c_1 \triangleq \sum_{\substack{k=-N+1\\k\neq 0}}^{N-1} (\gamma_{ttdk}^* \alpha_{ttdk} + \gamma_{ttdk} \beta_{ttdk}^*) +$

$\sum_{\substack{l=1\\l\neq t}}^{M_t} \sum_{k=-N+1}^{N-1} \gamma_{tldk}^* \alpha_{tldk} + \sum_{\substack{m=1\\m\neq t}}^{M_t} \sum_{k=-N+1}^{N-1} \gamma_{mtdk} \beta_{mtdk}^*,$

$c_2 \triangleq \sum_{\substack{k=-N+1\\k\neq 0}}^{N-1} |\gamma_{ttdk}|^2 + \sum_{\substack{l=1\\l\neq t}}^{M_t} \sum_{k=-N+1}^{N-1} |\gamma_{tldk}|^2$

$+ \sum_{\substack{m=1\\m\neq t}}^{M_t} \sum_{k=-N+1}^{N-1} |\gamma_{mtdk}|^2 + \gamma_t,$

[1] By defining, $\tilde{\boldsymbol{s}}_{\{t,m,l\}_{-d}} \triangleq \tilde{\boldsymbol{s}}_m|_{s_{\{t,m,l\},d}=0}$, it can be shown that, γ_{mtdk}, γ_{tldk} and γ_{ttdk} can be considered as correlation of $\tilde{\boldsymbol{s}}_{m_{-d}}$ and $\tilde{\boldsymbol{s}}_{t_{-d}}$, $\tilde{\boldsymbol{s}}_{t_{-d}}$ and $\tilde{\boldsymbol{s}}_{l_{-d}}$, $\tilde{\boldsymbol{s}}_{t_{-d}}$ and $\tilde{\boldsymbol{s}}_{t_{-d}}$ respectively.

$c_5 \triangleq \sum_{\substack{k=-N+1 \\ k\neq 0}}^{N-1}(|\alpha_{ttdk}|^2+|\beta_{ttdk}|^2)$
$+\sum_{\substack{l=1 \\ l\neq t}}^{M_t}\sum_{k=-N+1}^{N-1}|\alpha_{tldk}|^2+\sum_{\substack{m=1 \\ m\neq t}}^{M_t}\sum_{k=-N+1}^{N-1}|\beta_{mtdk}|^2.$

Since $c_0=c_4^*$, $c_1=c_3^*$ and c_1, c_5 are real coefficient, (C.3) is a real and non-negative function. Also for the mainlobe,

$$\sum_{m=1}^{M_t}|r_{m,m}(0)|^2=\sum_{\substack{m=1 \\ m\neq t}}^{M_t}\left(\sum_{n=1}^{N}|s_{m,n}|^2\right)^2+$$
$$\left(\sum_{\substack{n=1 \\ n\neq d}}^{N}|s_{t,n}|^2\right)^2+2|s_{t,d}|^2\sum_{\substack{n=1 \\ n\neq d}}^{N}|s_{t,n}|^2+|s_{t,d}|^4.$$

Defining, $d_2 \triangleq \sum_{\substack{m=1 \\ m\neq t}}^{M_t}\left(\sum_{n=1}^{N}|s_{m,n}|^2\right)^2+\left(\sum_{\substack{n=1 \\ n\neq d}}^{N}|s_{t,n}|^2\right)^2$ and $d_1 \triangleq 2\sum_{\substack{n=1 \\ n\neq d}}^{N}|s_{t,n}|^2$, we have,

$$\sum_{m=1}^{M_t}|r_{m,m}(0)|^2=|s_{t,d}|^4+d_1|s_{t,d}|^2+d_2. \tag{C.4}$$

C_1 Constraint It is straight-forward to show that,

$$\gamma_e \triangleq M_tN-\sum_{\substack{m=1 \\ m\neq t}}^{M_t}\sum_{n=1}^{N}|s_{m,n}|^2-\sum_{\substack{n=1 \\ n\neq d}}^{N}|s_{t,n}|^2. \tag{C.5}$$

Note: $\|\boldsymbol{S}\|_F^2=\sum_{\substack{m=1 \\ m\neq t}}^{M_t}\sum_{n=1}^{N}|s_{m,n}|^2+\sum_{\substack{n=1 \\ n\neq d}}^{N}|s_{t,n}|^2+|s_{t,d}|^2$.

C_2 Constraint The PAR constraint can be written as, $M_tN\max|s_{m,n}|^2\leqslant\gamma_p\|\boldsymbol{S}\|_F^2$. Defining $P_{-(t,d)}\triangleq\max\{|s_{m,n}|^2;(m,n)\neq(t,d)\}$, we obtain

$$M_tN\max\{|s_{t,d}|^2,P_{-(t,d)}\}\leqslant\gamma_p\left(|s_{t,d}|^2+\left\|\boldsymbol{S}_{-(t,d)}\right\|_F^2\right)$$

Defining,

$$\gamma_l\triangleq\frac{M_tNP_{-(t,d)}-\gamma_p\left\|\boldsymbol{S}_{-(t,d)}\right\|_F^2}{\gamma_p},\quad \gamma_u\triangleq\frac{\gamma_p\left\|\boldsymbol{S}_{-(t,d)}\right\|_F^2}{M_tN-\gamma_p},$$

Hence, $|s_{t,d}|^2\geqslant\gamma_l$ when $|s_{t,d}|^2\leqslant P_{-(t,d)}$, and $|s_{t,d}|^2\leqslant\gamma_u$ when $|s_{t,d}|^2\geqslant P_{-(t,d)}$.

C.2

Considering $a_2=a_0^*$, $b_2=b_0^*$, $c_4=c_0^*$ and $c_3=c_1^*$, the (4.16) and (4.17) can be written as [2],

[2]It is possible to consider $e^{j\phi}$ as the variable and solve the problem. However, we reformulate the problem in the real variable to enable computations in real domain to be closer to practical implementation.

$$\begin{aligned}\bar{f}\,(r,\phi) &= \frac{2\Re\{a_0 re^{j\phi}\} + a_1 + a_3 r^3}{2\Re\{b_0 re^{j\phi}\} + b_1 + b_3 r^3} \\ &= \frac{a_3 r^2 + 2(a_{0r}\cos\phi - a_{0i}\sin\phi)r + a_1}{b_3 r^2 + 2(b_{0r}\cos\phi - b_{0i}\sin\phi)r + b_1}\end{aligned} \tag{C.6}$$

$$\begin{aligned}\tilde{f}\,(r,\phi) &= \frac{2\Re\{c_0 r^2 e^{j2\phi}\} + 2\Re\{c_1 re^{j\phi}\} + c_2 + c_5 r^2}{r^4 + d_1 r^2 + d_2} \\ &= [(2c_{0r}\cos 2\phi - 2c_{0i}\sin 2\phi + c_5)r^2 \\ &+ 2(c_{1r}\cos\phi - c_{1i}\sin\phi)r + c_2]\frac{1}{r^4 + d_1 r^2 + d_2},\end{aligned} \tag{C.7}$$

where, $a_{0r} = \Re(a_0)$, $a_{0i} = \Im(a_0)$, $b_{0r} = \Re(b_0)$, $b_{0i} = \Im(b_0)$, $c_{0r} = \Re(c_0)$, $c_{0i} = \Im(c_0)$, $c_{1r} = \Re(c_1)$ and $c_{1i} = \Im(c_1)$.

C.3

As $f_o(r,\phi_0)$ is a fractional function, $\frac{\partial f_o(r,\phi_0)}{\partial r}$ is also a fractional function. Hence to find the roots of $\frac{\partial f_o(r,\phi_0)}{\partial r} = 0$ it is sufficient to find the roots of the numerator. By some mathematical manipulation it can be shown that the numerator can be written as (4.22), and the coefficients are,

$p_0 \triangleq 2\eta\Re\{\rho_0 e^{j\phi 0}\}, \quad p_1 \triangleq 2(\eta\rho_1 + (\eta-1)b_3^2\rho_2),$

$p_2 \triangleq 2(\eta\Re\{(\rho_3 + 2d_1\rho_0)e^{j\phi_0}\} + (\eta-1)(3b_3^2\rho_4 + 4b_3\rho_5\rho_2)),$

$p_3 \triangleq 4(\eta d_1\rho_1 + (\eta-1)((2\rho_5^2 + b_1b_3)\rho_2 + c_2b_3^2 + 6b_3\rho_5\rho_4)),$

$p_4 \triangleq 2(\eta\Re\{(\rho_6\rho_0 + 2d_1\rho_3)e^{j\phi_0}\} +$
$(\eta-1)(\rho_4(12\rho_5^2 + 6b_1b_3 + b_3^2d_1) + 4\rho_5(b_1\rho_2 + 2b_3c_2))),$

$p_5 \triangleq 2(\eta\rho_6\rho_1 + (\eta-1)(\rho_2(b_1^2 - d_2b_3^2) + b_3^2c_2d_1 +$
$4c_2(2\rho_5^2 + b_1b_3) + 4\rho_5\rho_4(3b_1 + b_3d_1))),$

$p_6 \triangleq 2(\eta\Re\{(\rho_6\rho_3 + 2d_1d_2\rho_0)e^{j\phi_0}\} + (\eta-1)(\rho_4(3b_1^2 - b_3^2d_2$
$+ 2d_1(2\rho_5^2 + b_1b_3)) + 4\rho_5(2b_1c_2 - b_3(d_2\rho_2 - c_2d_1)))),$

$p_7 \triangleq 4(\eta d_1d_2\rho_1 + (\eta-1)(b_1^2c_2 + 2(b_1d_1 - b_3d_2)\rho_5\rho_4$
$- (d_2\rho_2 - c_2d_1)(2\rho_5^2 + b_1b_3))),$

$p_8 \triangleq 2(\eta\Re\{(d_2^2\rho_0 + 2d_1d_2\rho_3)e^{j\phi_0}\} + (\eta-1)(\rho_4(b_1^2d_1$
$- 2d_2(2\rho_5^2 + b_1b_3)) - 4b_1\rho_5(d_2\rho_2 - c_2d_1))),$

$p_9 \triangleq 2(\eta d_2^2\rho_1 - (\eta-1)(b_1^2(d_2\rho_2 - c_2d_1) + 4b_1d_2\rho_5\rho_4)),$

$p_{10} \triangleq 2(\eta d_2^2\Re\{\rho_3 e^{j\phi_0}\} - (\eta-1)b_1^2d_2\rho_4),$

where, $\rho_0 \triangleq a_3b_0 - b_3a_0$, $\rho_1 \triangleq a_3b_1 - a_1b_3$, $\rho_2 \triangleq c_5 + 2\Re\{c_0e^{j2\phi_0}\}$, $\rho_3 \triangleq b_1a_0 - a_1b_0$, $\rho_4 \triangleq \Re\{c_1e^{j\phi_0}\}$, $\rho_5 \triangleq \Re\{b_0e^{j\phi_0}\}$ and $\rho_6 \triangleq d_1^2 + 2d_2$.

C.4

After substituting $\cos(\phi) = (1-\tan^2(\frac{\phi}{2}))/(1+\tan^2(\frac{\phi}{2}))$, $\sin(\phi) = 2\tan(\frac{\phi}{2})/(1+\tan^2(\frac{\phi}{2}))$ in $\frac{\partial f_o(r_e^\star,\phi)}{\partial\phi}$ and considering $z \triangleq \tan(\frac{\phi}{2})$, we encounter with a fractional function. In this case it is sufficient to find the roots of nominator. It can be shown that the nominator can be written as, (4.25), where,

$$q_0 \triangleq 2r_e^\star(\eta\xi_0(2\xi_3-\xi_2) + (1-\eta)(c_{1i}-2\xi_9)(\xi_4^2-4\xi_6(\xi_4-\xi_6))),$$

$$q_1 \triangleq 4r_e^\star(\eta\xi_0\xi_1 + (1-\eta)(4\xi_7(2\xi_9-c_{1i})(\xi_4-2\xi_6) + (4\xi_8-c_{1r})(\xi_4^2-4\xi_6(\xi_4-\xi_6)))),$$

$$q_2 \triangleq 4r_e^\star(\eta\xi_0(4\xi_3-\xi_2) + (1-\eta)(-8\xi_7(4\xi_8-c_{1r})(\xi_4-2\xi_6) + \xi_4^2(4\xi_9+c_{1i}) + 4(r_e^{\star 2}\xi_5(2\xi_9-c_{1i}) - 6\xi_6\xi_9(\xi_4-\xi_6)))),$$

$$q_3 \triangleq 4r_e^\star(3\eta\xi_0\xi_1 + (1-\eta)(\xi_4^2(4\xi_8-3c_{1r}) + 8\xi_{10} + 4\xi_{11} + 4(\xi_5r_e^{\star 2}(c_{1r}-8\xi_8) - 2\xi_7^2c_{1r} - 2\xi_6(2\xi_6\xi_8 - \xi_7(14\xi_9-c_{1i}))))),$$

$$q_4 \triangleq 8r_e^\star(3\eta\xi_0\xi_3 + (1-\eta)(\xi_9(5\xi_4^2 - 24r_e^{\star 2}\xi_5) + 2\xi_4(4\xi_7c_{1r} + \xi_6c_{1i}) - 4\xi_6(16\xi_7\xi_8 + \xi_9\xi_6))),$$

$$q_5 \triangleq 4r_e^\star(3\eta\xi_0\xi_1 + (1-\eta)(-\xi_4^2(4\xi_8+3c_{1r}) + 8\xi_{10} - 4\xi_{11} + 4(\xi_5r_e^{\star 2}(c_{1r}+8\xi_8) - 2\xi_7^2c_{1r} + 2\xi_6(2\xi_6\xi_8 - \xi_7(14\xi_9+c_{1i}))))),$$

$$q_6 \triangleq 4r_e^\star(\eta\xi_0(4\xi_3+\xi_2) + (1-\eta)(8\xi_7(4\xi_8+c_{1r})(\xi_4+2\xi_6) + \xi_4^2(4\xi_9-c_{1i}) + 4(r_e^{\star 2}\xi_5(2\xi_9+c_{1i}) + 6\xi_6\xi_9(\xi_4+\xi_6)))),$$

$$q_7 \triangleq 4r_e^\star(\eta\xi_0\xi_1 + (1-\eta)(4\xi_7(2\xi_9+c_{1i})(\xi_4+2\xi_6) - (4\xi_8+c_{1r})(\xi_4^2+4\xi_6(\xi_4+\xi_6)))),$$

$$q_8 \triangleq 2r_e^\star(\eta\xi_0(2\xi_3+\xi_2) - (1-\eta)(c_{1i}+2\xi_9)(\xi_4^2+4\xi_6(\xi_4+\xi_6))),$$

where, $\xi_0 \triangleq r_e^{\star 4} + r_e^{\star 2}d_1 + d_2$, $\xi_1 \triangleq r_e^{\star 2}(a_3b_{0r} - a_{0r}b_3) + (a_1b_{0r} - a_{0r}b_1)$, $\xi_2 \triangleq r_e^{\star 2}(a_3b_{0i} - a_{0i}b_3) + (a_1b_{0i} - a_{0i}b_1)$, $\xi_3 \triangleq r_e^\star(a_{0r}b_{0i} - a_{0i}b_{0r})$, $\xi_4 \triangleq r_e^{\star 2}b_3 + b_1$, $\xi_5 \triangleq b_{0r}^2 - 2b_{0i}^2$, $\xi_6 \triangleq r_e^\star b_{0r}$, $\xi_7 \triangleq r_e^\star b_{0i}$, $\xi_8 \triangleq r_e^\star c_{0r}$, $\xi_9 \triangleq r_e^\star r_{0i}$, $\xi_{10} \triangleq \xi_4(2\xi_6\xi_8 - 5\xi_7\xi_9)$ and $\xi_{11} \triangleq \xi_4(\xi_6c_{1r} - \xi_7c_{1i})$.

C.5

By substituting $r = 1$ in (4.20) and (4.21), the objective function under C_4 constraint can be written as, (4.31), where,

$$\begin{aligned}
&h_0 \triangleq b_0,\ h_1 \triangleq b_1 + b_3,\ h_2 \triangleq b_2,\ g_0 \triangleq c_0 b_0 \frac{1-\eta}{M_t N^2},\ g_6 \triangleq g_0^* \\
&g_1 \triangleq (c_0 b_1 + c_1 b_0)\frac{1-\eta}{M_t N^2}, \quad g_5 \triangleq g_1^* \\
&g_2 \triangleq (c_0 b_2 + c_1 b_1 + c_2 b_0)\frac{1-\eta}{M_t N^2} + a_0\eta, \quad g_4 \triangleq g_2^*, \\
&g_3 \triangleq (c_1 b_2 + c_2 b_1 + c_3 b_0)\frac{1-\eta}{M_t N^2} + a_1\eta.
\end{aligned} \tag{C.8}$$

Appendix D

Appendices of Chapter 5

D.1

It is readily confirmed that the constraint $\mathbf{X}_n = \bar{\mathbf{s}}_n \bar{\mathbf{s}}_n^\dagger$ is equivalent to $\text{Rank}(\mathbf{X}_n - \bar{\mathbf{s}}_n \bar{\mathbf{s}}_n^\dagger) = 0$. Further, it can be equivalently expressed as $1 + \text{Rank}(\mathbf{X}_n - \bar{\mathbf{s}}_n \bar{\mathbf{s}}_n^\dagger) = 1$. Since 1 is positive definite, it follows from the Guttman rank additivity formula [191] that $1 + \text{Rank}(\mathbf{X}_n - \bar{\mathbf{s}}_n \bar{\mathbf{s}}_n^\dagger) = \text{Rank}(\mathbf{Q}_n)$. Moreover, it follows from $\mathbf{X}_n = \bar{\mathbf{s}}_n \bar{\mathbf{s}}_n^\dagger$ and $1 \succ 0$ that $\mathbf{Q}_n$ has to be positive semi-definite. These imply that the constraint $\mathbf{X}_n = \bar{\mathbf{s}}_n \bar{\mathbf{s}}_n^\dagger$ in (3.33) can be replaced with a rank and semi-definite constraints on matrix $\mathbf{Q}_n$. Hence, the optimization problem (3.33) can be recast as follows,

$$\begin{cases} \min\limits_{\mathbf{S}, \mathbf{X}_n} & \sum\limits_{n=1}^{N} \text{Tr}(\mathbf{A}_u \mathbf{X}_n) & \text{(D.1a)} \\ s.t. & \text{(5.6b)}, \text{(5.6c)}, \text{(5.6d)}, \text{(5.6e)}, \text{(5.6f)}, \text{(5.6g)} & \text{(D.1b)} \\ & \mathbf{Q}_n \succcurlyeq \mathbf{0}, & \text{(D.1c)} \\ & \text{Rank}(\mathbf{Q}_n) = 1, & \text{(D.1d)} \end{cases}$$

Now, we show that the optimization problem (3.3.1) is equivalent to (D.1). Let $\rho_{n,1} \leq \rho_{n,2} \leq \cdots \leq \rho_{n,M+1}$ and $\nu_{n,1} \leq \nu_{n,2} \leq \cdots \leq \nu_{n,M}$ denote the eigenvalues of $\mathbf{Q}_n$ and $\mathbf{V}_n^\dagger \mathbf{Q}_n \mathbf{V}_n$, respectively. From the constraint $b_n \mathbf{I}_M - \mathbf{V}_n^\dagger \mathbf{Q}_n \mathbf{V}_n \succcurlyeq 0$, we have $\nu_{n,i} \leq b_n, i = 1, 2, \cdots, M$ for any $\mathbf{V}_n$ and $\mathbf{Q}_n$ in the feasible set of (3.3.1). Additionally, it follows from [155, Corollary 4.3.16] that $0 \leq \rho_{n,i} \leq \nu_{n,i}, i = 1, 2, \cdots, M$ for any $\mathbf{V}_n$ and $\mathbf{Q}_n$ in the feasible set of (3.3.1). Hence, we observe that,

$$\begin{aligned} \mathbf{0} &\preccurlyeq \text{Diag}([\rho_{n,1}, \cdots, \rho_{n,M}]^T) \\ &\preccurlyeq \text{Diag}([\nu_{n,1}, \cdots, \nu_{n,M}]^T) \preccurlyeq b_n \mathbf{I}_M, \end{aligned} \tag{D.2}$$

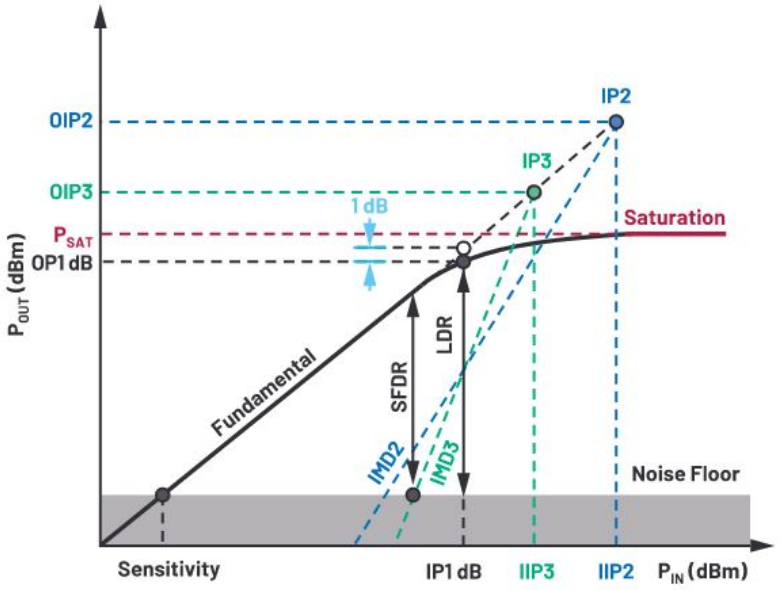

FIGURE D.1: The non-linearity behavior of PA [192].

for any $\mathbf{V}_n$ and $\mathbf{Q}_n$ in the feasible set of (3.3.1). It is easily observed from (3.3.1) and (D.2) that, by properly selecting η, the optimum value of $\mathbf{V}_n$ will be equal to the eigenvectors of $\mathbf{Q}_n$ corresponding to its M smallest eigenvalues and the optimum values of $b_n, \rho_{n,1}, \cdots, \rho_{n,M}, \nu_{n,1}, \cdots, \nu_{n,M}$ will be equal to zero. This implies that the optimum value of $\mathbf{Q}_n$ in (D.2) possesses one nonzero and M zero eigenvalues. This completes the proof.

D.2

Figure D.1 shows the non-linearity behavior of a PA. Based on this figure, the PA curve is linear when the input power is between a Sensitivity level and IP1 dB value. Beyond that, by increasing the input level, the output level will be entered to the non-linear region and converges to a saturation power. Therefore, the maximum power that can be obtained by PA without distortion is OP1 dB, corresponding to the IP1 dB input level. It means that the deviation of the input power should not be large near the IP1 dB value.

Appendix E

Appendices of Chapter 6

E.1

Defining, $\boldsymbol{Q} \triangleq \boldsymbol{s}^{\dagger}\boldsymbol{T}_c(\boldsymbol{w}^{(k+1)})\boldsymbol{s} + \frac{\rho}{2}\boldsymbol{h}(\boldsymbol{w}^{(k+1)})^{\dagger}\boldsymbol{h}(\boldsymbol{w}^{(k+1)})$, $b \triangleq -\frac{\rho}{2}\boldsymbol{h}(\boldsymbol{w}^{(k+1)})^{\dagger}(\kappa - u^{(k)})$ and $\mu \triangleq |\kappa - u^{(k)^*}|^2$, (6.35) can be written as, $\mathcal{L}_{\rho}\left(\boldsymbol{w}^{(k+1)}, \boldsymbol{s}, u^{(k)}\right) = \boldsymbol{s}^{\dagger}\boldsymbol{Q}\boldsymbol{s} + \boldsymbol{s}^{\dagger}\boldsymbol{b} + \boldsymbol{b}^{\dagger}\boldsymbol{s} + \mu$. Therefore, $\mathcal{L}_{\rho}\left(\boldsymbol{w}^{(k+1)}, \boldsymbol{s}, u^{(k)}\right) = \sum_{k=1}^{N}\sum_{n=1}^{N} s_n^* q_{n,k} s_n + \sum_{n=1}^{N} s_n^* b_n + \sum_{n=1}^{N} s_n b_n^* + \mu$. By some mathematical manipulation it can be shown that $\mathcal{L}_{\rho}\left(\boldsymbol{w}^{(k+1)}, \boldsymbol{s}, u^{(k)}\right) = c_0 s_d + c_1 + c_2 s_d^*$, where,

$$
\begin{aligned}
c_0 &= \textstyle\sum_{n=1}^{N} s_n^* q_{n,d} + b_d^*, \quad c_0 = \sum_{n=1}^{N} s_n q_{d,n} + b_d \\
c_1 &= \sum_{\substack{k=1 \\ k\neq d}}^{N}\sum_{\substack{n=1 \\ n\neq d}}^{N} s_n^* q_{n,k} s_n + \sum_{\substack{n=1 \\ n\neq d}}^{N} s_n^* b_n + \sum_{\substack{n=1 \\ n\neq d}}^{N} s_n b_n^* + \mu + q_{d,d},
\end{aligned}
$$

where, $q_{n,k}$ and b_n $(k, n = \{1, \dots\})$ are the the entries of $\boldsymbol{Q}$ and $\boldsymbol{b}$ respectively.

Appendix F

Appendices of Chapter 7

F.1

Calculating the coefficients of $f_{au}(\mathbf{x}_t)$: The k^{th} entry of $\mathbf{F}\bar{\mathbf{x}}_t$ and $\mathbf{w} \odot \mathbf{F}\bar{\mathbf{x}}_t^{r\,*}$ in (7.7) can be written as,

$$(\mathbf{F}\bar{\mathbf{x}}_t)_k = \alpha_1 \bar{x}_{t,d} + \gamma_1, \quad (\mathbf{w} \odot \mathbf{F}\bar{\mathbf{x}}_t^{r\,*})_k = \beta_2 \bar{x}_{t,d}^* + \gamma_2.$$

where, $\bar{x}_{t,d}$ denotes the d^{th} entry of $\mathbf{x}_t$ and $\alpha_1 \triangleq w_k e^{-j\frac{2\pi(k-1)(n-1)}{2N-1}}$, $\beta_2 \triangleq e^{-j\frac{2\pi(k-1)(n-1)}{2N-1}}$, $\gamma_1 \triangleq \sum_{\substack{n=1 \\ n\neq 2N-d}}^{2N-1} w_k \bar{x}_{t,N-n+1}^* e^{-j\frac{2\pi(k-1)(n-1)}{2N-1}}$ and $\gamma_2 \triangleq \sum_{\substack{n=1 \\ n\neq d}}^{2N-1} \bar{x}_{t,n} e^{-j\frac{2\pi(k-1)(n-1)}{2N-1}}$. Therefore,

$$(\mathbf{w} \odot \mathbf{F}\bar{\mathbf{x}}_t^{r\,*} \odot \mathbf{F}\bar{\mathbf{x}}_t)_k = \alpha_{tdk} \bar{x}_{t,d} + \beta_{tdk} \bar{x}_{t,d}^* + \gamma_{tdk}, .$$

where, $\alpha_{tdk} \triangleq \alpha_1\gamma_2$, $\beta_{tdk} = \beta_2\gamma_1$, $\gamma_{tdk} = \alpha_1\beta_2 + \gamma_1\gamma_2$. Substituting the aforementioned equation in $f_{au}(\mathbf{x}_t)$ we have,

$$f_{au}(\mathbf{x}_t) = a_{au,0} x_{t,d}^2 + a_{au,1} x_{t,d} + a_{au,2} + a_{au,3} x_{t,d}^* + a_{au,4} {x_{t,d}^*}^2.$$

where, $a_{au,0} \triangleq \frac{1}{2N-1}\sum_{k=1}^{2N-1} \alpha_{tdk}\beta_{tdk}$, $a_{au,4} \triangleq a_{au,0}^*$, $a_{au,1} \triangleq \frac{1}{2N-1}\sum_{k=1}^{2N-1}(\alpha_{tdk}\gamma_{tdk}^* + \beta_{tdk}^*\gamma_{tdk})$, $a_{au,3} \triangleq a_{au,1}^*$ and $a_{au,2} \triangleq \frac{1}{2N-1}\sum_{k=1}^{2N-1}(|\alpha_{tdk}|^2 + |\beta_{tdk}|^2 + |\gamma_{tdk}|^2)$.

Calculating the coefficients of $f_{cr}(\mathbf{x}_t, \mathbf{X}_{-t})$: By some mathematical manipulation it can be shown that,

$$f_{cr}(\mathbf{x}_t, \mathbf{X}_{-t}) = \sum_{\substack{m=1 \\ m\neq t}}^{M} \|\mathbf{V}_m \bar{\mathbf{x}}_t\|_2^2,$$

where, $\mathbf{V}_m \triangleq \mathbf{Diag}\,(\mathbf{w} \odot \mathbf{F}\bar{\mathbf{x}}_m^{r\,*}) \in \mathbb{C}^{(2N-1)\times(2N-1)}$. By some mathematical manipulation it can be shown that the k^{th} entry of $\mathbf{V}_m\bar{\mathbf{x}}_t$ can be obtained by, $(\mathbf{V}_m\bar{\mathbf{x}}_t)_k = \alpha_{mdk} x_{t,d} + \gamma_{mdk}$, where, $\alpha_{mdk} \triangleq v_{mdk}$ and $\gamma_{mdk} \triangleq \sum_{\substack{n=1 \\ n\neq d}}^{2N-1} v_{mnk} x_{t,n}$ and v_{mnk} denotes the n^{th} and

k^{th} entry of matrix $\mathbf{V}_m$. Substituting the aforementioned equation in $f_{cr}(\mathbf{x}_t, \mathbf{X}_{-t})$ we have,

$$f_{cr}(\mathbf{x}_t, \mathbf{X}_{-t}) = a_{cr,0}x_{t,d} + a_{cr,1} + a_{cr,2}x^*_{t,d}.$$

where, $a_{cr,0} \triangleq \sum_{\substack{n=1 \\ n\neq d}}^{2N-1} \bar{x}^*_{t,n} v_{mnd}$, $a_{cr,2} \triangleq a^*_{cr,0}$ and $a_{cr,1} \triangleq v_{mdd} + \sum_{\substack{n=1 \\ n\neq d}}^{2N-1} \sum_{\substack{n'=1 \\ n'\neq d}}^{2N-1} \bar{x}^*_{t,n} v_{mnn'} \bar{x}_{t,n'}$. Adding, $f_{au}(\mathbf{x}_t)$ and $f_{cr}(\mathbf{x}_t, \mathbf{X}_{-t})$ we have,

$$f_{cr,au}(\mathbf{x}_t, \mathbf{X}_{-t}) = a_0 x^2_{t,d} + a_1 x_{t,d} + a_2 + a_3 x^*_{t,d} + a_4 {x^*_{t,d}}^2,$$

where, $a_0 \triangleq a_{au,0}$, $a_1 \triangleq a_{au,1} + a_{cr,0}$, $a_2 \triangleq a_{au,2} + a_{cr,1}$, $a_3 \triangleq a^*_1$ and $a_4 \triangleq a^*_0$.

F.2

SILR coefficients Let us assume that

$$\boldsymbol{F}_{\mathcal{U}} \triangleq \sum_{k\in\mathcal{U}} \mathbf{f}_k \mathbf{f}_k^\dagger \in \mathbb{C}^{N\times N},$$

and $u_{n,l}$ indicates (n,l)-th element ($n = 1, 2, \ldots, N$, $l = 1, 2, \ldots, N$) of matrix $\boldsymbol{F}_{\mathcal{U}}$. The nominator in (7.11) can be written as

$$\begin{aligned} \sum_{m=1}^{M} \left\| \mathbf{f}_k^\dagger \mathbf{x}_m \right\|^2 | k \in \mathcal{U} &= \sum_{m=1}^{M} \sum_{k\in\mathcal{U}} \mathbf{x}_m^\dagger \mathbf{f}_k \mathbf{f}_k^\dagger \mathbf{x}_m = \textstyle\sum_{m=1}^{M} \mathbf{x}_m^\dagger \boldsymbol{F}_{\mathcal{U}} \mathbf{x}_m \\ &= \sum_{m=1}^{M} \sum_{n=1}^{N} \sum_{l=1}^{N} x^*_{m,n} u_{n,l} x_{m,l} \\ &= a_0 x_{t,d} + a_1 + a_2 x^*_{t,d} \end{aligned} \tag{F.1}$$

where

$$\begin{aligned} a_0 &= \sum_{\substack{n=1 \\ n\neq d}}^{N} x^*_{t,n} u_{n,d}, \\ a_1 &= \sum_{\substack{n=1 \\ n\neq d}}^{N} \sum_{n,l=1}^{N} x^*_{m,n} u_{n,l} x_{m,l} + \sum_{\substack{n,l=1 \\ n,l\neq d}}^{N} x^*_{t,n} u_{n,l} x_{t,l} + u_{d,d}, \end{aligned} \tag{F.2}$$

and $a_2 = a^*_0$. Similarly, by defining

$$\boldsymbol{F}_{\mathcal{V}} \triangleq \sum_{k\in\mathcal{V}} \mathbf{f}_k \mathbf{f}_k^\dagger \in \mathbb{C}^{N\times N}$$

the denominator in (7.11) is,

$$\sum_{m=1}^{M} \left\| \mathbf{f}_k^{\dagger} \mathbf{x}_m \right\|^2 | k \in \mathcal{V} = b_0 x_{t,d} + b_1 + b_2 x_{t,d}^*, \tag{F.3}$$

where

$$\begin{aligned} b_0 &= \sum_{\substack{n=1 \\ n \neq d}}^{N} x_{t,n}^* v_{n,d}, \\ b_1 &= \sum_{\substack{n=1 \\ n \neq d}}^{N} \sum_{n,l=1}^{N} x_{m,n}^* v_{n,l} x_{m,l} + \sum_{\substack{n,l=1 \\ n,l \neq d}}^{N} x_{t,n}^* v_{n,l} x_{t,l} + v_{d,d}, \end{aligned} \tag{F.4}$$

with $b_2 = b_0^*$, and $v_{n,l}$ are the elements of $\boldsymbol{F}_{\mathcal{V}}$.

ICCL coefficients For (7.13), it can be shown that,

$$\sum_{m=1}^{M} \sum_{\substack{m'=1 \\ m' \neq m}}^{M} \sum_{l=-N+1}^{N-1} |r_{m,m'}(l)|^2 = \gamma_t + 2 \sum_{\substack{m=1 \\ m \neq t}}^{M} \sum_{l=-N+1}^{N-1} |r_{m,t}(l)|^2, \tag{F.5}$$

where

$$\gamma_t \triangleq \sum_{\substack{m=1 \\ m \neq t}}^{M} \sum_{\substack{m'=1 \\ m' \neq m,t}}^{M} \sum_{l=-N+1}^{N-1} |r_{m,m'}(l)|^2.$$

Further, it would be easy to show

$$r_{m,t}(l) = \alpha_{mtdl} x_{t,d} + \gamma_{mtdl} \tag{F.6}$$

where $\alpha_{mtdl} = x_{m,d-l} I_A(d-l)$, and

$$\gamma_{mtdl} = \sum_{\substack{n=1 \\ n \neq d-l}}^{N-l} x_{m,n} x_{t,n+l}^*, \tag{F.7}$$

where, $I_A(p)$ is the indicator function of set $A = \{1, \ldots, N\}$, i. e., $I_A(p) = \begin{cases} 1, & p \in A \\ 0, & p \notin A \end{cases}$.

Thus,

$$\sum_{m=1}^{M} \sum_{\substack{m'=1 \\ m' \neq m}}^{M} \sum_{l=-N+1}^{N-1} |r_{m,m'}(l)|^2 = c_0 x_{t,d} + c_1 + c_2 x_{t,d}^*, \tag{F.8}$$

where

$$c_0 = \frac{2}{(2MN)^2} \sum_{\substack{m=1 \\ m \neq t}}^{M} \sum_{l=-N+1}^{N-1} \alpha_{mtdl} \gamma_{mtdl}^*, \tag{F.9}$$

$$c_1 = \frac{1}{(2MN)^2}(\gamma_t + 2\sum_{\substack{m=1\\m\neq t}}^{M}\sum_{l=-N+1}^{N-1}|\alpha_{mtdl}|^2 + 2\sum_{\substack{m=1\\m\neq t}}^{M}\sum_{l=-N+1}^{N-1}|\gamma_{mtdl}|^2), \tag{F.10}$$

and $c_2 = c_0^*$.

F.3

Equation (7.20) can be expressed as,

$$g(\phi) = \theta\frac{g_a(\phi)}{g_b(\phi)} + (1-\theta)g_c(\phi), \tag{F.11}$$

where

$$g_a(\phi) = a_0e^{j\phi} + a_1 + a_2e^{-j\phi},$$

$$g_b(\phi) = b_0e^{j\phi} + b_1 + b_2e^{-j\phi},$$

$$g_c(\phi) = c_0e^{j\phi} + c_1 + c_2e^{-j\phi}.$$

The derivative of $g(\phi)$ can be written as,

$$g'(\phi) = \theta\frac{g_a'(\phi)g_b(\phi) - g_b'(\phi)g_a(\phi)}{g_b^2(\phi)} + (1-\theta)g_c'(\phi). \tag{F.12}$$

By some standard mathematical manipulation $g'(\phi)$ can be written as

$$g'(\phi) = \frac{e^{j3\phi}\sum_{p=0}^{6}q_pe^{jp\phi}}{(b_0e^{j\phi} + b_1 + b_2e^{-j\phi})^2}, \tag{F.13}$$

where

$$\begin{aligned}
q_0 =& j(1-\theta)c_0b_0^2,\\
q_1 =& j2(1-\theta)c_0b_0b_1,\\
q_2 =& j(\theta(a_0b_1 - b_0a_1) + (1-\theta)(2c_0b_0b_2 + c_0b_1^2 - c_2b_0^2))\\
q_3 =& j2(\theta(a_0b_2 - a_2b_0) + (1-\theta)b_1(c_0b_2 - c_2b_0)),\\
q_4 =& q_2^*, \quad q_5 \triangleq q_1^*, \quad q_6 \triangleq q_0^*.
\end{aligned} \tag{F.14}$$

Bibliography

[1] W. Rowe, P. Stoica, and J. Li, "Spectrally constrained waveform design [sp tips tricks]," *IEEE Signal Processing Magazine*, vol. 31, no. 3, pp. 157–162, May 2014.

[2] H. He, P. Stoica, and J. Li, "Designing unimodular sequence sets with good correlations; including an application to MIMO radar," *IEEE Trans. Signal Process.*, vol. 57, no. 11, pp. 4391–4405, Nov 2009.

[3] J. Song, P. Babu, and D. P. Palomar, "Sequence set design with good correlation properties via majorization-minimization," *IEEE Trans. Signal Process.*, vol. 64, no. 11, pp. 2866–2879, June 2016.

[4] M. Y. Keegan Garcia and A. Purkovic, "Texas instrument: The fundamentals of millimeter wave radar sensors," https://www.ti.com/lit/wp/spyy005a/spyy005a.pdf?ts=1656513991652&ref_url=https%253A%252F%252Fwww.ti.com%252Fsensors%252Fmmwave-radar%252Foverview.html, accessed: 2022-07-03.

[5] F. Engels, P. Heidenreich, M. Wintermantel, L. Stäcker, M. Al Kadi, and A. M. Zoubir, "Automotive radar signal processing: Research directions and practical challenges," *IEEE Journal of Selected Topics in Signal Processing*, vol. 15, no. 4, pp. 865–878, 2021.

[6] S. Xiao, M. Zhou, and Y. Zhang, "Millimeter wave technology in wireless pan, lan, and man," 2007.

[7] N. Kathuria and B.-C. Seet, "24 ghz flexible antenna for doppler radar-based human vital signs monitoring," *Sensors*, vol. 21, no. 11, 2021. [Online]. Available: https://www.mdpi.com/1424-8220/21/11/3737

[8] U. D. TANIMOTO Yudai and S. Keisuke, "Millimeter-wave traffic monitoring radar using high-resolution direction of arrival estimation," https://www.omron.com/global/en/assets/file/technology/omrontechnics/vol52/OMT_Vol52_006EN.pdf, accessed: 2022-07-03.

[9] M. Y. Keegan Garcia and A. Purkovic, "Texas instrument: The fundamentals of millimeter wave radar sensors," https://www.ti.com/lit/wp/spyy002b/spyy002b.pdf?ts=1656838481708&ref_url=https%253A%252F%252Fwww.google.com%252F, accessed: 2022-07-03.

[10] F. Yanovsky, "Millimeter-wave radar: Principles and applications," in *Millimeter Wave Technology in Wireless PAN, LAN, and MAN*, Y. Z. Shao-Qiu Xiao, Ming-Tuo Zhou, Ed. Auerbach Publications CRC Press, 2008, ch. 10.

[11] J. Guerci, *Cognitive Radar: The Knowledge-Aided Fully Adaptive Approach*, ser. Artech House Radar Library. Artech House, 2010. [Online]. Available: http://books.google.com/books?id=8Mn_C-iOzeEC

[12] M. A. Wayne Stark and M. Maher, "Digital code modulation (dcm) radar for automotive application," https://www.uhnder.com/images/data/DCM_Radar_for_Automotive_Application_Final.pdf, accessed: 2022-07-03.

[13] V. Giannini, D. Guermandi, Q. Shi, A. Medra, W. Van Thillo, A. Bourdoux, and P. Wambacq, "A 79 ghz phase-modulated 4 ghz-bw cw radar transmitter in 28 nm cmos," *IEEE Journal of Solid-State Circuits*, vol. 49, no. 12, pp. 2925–2937, 2014.

[14] D. Guermandi, Q. Shi, A. Dewilde, V. Derudder, U. Ahmad, A. Spagnolo, I. Ocket, A. Bourdoux, P. Wambacq, J. Craninckx, and W. Van Thillo, "A 79-ghz 2 × 2 mimo pmcw radar soc in 28-nm cmos," *IEEE Journal of Solid-State Circuits*, vol. 52, no. 10, pp. 2613–2626, 2017.

[15] A. Bourdoux, U. Ahmad, D. Guermandi, S. Brebels, A. Dewilde, and W. Van Thillo, "Pmcw waveform and mimo technique for a 79 ghz cmos automotive radar," in *2016 IEEE Radar Conference (RadarConf)*, 2016, pp. 1–5.

[16] O. F. Garcia, "Signal processing for mmwave mimo radar," Ph.D. dissertation, University of Gavle, 2015.

[17] J. Li and P. Stoica, *MIMO Radar Signal Processing*. John Wiley & Sons, Inc., Hoboken, NJ, 2009.

[18] H. Sun, F. Brigui, and M. Lesturgie, "Analysis and comparison of MIMO radar waveforms," in *2014 International Radar Conference*, Oct 2014, pp. 1–6.

[19] D. J. Rabideau, "Doppler-offset waveforms for MIMO radar," in *2011 IEEE RadarCon (RADAR)*, May 2011, pp. 965–970.

[20] C. Nunn and G. Coxson, "Best-known autocorrelation peak sidelobe levels for binary codes of length 71 to 105," *IEEE Trans. Aerosp. Electron. Syst.*, vol. 44, no. 1, pp. 392–395, Jan 2008.

[21] H. He, J. Li, and P. Stoica, *Waveform design for active sensing systems: a computational approach*. Cambridge University Press, 2012.

[22] Y. Li and S. A. Vorobyov, "Fast algorithms for designing unimodular waveform(s) with good correlation properties," *IEEE Trans. Signal Process.*, vol. 66, no. 5, pp. 1197–1212, March 2018.

[23] J. Liang, H. C. So, J. Li, and A. Farina, "Unimodular sequence design based on alternating direction method of multipliers," *IEEE Trans. Signal Process.*, vol. 64, no. 20, pp. 5367–5381, 2016.

[24] M. Alaee-Kerahroodi, M. Modarres-Hashemi, and M. M. Naghsh, "Designing sets of binary sequences for MIMO radar systems," *IEEE Trans. Signal Process.*, pp. 1–1, 2019.

[25] T. Aittomaki and V. Koivunen, "Low-complexity method for transmit beamforming in MIMO radars," in *2007 IEEE International Conference on Acoustics, Speech and Signal Processing - ICASSP '07*, vol. 2, April 2007, pp. II–305–II–308.

[26] Z. Cheng, Z. He, S. Zhang, and J. Li, "Constant modulus waveform design for MIMO radar transmit beampattern," *IEEE Trans. Signal Process.*, vol. 65, no. 18, pp. 4912–4923, Sep. 2017.

[27] X. Yu, G. Cui, J. Yang, L. Kong, and J. Li, "Wideband MIMO radar waveform design," *IEEE Trans. Signal Process.*, vol. 67, no. 13, pp. 3487–3501, July 2019.

[28] P. Stoica, J. Li, and Y. Xie, "On probing signal design for MIMO radar," *IEEE Trans. Signal Process.*, vol. 55, no. 8, pp. 4151–4161, Aug 2007.

[29] P. Stoica, J. Li, and X. Zhu, "Waveform synthesis for diversity-based transmit beampattern design," *IEEE Trans. Signal Process.*, vol. 56, no. 6, pp. 2593–2598, June 2008.

[30] G. Cui, H. Li, and M. Rangaswamy, "MIMO radar waveform design with constant modulus and similarity constraints," *IEEE Trans. Signal Process.*, vol. 62, no. 2, pp. 343–353, Jan 2014.

[31] G. Cui, X. Yu, V. Carotenuto, and L. Kong, "Space-time transmit code and receive filter design for colocated MIMO radar," *IEEE Trans. Signal Process.*, vol. 65, no. 5, pp. 1116–1129, March 2017.

[32] H. Xu, R. S. Blum, J. Wang, and J. Yuan, "Colocated MIMO radar waveform design for transmit beampattern formation," *IEEE Trans. Aerosp. Electron. Syst.*, vol. 51, no. 2, pp. 1558–1568, April 2015.

[33] J. Li, P. Stoica, and X. Zheng, "Signal synthesis and receiver design for MIMO radar imaging," *IEEE Trans. Signal Process.*, vol. 56, no. 8, pp. 3959–3968, Aug 2008.

[34] J. Lipor, S. Ahmed, and M. Alouini, "Fourier-based transmit beampattern design using MIMO radar," *IEEE Trans. Signal Process.*, vol. 62, no. 9, pp. 2226–2235, May 2014.

[35] T. Bouchoucha, S. Ahmed, T. Al-Naffouri, and M. Alouini, "DFT-based closed-form covariance matrix and direct waveforms design for MIMO radar to achieve desired beampatterns," *IEEE Trans. Signal Process.*, vol. 65, no. 8, pp. 2104–2113, April 2017.

[36] S. Ahmed, J. S. Thompson, Y. R. Petillot, and B. Mulgrew, "Unconstrained synthesis of covariance matrix for MIMO radar transmit beampattern," *IEEE Trans. Signal Process.*, vol. 59, no. 8, pp. 3837–3849, Aug 2011.

[37] E. Raei, M. Alaee-Kerahroodi, and M. B. Shankar, "Spatial- and range- ISLR trade-off in MIMO radar via waveform correlation optimization," *IEEE Transactions on Signal Processing*, vol. 69, pp. 3283–3298, 2021.

[38] E. Raei, M. Alaee-Kerahroodi, B. S. M. R., and B. Ottersten, "Transmit beampattern shaping via waveform design in cognitive MIMO radar," in *ICASSP*, 2020, pp. 4582–4586.

[39] E. Raei, M. Alaee-Kerahroodi, and B. S. M. R., "Beampattern shaping for coexistence of cognitive MIMO radar and MIMO communications," in *2020 IEEE 11th Sensor Array and Multichannel Signal Processing Workshop (SAM)*, 2020, pp. 1–5.

[40] W. Fan, J. Liang, and J. Li, "Constant modulus MIMO radar waveform design with minimum peak sidelobe transmit beampattern," *IEEE Trans. Signal Process.*, vol. 66, no. 16, pp. 4207–4222, Aug 2018.

[41] K. Alhujaili, V. Monga, and M. Rangaswamy, "Transmit MIMO radar beampattern design via optimization on the complex circle manifold," *IEEE Trans. Signal Process.*, vol. 67, no. 13, pp. 3561–3575, July 2019.

[42] W. Fan, J. Liang, G. Yu, H. C. So, and G. Lu, "MIMO radar waveform design for quasi-equiripple transmit beampattern synthesis via weighted l_p-minimization," *IEEE Trans. Signal Process.*, vol. 67, no. 13, pp. 3397–3411, July 2019.

[43] E. Raei, M. Alaee-Kerahroodi, and B. M. R. Shankar, "Waveform design for beampattern shaping in 4d-imaging mimo radar systems," in *2021 21st International Radar Symposium (IRS)*, 2021, pp. 1–10.

[44] A. Aubry, A. De Maio, and Y. Huang, "MIMO radar beampattern design via PSL/ISL optimization," *IEEE Trans. Signal Process.*, vol. 64, no. 15, pp. 3955–3967, Aug 2016.

[45] L. Wu, P. Babu, and D. P. Palomar, "Transmit waveform/receive filter design for MIMO radar with multiple waveform constraints," *IEEE Trans. Signal Process.*, vol. 66, no. 6, pp. 1526–1540, March 2018.

[46] X. Yu, G. Cui, L. Kong, J. Li, and G. Gui, "Constrained waveform design for colocated MIMO radar with uncertain steering matrices," *IEEE Trans. Aerosp. Electron. Syst.*, vol. 55, no. 1, pp. 356–370, 2019.

[47] M. Alaee-Kerahroodi, E. Raei, S. Kumar, and B. S. M. R. R., "Cognitive radar waveform design and prototype for coexistence with communications," *IEEE Sensors Journal*, vol. 22, no. 10, pp. 9787–9802, 2022.

[48] H. He, P. Stoica, and J. Li, "Waveform design with stopband and correlation constraints for cognitive radar," in *2nd International Workshop on Cognitive Information Processing (CIP)*, June 2010, pp. 344–349.

[49] J. Liang, H. C. So, C. S. Leung, J. Li, and A. Farina, "Waveform design with unit modulus and spectral shape constraints via lagrange programming neural network," *IEEE Journal of Selected Topics in Signal Processing*, vol. 9, no. 8, pp. 1377–1386, 2015.

[50] K. Alhujaili, X. Yu, G. Cui, and V. Monga, "Spectrally compatible MIMO radar beampattern design under constant modulus constraints," *IEEE Transactions on Aerospace and Electronic Systems*, vol. 56, no. 6, pp. 4749–4766, 2020.

[51] M. Alaee-Kerahroodi, S. Kumar, M. R. B. Shankar, and K. V. Mishra, "Discrete-phase sequence design with stopband and PSL constraints for cognitive radar," in *2020 17th European Radar Conference (EuRAD)*, 2021, pp. 17–20.

[52] B. Tang and J. Li, "Spectrally constrained MIMO radar waveform design based on mutual information," *IEEE Transactions on Signal Processing*, vol. 67, no. 3, pp. 821–834, 2019.

[53] A. Aubry, A. De Maio, M. A. Govoni, and L. Martino, "On the design of multi-spectrally constrained constant modulus radar signals," *IEEE Trans. Signal Process.*, vol. 68, pp. 2231–2243, 2020.

[54] Y. Jing, J. Liang, D. Zhou, and H. C. So, "Spectrally constrained unimodular sequence design without spectral level mask," *IEEE Signal Processing Letters*, vol. 25, no. 7, pp. 1004–1008, 2018.

[55] L. Wu and D. P. Palomar, "Sequence design for spectral shaping via minimization of regularized spectral level ratio," *IEEE Transactions on Signal Processing*, vol. 67, no. 18, pp. 4683–4695, 2019.

[56] B. Kang, O. Aldayel, V. Monga, and M. Rangaswamy, "Spatio-spectral radar beampattern design for coexistence with wireless communication systems," *IEEE Transactions on Aerospace and Electronic Systems*, vol. 55, no. 2, pp. 644–657, 2019.

[57] E. Raei, S. Sedighi, M. Alaee-Kerahroodi, and M. Shankar, "MIMO radar transmit beampattern shaping for spectrally dense environments," *arXiv preprint arXiv:2112.06670*, 2021.

[58] E. Raei, M. Alaee-Kerahroodi, P. Babu, and M. R. B. Shankar, "Design of MIMO radar waveforms based on lp-norm criteria," 2021.

[59] E. Raei, M. Alaee-Kerahroodi, and M. R. Bhavani Shankar, "Admm based transmit waveform and receive filter design in cognitive radar systems," in *2020 IEEE Radar Conference (RadarConf20)*, 2020, pp. 1–6.

[60] E. Raei, M. Alaee-Kerahroodi, B. S. M. R, and B. Ottersten, "Designing MPSK sequences and doppler filter bank in cognitive radar systems," in *2019 International Radar Conference*, 2019, pp. 1–6.

[61] E. Raei, M. Modarres-Hashemi, and M. R. Bhavani Shankar, "Range cell migration correction by fractional fourier transform in synthetic aperture radars," in *2019 20th International Radar Symposium (IRS)*, 2019, pp. 1–10.

[62] A. Augusto, N. Mohammad, Mahdi, R. Ehsan, A.-K. Mohammad, and M. Bhavani, Shankar, *Radar Waveform Design Based on Optimization Theory*. IET, 2020, ch. Optimizing radar transceiver for Doppler processing via non-convex programming, pp. 63–92.

[63] S. D. Blunt and E. L. Mokole, "Overview of radar waveform diversity," *IEEE Aerospace and Electronic Systems Magazine*, vol. 31, no. 11, pp. 2–42, 2016.

[64] M. Kumar and V. Chandrasekar, "Intrapulse polyphase coding system for second trip suppression in a weather radar," *IEEE Transactions on Geoscience and Remote Sensing*, vol. 58, no. 6, pp. 3841–3853, 2020.

[65] J. M. Baden, "Efficient optimization of the merit factor of long binary sequences," *IEEE Trans. Inf. Theory*, vol. 57, no. 12, pp. 8084–8094, Dec 2011.

[66] "Texas instrument: MIMO radar, application report, swra554," https://www.ti.com/lit/an/swra554a/swra554a.pdf, accessed: 2021-03-15.

[67] C. Hammes, B. S. M. R., and B. Ottersten, "Generalized multiplexed waveform design framework for cost-optimized mimo radar," *IEEE Trans. Signal Process.*, vol. 69, pp. 88–102, 2021.

[68] "Ultra-small, economical and cheap radar made possible thanks to chip technology," https://www.imec-int.com/en/imec-magazine/imec-magazine-march-2018/ultra-small-economical-and-cheap-radar-made-possible-thanks-to-chip-technology, accessed: 2021-03-15.

[69] J. R. Guerci, R. M. Guerci, M. Ranagaswamy, J. S. Bergin, and M. C. Wicks, "CoFAR: Cognitive fully adaptive radar," in *2014 IEEE Radar Conference*, 2014, pp. 0984–0989.

[70] P. Stinco, M. Greco, F. Gini, and B. Himed, "Cognitive radars in spectrally dense environments," *IEEE Aerospace and Electronic Systems Magazine*, vol. 31, no. 10, pp. 20–27, 2016.

[71] S. Z. Gurbuz, H. D. Griffiths, A. Charlish, M. Rangaswamy, M. S. Greco, and K. Bell, "An overview of cognitive radar: Past, present, and future," *IEEE Aerospace and Electronic Systems Magazine*, vol. 34, no. 12, pp. 6–18, 2019.

[72] A. De Maio and A. Farina, "The role of cognition in radar sensing," in *2020 IEEE Radar Conference (RadarConf20)*, 2020, pp. 1–6.

[73] P. Stoica, H. He, and J. Li, "New algorithms for designing unimodular sequences with good correlation properties," *IEEE Trans. Signal Process.*, vol. 57, no. 4, pp. 1415–1425, Apr 2009.

[74] ——, "On designing sequences with impulse-like periodic correlation," *IEEE Signal Processing Letters*, vol. 16, no. 8, pp. 703–706, Aug 2009.

[75] J. Song, P. Babu, and D. Palomar, "Optimization methods for designing sequences with low autocorrelation sidelobes," *IEEE Trans. Signal Process.*, vol. 63, no. 15, pp. 3998–4009, Aug 2015.

[76] J. Song, P. Babu, and D. P. Palomar, "Sequence design to minimize the weighted integrated and peak sidelobe levels," *IEEE Trans. Signal Process.*, vol. 64, no. 8, pp. 2051–2064, Apr 2016.

[77] L. Zhao, J. Song, P. Babu, and D. P. Palomar, "A unified framework for low autocorrelation sequence design via Majorization-Minimization," *IEEE Trans. Signal Process.*, vol. 65, no. 2, pp. 438–453, Jan 2017.

[78] M. Alaee-Kerahroodi, A. Aubry, A. De Maio, M. M. Naghsh, and M. Modarres-Hashemi, "A coordinate-descent framework to design low PSL/ISL sequences," *IEEE Trans. Signal Process.*, vol. 65, no. 22, pp. 5942–5956, Nov 2017.

[79] J. M. Baden, B. O'Donnell, and L. Schmieder, "Multiobjective sequence design via gradient descent methods," *IEEE Trans. Aerosp. Electron. Syst.*, vol. 54, no. 3, pp. 1237–1252, June 2018.

[80] R. Lin, M. Soltanalian, B. Tang, and J. Li, "Efficient design of binary sequences with low autocorrelation sidelobes," *IEEE Trans. Signal Process.*, vol. 67, no. 24, pp. 6397–6410, Dec 2019.

[81] Y. Bu, X. Yu, J. Yang, T. Fan, and G. Cui, "A new approach for design of constant modulus discrete phase radar waveform with low wisl," *Signal Processing*, vol. 187, p. 108145, 2021. [Online]. Available: https://www.sciencedirect.com/science/article/pii/S0165168421001833

[82] S. P. Sankuru and P. Babu, "A fast iterative algorithm to design phase-only sequences by minimizing the isl metric," *Digital Signal Processing*, vol. 111, p. 102991, 2021. [Online]. Available: https://www.sciencedirect.com/science/article/pii/S1051200421000300

[83] W. Fan, J. Liang, G. Yu, H. C. So, and G. Lu, "Minimum local peak sidelobe level waveform design with correlation and/or spectral constraints," *Signal Processing*, vol. 171, p. 107450, 2020. [Online]. Available: https://www.sciencedirect.com/science/article/pii/S0165168419305018

[84] W. Fan, J. Liang, H. C. So, and G. Lu, "Min-max metric for spectrally compatible waveform design via log-exponential smoothing," *IEEE Transactions on Signal Processing*, vol. 68, pp. 1075–1090, 2020.

[85] G. Cui, X. Yu, M. Piezzo, and L. Kong, "Constant modulus sequence set design with good correlation properties," *Signal Processing*, vol. 139, pp. 75–85, 2017.

[86] M. Alaee-Kerahroodi, M. R. Bhavani Shankar, K. V. Mishra, and B. Ottersten, "Meeting the lower bound on designing set of unimodular sequences with small aperiodic/periodic isl," in *2019 20th International Radar Symposium (IRS)*, 2019, pp. 1–13.

[87] G. Jin, A. Aubry, A. De Maio, R. Wang, and W. Wang, "Quasi-orthogonal waveforms for ambiguity suppression in spaceborne quad-pol sar," *IEEE Transactions on Geoscience and Remote Sensing*, pp. 1–17, 2021.

[88] S. P. Sankuru, R. Jyothi, P. Babu, and M. Alaee-Kerahroodi, "Designing sequence set with minimal peak side-lobe level for applications in high resolution radar imaging," *IEEE Open Journal of Signal Processing*, vol. 2, pp. 17–32, 2021.

[89] R. Lin and J. Li, "On binary sequence set design with applications to automotive radar," in *ICASSP 2020 - 2020 IEEE International Conference on Acoustics, Speech and Signal Processing (ICASSP)*, 2020, pp. 8639–8643.

[90] W. Fan, J. Liang, Z. Chen, and H. C. So, "Spectrally compatible aperiodic sequence set design with low cross- and auto-correlation psl," *Signal Processing*, vol. 183, p. 107960, 2021. [Online]. Available: https://www.sciencedirect.com/science/article/pii/S0165168420305041

[91] H. Esmaeili-Najafabadi, M. Ataei, and M. F. Sabahi, "Designing sequence with minimum PSL using chebyshev distance and its application for chaotic MIMO radar waveform design," *IEEE Trans. Signal Process.*, vol. 65, no. 3, pp. 690–704, Feb 2017.

[92] S. Boyd, S. P. Boyd, and L. Vandenberghe, *Convex optimization*. Cambridge University Press, 2004.

[93] J. Song, P. Babu, and D. P. Palomar, "Sparse generalized eigenvalue problem via smooth optimization," *IEEE Trans. Signal Process.*, vol. 63, no. 7, pp. 1627–1642, 2015.

[94] R. Seidel and M. Sharir, "Top-down analysis of path compression," *SIAM Journal on Computing*, vol. 34, no. 3, pp. 515–525, 2005. [Online]. Available: https://doi.org/10.1137/S0097539703439088

[95] M. R. B. Shankar and K. V. S. Hari, "Reduced complexity equalization schemes for zero padded ofdm systems," *IEEE Signal Processing Letters*, vol. 11, no. 9, pp. 752–755, 2004.

[96] G. H. Golub and C. F. Van Loan, *Matrix Computations*, 3rd ed. The Johns Hopkins University Press, 1996.

[97] H. He, J. Li, and P. Stoica, *Waveform Design for Active Sensing Systems*. Cambridge University Press, 2012.

[98] K. Mohammad, Alaee, A. Augusto, N. Mohammad, Mahdi, M. Antonio, De, and H. Mahmoud, Modarres, *Radar Waveform Design Based on Optimization Theory*. Institution of Engineering and Technology, 2020, ch. A computational design of phase-only (possibly binary) sequences for radar systems, pp. 63–92.

[99] M. Skolnik, *Radar Handbook, Third Edition*, ser. Electronics electrical engineering. McGraw-Hill Education, 2008.

[100] M. Alaee-Kerahroodi, K. V. Mishra, and B. S. M.R., "Radar beampattern design for a drone swarm," in *2019 53rd Asilomar Conference on Signals, Systems, and Computers*, 2019, pp. 1416–1421.

[101] E. Raei, M. Alaee-Kerahrood, and M. R. B. Shankar, "Spatial- and range-ISLR trade-off in MIMO radar via waveform correlation optimization," 2021.

[102] S. J. Wright, "Coordinate descent algorithms," *Mathematical Programming*, vol. 151, no. 1, pp. 3–34, 2015.

[103] Z. Cheng, B. Liao, Z. He, and J. Li, "Transmit signal design for large-scale MIMO system with 1-bit DACs," *IEEE Transactions on Wireless Communications*, vol. 18, no. 9, pp. 4466–4478, 2019.

[104] T. Wei, L. Wu, M. Alaee-Kerahroodi, and M. R. Bhavani Shankar, "Transmit beampattern synthesis for planar array with one-bit DACs," in *2021 21st International Radar Symposium (IRS)*, 2021.

[105] J. Li and P. Stoica, *MIMO Radar Diversity Means Superiority*. Wiley-IEEE Press, 2009, pp. 594–. [Online]. Available: http://ieeexplore.ieee.org.proxy.bnl.lu/xpl/articleDetails.jsp?arnumber=5236931

[106] M. Hong, M. Razaviyayn, Z. Luo, and J. Pang, "A unified algorithmic framework for block-structured optimization involving big data: With applications in machine learning and signal processing," *IEEE Signal Processing Magazine*, vol. 33, no. 1, pp. 57–77, 2016.

[107] M. Razaviyayn, M. Hong, and Z.-Q. Luo, "A unified convergence analysis of block successive minimization methods for nonsmooth optimization," 2012.

[108] M. Hong, M. Razaviyayn, Z.-Q. Luo, and J.-S. Pang, "A unified algorithmic framework for block-structured optimization involving big data," 2015.

[109] U. Niesen, D. Shah, and G. W. Wornell, "Adaptive alternating minimization algorithms," *IEEE Transactions on Information Theory*, vol. 55, no. 3, pp. 1423–1429, 2009.

[110] K. V. Mishra, M. R. Bhavani Shankar, V. Koivunen, B. Ottersten, and S. A. Vorobyov, "Toward millimeter-wave joint radar communications: A signal processing perspective," *IEEE Signal Processing Magazine*, vol. 36, no. 5, pp. 100–114, Sep. 2019.

[111] A. Hassanien, M. G. Amin, Y. D. Zhang, and F. Ahmad, "Signaling strategies for dual-function radar communications: an overview," *IEEE Aerospace and Electronic Systems Magazine*, vol. 31, no. 10, pp. 36–45, October 2016.

[112] B. Paul, A. R. Chiriyath, and D. W. Bliss, "Survey of rf communications and sensing convergence research," *IEEE Access*, vol. 5, pp. 252–270, 2017.

[113] S. H. Dokhanchi, M. R. Bhavani Shankar, M. Alaee-Kerahroodi, T. Stifter, and B. Ottersten, "Adaptive waveform design for automotive joint radar-communications system," in *ICASSP 2019 - 2019 IEEE International Conference on Acoustics, Speech and Signal Processing (ICASSP)*, May 2019, pp. 4280–4284.

[114] S. H. Dokhanchi, B. S. Mysore, K. V. Mishra, and B. Ottersten, "A mmwave automotive joint radar-communications system," *IEEE Transactions on Aerospace and Electronic Systems*, vol. 55, no. 3, pp. 1241–1260, June 2019.

[115] S. H. Dokhanchi, M. R. B. Shankar, Y. A. Nijsure, T. Stifter, S. Sedighi, and B. Ottersten, "Joint automotive radar-communications waveform design," in *2017 IEEE 28th Annual International Symposium on Personal, Indoor, and Mobile Radio Communications (PIMRC)*, Oct 2017, pp. 1–7.

[116] D. Cohen, K. V. Mishra, and Y. C. Eldar, "Spectrum sharing radar: Coexistence via xampling," *IEEE Transactions on Aerospace and Electronic Systems*, vol. 54, no. 3, pp. 1279–1296, June 2018.

[117] M. Alaee-Kerahroodi, K. V. Mishra, M. R. Bhavani Shankar, and B. Ottersten, "Discrete-phase sequence design for coexistence of MIMO radar and MIMO communications," in *2019 IEEE 20th International Workshop on Signal Processing Advances in Wireless Communications (SPAWC)*, July 2019, pp. 1–5.

[118] S. Haykin, "Cognitive radar: a way of the future," *IEEE Signal Processing Magazine*, vol. 23, no. 1, pp. 30–40, Jan 2006.

[119] M. S. Greco, F. Gini, P. Stinco, and K. Bell, "Cognitive radars: On the road to reality: Progress thus far and possibilities for the future," *IEEE Signal Processing Magazine*, vol. 35, no. 4, pp. 112–125, July 2018.

[120] F. Engels, P. Heidenreich, A. M. Zoubir, F. K. Jondral, and M. Wintermantel, "Advances in automotive radar: A framework on computationally efficient high-resolution frequency estimation," *IEEE Signal Processing Magazine*, vol. 34, no. 2, pp. 36–46, March 2017.

[121] S. M. Patole, M. Torlak, D. Wang, and M. Ali, "Automotive radars: A review of signal processing techniques," *IEEE Signal Processing Magazine*, vol. 34, no. 2, pp. 22–35, March 2017.

[122] M. Alaee-Kerahroodi, S. Sedighi, B. Shankar M.R., and B. Ottersten, "Designing (in)finite-alphabet sequences via shaping the radar ambiguity function," in *ICASSP 2019 - 2019 IEEE International Conference on Acoustics, Speech and Signal Processing (ICASSP)*, May 2019, pp. 4295–4299.

[123] Y.-C. Wang, X. Wang, H. Liu, and Z.-Q. Luo, "On the design of constant modulus probing signals for MIMO radar," *IEEE Trans. Signal Process.*, vol. 60, no. 8, pp. 4432–4438, Aug 2012.

[124] Z. Luo, W. Ma, A. M. So, Y. Ye, and S. Zhang, "Semidefinite relaxation of quadratic optimization problems," *IEEE Signal Processing Magazine*, vol. 27, no. 3, pp. 20–34, May 2010.

[125] L. Li, H. Yang, G. Cui, L. Kong, and X. Yang, "Efficient phase-modulated waveform design for active sensing systems," in *2014 IEEE Radar Conference*, May 2014, pp. 1006–1009.

[126] S. Zhang and Y. Huang, "Complex quadratic optimization and semidefinite programming," *SIAM Journal on Optimization*, vol. 16, no. 3, pp. 871–890, 2006. [Online]. Available: https://doi.org/10.1137/04061341X

[127] A. M.-C. So, J. Zhang, and Y. Ye, "On approximating complex quadratic optimization problems via semidefinite programming relaxations," *Mathematical Programming*, vol. 110, no. 1, pp. 93–110, Jun 2007. [Online]. Available: https://doi.org/10.1007/s10107-006-0064-6

[128] M. Grant and S. Boyd, "CVX: Matlab software for disciplined convex programming, version 2.1," http://cvxr.com/cvx, Mar. 2014.

[129] G. Cui, X. Yu, G. Foglia, Y. Huang, and J. Li, "Quadratic optimization with similarity constraint for unimodular sequence synthesis," *IEEE Transactions on Signal Processing*, vol. 65, no. 18, pp. 4756–4769, Sep. 2017.

[130] A. De Maio, Y. Huang, M. Piezzo, S. Zhang, and A. Farina, "Design of optimized radar codes with a peak to average power ratio constraint," *IEEE Trans. Signal Process.*, vol. 59, no. 6, pp. 2683–2697, June 2011.

[131] D. R. Fuhrmann and G. S. Antonio, "Transmit beamforming for MIMO radar systems using signal cross-correlation," *IEEE Trans. Aerosp. Electron. Syst.*, vol. 44, no. 1, pp. 171–186, January 2008.

[132] D. J. Rabideau, "MIMO radar waveforms and cancellation ratio," *IEEE Trans. Aerosp. Electron. Syst.*, vol. 48, no. 2, pp. 1167–1178, 2012.

[133] H. Deng, Z. Geng, and B. Himed, "MIMO radar waveform design for transmit beamforming and orthogonality," *IEEE Trans. Aerosp. Electron. Syst.*, vol. 52, no. 3, pp. 1421–1433, June 2016.

[134] K. Alhujaili, V. Monga, and M. Rangaswamy, "MIMO radar beampattern design under joint constant modulus and orthogonality constraints," in *2018 52nd Asilomar Conference on Signals, Systems, and Computers*, Oct 2018, pp. 1899–1904.

[135] M. Deng, Z. Cheng, Y. Lu, Z. He, and G. Ren, "Waveform design for MIMO radar transmit beampattern formation with good range sidelobes," in *2019 IEEE Radar Conference*, April 2019, pp. 1–5.

[136] A. Hassanien and S. A. Vorobyov, "Phased-MIMO radar: A tradeoff between phased-array and MIMO radars," *IEEE Trans. Signal Process.*, vol. 58, no. 6, pp. 3137–3151, June 2010.

[137] D. R. Fuhrmann, J. P. Browning, and M. Rangaswamy, "Signaling strategies for the hybrid MIMO phased-array radar," *IEEE Journal of Selected Topics in Signal Processing*, vol. 4, no. 1, pp. 66–78, 2010.

[138] J. Yang, A. Aubry, A. De Maio, X. Yu, and G. Cui, "Design of constant modulus discrete phase radar waveforms subject to multi-spectral constraints," *IEEE Signal Processing Letters*, pp. 1–1, 2020.

[139] W. Huang, M. M. Naghsh, R. Lin, and J. Li, "Doppler sensitive discrete-phase sequence set design for MIMOs radar," *IEEE Trans. Aerosp. Electron. Syst.*, pp. 1–1, 2020.

[140] X. Yu, G. Cui, J. Yang, J. Li, and L. Kong, "Quadratic optimization for unimodular sequence design via an ADPM framework," *IEEE Trans. Signal Process.*, pp. 1–1, 2020.

[141] X. Yu, G. Cui, J. Yang, and L. Kong, "MIMO radar transmit–receive design for moving target detection in signal-dependent clutter," *IEEE Transactions on Vehicular Technology*, vol. 69, no. 1, pp. 522–536, 2020.

[142] R. A. Horn and C. R. Johnson, *Matrix Analysis*, 2nd ed. USA: Cambridge University Press, 2012.

[143] K. Deb, *Multi-objective optimization using evolutionary algorithms*. John Wiley & Sons, 2001, vol. 16.

[144] A. De Maio and Y. Huang, "New results on fractional QCQP with applications to radar steering direction estimation," *IEEE Signal Processing Letters*, vol. 21, no. 7, pp. 895–898, 2014.

[145] W. Dinkelbach, "On nonlinear fractional programming," *Management Science*, vol. 13, no. 7, pp. 492–498, 1967.

[146] S. Sedighi, K. V. Mishra, M. R. B. Shankar, and B. Ottersten, "Localization with one-bit passive radars in narrowband internet-of-things using multivariate polynomial optimization," 2020.

[147] A. Gharanjik, M. Soltanalian, M. R. B. Shankar, and B. Ottersten, "Grab-n-pull: A max-min fractional quadratic programming framework with applications in signal and information processing," *Signal Processing*, vol. 160, pp. 1 – 12, 2019.

[148] A. Aubry, A. De Maio, B. Jiang, and S. Zhang, "Ambiguity function shaping for cognitive radar via complex quartic optimization," *IEEE Trans. Signal Process.*, vol. 61, no. 22, pp. 5603–5619, Nov 2013.

[149] A. Aubry, A. De Maio, A. Zappone, M. Razaviyayn, and Z. Luo, "A new sequential optimization procedure and its applications to resource allocation for wireless systems," *IEEE Trans. Signal Process.*, vol. 66, no. 24, pp. 6518–6533, 2018.

[150] B. Chen, S. He, Z. Li, and S. Zhang, "Maximum block improvement and polynomial optimization," *SIAM Journal on Optimization*, vol. 22, no. 1, pp. 87–107, Jan 2012.

[151] D. Bertsekas, *Nonlinear Programming*. Athena Scientific, 1999.

[152] C. A. C. Coello, G. B. Lamont, and D. A. V. Veldhuizen, *Evolutionary Algorithms for Solving Multi-Objective Problems (Genetic and Evolutionary Computation)*. Berlin, Heidelberg: Springer-Verlag, 2006.

[153] Y. Li, S. A. Vorobyov, and Z. He, "Design of multiple unimodular waveforms with low auto- and cross-correlations for radar via majorization-minimization," in *2016 24th European Signal Processing Conference (EUSIPCO)*, Aug 2016, pp. 2235–2239.

[154] K. Shen and W. Yu, "Fractional programming for communication systems—part i: Power control and beamforming," *IEEE Transactions on Signal Processing*, vol. 66, no. 10, pp. 2616–2630, 2018.

[155] R. A. Horn and C. R. Johnson, *Matrix analysis*. Cambridge university press, 2012.

[156] J. C. Bezdek and R. J. Hathaway, "Convergence of alternating optimization," *Neural, Parallel & Scientific Computations*, vol. 11, no. 4, pp. 351–368, 2003.

[157] J. R. Senning, "Computing and estimating the rate of convergence," 2007.

[158] "Cvx package," http://cvxr.com/cvx/, accessed: 2021-06-07.

[159] A. Aubry, V. Carotenuto, A. De Maio, A. Farina, A. Izzo, and R. S. L. Moriello, "Assessing power amplifier impairments and digital predistortion on radar waveforms for spectral coexistence," *IEEE Transactions on Aerospace and Electronic Systems*, vol. 58, no. 1, pp. 635–650, 2022.

[160] A. Aubry, A. D. Maio, and M. M. Naghsh, "Optimizing radar waveform and doppler filter bank via generalized fractional programming," *IEEE Journal of Selected Topics in Signal Processing*, vol. 9, no. 8, pp. 1387–1399, Dec 2015.

[161] L. Zhao and D. P. Palomar, "Maximin joint optimization of transmitting code and receiving filter in radar and communications," *IEEE Trans. Signal Process.*, vol. 65, no. 4, pp. 850–863, Feb 2017.

[162] J.-P. Crouzeix and J. A. Ferland, "Algorithms for generalized fractional programming," *Math. Program.*, vol. 52, pp. 191–207, 05 1991.

[163] D. R. Hunter and K. Lange, "A tutorial on mm algorithms," *The American Statistician*, vol. 58, no. 1, pp. 30–37, 2004. [Online]. Available: https://doi.org/10.1198/0003130042836

[164] A. Aubry, A. DeMaio, A. Farina, and M. Wicks, "Knowledge-aided (potentially cognitive) transmit signal and receive filter design in signal-dependent clutter," *IEEE Trans. Aerosp. Electron. Syst.*, vol. 49, no. 1, pp. 93–117, Jan 2013.

[165] J. Capon, "High-resolution frequency-wavenumber spectrum analysis," *Proceedings of the IEEE*, vol. 57, no. 8, pp. 1408–1418, Aug 1969.

[166] M. M. Naghsh, M. Modarres-Hashemi, M. Alaee-Kerahroodi, and E. H. M. Alian, "An information theoretic approach to robust constrained code design for MIMO radars," *IEEE Trans. Signal Process.*, vol. 65, no. 14, pp. 3647–3661, July 2017.

[167] M. M. Naghsh, M. Soltanalian, and M. Modarres-Hashemi, "Radar code design for detection of moving targets," *IEEE Trans. Aerosp. Electron. Syst.*, vol. 50, no. 4, pp. 2762–2778, October 2014.

[168] S. Boyd, N. Parikh, E. Chu, B. Peleato, and J. Eckstein, "Distributed optimization and statistical learning via the alternating direction method of multipliers," *Foundations and Trends® in Machine Learning*, vol. 3, no. 1, pp. 1–122, 2011. [Online]. Available: http://dx.doi.org/10.1561/2200000016

[169] M. Razaviyayn, M. Hong, and Z.-Q. Luo, "A unified convergence analysis of block successive minimization methods for nonsmooth optimization," *SIAM Journal on Optimization*, vol. 23, no. 2, pp. 1126–1153, Sep 2013.

[170] P. Setlur and M. Rangaswamy, "Waveform design for radar STAP in signal dependent interference," *IEEE Transactions on Signal Processing*, vol. 64, no. 1, pp. 19–34, Jan 2016.

[171] S. M. O'Rourke, P. Setlur, M. Rangaswamy, and A. L. Swindlehurst, "Quadratic semidefinite programming for waveform-constrained joint filter-signal design in stap," *IEEE Transactions on Signal Processing*, vol. 68, pp. 1744–1759, 2020.

[172] L. Zheng, M. Lops, Y. C. Eldar, and X. Wang, "Radar and communication coexistence: An overview: A review of recent methods," *IEEE Signal Processing Magazine*, vol. 36, no. 5, pp. 85–99, 2019.

[173] J.-H. Lim, D.-W. Lim, B. L. Cheong, and M.-S. Song, "Spectrum sharing in weather radar networked system: Design and experimentation," *IEEE Sensors Journal*, vol. 19, no. 5, pp. 1720–1729, 2019.

[174] M. Alaee-Kerahroodi, E. Raei, S. Kumar, and M. R. B. Shankar, "Coexistence of communications and cognitive mimo radar: Waveform design and prototype," 2021.

[175] H. Griffiths, L. Cohen, S. Watts, E. Mokole, C. Baker, M. Wicks, and S. Blunt, "Radar spectrum engineering and management: Technical and regulatory issues," *Proceedings of the IEEE*, vol. 103, no. 1, 2015.

[176] A. F. Martone, K. D. Sherbondy, J. A. Kovarskiy, B. H. Kirk, C. E. Thornton, J. W. Owen, B. Ravenscroft, A. Egbert, A. Goad, A. Dockendorf, R. M. Buehrer, R. M. Narayanan, S. D. Blunt, and C. Baylis, "Metacognition for radar coexistence," in *2020 IEEE International Radar Conference (RADAR)*, 2020, pp. 55–60.

[177] A. F. Martone, K. D. Sherbondy, J. A. Kovarskiy, B. H. Kirk, J. W. Owen, B. Ravenscroft, A. Egbert, A. Goad, A. Dockendorf, C. E. Thornton, R. M. Buehrer, R. M. Narayanan, S. Blunt, and C. Baylis, "Practical aspects of cognitive radar," in *2020 IEEE Radar Conference (RadarConf20)*, 2020, pp. 1–6.

[178] A. F. Martone and A. Charlish, "Cognitive radar for waveform diversity utilization," in *2021 IEEE Radar Conference (RadarConf21)*, 2021, pp. 1–6.

[179] A. F. Martone, K. D. Sherbondy, J. A. Kovarskiy, B. H. Kirk, R. M. Narayanan, C. E. Thornton, R. M. Buehrer, J. W. Owen, B. Ravenscroft, S. Blunt, A. Egbert, A. Goad, and C. Baylis, "Closing the loop on cognitive radar for spectrum sharing," *IEEE Aerospace and Electronic Systems Magazine*, vol. 36, no. 9, pp. 44–55, 2021.

[180] J. Li and P. Stoica, *MIMO radar signal processing*. John Wiley & Sons, 2008.

[181] A. Khawar, A. Abdelhadi, and C. Clancy, *MIMO radar waveform design for spectrum sharing with cellular systems: a MATLAB based approach.* Springer, 2016.

[182] B. H. Kirk, K. A. Gallagher, J. W. Owen, R. M. Narayanan, A. F. Martone, and K. D. Sherbondy, "Cognitive software defined radar: A reactive approach to rfi avoidance," in *2018 IEEE Radar Conference (RadarConf18)*, 2018, pp. 0630–0635.

[183] D. Ma, N. Shlezinger, T. Huang, Y. Liu, and Y. C. Eldar, "Joint radar-communication strategies for autonomous vehicles: Combining two key automotive technologies," *IEEE Signal Processing Magazine*, vol. 37, no. 4, pp. 85–97, 2020.

[184] "Ettus research," https://www.ettus.com/, accessed: 2021-01-19.

[185] "National instruments," https://www.ni.com/en-gb.html, accessed: 2021-01-19.

[186] "Overview of the LabVIEW communications application frameworks," https://www.ni.com/en-gb/innovations/white-papers/14/overview-of-the-labview-communications-application-frameworks.html, accessed: 2021-01-21.

[187] "NI labview LTE framework," https://www.ni.com/en-us/support/documentation/supplemental/16/labview-communications-lte-application-framework-2-0-and-2-0-1.html, accessed: 2021-01-24.

[188] F. Laforest, "Generic models: a new approach for information systems design," in *Proceedings of the Third Basque International Workshop on Information Technology - BIWIT'97 - Data Management Systems*, 1997, pp. 189–196.

[189] P. Borwein and R. Ferguson, "Polyphase sequences with low autocorrelation," *IEEE Transactions on Information Theory*, vol. 51, no. 4, pp. 1564–1567, Apr 2005.

[190] J. Yang, A. Aubry, A. De Maio, X. Yu, G. Cui, and S. Iommelli, "Constant modulus discrete phase radar waveforms design subject to multi-spectral constraints," in *2020 IEEE 7th International Workshop on Metrology for AeroSpace (MetroAeroSpace)*, 2020, pp. 28–31.

[191] M. S. Gowda and R. Sznajder, "Schur complements, Schur determinantal and Haynsworth inertia formulas in Euclidean Jordan algebras," *Linear Algebra Appl*, vol. 432, pp. 1553–1559, 2010.

[192] "RAQ issue 195: A guide for choosing the right RF amplifier for your application," https://www.analog.com/en/analog-dialogue/raqs/raq-issue-195.html, accessed: 2022-02-25.